MSc

2.º CICLO

FCUP
2016

Studying evolved stars with Herschel observations

João Manuel da Silva Santos

U.PORTO
FACULDADE DE CIÊNCIAS
UNIVERSIDADE DO PORTO

Studying evolved stars with Herschel observations

João Manuel da Silva Santos

Dissertação de Mestrado apresentada à
Faculdade de Ciências da Universidade do Porto
Mestrado em Astronomia

2016

MSc

Studying evolved stars with Herschel observations

João Manuel da Silva Santos
Mestrado em Astronomia
Departamento de Física e Astronomia
2016

Orientador
Carmen Sánchez Contreras, Research Scientist
Centro de Astrobiología (CAB), CSIC-INTA

Coorientador
Pedro Garcia Lario, Research Scientist
European Space Astronomy Centre (ESAC)

U.PORTO

FC FACULDADE DE CIÊNCIAS
UNIVERSIDADE DO PORTO

Todas as correções determinadas pelo júri, e só essas, foram efetuadas.

O Presidente do Júri,

Porto, ______/______/_________

MSc

Faculdade de Ciências da Universidade do Porto

Departamento de Física e Astronomia

Studying evolved stars with Herschel observations

Master's degree in Astronomy

João Manuel da Silva Santos

Supervisor:

Carmen Sanchez Contreras, CAB/INTA-CSIC

Co-supervisor:

Pedro Garcia Lario, ESAC

2015/2016

Acknowledgments

This work would not have been possible without the opportunity and financing provided by ESAC Human Resources and the Science Operations Department in collaboration with the ESAC Faculty and the ESA Education Office.

I would like to thank my supervisor Dr. Carmen Sánchez Contreras for her tireless support and for being always so helpful, steering me in the right direction. I thank my co-supervisor Dr. Pedro García-Lario for his mentoring and comments during the progress of this work. I leave a word of gratitude to Jésus Medina (PhD student) for providing the spectral data and with whom I used to meet almost weekly to discuss the progress of our work. I also would like to thank the Herschel/PACS expert Dr. Elena Puga for the enlightening meetings and advice.

I thank my friends from CAB and ESAC for their comments and thoughts, and for contributing for the most amazing trainee experience. Finally I want to thank my parents for their unconditional support. This accomplishment would not have been possible without them.

João Santos

Abstract

A systematic inspection of the far-infrared (FIR) properties of evolved stars allows not only to constrain physical models, but also to understand the chemical evolution that takes place in the end of their lives.

In this work we intend to study the circumstellar envelopes (CSE) on a sample of stars in the THROES catalogue from AGB/post-AGB stars to planetary nebulae using photometry and spectroscopy provided by the PACS instrument on-board Herschel telescope. In the first part we are interested in obtaining an estimate of the size of FIR emitting region and to sort our targets in two classes: point-like and extended. Secondly, we focus on the molecular component of the envelope traced by carbon monoxide (CO) rotational lines. We conduct a line survey on a sample of evolved stars by identifying and measuring flux of both ^{12}CO and ^{13}CO isotopologues in the PACS range, while looking at the overall properties of the sample. Lastly, we will be interested in obtaining physical parameters of the CSE, namely gas temperature, mass and mass-loss rate on a sample of carbon stars. For that, we make use of PACS large wavelength coverage, which enables the simultaneous study of a large number of CO transitions, to perform the rotational diagram analysis.

We report the detection of CO emission in a high number of stars from the catalogue, which were mostly classified as point-like targets with a few exceptions of planetary nebulae. High J rotational number transitions were detected in a number of targets, revealing the presence of a significant amount of hot gas (T $\sim 400-900$ K) and high mass-loss rates. We conclude that Herschel/PACS is in a privileged position to detect a new population of warmer gas, typically missed in sub-mm/mm observations.

Keywords: Evolved stars; Circumstellar envelope, far-infrared, mass-loss rate

Resumo

Uma inspeção sistemática das propriedades de estrelas evoluídas no infra-vermelho longínquo (FIR) permite não só refinar modelos físicos como também perceber a evolução química na fase final das suas vidas.

Neste trabalho pretende-se estudar o envelope circum-estelar (CSE) numa amostra de estrelas do catálogo THROES, desde AGB/post-AGB até nebulosas planetárias, usando fotometria e espetroscopia do instrumento PACS a bordo do telescópio Herschel. Primeiramente, estamos interessados em estimar a dimensão da região que emite no FIR, separando objetos pontuais de extensos. De seguida, concentramo-nos na componente molecular do envelope, em particular na medição do fluxo de transições rotacionais dos isotopólogos da molecula de monóxido de carbono: ^{12}CO e ^{13}CO. Por último, estamos interessados em obter parâmetros físicos do CSE, nomeadamente temperatura, massa de gás e taxa de perda de massa num conjunto de estrelas de carbono. Para tal, fazendo uso da grande cobertura de comprimento de onda de Herschel/PACS que nos permite estudar um grande número de transições simultaneamente, analisamos o chamado diagrama rotacional.

Detetou-se emissão de CO num número elevado de objetos do catálogo, maioritariamente classificados como objetos pontuais excetuando algumas nebulosas planetárias. Encontraram-se transições correspondentes a elevados níveis rotacionais que revelam a presença de uma quantidade significativa de gás quente (T $\sim 400 - 900$ K) assim como taxas de perda de massa elevadas. Conclui-se que Herschel/PACS é capaz de identificar uma nova população de gás quente tipicamente não detetável em observações no sub-mm/mm.

Palavras-chave: Estrelas evoluídas, envelope circum-estelar, infravermelho longínquo, taxa de perda de massa

Contents

List of Figures

List of Tables

Acronyms & Abbreviations

AGB Asymptotic-giant-branch

AIC Akaike's information criterion

BIC Bayesian information criterion

CI Confidence interval

CSE Circumstellar envelope

FIR Far infra-red

FWHM Full width at half maximum

GCV Generalized cross-validation

HPF High-pass filter

HSA Herschel Science Archive

HST Hubble Space Telescope

IRAS Infrared Astronomical Satellite

LTE Local thermodynamic equilibrium

MIR Mid infra-red

NIR Near infra-red

PACS Photoconductor Array Camera and Spectrometer

PN Planetary nebula

PPN Pre-planetary nebula

PSF Point spread function

RMSE root-mean-square error

SNR Signal-to-noise ratio

THROES Catalogue of Herschel Observations of Evolved Stars

WD White-dwarf

Chapter 1

Introduction

1.1 Post-main sequence evolution of low-to-intermediate-mass stars

As the hydrogen in the stellar core is depleted, the star drifts away from the main-sequence in the Hertzsprung-Russell diagram. Soon it begins to fuse helium in its core producing carbon and oxygen while burning hydrogen in a surrounding spherical shell. This process causes the star to gradually grow in size and luminosity, but to decrease its effective temperature. This marks the beginning of the red giant phase where the convective motions in the upper layers start to alter the chemical composition at the surface. These flows bring material from the core to the top inducing convective mixing in a phenomenon known as "dredge-up" that has been studied with spectroscopy for many evolved stars.

1.1.1 From the AGB to the WD stage

The fate of these stars depends critically on their mass. Asymptotic giant branch (AGB) stars are an advanced evolutionary phase of low-to-intermediate mass stars powered by nuclear burning. At this stage the core is electron-degenerate, made of carbon and oxygen. The He-core phase was about 10 times shorter than the H-core burning phase, and this following phase will be even shorter. For stars with initial (main-sequence) mass of less than 8 $M_{\odot}$, carbon does not ignite, so the C/O core contracts, becoming increasingly electron-degenerate. This means that during the early AGB phase, the He shell burning

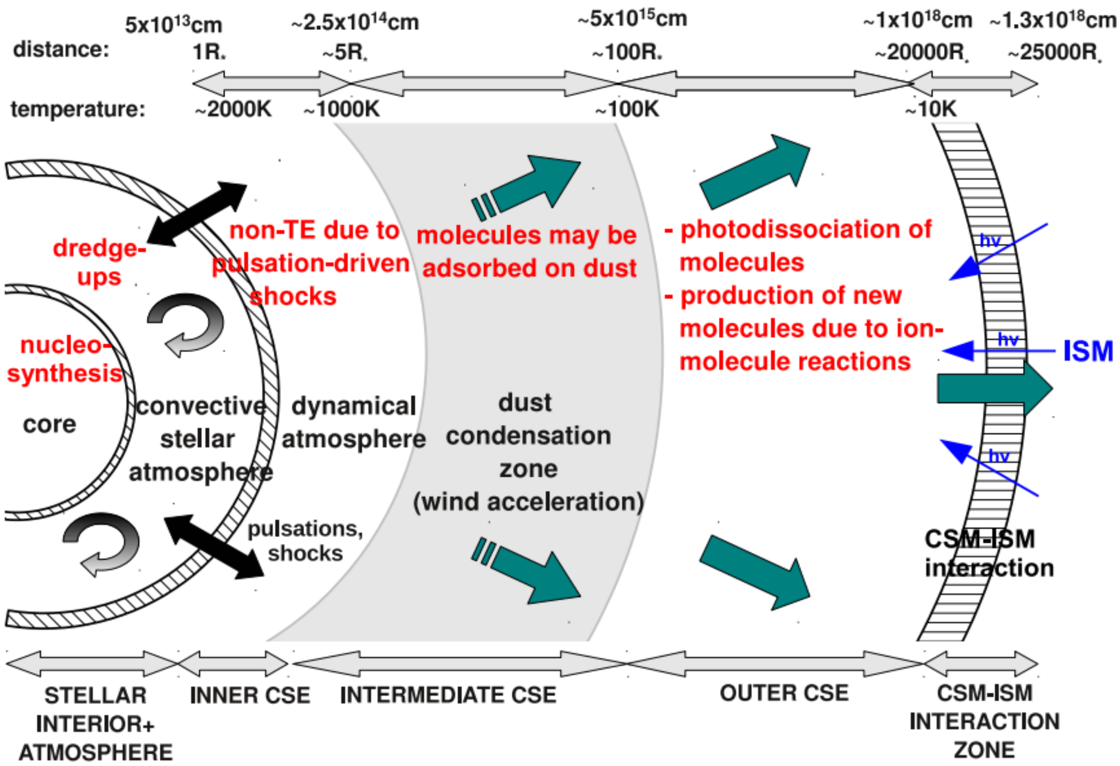

Fig. 1.1: Schematic diagram of an AGB star (Decin, 2012) showing some physical mechanisms that take place in these stars and in their environment. The distance is in units of stellar radius R_*.

dominates the energy output of the star. A recent review about the evolution throughout the asymptotic giant branch was presented by Herwig (2005).

Figure 1.1 shows a schematic view from the inside of an AGB star to its surroundings. A "tiny" core is surrounded by an extended envelope up to several hundred $R_* = \mathrm{R}_\odot$. The gas and dust that are able to escape the gravitational attraction form a cool (<1500 K), stellar wind best studied in the infrared. These stellar winds and the mass loss process in general, create huge extended circumstellar shells extending up to 3 pc in some cases. To understand the wind acceleration mechanisms and to derive the intricate structure of the envelopes, it is important to understand the later evolutionary stages of the bulk of stars in our Galaxy. Indeed, using a standard Salpeter initial mass function (IMF), 97% of all stars will eventually go through the AGB phase where mass-loss dominates stellar evolution, i.e., the star cannot be regarded as a sphere of gas in hydrostatic equilibrium anymore. The effect of nucleosynthesis and subsequent convective mixing determine the abundance structure of the stellar layers. Thermodynamic equilibrium and non-equilibrium reactions as well as ion-molecule reactions and dust condensation take place.

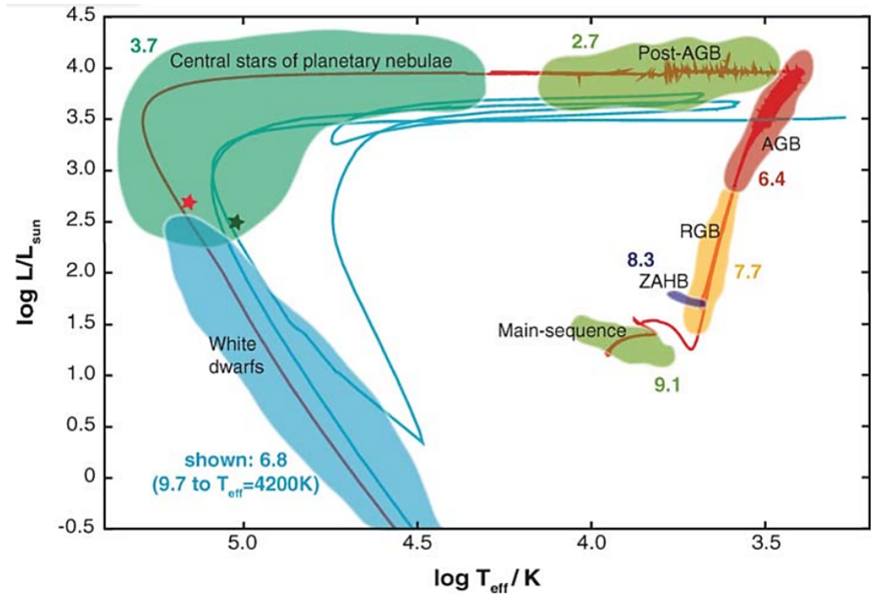

Fig. 1.2: Evolutionary tracks in a Hertzprung-Russell diagram of a 2 $M_{\odot}$ star (Herwig, 2005). The numbers indicate the logarithm of the approximate duration of each phase.

The final phase of AGB evolution is characterised by thermonuclear flashes, or pulses, causing instabilities. Every time a dominant nuclear burning event occurs, a dredge-up may follow. After the first event in the end of the H-burning phase, another convective mixing can be induced in the end of the He-burning phase. A later, third event actually originates a class of star named carbon-star, that we will study further on. The actual physics of AGB stars and their properties are beyond the scope of this thesis. Instead, we will be interested in studying the circumstellar shells, privileged by the view of the Herschel Space Observatory.

Once a solar-like star has exhausted its nuclear fuel, its core collapses into a white dwarf (WD) and the outer layers are expelled as a planetary nebula. In between, there is a short-lived stage ($\sim 10^3$ yr) named pre-planetary nebula (PPN) that is observationally quite distinct. This subject was reviewed, for example, by Winckel (2003).

Figure 1.2 depicts the evolutionary tracks of a 2 $M_{\odot}$ star from the main sequence to the WD stage. Post-AGB (or PPN) stars are stars that are not massive enough to fuse carbon, but are still too cold to ionise the circumstellar envelope (CSE) ejected during the AGB phase. One of the most well studied PPNs is AFGL 618 (e.g. Sánchez Contreras et al. 2002; 2004; Bujarrabal et al. 2010; Soria et al. 2013). The shape of the circumstellar envelope is more often than not far from spherical symmetry with constant mass-loss rate.

That is, for example, the case of AFGL 618 (the Westbrook Nebula). Figure 1.3 shows a picture of this object taken with the Wide Field Camera aboard HST in a field-of-view of $0.3' \times 0.3'$, together with another PPN - AFGL 2688 (the Egg Nebula) also imaged with Hubble. The detection of a very small ionised region in AFGL 618 suggests that this PPN is just about to enter the PN stage.

In a dark night in 1764, Charles Messier observed the first planetary nebula and recorded the observation as the number 27 of his catalogue of nebulous objects. Later, with better telescope resolution, some nebulae were found to be made up of stars - they were named galaxies, while other remained as gaseous material. PN were further distinguished from other galactic diffuse nebulae because they have definite structures and were often associated with a central star. This distinction became even more obvious with spectroscopy.

The spectra of PN are dominated by dust cooling or emission lines. The first emission line identified was a Balmer line of hydrogen ($H\beta$), although stronger, unknown lines could be seen in the spectrum at that time. A number of strong nebular lines remained unidentified for many years and there was some speculation about a mysterious element named "nebulium". Bowen (1928) identified 8 of the strongest nebular lines as being due to metastable states of [NI], [OII] and [OIII]. These metastable states lie a few electron volts above the ground state and are collisionally excited by electrons released upon photoionisation of hydrogen. The presence of highly excited, strong optical lines of oxygen was explained by Bowen (1935) as the result of fluorescence mechanisms[1]. Better observations led to the discovery that the emission lines in PN are broad, or even split as consequence of gas expansion. Table 3.1 shows some common atomic and fine-structure lines in the far-infrared. This lines are observed because the gas is extremely rarefied. Figure 1.3 shows an impressive example of a composite optical image of NGC 6537, a high-excitation PN.

As the gaseous envelope expands away a dense white dwarf (WD) is left behind. Note that for very low-mass stars the WD may be He rich, since they will probably lose their envelope before the He flash[2]. Therefore, all central stars of PN are expected to evolve to

[1] Emission due to excitation by radiation.

[2] Although this is probably not the origin of He-rich WDs since this process takes too long. Accretion from a

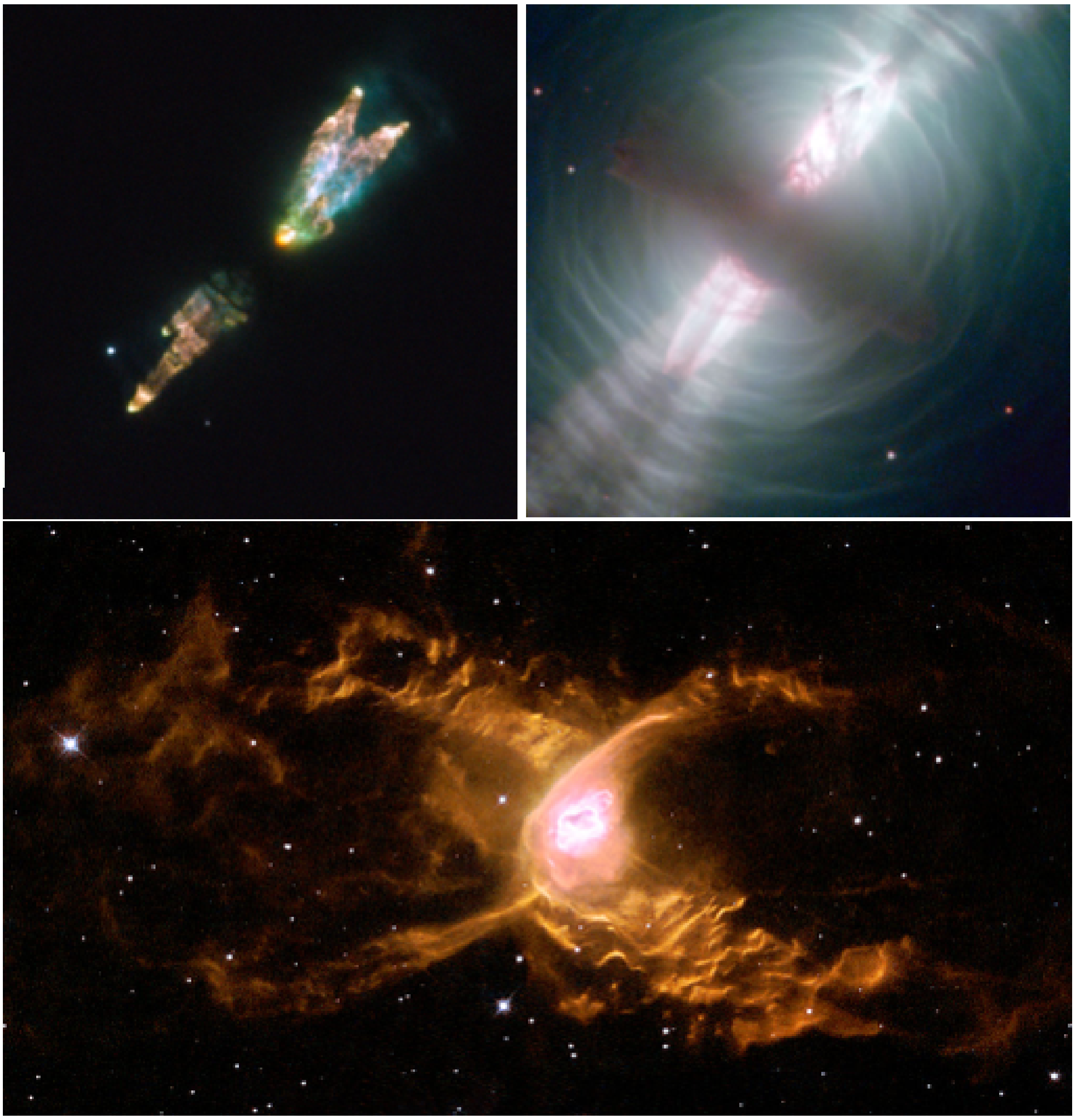

Fig. 1.3: Top: HST WFC3 camera images of AFGL 618 and AFGL 2688 (Credit: ESA/Hubble & NASA); Bottom: Composite HST image of NGC 6537 (Credit: ESA & Garrelt Mellema, Leiden University).

become WDs, but not all WDs necessarily pass through the PN stage. WDs are mostly composed of electron-degenerate matter so they are supported against collapse by the degeneracy pressure[3] of the electron gas in their interior. They slowly cool and radiate away stored thermal energy for a time superior to the age of the Universe.

binary companion is the most plausible scenario.

[3]Electrons resist compression due to Pauli's exclusion principle.

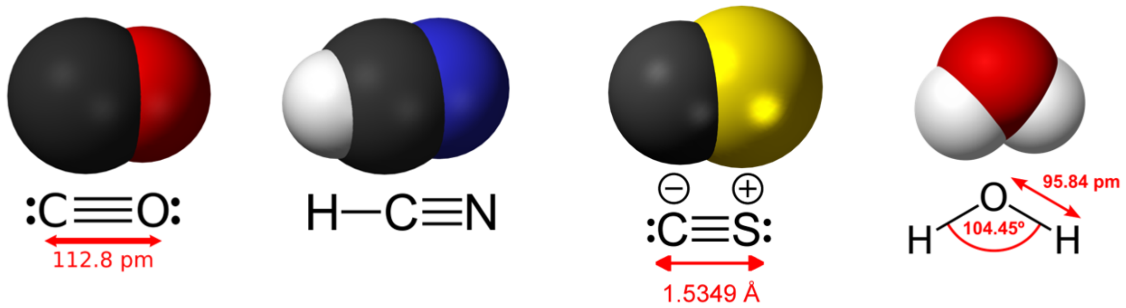

Fig. 1.4: A representation of some of the most common molecules in CSEs and their Lewis structure.

1.1.2 Overview of the gas chemistry of CSEs

The chemical composition of the circumstellar envelope (CSE) reflects the nucleosynthesis and the dredge-up mechanism that took place deep inside the star.

The gas composition of the CSE is partly determined by the carbon-to-oxygen (C/O) ratio. A C/O>1 implies that all the oxygen is locked in CO, giving no room for the creation of other oxygen-bearing molecules. This leads to the so-called carbon stars. On the other hand, a C/O<1 means that no carbon-bearing molecules apart from CO could ever form, leading to an oxygen-rich (O-rich) environment. Stars with a C/O-ratio $\sim$ 1 are called S-type stars and are believed to be an intermediate evolutionary stage between O-rich and C-rich stars. Spectra of O-rich stars are usually dominated by refractory species such as SiO, TiO and AlO, whereas the spectra of C-rich stars are dominated by CO lines. This simplified picture has been challenged by the detection of SiO in C-rich stars and HCN and CO_2 in O-rich AGBs (Decin 2012, and references therein), which are not predicted by thermodynamic equilibrium models. In fact, the formation of carbon molecules in oxygen-rich environments is now thought to be the result of shock-induced non-equilibrium chemistry in the inner CSE (Duari et al. 1999).

Besides these classic chemical types there are also the OH/IR stars, which are basically stars that are bright in the IR and show a characteristic, U-shaped hydroxyl (OH) maser line that can be used to measure the expansion velocity of the gas. These are believed to be massive counterparts of O-rich stars in a stage between the AGB and PPN phase.

Research in evolved stars is not slowing down and a lot of questions remain open. For example: what are the physical processes that shape the CSE? what drives the mass-loss? what is the chemical/mass content of these objects and how does that affect their evolution? The astronomic community eagerly waits for more results of the Atacama Large Millimeter/submillimeter Array (ALMA) which will make possible direct imaging of the dust condensation zone in AGB stars as well as CO mapping with unprecedented resolution. Meanwhile, infrared Astronomy continues to supply important insights.

1.2 Infrared astronomy

The infrared region of the spectrum is of great scientific interest, not only because it is where cool objects (100-1000 K) radiate the majority of their energy, but also because of its rich variety of atomic, ionic, molecular and solid-state (dust) spectral features. Measurements at these wavelengths permit to infer physical parameters such as temperature, density and velocity, which are linked to processes taking place in evolved stars.

To date, almost 200 molecules have been detected[4] in the ISM and CSEs around evolved stars. However, a large number are only detected in the nearest carbon-rich AGB star IRC+10216 (e.g. Agúndez et al. 2014; Cernicharo et al. 2015). The chemical content of this object is rather impressive, in particular in the far-infrared and sub-mm, where rotational transitions are found.

The great advantage of infrared space telescopes is that they are not affected by atmospheric absorption. The Infrared Astronomical Satellite (IRAS) was the first IR space mission and found about 270000 sources, many of them AGB stars, very faint in visible wavelengths. The Infrared Space Observatory (ISO) came next with considerable improvements in both photometry and spectroscopy. It led to a huge advance in the understanding of the mass-loss phenomenon and allowed spectroscopic identification of many new dust species. Spitzer was also important, offering a somewhat better angular resolution and sensitivity than ISO. AKARI was launched in 2006 equipped with a photodetector and a camera operating in the NIR-to-MIR range. It was used, for example, to image extended emission around AGB stars.

[4] http://www.astro.uni-koeln.de/cdms/molecules

Finally, with Herschel infrared astronomy leaped forward thanks to its impressive wavelength coverage, well beyond ISO, great sensitivity and spectral resolution.

1.3 The Herschel Space Observatory

Herschel[5] was the largest infrared telescope ever built (Pilbratt et al. 2010). It was launched from the European spaceport in Kourou, French Guyana and remained active from 2009 to 2013. In this short period it provided a wealth of scientific data in virtually every branch of modern astronomy, from galaxy formation and evolution (e.g. Molinari et al., 2010; Cortese et al., 2013) to star formation (e.g. André et al. 2013; Palmeirim et al. 2013; Könyves et al., 2015), chemistry in the solar system and across the Universe (e.g. Muller et al. 2016; Bockelee 2014). It has been used even to probe dark matter (e.g. Amblard et al. 2011, Lacey et al. 2014). In particular, it has provided important insights into the very nature of evolved stars while enabling deeper understanding of the later stages of stellar evolution (Decin, 2012, and references therein). An overview of the first results of the Herschel mission was given by García-Lario (2012).

In this thesis we used data from the Photodetector Array and Camera Spectrometer (PACS), which is one of the three instruments on-board Herschel (Poglitsch et al. 2010).

1.3.1 PACS photometer

PACS photometer has 3 imaging bands: blue, green and red, centred around 70, 100 and 160 μm respectively (figure 1.6) and it is diffraction-limited. The field-of-view is of $3.5' \times 1.75'$. Projected onto the sky, pixel sizes are 3.2" and 6.4" in the blue/green and red bands respectively. The map-maker algorithms regrids the data from the pixel values of the detector array into maps projected on the sky, which allows to achieve a pixel size of 1.6" and 3.2" in those bands.

There are three observing modes: (1) - point-source photometry in chopping-nodding technique; (2) - scan map (small and larger fields) and (3) - scan map within PACS/SPIRE

[5] Herschel is an ESA space observatory with science instruments provided by European-led Principal Investigator consortia and with important participation from NASA.

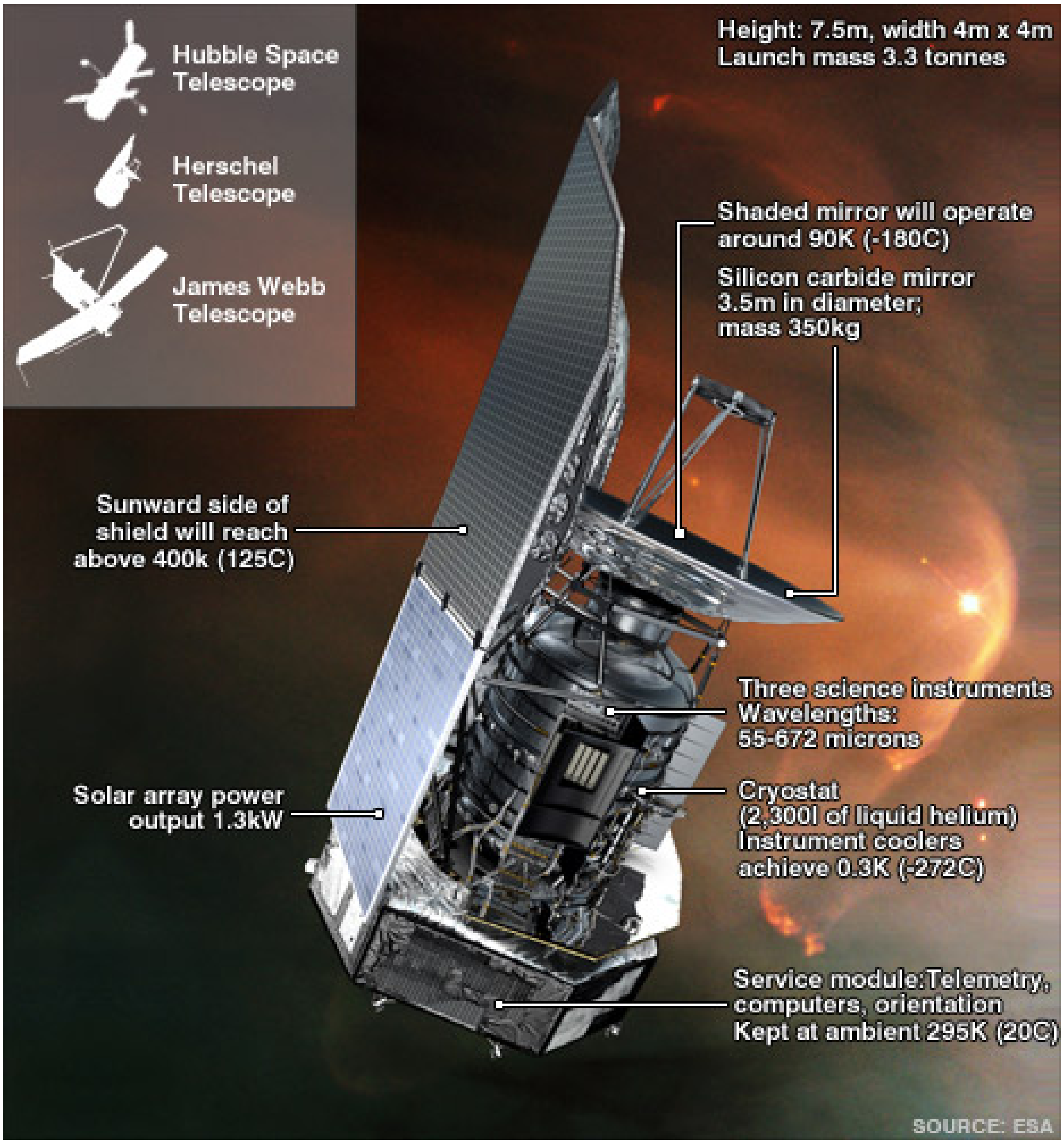

Fig. 1.5: Herschel design overview. Credit: ESA.

parallel mode. The scan technique is the most routinely used. It is in fact the default mode to observe large areas of the sky, but also recommended for point-sources (Poglitsch et al. 2010). There are several types of photometry maps that correspond to different data reduction techniques and better suit different targets. We discuss the use of high-pass-filter maps versus Jscanam maps further on.

The absolute flux calibration of the photometer is based on models of standard stars in the three filters: α Boo (Arcturus), α Tau, β And, α Ceti and γ Dra. Currently, the relative photometric accuracy is around 2% in all bands and the absolute flux calibration accuracy is mainly limited by the 5% uncertainty of the standard models (Balog et al.

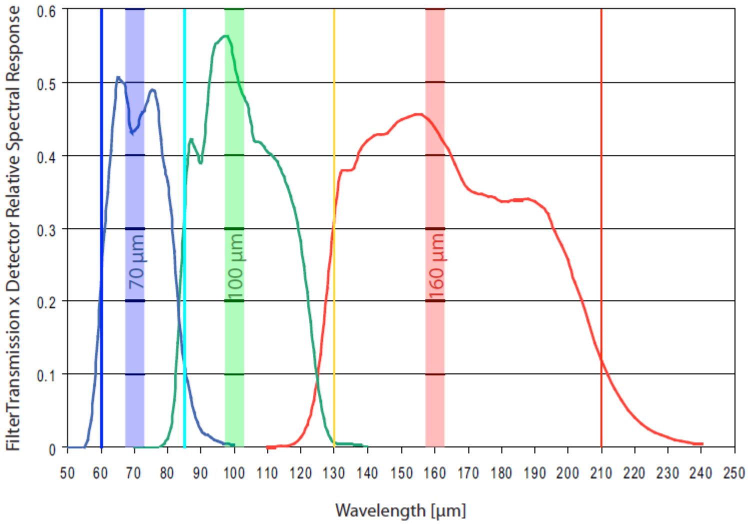

Fig. 1.6: Filter transmissions of the PACS photometer (Poglitsch et al. 2010). The reference wavelengths are 70 (blue), 100 (green) and 160 (red) μm.

2013).

An example of the scientific capabilities of the photometer were showcased in two papers (Mayer et al. 2013; 2014) where the authors report the detection of Archmidean spirals around R Aqr, W Aql and π^1Gruis (PI GRU), thus presenting solid evidence of a binary companion in all of them.

The final photometry products, namely high-pass-filter maps and Jscanam maps used in this thesis were downloaded from the public Herschel Science Archive (HSA) and they were not reprocessed.

1.3.2 PACS spectrometer

The spectrometer is a medium resolution, integral field unit that uses two Ge-Ga photoconductors arrays with 16×25 pixels (Poglitsch et al. 2010). One usually adopts the word "pixel" for the spectral pixels, while calling the 5×5 array "spaxels", which stands for "spatial pixels". However, in this work we will use at times both terms indistinctly, though the context will provide its clear meaning. The spaxel size is $9.4'' \times 9.4''$, hence the field-of-view is of $47'' \times 47''$. Figure 1.7 depicts the spectrometer concept. The integral-field unit provides 25 spectra in a large area of the sky in the 51-220 μm wavelength range. A diffraction grating is a reflective optical element with parallel, equally spaced grooves. For PACS the grating is 32 cm long and has 8.5 ± 0.05 grooves per mm which means that 2720

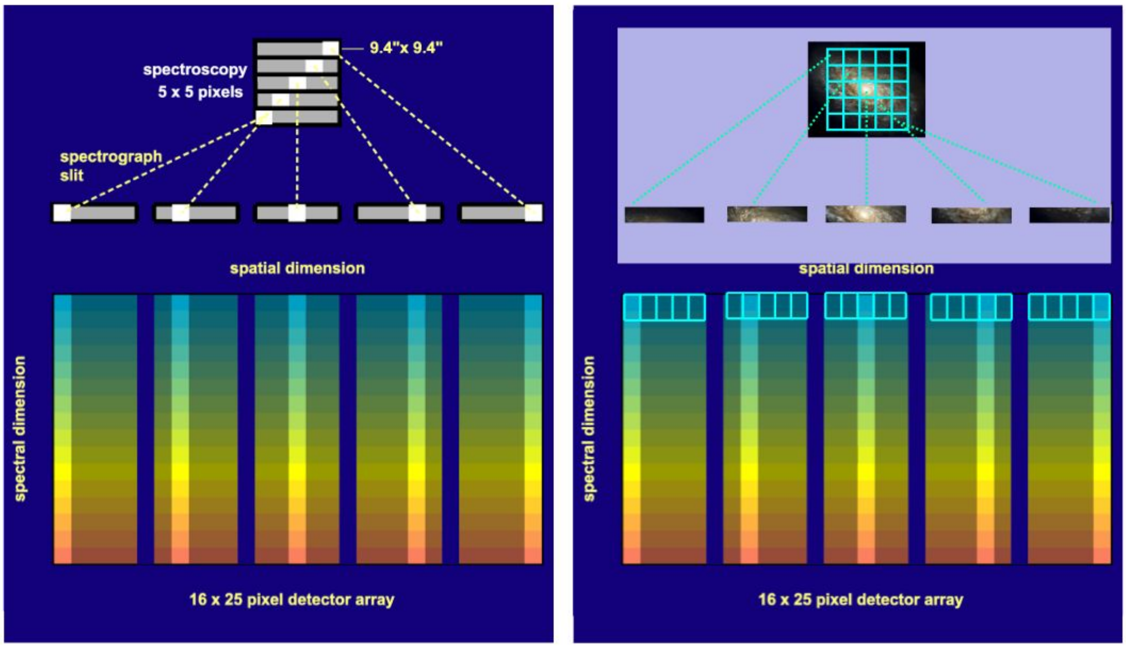

Fig. 1.7: Integral-field spectrometer concept. Credit: PACS observer Manual.

grooves cover the length of the grating.

PACS spectrometer has a resolving power $R = \lambda/\Delta\lambda$ between 940 and 5500, i.e. a wavelength-dependent spectral resolution of $\sim 55 - 320$ km s^{-1}.

There are three main observing modes: (1) - chopped line spectroscopy (for single lines); (2) - chopped range spectroscopy (large range) and (3) - wavelength switching mode, for single lines in extended sources. Recently the unchopped mode was also added.

The PACS spectrometer flux calibration accuracy is constrained by detector response drifts and pointing jitter, limiting both the absolute flux accuracy and relative accuracy within a band. The accuracy to assume when comparing relative line fluxes within a spectral band is around 10% between $70 - 100$ μm and 20% between $100 - 190$ μm. There is also another source of uncertainty when comparing flux in different spaxels of typically 10%.

PACS has been crucial to reveal the gas and dust content of circumstellar envelopes around AGB/post-AGB stars. In this context it allowed, for example, the discovery of the 69 μm feature attributed to crystalline olivine, or forsterite, in a sample of 48 targets (Blommaert et al. 2014). It also revealed the impressive molecular content of IRC+10216, one of the most well studied AGB stars (Decin et al., 2010), with the detection of very high rotational level transitions of SiO, SiS and CO. More recenlty it permitted the detection of warm H_2O vapor in carbon-rich AGB stars (Lombaert et al. 2016).

All PACS spectra used in this thesis were already fully reduced and available through the THROES website.

1.4 The THROES catalogue

THROES stands for "caTalogue of HeRschel Observations of Evolved Stars" and contains a collection of Herschel PACS and SPIRE[6] spectra of over 100 evolved stars from AGBs to PPN and PN (Ramos-Medina et al. in prep.). Most stars are classified as low-to-intermediate mass stars ($< 8\ M_\odot$), but there are also few massive, hypergiant stars. Table A.1 summarises the number of stars organised in several classes in the catalogue with downloadable spectrum.

Table 1.1: Number of fully-reduced, available spectra in the THROES catalogue for each class.

<table>
<tr><th>Class</th><th>number</th><th></th></tr>
<tr><td>O-rich</td><td>22</td><td rowspan="4">AGB (43)</td></tr>
<tr><td>C-rich</td><td>16</td></tr>
<tr><td>S</td><td>4</td></tr>
<tr><td>C/S</td><td>1</td></tr>
<tr><td>OH/IR</td><td>15</td><td></td></tr>
<tr><td>post-AGB/PPN</td><td>28</td><td></td></tr>
<tr><td>PN</td><td>26</td><td></td></tr>
<tr><td>unclassified</td><td>1</td><td></td></tr>
<tr><td>total</td><td>113</td><td></td></tr>
</table>

At the moment of writting there are 113 stars in the catalogue with fully reduced spectrum, mostly AGB stars of types oxygen rich (O-rich), carbon rich (C-rich) and S type. The classification of MGE 4218 is not known with certainty so it was catalogued as a probable C or S (C/S) type. The only unclassified star in the catalogue is a blue supergiant[7] (HDE 269006). The remaining targets are PPN and PN in almost equal numbers.

[6] SPIRE - Spectral and Photometric Imaging Receiver is another Herschel instrument.

[7] SIMBAD classification.

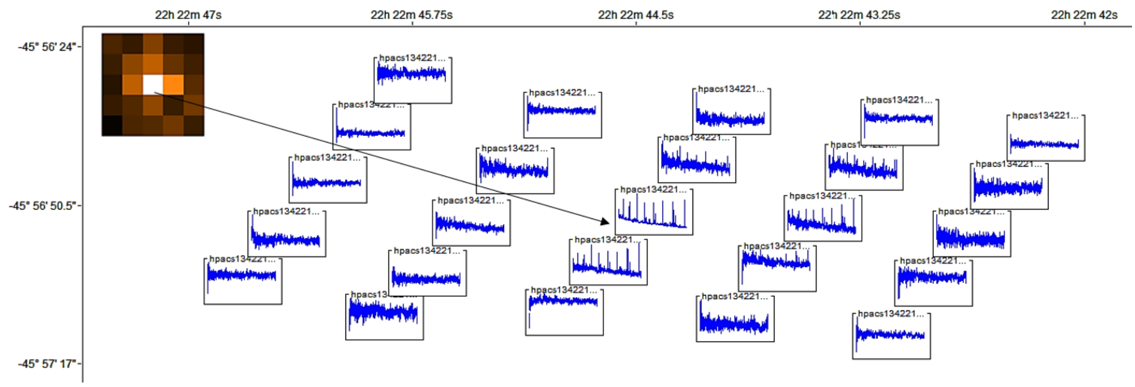

Fig. 1.8: An example of the spectrometer raster for the point-like target π^1Gruis. A cube slice at a selected wavelength channel is shown in the top left corner.

1.4.1 Data reduction and science ready products

All PACS range spectra used in this thesis were already available through the catalogue website and fully reduced. To build the catalogue, the data was obtained from the Herschel Science Archive (HSA) and the reduction was done interactively using the HIPE[8] software.

At the moment of writing, in the catalogue one can download 2 types of spectral data: (1) - rebinned cubes (figure 1.8) which contain one spectrum store in each spaxel of the 5×5 array and (2) - 1D spectra which are the central spaxel with point-source correction applied and scaled to the flux level of the central 3×3 superspaxel. In this thesis we used both products. In the example shown in figure 1.8 one sees that the actual usable spectra are found in the centre of the array, while the outer spaxels only contain background noise. This is, of course, what one expects to find for a point-like target. Moreover, in the website one can display the (FIR) SED of a star and compare fluxes observed with PACS to previous missions such as IRAS and AKARI.

Although PACS spectrometer observed between $51 - 210$ μm it suffered from spectral leakage (order overlap) in the ranges $51 - 55$ μm, $95 - 105$ μm and $190 - 210$ μm so the continuum shapes and flux densities in those ranges are not reliable. For that reason, these small ranges were cropped out of the final spectra. Another issue sometimes seen is a dip in the continuum that looks like a broad absorption feature situated between $62 - 63$ μm. This is interpreted as a filter artifact[9].

[8] Herschel Interactive Processing Environment (Ott, 2010)

[9] http://herschel.esac.esa.int/twiki/bin/view/Public/DpKnownIssues

1.4.2 Characterisation of the sample of stars

As mentioned before, the catalogue contains stars of various spectral types and evolutionary stages, thus different physical-chemical conditions in the CSE which we intend to investigate. In this section we expose the most important features that are relevant for this study.

The classic IRAS two-colour diagram is a way to infer the dust/gas properties of the CSE. Photometric data in IRAS bands at 12, 25, 60 and 100 μm are also provided in the THROES website and in the appendix in table A.2.

Following van der Veen & Habing (1988), IRAS colours are defined as:

$$[12] - [25] = -2.5 \ \log\left(\frac{F_\lambda(12)}{F_\lambda(25)}\right) \tag{1.1}$$

$$[25] - [60] = -2.5 \ \log\left(\frac{F_\lambda(25)}{F_\lambda(60)}\right) \tag{1.2}$$

where F_λ is the flux at a given wavelength. Figure 1.9 presents the IRAS two-colour diagram for the THROES targets with boxplots for each class. The AGB class (represented by black symbols) is further divided into 3 chemical types: O-rich, S and C-rich, corresponding to spectral types M, S and C respectively. The size of the boxplot is defined by the inter-quartile range (IQR) from $Q_1 = 25^{\text{th}}$ to $Q_3 = 75^{\text{th}}$ percentiles, while the whiskers extend to the most extreme data points not considered outliers, i.e., points that are outside $Q_1 - 1.5 \times \text{IQR}$ or $Q_3 + 1.5 \times \text{IQR}$. If the data is normally distributed this corresponds to $\pm 2.7\sigma$ that is 99.7% coverage. We see a clear separation between some classes. While AGB stars occupy the bottom left corner of the diagram with negative colours, the OH/IR and PN groups cluster around the centre, although the latter has greater scatter. Regarding AGBs, there is a notorious difference between the median colours of the sample of oxygen stars and carbon stars, which is probably a consequence of different dust properties because oxygen- and carbon-rich dust have different emissivities. The median [25]-[60] colours are -1.8 and -1.5 for the O-rich and C-rich groups respectively. Since these colours are linked to the black-body dust-cooling continuum, the diagram also provides a comparison between temperature conditions in the CSE. Hence, a distinction is also very clear in terms of tem-

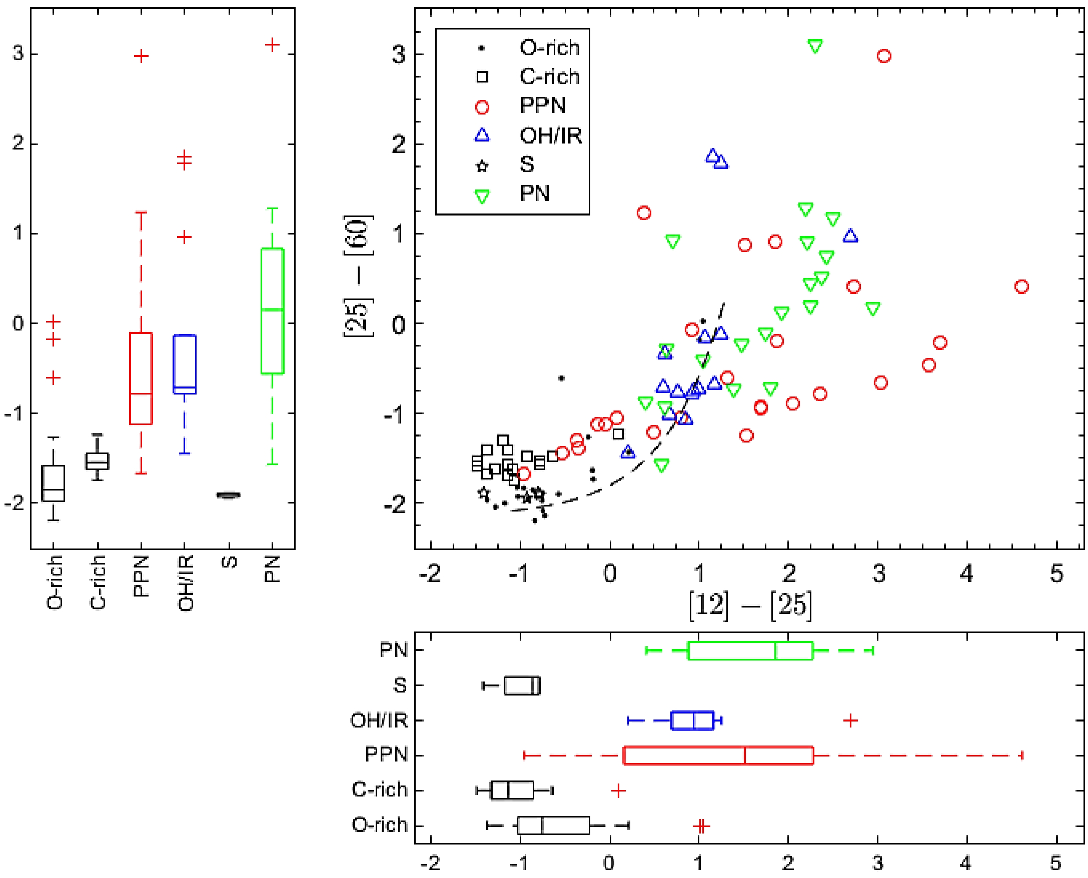

Fig. 1.9: IRAS color-color diagram of the THROES sample. The dashed line is the empiric relation for O-rich and OH/IR stars (see text).

perature, with the AGBs populating the hotter, lower left side of the diagram, while on the right side we find mainly PPN and PN with cold (T<200 K) dust emission.

Van der Veen & Habing (1988) concluded that O-rich and OH/IR stars follow a evolutionary track towards increasing IRAS colours, and found the following empiric relation:

$$[25] - [60] = -2.15 + 0.35\ e^{1.5\ ([12]-[25])} \tag{1.3}$$

which is draw in figure 1.9 as well. So the points located to the right of the main cluster of O-rich stars at $[12] - [25] \sim -1$ in our sample are likely to be relatively older stars. At that time the authors interpreted this trend as evidence that a star with a given mass starts the evolutionary track at the lower left side of the diagram and then evolves to the upper right to become a OH/IR star, with increasing mass-loss rates. There is 1 OH/IR star which is flagged as an outlier because it seems unusually cold

Variability is another characteristic of many evolved stars and it is linked to radial pulsations and mass-loss. In fact, most of the AGB stars in this sample are known to be variable. There are several Mira variables[10] (e.g. omi Cet, AFGL 3116, etc.), semi-regular[11] (e.g. U Hya, CIT 6, etc.) and RV Tau variables[12] (e.g. U Mon, AC Her, etc). The complete list of targets can be found in table A.1 in the appendix.

In what regards spectral features, namely atomic/ionic and molecular lines, we devote a section to the identification of the most common chemical species found in our spectra in chapter 3.

To sum up, THROES contains a heterogeneous sample of evolved stars whose study allows to draw a complete picture of the physical-chemical conditions in the end of their lives.

1.5 Outline of the thesis

This thesis is essentially divided in three parts. Each chapter starts with a brief introduction to the topic and in the end a summary is presented with the main conclusions. In the first part, we are interested in obtaining an estimate of the angular size of our targets, or at least an upper limit for point-like sources. For that, we fitted spectral cubes and photometry maps with a 2D-Gaussian model and established comparisons whenever possible. This procedure and discussion can be found on chapter 2. In the second part we explore the molecular content of these targets and conduct a CO survey in our spectra, while looking for correlations between line fluxes and continuum fluxes. We present a PACS colour-colour diagram that is able to separate stars in different evolutionary stages. We also compute isotopologue ratios. In chapter 4, we estimate physical conditions such as temperature and column density . Focusing on CO lines, we obtained the so-called rotational diagram for a sample of carbon-rich targets spanning several evolutionary stages from AGB stars to planetary nebulae. We also estimate the mass-loss rate from the derived gas mass. In chapter 5 we present final remarks and future prospects.

[10] Miras have very regular pulsations with an average period of $\sim$ 400 days (V-band)

[11] Semi-regular stars show irregularities in their pulsations (20-2000 days)

[12] They are very luminous stars (few thousand $L_\odot$) with periodicity of 40-150 days.

Chapter 2

Point-like and extended far-infrared sources

Our initial sample of PACS range observations stored in the THROES catalogue is diverse, containing 113 objects in different evolutionary stages. We want to estimate the angular extent of the emission traced by PACS and further classify them as point-like or extended targets compared to PACS field-of-view.

The method we present here is to fit a Gaussian model directly to spectral cubes. We will present the main issues regarding this procedure and how to partly overcome them. Moreover, we perform the same routine in photometry counterparts to assess the reliability of the procedure and we compare the results.

2.1 PACS point-spread-function

First of all, we have to understand how the images are produced. The point-spread-function, hereafter PSF, is the response of an imaging system to a point source and it is crucial to understand an astronomical observation. In other words, it describes how the observed flux is smeared by the optics.

Whereas in ground based telescopes the PSF is dominated by the astronomical seeing (except in radio wavelengths), in space, Herschel is actually diffraction-limited (Poglitsch et al. 2010), i.e., it is capable of observing at its theoretical limit. Thus an Herschel observation will be limited by its maximum angular resolution. In our case the resulting image will be a convolution (notated $*$) of the observed flux, the PSF and the effect of the

PACS squared detector array:

$$image = true\ image * PSF * pixel\ size \tag{2.1}$$

At this point it is important to refer that the spectrometer usually does not properly sample (spatially) the PSF with a single pointing due to the large spaxel size. We will address this issue further on. In what follows we will indistinctly use the terms PSF and beam as synonyms of the same entity.

We first focused on measuring the PSF size for both PACS spectrometer and photometer, instead of taking the commonly assumed values in literature. Essentially we will be measuring the term $[PSF * pixel\ size]$ in equation 2.1, which will be different for both instruments. Obviously the true PSF of a given observation may differ from the model due to pointing jitter and other effects, but at least by doing this in a systematic way we get a grasp of the range of possible values one can expect to find. This allows not only a deeper understanding of the instrumental response, but also a way to better separate true point-like from extended sources. The first ones should have a FWHM comparable to the PSF while the extended sources would fill the $47'' \times 47''$ spectrometer field-of-view (FOV).

2.1.1 A 2D elliptical Gaussian model

The inner-part of the of the diffraction pattern can be approximated by a 2-dimensional Gaussian function $f(x, y)$ for its simplicity and efficiency. The model is given by:

$$f(x,y) = P \exp\left(-\left(A(x-x_o)^2 + 2B(x-x_o)(y-y_o) + C(y-y_o)^2\right)\right) \tag{2.2}$$

with:

$$A = \frac{\cos^2\theta}{2\sigma_x^2} + \frac{\sin^2\theta}{2\sigma_y^2} \tag{2.3}$$

$$B = \frac{\sin 2\theta}{4\sigma_x^2} - \frac{\sin 2\theta}{4\sigma_y^2} \tag{2.4}$$

$$C = \frac{\sin^2\theta}{2\sigma_x^2} + \frac{\cos^2\theta}{2\sigma_y^2} \tag{2.5}$$

where P is the peak intensity, x_0 and y_0 are the peak coordinates, θ is the position angle measured counterclockwise and σ_x and σ_y are the dispersion (or width) of the gaussian in two orthogonal directions, which will be either the major or minor axis depending on the axis from where the rotation starts. The FWHM $= 2\sqrt{2\ln 2}\,\sigma \sim 2.355\,\sigma$ is then computed for both directions so that we get the major axis of the ellipse a and the minor axis b, at half-intensity. Figure 2.1 depicts a 81×81 resolution image with a mock, unit-normalised-gaussian distribution.

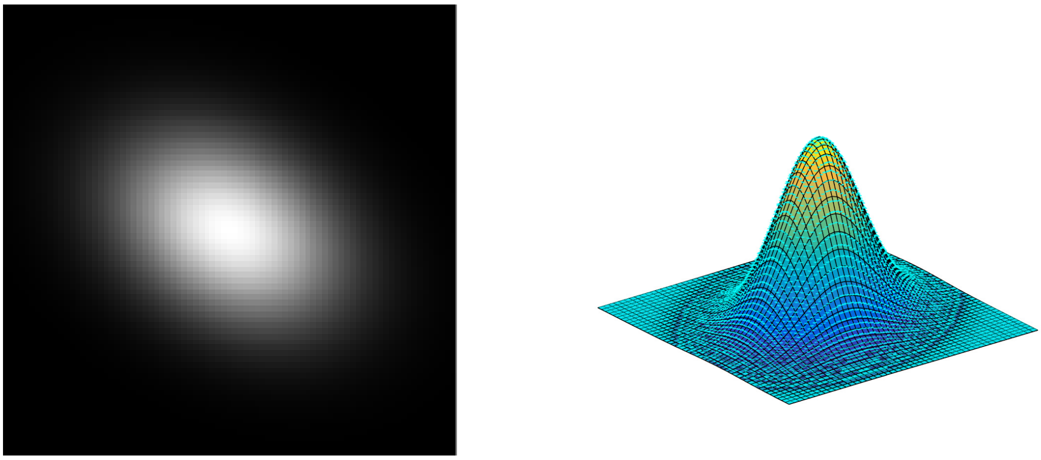

Fig. 2.1: Gaussian model validation with mock data; left: 2D-gaussian distribution; right: Visualisation in 3D.

To perform the fit we used a Trust-Region-Reflective numeric algorithm (e.g. review from Yuan 2015) which is basically a mathematical optimization operation in the least-squares sense, very effective for solving non-linear problems.

Given the variance σ_i^2 (not to be confused with the gaussian width) associated with each data point, the weights are defined as: $w_i = 1/\sigma_i^2$. The code was implemented in MATLAB by making use of the function *fit*[1]. To check the goodness of fit we analysed the root-mean-squared-error (RMSE), also know as the standard error of the regression, which is defined as the square root of the sum of the squared residuals divided by the number of degrees of freedom. The latter is defined as the number of response values minus the number of parameters. The RMSE should be small in a good fit.

[1] http://es.mathworks.com/help/curvefit/fit.html

2.1.2 PACS Spectrometer: modelling Neptune

In this section we intend to measure the spectrometer beam size. As aforementioned, its shape is not fully Gaussian as it may show a triple lobe morphology. However, it should be a fairly good approximation in the inner region.

The beam efficiencies have been measured via raster maps on Neptune at a few selected wavelengths, where several telescope pointings are combined to produce a better sampled image. At the moment we were carrying this study, the beam size had been computed for an older version of the calibration files. To obtain the newest possible estimates and to re-check if the code implementation is correct, we decided to compute ourselves the dependence of the beam size with wavelength. For that we used version 6 of calibration files, which are the most recent ones[2]. We downloaded from the calibration web page peak normalised images multiplied by the point-source correction calibration and interpolated into a final 0.5" grid. The raster maps are available for the following wavelength channels: [55, 62, 68, 73, 75, 84, 94, 110, 125, 136, 145, 150, 168, 187] μm and different positions in the field-of-view. The images where the target is too close to the border were excluded, hence we ended up with 153 usable images. Our code was validated by comparing the results with HIPE's task *sourceFitting*, which fits a similar model and returns the same parameters and excellent agreement was found.

We start by creating a circular mask to crop the image around the object. The brightest pixel provides the initial guess for the peak intensity and central coordinates. An example is shown in figure 2.2 where the Neptune map and the fit residuals at 168 μm for a given position in the FOV are presented. Some residual flux in the outer part is visible, despite being mostly under a 15% level.

The fitting procedure was repeated in a systematic way for 153 images, i.e., different positions of Neptune in the field-of-view and 14 available wavelength channels. That is at least 10 images per channel. Then, we defined $\Phi_{\rm PSF}$ as the equivalent circular FWHM (or

[2] http://herschel.esac.esa.int/twiki/bin/view/Public/PacsCalibrationWeb#PACS_calibration_and_performance

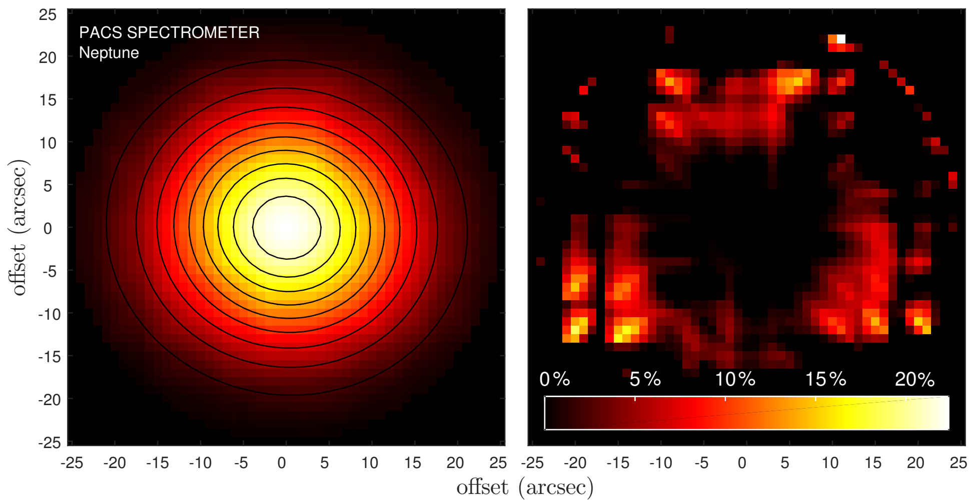

Fig. 2.2: Neptune raster observation at 168μm, mod7 (px = 0.5"). Left: data and model contours; Right: fit residuals in percentage scale.

simply "beam size") by averaging the major and minor axis at half-intensity as follows:

$$\Phi_{\rm PSF} = \sqrt{a.b} \tag{2.6}$$

such that the uncertainty propagates approximately as:

$$\delta_\Phi \approx \sqrt{\left|\frac{\partial \Phi}{\partial a}\right|^2 \delta_a^2 + \left|\frac{\partial \Phi}{\partial b}\right|^2 \delta_b^2} = (a.b)^{-1/2}\sqrt{b^2\delta_a^2 + a^2\delta_b^2} \tag{2.7}$$

where δ_a and δ_b are the major and minor axis standard deviation respectively. The values obtained for each position are averaged so that we obtain an estimate of the beam size for each channel. The results are presented in figure 2.3. Besides a fluctuation with typical standard deviation of 0.2" in every channel, essentially two features can be seen: (1) - the beam size stays roughly constant at least up to 100μm, from where (2) - it increases almost linearly with wavelength λ. In fact, we found a best-linear fit for the latter component given by:

$$\Phi_{\rm PSF}(\lambda) = 0.036\lambda + 5 \tag{2.8}$$

with $R^2 = 0.96$ (coefficient of determination) and 95% CIs $[0.027, 0.045]$, and $[4, 7]$ on the slope and intercept respectively. The FWHM values we obtained agree very well with the ones reported in the data analysis guide for older versions of the calibration files, thus ensuring that the model and its implementation are working properly. The results

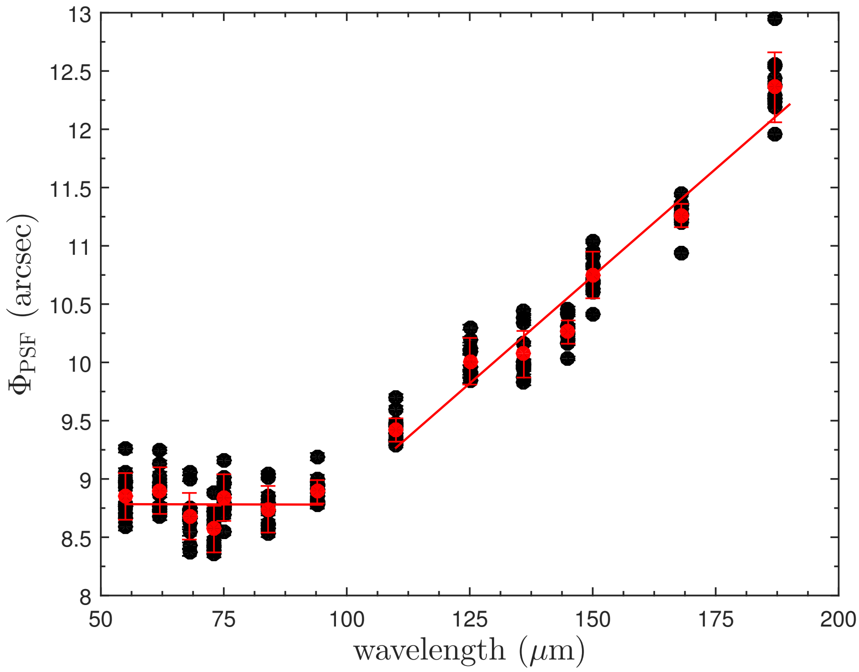

Fig. 2.3: Variation of the beam FWHM (modelling Neptune) with wavelength, across the field-of-view. The red points are average values with standard deviation error bars and the red lines are best-linear-fits.

are listed in table 2.1. The FWHM as a function of wavelength currently provided by in the HSA with every OBSID is reproduced in the appendix in figure B.1. There is a difference in the way the results are shown, namely by the use of a interpolation to achieve a smooth curve. Nevertheless we see a good qualitative agreement. The complete table with all measurements at different positions and wavelength channels can be found in the appendix (table A.3).

2.1.3 PACS Photometer: modeling Vesta

The PSF of the PACS photometer is characterised by a narrow core, a tri-lobe structure at few percent level and faint diffraction "rings" (Lutz 2015).

For PACS photometer, current best PSFs have been determined on mapping observations of the asteroid Vesta. Recently Bocchio el al. (2016) compared Vesta observations to Mars, which is brighter, thus used to better trace the faint wings. Again, as we are only interested in measuring the FWHM, we only studied Vesta photometric data.

The shape and width of the PSF depends on the observation mode: an elongation along the scan direction and an overall broadening for higher scan speeds is expected (e.g. Lutz

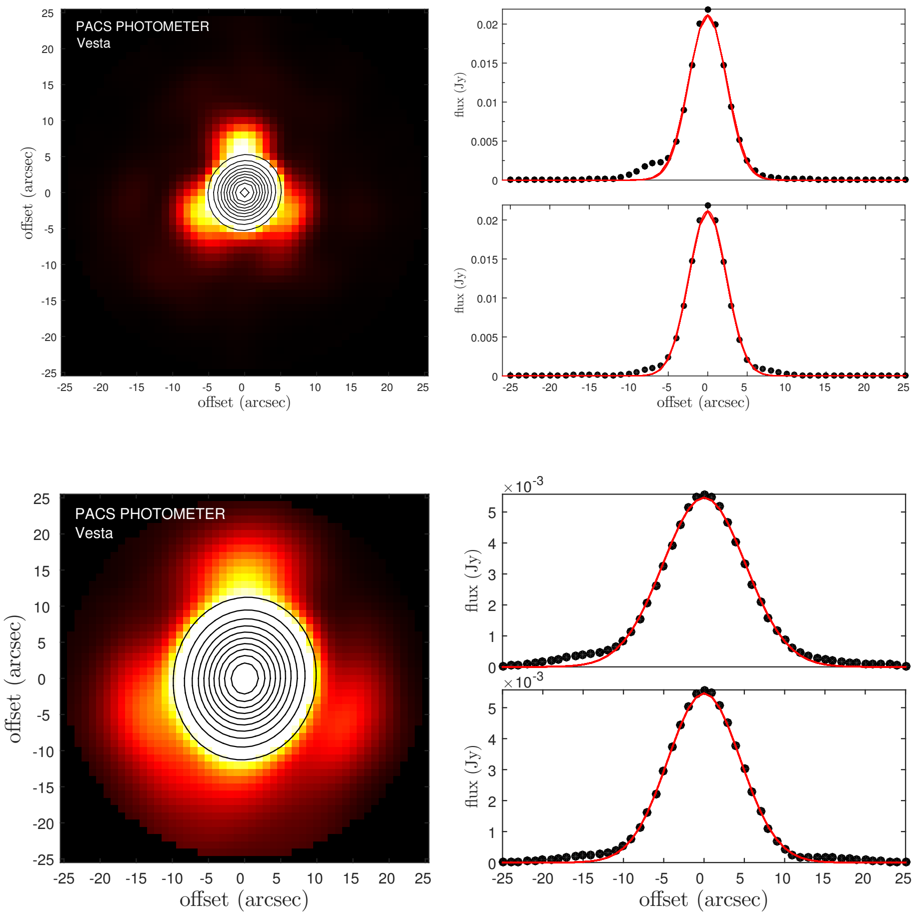

Fig. 2.4: Photometer PSF in the blue band (top) and red band (bottom) modeled for the asteroid Vesta (px = 1"). The flux levels were chosen to enhance the 3-lobe visibility. On the right side two orthogonal projections are displayed.

2015). For example, for a given observation with array-to-map angle of $+63^{o}$ we obtained a size variation from 5.4" for the slow mode (10"/s) to 7.2" in the fast mode (60"/s) in the blue band and from 11.2" to 12.4" in the red band.

We fitted Vesta observations with the same model as we as we did for Neptune, this time for different angles ($+63^{o}$, $+42^{o}$, -42^{o}) and data reduction steps in both red and blue bands. These observations were interpolated to achieve a sampling of 1". Photometry maps are usually requested at the standard medium scan speed (20"/s) which produces a fairly circular inner gaussian profile, at least in the blue range. For example, for recentered observations the ellipticity in the blue band is 0.05 while in the red band is 0.13. The latter translates in a difference of $\sim 1.5''$ between the major and minor axis of the ellipse. Hence, when comparing the PSF to a particular observation one should try to match both the scan speed and the position angle. The latter is not always possible simply because

Table 2.1: Average PACS FWHM derived for the spectrometer and photometer (scan speed 20"/s) using Neptune and Vesta observations respectively.

PACS spectrometer	
wavelength (μm)	$\Phi_{\rm PSF}$ (arcsec)
55	8.8 ± 0.2
62	8.9 ± 0.2
68	8.7 ± 0.2
73	8.6 ± 0.2
75	8.8 ± 0.2
84	8.7 ± 0.2
94	8.9 ± 0.1
110	9.4 ± 0.1
125	10 ± 0.2
136	10.1 ± 0.2
145	10.3 ± 0.1
150	10.7 ± 0.2
168	11.3 ± 0.1
187	12.4 ± 0.3
PACS photometer	
Camera	$\Phi_{\rm PSF}$ (arcsec)
Blue (70)	5.5 ± 0.3
Red (160)	11 ± 0.4

there is no PSF model data for every possible orientation.

Therefore, we focused on studying Vesta observations performed in the same scan speed mode as our targets. We used 23 images: 11 in the blue band and 12 in the red band. Figure 2.4 shows two examples of the fit in both bands. It is clear that the Gaussian model is not capable of fitting the faint extended wings, but as far we are concerned, we intend to obtain an estimate of the FWHM so the approximation in the inner region is very good. The complete table with the parameters derived for these 23 images can be found in the appendix A.4. Repeating the fit for the remaining images we found an average FWHM (with standard deviation) of $\sim 5.5'' \pm 0.3$ and $\sim 10.9'' \pm 0.4$ in the blue and red bands respectively. These results are also listed in table 2.1. For recentered observations which are in principle corrected for pointing jitter effects and inaccuracies of the spatial calibration, we obtained a FWHM of $\sim 5.6''$ and $\sim 11.3''$ in very good agreement with values in literature (Bocchio el al. 2016).

We also confirmed that the scanning direction does not affect the shape and size of the PSF for medium scan speeds as stated by Bocchio et al. (2016). This means that the average FWHM of a target can be directly compared to the average beam FWHM for any angle, i.e., matching the PSF model to a given target for the exact same angle is not so important on average terms. Note, of course, this arises from the fact that we are only modelling the inner core of the PSF.

At this stage we have computed the size of PACS beam sampled by the 2 instruments and estimated the uncertainty of this quantity. With this in mind we are able to establish a range of possible values one expects to obtain when fitting other point-like targets, as we will present in the next sections.

2.2 Fitting spectral cubes

In this section we explain how we fitted directly PACS rebinned cubes. For every wavelength step (normally from 55-190 μm) we obtain an image of the object and perform the fit as aforementioned.

Note that spectral cubes were never designed for imaging purposes in first place, so a careful inspection of the results was necessary. Furthermore, we know beforehand that the fit is not going to be nearly as good as in the previous Neptune or Vesta data due to the much larger spaxel size (9.4"). In particular, for point-like objects the PSF will be spatially undersampled as we have concluded from figure 2.3 where we see that the PSF size is actually even smaller than the spaxel in the bluest part of the spectrum.

This represents a violation of the Nyquist-Shannon sampling theorem that states that a signal is completely determined when the sampling rate is higher than twice the maximum frequency of the signal. This means in this case that at least 2-to-3 detectors should fit within the FWHM of the telescope PSF to prevent loss of spatial information (Regibo 2012). Thus the parameters obtained in these conditions are unreliable. However, this approach may still be useful to simply try to find out whether the source is point-like or

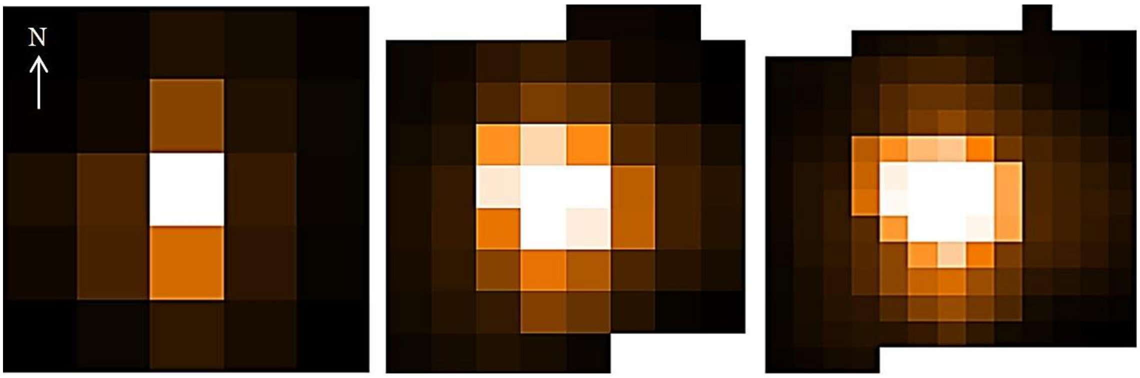

Fig. 2.5: Example of a 5 × 5 PACS rebinned cube (left) and two interpolated cubes (right) at $\lambda \sim 155\mu$m. This target is the pre-planetary nebula AFGL 618. From left to right the spaxel size is 9.4″, 4.7″ and 3″.

extended. In addition, not only the position angle is harder to be perceived with such little resolution, it can also be artificially produced due to the uneven grid of the spectrometer footprint.

To improve this procedure, we also performed the fit in interpolated cubes obtained using HIPE task *specInterpolate*. In this kind of cube the number of spaxels is increased to a desired value. An example of these cubes is illustrated in figure 2.5.

2.2.1 Fitting channel by channel

We want to model the $5 \times 5 \times N$ cube that contains 25 spectra of a given object in 2 or 4 wavelength ranges, depending on how the observation was carried. For each layer of the cube, i.e. each wavelength step, we obtain a 5×5 image and perform the Gaussian fit.

We obtain an average FWHM, notated $\Phi = \sqrt{a.b}$, by averaging the derived major and minor axis at half-maximum for each wavelength step. Additionally, we compute a weighted average around selected wavelengths to directly compare to our beam size. For an arbitrary parameter, x:

$$\bar{x} = \frac{\sum_{i=1}^{n} \left(x_i \sigma_i^{-2}\right)}{\sum_{i=1}^{n} \sigma_i^{-2}} \tag{2.9}$$

so that the variance of the mean is given by;

$$\sigma_{\bar{x}}^2 = \frac{1}{\sum_{i=1}^{n} \sigma_i^{-2}} \tag{2.10}$$

We deconvolve the obtained average size with the corresponding beam FWHM (table 2.1) using:

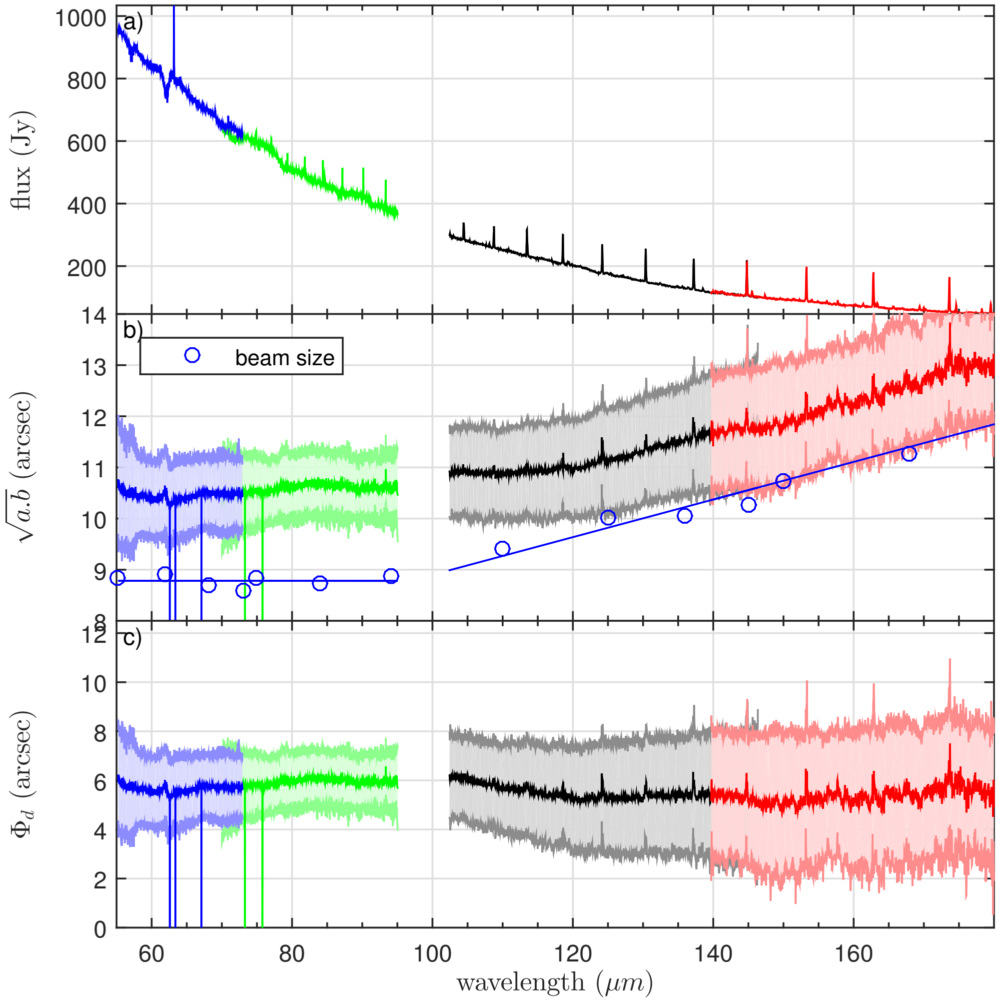

Fig. 2.6: Fitting rebinned cubes layer-by-layer: the case study of AFGL 618. Top: PACS range spectra; Middle: average FWHM; Bottom: deconvolved size. The shaded area corresponds to 2σ bounds.

$$\Phi_d = \sqrt{\Phi^2 - \Phi_{\rm PSF}^2} \tag{2.11}$$

at selected wavelengths, with errors given approximately by:

$$\delta_{\Phi_d} = (\Phi^2 - \Phi_{\rm PSF}^2)^{-1/2}\sqrt{\Phi^2\delta_\Phi^2 + \Phi_{\rm PSF}^2\delta_{\Phi_{\rm PSF}}^2} \tag{2.12}$$

Note that equation 2.12 does not include absolute flux calibration errors.

Next we present a case study to exemplify the fitting across wavelength of AFGL 618. Figure 2.6 shows a PACS range spectra in the top pannel, the average FWHM in the middle and the deconvolved size in the bottom. For displaying purposes the entire range was deconvolved using the linear regression models, so that one can see that when subtracting the PSF from the image, the derived FWHM remains approximately constant with wavelength. AFGL 618 is regarded as a point-like target as observed with Herschel/PACS instrument. However, we see that for wavelengths shorter than 100 μm its average FWHM is systematically larger than the beam, well beyond the formal errors. We believe this is just a consequence of the square detector footprint blurring the image, as we know that its effect dominates in this range. In the reddest part of the spectra, the beam size increases almost linearly and so it does the Gaussian size of AFGL 618. However, in this portion of the spectrum, the measured size pretty much agrees with the beam size at a confidence level of 2σ. The sudden drops in size are due to channels with null variance for which the weighted-least-squares method fails. We also note that the estimated standard errors here are much larger than before, about 1-2".

An interesting feature that can be seen in few targets is what we call "extended line emission". In AFGL 618 it is pretty clear that some lines are slightly more extended than the continuum (figure 2.6). The ionised species found in the spectra of NGC 6537 are also a good example of extended emission. In figure 2.7 we show the spectral cube layers around an ionised carbon line ([CII]) where we see a clear difference in the flux contours compared to the continuum region. These larger sizes at line positions are rare and definitely not common in molecular emission. In other cases we observe that the derived FWHM stays constant with wavelength while in other targets the FWHM decreases at line positions. Regibo (2012) only found the latter case in their sample and attributes this effect to the instrumental design.

The fitting procedure was repeated, when possible, for the remaining targets in the catalogue. About 30 targets were excluded because they were not observed in the entire PACS range, but in rather small portions of the spectrum (~ 3 μm bands) so the fit results are not trustworthy. The FWHM was deconvolved at selected wavelengths by averaging it around an arbitrarily small number of channels. We chose 30, which is about 0.5 μm. The fit was also performed in continuum modelled cubes, i.e., cubes that contain spectra without spectral lines to verify if they impact significantly the derived FWHM. This was

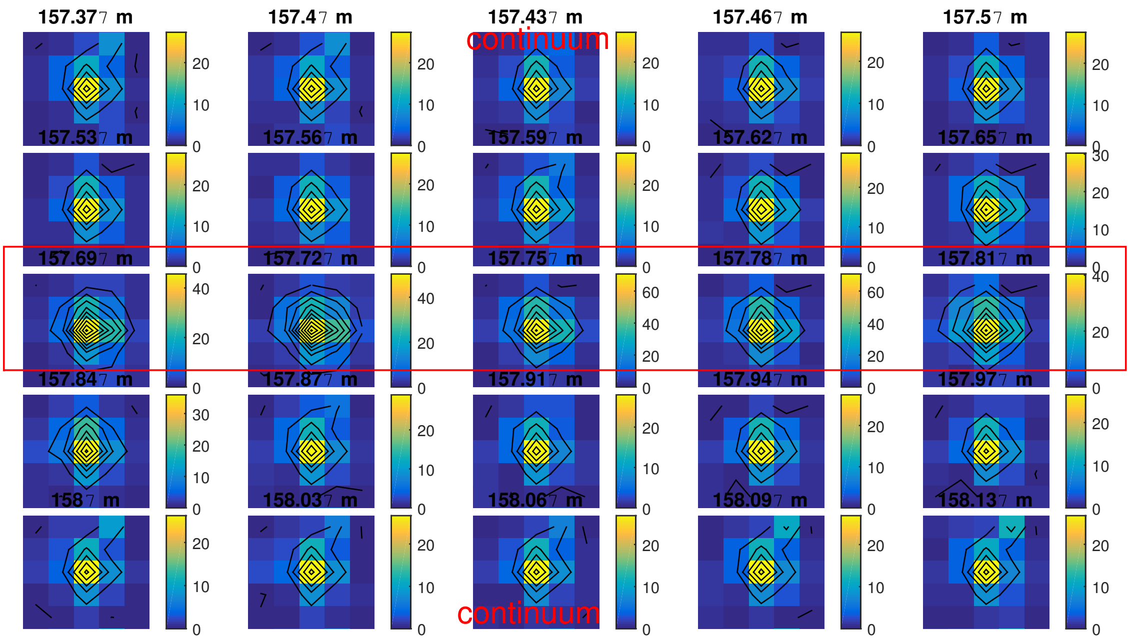

Fig. 2.7: Flux density contours around the [CII] line (157.7μm),in NGC 6537. The red box encloses the channels closer to the line peak position.

achieved by fitting a low-order polynomial to the spectra and masking out the lines using HIPE. We concluded that due to averaging their effect is mitigated, hence the reported sizes across wavelength reflect the FWHM of the continuum.

The fitting routine for this kind of data is much more sensitive to the peak intensity and flux ratios between the central and outer spaxels. For example, the fit is usually not good for very faint and noisy targets and it may fail to converge in targets where the peak intensity is not centred in the array. In particular, for point-like targets the relative (statistical) uncertainty in the FWHM can be quite high (up to 40%). It is difficult to evaluate the goodness of the fit in these conditions so a careful comparison with other data, methods and even literature is needed to assess the reliability of this procedure. This was achieved by comparing the FWHM for a "control-sample" of 20 targets for which we have photometry data. Before that we will explain in the next section how we used interpolated cubes to overcome the sampling limitation.

2.2.2 Interpolated cubes

HIPE has an algorithm - *specInterpolate*[3] that is able to do a linear interpolation to increase spatial resolution. However we are not interested in increasing the sampling too much, otherwise we would be including artifacts and unpredictable interpolation errors that HIPE currently does not provide. Thus we chose to double the spatial resolution so that the spaxel corresponds to $4.7''$. Note that single pointing observations do not allow reconstruction of the true morphology of the target, thus we regard our interpolated cubes as merely reasonable approximations.

2.3 Photometry maps

We cross-matched our target's table with entries in the HSA and we found 45 observed targets with PACS photometer, most of them first published in Cox et al. (2012). We obtained a total of 180 photometry maps of two types: scanamorphous maps (Jscanam) and high-pass-filter (HPF). An inspection of the data made us exclude objects that do not show a centrally peaked flux, for that a Gaussian model would be inappropriate. They exhibit instead bright arcs and rings, such is the case of NGC 40 and NGC 6781, two extended PN. We devote a section to extended targets further on. We ended up with a total of 37 targets, among which AGBs and PPNs and we performed the 2D-Gaussian fit in blue and red bands.

Figure 2.8 shows an example of Jscanam maps in the blue and red bands of the AGB star X Her. Filaments and arcs are visible in the FIR image of this target which was interpreted as a consequence of interaction between wind ejected by the star and the interstellar medium (Jorissen et al. 2011). All sorts of interesting features can be found in some of these photometry maps, but we will focus on deriving the FWHM of the inner emission. As mentioned before, the aim of this procedure is to assess the reliability of the sizes obtained from fitting spectral cubes, but we could not help noticing some correlations and other interesting aspects revealed by photometry maps.

[3] http://herschel.esac.esa.int/hcss-doc-13.0/load/pacs$_{s}$*pec/html/PdrgS.Chp.4d.pointVSraster.html*

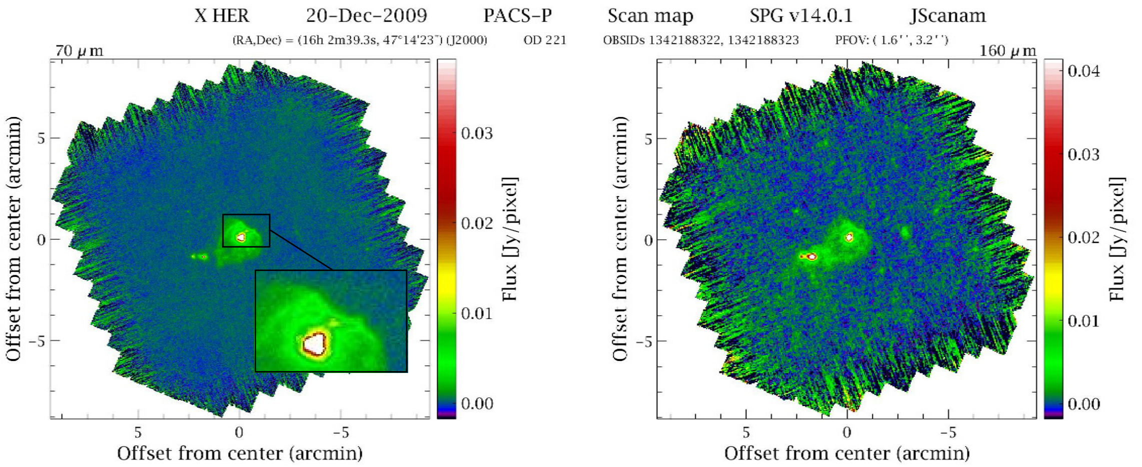

Fig. 2.8: Photometry postcard obtained from the Herschel Science Archive (adapted) for the AGB star X Her. Left: Blue JScanam map; right: Red Jscanam map.

2.3.1 High-pass-filter vs Jscanam

We want to assess an eventual dependence of the derived parameters on the map-maker algorithm. We considered high-pass-filter (used for point-like sources) and Jscanam maps (used for point-like and extended). There is a third type named UNIMAP which is not available for every target in the HSA because it is not the default algorithm.

In HPF maps a small-sized filter is used to boost point source sensitivity, so that the wings of the PSF and faint extended emission disappear, plus overall flux losses can occur (Popesso et al. 2012). This could be an issue if the target is not masked *a priori*.

Jscanam is the (jython-) HIPE implementation of the scanamorphos algorithm developed by Helene Roussel[4]. Since PACS photometer detectors are bolometers[5], their signal is dominated by the low-frequency, uncorrelated $1/f$ noise (e.g. Graciá et al. 2015). In order to solve this problem, Jscanam maps combine scan plus cross-scan observing modes, where the region of interest is observed first in a given scan direction and then scanned again in a perpendicular direction.

Besides the 6 parameters in equation 2.5, we define the flux F which corresponds to the volume under the gaussian surface as:

[4] http://www2.iap.fr/users/roussel/herschel

[5] Bolomoters measure the power of incident radiation via heating of materials with a temperature dependent electrical resistance.

$$F = 2\pi P \sigma_x \sigma_y \tag{2.13}$$

with standard errors given by:

$$\delta F \approx F \sqrt{\left(\frac{\delta P}{P}\right)^2 + \left(\frac{\delta \sigma_x}{\sigma_x}\right)^2 + \left(\frac{\delta \sigma_y}{\sigma_y}\right)^2} \tag{2.14}$$

In figure 2.9 we compare peak intensities, flux (not background subtracted) and FWHM obtained from these 2 types of photometry maps in both blue and red bands. These results are listed in tables A.5 and A.6 in the appendices. Overall the fitted peak intensities and integrated fluxes agree within the absolute flux uncertainties (<10%) with the obvious exception of R Cas which has a measured peak 30% higher in high-pass-filter maps. This goes against the global trend which is the inverse scenario with the Jscanan maps providing larger peak intensities in both bands. This could be related to the lack of source masking prior to filter usage. Indeed, the best agreement between these 2 map-makers was found on targets where we are sure that the masking was performed since the mask is made available in the downloadable products from the archive. U Hya is the second faintest target in this 37-target sample and the derived fluxes obtained from the two maps disagree above 10% in the red band, despite agreeing very well in the blue band. Naturally, the discrepancy is also seen the size ratio. An inspection of the data does not reveal apparent problems in U Hya neither in R Cas, so a probable explanation for this behaviour lies on the map-maker algorithms themselves.

Another noticeable pattern is that peak intensities are always higher in the blue band, spanning a couple of orders of magnitude. Furthermore, when we compare the derived FWHM from these 2 map-makers we see that the ratio is mostly above 1, with the high-pass-filter maps resulting in slightly larger FWHMs (up to 6%). Thus, when the integrated flux is computed, these two quantities balance each other as expressed in equation 2.13 in such way that the flux ratio is around 1 with smaller scatter.

We conclude that the difference in FWHM obtained from high-pass-filter maps and Jscanan maps is not meaningful for our purposes and it is, in fact, of about only 2% in the blue band and 1% in the red band on average. Nevertheless to avoid improper masking

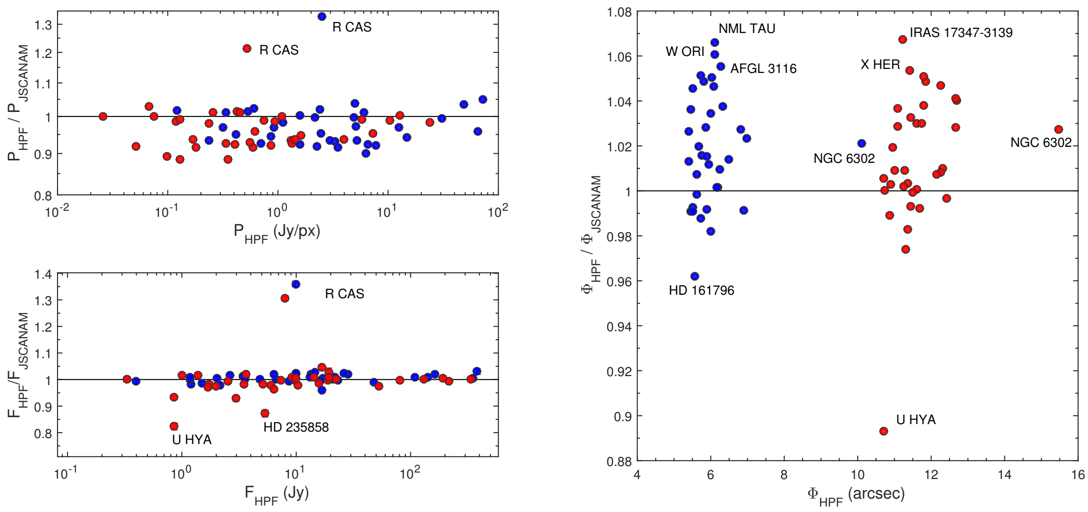

Fig. 2.9: Results comparison between HPF maps and Jscanam maps. Blue and red points correspond to results obtained for the blue and red bands respectively. Left: peak intensity ratio (top) and flux ratio (bottom). Right: FHWM ratio.

issues we decided to use only Jscanan maps in what follows.

2.3.2 Correlations from photometry maps

In figure 2.10 we compare the blue and red FWHM. We observe that there is a linear correlation between the FWHM in two bands (Φ_{70} and Φ_{160}). The density curves intend to show the FWHM and peak intensity scatter. Essentially one verifies that there is a larger scatter in the red band FWHM compared to the blue band, whereas the inverse occurs when one compares peak intensities.

The largest target in this 37-targets sample is NGC 6302 with a FWHM of $\Phi_{70} = 9.9''$ and $\Phi_{160} = 15.1''$, in the blue and red bands respectively. This young planetary nebula also shows the highest red-to-blue flux ratio being 40% brighter in the red band. The FIR excess is probably consequence of cold dust. NGC 6302 could be a great target to compare to spectroscopy imaging results to photometry due to its extension, but a PACS/spectrometer mispointing prevents us from doing proper analysis.

The brightest targets are, by far, AFGL 2688 and IRC+10216 which seem to be somewhat extended in the blue band with $\Phi_{70} = 6.9''$ and $\Phi_{70} = 6.8''$ respectively ($\Phi_{\rm PSF} = 5.5''$). It is interesting that while IRC+10216 is circular with an ellipticity $e = 1 - b/a = 0.05$, consistent with the observed spherical shells (e.g. Cernicharo et al. 2015), AFGL 2688 has

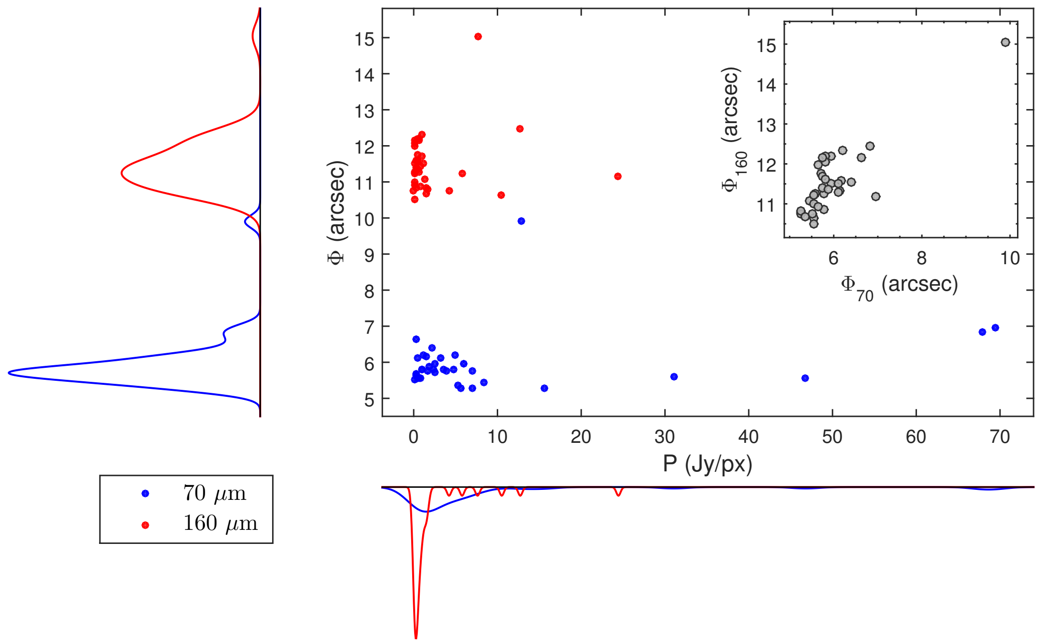

Fig. 2.10: Peak intensity versus FWHM obtained for Jscanam maps. The color code corresponds to the blue and red photometric bands. The smaller pannel illustrates the correlation between the derived sizes in both bands.

a difference between major and minor axis of 0.9", which translates into a ellipticity of 0.12. We found an elongation along a position angle of 58°, in agreement with the thermal emission observed in the radio at P.A=53° (Jura et al. 2000). One of the puzzling features of this nebula is the fact that the symmetry axis of the optical and near-infrared lobes is at P.A=15°, but the symmetry axis at radio wavelengths, including CO emission, is at P.A=53° − 60° (Goto et al. 2002). So does it seems to be the case of FIR emission. Here it is important to note that the emission we observe with PACS photometer is a superposition of the continuum together with spectral lines, namely the dominant carbon-monoxide lines. In the red band the ellipticity of AFGL 2688 slightly increases and yet the FWHM is consistent with the PSF FWHM derived for Vesta. The P.A increases to 73°, but this result is intrinsically not so accurate due to the camera's larger pixel.

Figure 2.11 shows the linear correlation between red band and blue band fluxes. We found that most targets are brighter in the blue band with the exception of NGC 6302 and IRAS 22036+5306. HD 44179 (The red rectangle) has a $F_{red}/F_{blue} \approx 1$.

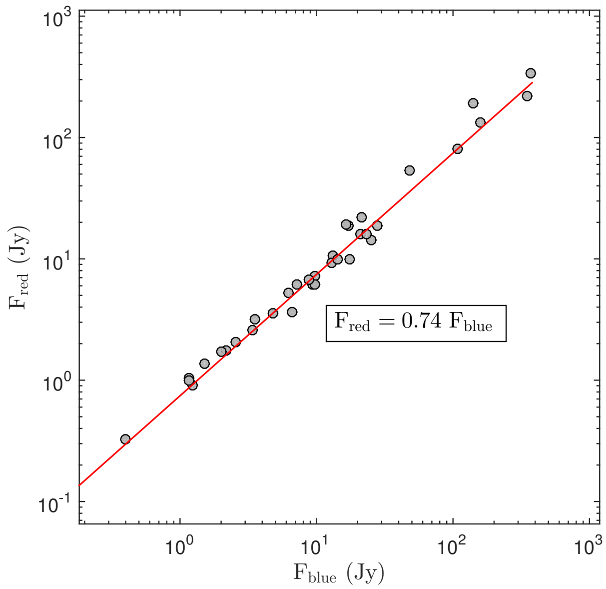

Fig. 2.11: Relation between the integrated flux in the blue and red bands. The red line corresponds to the best linear least-squares fit.

2.3.3 Extended sources: rings and arcs

To finish the topic regarding photometry maps, we present some final considerations about extended sources revealed through this data. Figure 2.12 shows an example of planetary nebula in which the extended FIR emission is clearly not well modelled by a Gaussian function. The remaining 7 PN can be found in the appendix of figures. Some of them exhibit arcs such NGC 40 and NGC 6445. The largest target in the complete sample is definitely NGC 6781 with an angular distance between intensity peaks in the E-W direction of approximately 100″. On the other hand, NGC 7026 looks more compact and fits inside PACS field-of-view. But since it shows double-peaked emission in the blue band it was also separated from the remaining targets.

Although the blue band photometry reveals interesting features, in some cases in the red band that information is lost due to halving of angular resolution. Thus in the red band one can approximate the observed flux density distribution of NGC 7009 and NGC 7026 by a 2D-Gaussian quite well. The results are shown in table 2.2 and figure 2.13. The error bars are the propagated statistical uncertainties. These are good examples to compare with PACS spectroscopy imaging.

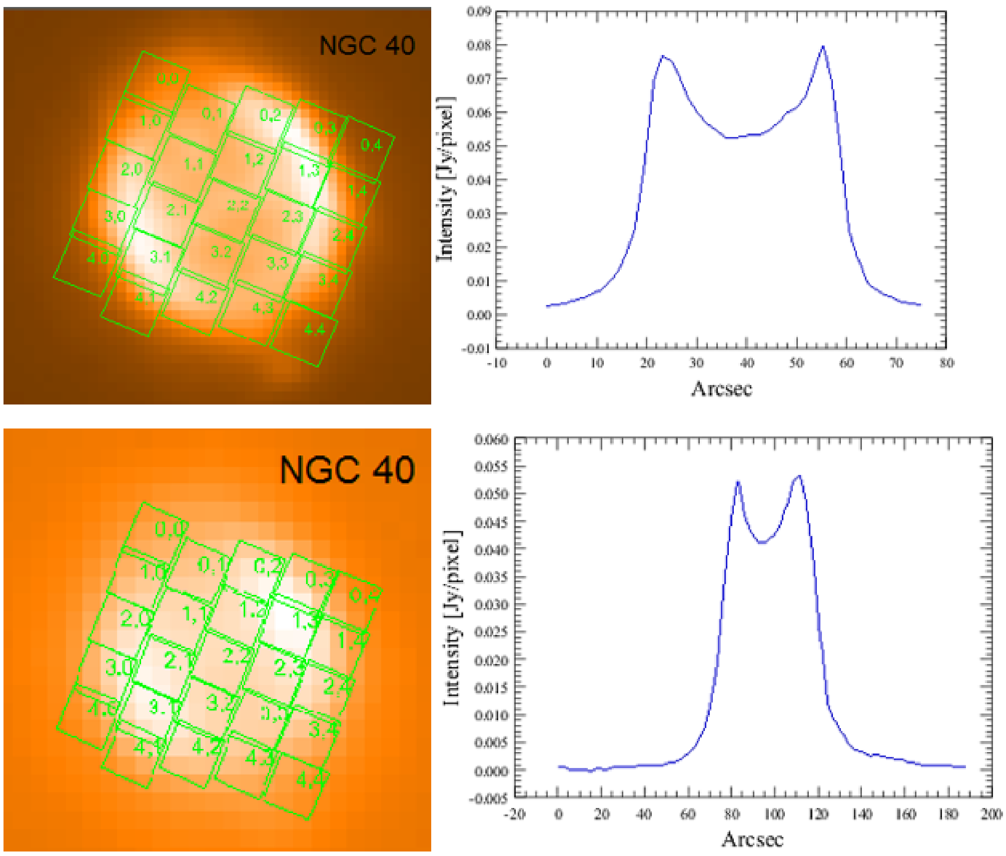

Fig. 2.12: PACS photometry maps (blue - top, red - bottom) with PACS spectrometer footprint overlaid. In every map North points upwards and East to the left. On the right side an intensity profile in the E-W direction is shown.

Table 2.2: Gaussian model parameters for red band photometry of 2 planetary nebulae.

Target	P (Jy/px)	a (arcsec)	b (arcsec)	Φ (arcsec)	$\theta°$	RMSE
NGC 7009	0.17±0.0002	25.45±0.05	22.35±0.04	23.85±0.07	70.2±0.6	0.0003
NGC 7026	0.2156±0.0004	16.28±0.05	14.76±0.05	15.50±0.07	53±1	0.0004

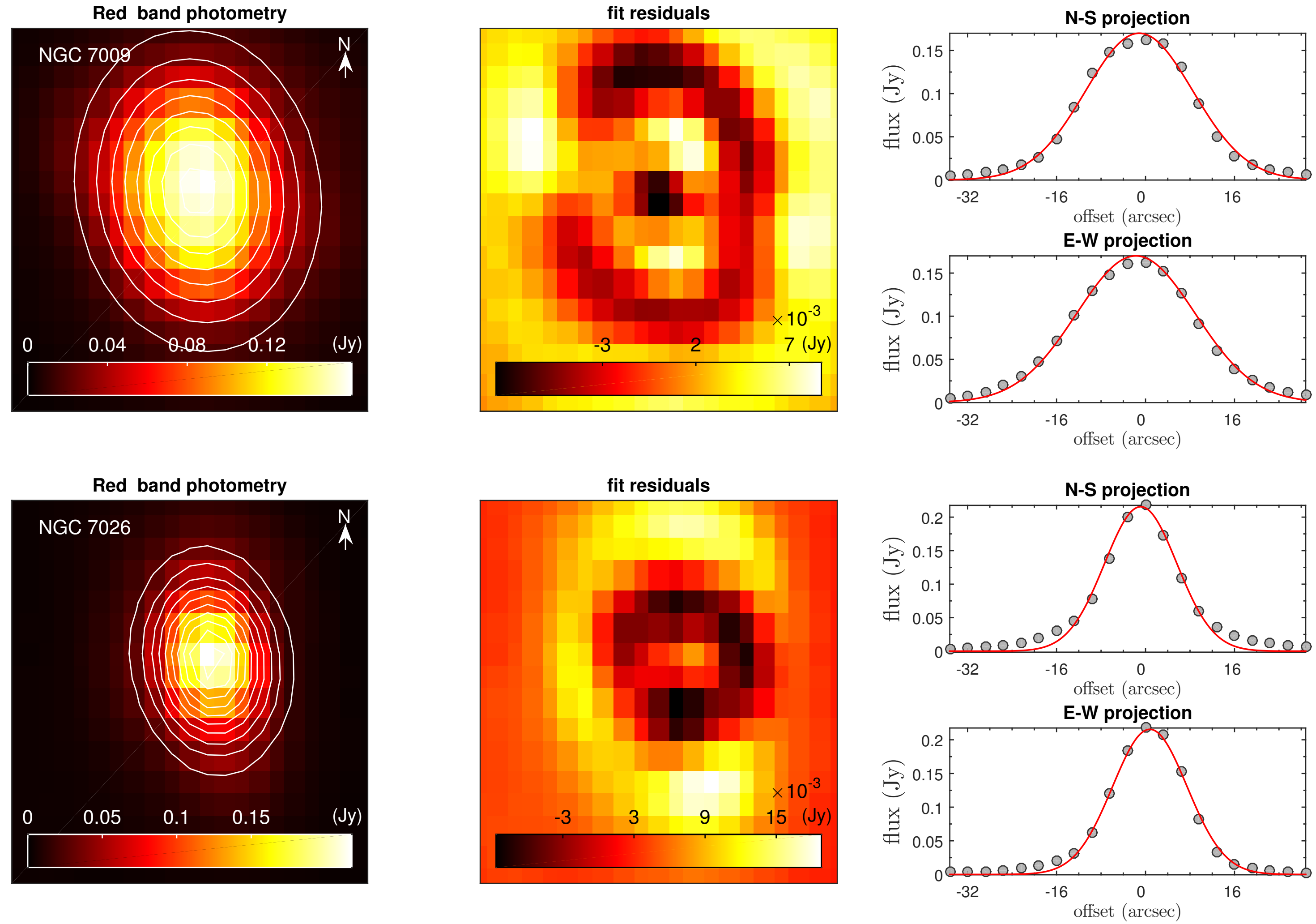

Fig. 2.13: Gaussian fitting results for NGC 7009 (top row) and NGC 7026 (bottom row) in the red band. On the right side, N-S and E-W projections are presented.

2.4 Comparison of results and caveats

Finally, we established a comparison between these 3 types of data: rebinned cubes, interpolated cubes and photometry maps, and compared each one of them with the PSF we had studied before. Taking the photometry results as reference, we want to check the reliability of the spectral cubes fitting.

It is important to remind that the FWHM estimate obtained from the photometry corresponds to an integrated flux in a given bandwidth, whereas in the spectral cubes we have estimates across wavelength range. Thus, to be able to compare the results we averaged the spectroscopic FWHM within approximately the same coverage of the photometry bands (figure 1.6). This is by no means a rigorous treatment, but it should yield a robust result.

We established comparisons for targets that have an observed large spectral range. This criterion excluded R Lep, U Hya, W Ori, Y Cvn and ST Her which, in addition, are faint sources (bellow 15 Jy) in the PACS spectral range. RT Cap is even fainter, showing a noisy continuum. A visual inspection of the spectral cubes permits to conclude it is point-like and of course the fit results are not good at all. This is confirmed by the FWHM derived from the photometry which is also very close to the PSF. For these reasons, it was also excluded from comparison. Since we do not have blue band photometry of IRAS 10178-5958 and U Mon they were also excluded. Besides these limitations, the code does not converge for X Her when fitting spectral cubes in the red band as it also very faint, neither does it show centrally peaked flux. For KHI Cyg the code does not converge in the blue band when using interpolated cubes. IRC+10216 was also excluded because it was not observed in the same range as the other targets. NGC 6302 suffers from severe mispointing in PACS spectral cubes, so we avoided fitting this target as well. IRAS 17347-3139 was retrieved from the archive in a later search so it was not available when the comparison was made. Since the task of obtaining interpolated cubes is quite time consuming they were also not available for every target.

This being said, we put together a control sample of 20 targets (figure 2.14) for which

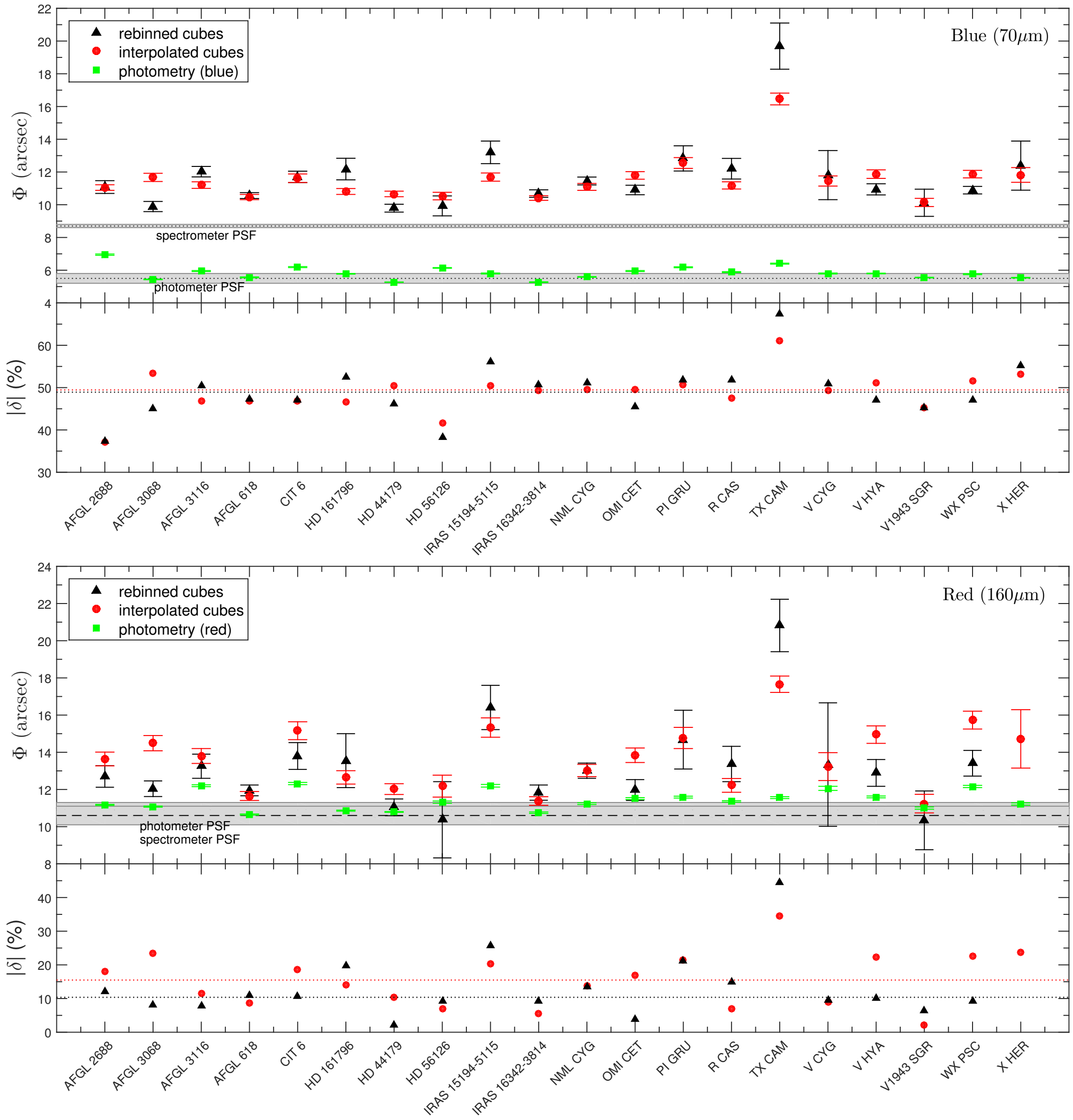

Fig. 2.14: Comparison between the derived sizes from rebinned cubes (px = 9.4"), interpolated cubes (px = 4.7") and photometry maps with px = 1.6" (70μm) and 3.2" (160μm), for 20 objects of different classes in the blue (top) and red (bottom) bands; $\delta = 1 - \Phi\text{phot}/\Phi_{\text{spec}}$ computed for rebinned and interpolated cubes.

we compared the derived FWHM using different kinds of data. The results are listed in table 2.3. Taking the photometry sizes as reference, a systematic difference of around 49% relative to them was found for both rebinned cubes and interpolated cubes in the blue band. This is a consequence of the much larger spectrometer spaxel size that is convolved with the image, which in turn means that the PSF FWHM is also distinct as shown in the upper diagram. However, in the red band the agreement is much better and we found a median absolute difference of 16% for interpolated cubes, which always produce larger estimates than the photometry. For rebinned cubes, the absolute difference is typically around 10%.

Table 2.3: A sample of 20 targets with FWHM derived from photometry maps, rebinned cubes and interpolated cubes.

Target name	Photometry		Rebinned cubes		Interpolated cubes	
	$\Phi_{\rm blue}('')$	$\Phi_{\rm red}('')$	$\Phi_{\rm blue}('')$	$\Phi_{\rm red}('')$	$\Phi_{\rm blue}('')$	$\Phi_{\rm red}('')$
AFGL 2688	6.95±0.04	11.17±0.03	11.1±0.4	12.7±0.6	11±0.2	13.6±0.4
AFGL 3068	5.44±0.02	11.08±0.03	9.9±0.3	12±0.4	11.7±0.2	14.5±0.4
AFGL 3116	5.95±0.03	12.2±0.05	12±0.3	13.2±0.7	11.2±0.2	13.8±0.4
AFGL 618	5.56±0.03	10.65±0.03	10.6±0.2	12±0.3	10.5±0.2	11.6±0.2
CIT 6	6.19±0.03	12.32±0.06	11.7±0.4	13.8±0.7	11.6±0.3	15.2±0.5
HD 161796	5.78±0.02	10.86±0.03	12.2±0.7	14±2	10.8±0.2	12.7±0.4
HD 44179	5.27±0.01	10.79±0.02	9.8±0.2	11±0.4	10.7±0.2	12±0.3
HD 56126	6.14±0.02	11.32±0.06	9.9±0.6	10±2	10.5±0.2	12.2±0.6
IRAS 15194-5115	5.8±0.03	12.2±0.07	13.2±0.7	16.4±1	11.7±0.3	15.3±0.5
IRAS 16342-3814	5.27±0.02	10.75±0.04	10.7±0.2	11.8±0.4	10.4±0.1	11.4±0.2
NML CYG	5.59±0.02	11.24±0.05	11.5±0.2	13±0.4	11.1±0.2	13±0.3
OMI CET	5.95±0.03	11.51±0.05	10.9±0.3	12±0.6	11.8±0.2	13.8±0.4
PI GRU	6.18±0.03	11.59±0.05	12.8±0.8	15±2	12.5±0.3	14.8±0.6
R CAS	5.88±0.03	11.36±0.04	12.2±0.6	13.4±1	11.2±0.2	12.2±0.4
TX CAM	6.4±0.03	11.56±0.05	20±1	21±1	16.5±0.4	17.7±0.4
V CYG	5.8±0.03	12.06±0.11	12±2	13±3	11.4±0.3	13.2±0.8
V HYA	5.8±0.02	11.6±0.05	10.9±0.3	12.9±0.7	11.9±0.3	15±0.5
V1943 SGR	5.55±0.02	11±0.06	10.1±0.8	11±2	10.1±0.3	11.2±0.5
WX PSC	5.76±0.03	12.16±0.06	10.9±0.2	13.4±0.7	11.9±0.2	15.7±0.5
X HER	5.54±0.02	11.22±0.06	13±2	bad fit	11.8±0.5	15±2

To actually compare the blue band results one has to deconvolve the FWHM using equation 2.11. However, this formula is only valid when $\Phi \gg \Phi_{\rm PSF}$. It turns out that looking at the green points in figure 2.14 we see that the derived FWHM is, in general, consistent with the photometer PSF, i.e., they are point-like. There is no agreement between the deconvolved FWHMs from the 3 types of data in the blue band even for the exceptional cases of AFGL 2688 and TX CAM, which seem slightly extended with a deconvolved FWHM of 4.3" and 3.3" respectively. If we do the same to the FWHM from rebinned cubes, for example, we get 6.7" and 17.6", in complete disagreement. In the case of TX CAM the fit result for spectroscopy are clearly problematic anyway.

This is not a surprise knowing that for point-like targets in the blue band we have in fact just 1 point within the FWHM to fit the Gaussian surface, so the results are expected not to be reliable. In the red band, the photometer and spectrometer Φ_{PSF} is essentially the same. There is an overall agreement between the derived sizes with a few exceptions. While it agrees rather well for HD 44179, HD 56126, OMI CET and V1943 Sgr, it deviates a lot for IRAS 15194-5115, PI GRU and TX CAM. Some targets, namely AFGL 3116, CIT 6, IRAS 15194-5115, V CYG and WX PSC look slightly extended. Deconvolving these sizes further increases the disagreement between the derived FWHM.

The use of interpolated cubes does not seem to provide better estimates than the ones from rebinned cubes, in the sense that they are not closer to the results obtained from photometry. The interpolated cubes were not so useful after all in none of the bands.

In the previous section we fitted the red band images of NGC 7009 and NGC 7026 after concluding that the double-peaked flux seen in the blue band is smeared by the larger pixel size of the red camera. Because these two targets are clearly extended (table 2.2), they should allow a decent comparison between photometry and spectroscopy imaging. The average FWHMs we obtained from rebinned cubes are $23.2'' \pm 0.8$ and $18.3'' \pm 0.8$ respectively. The first one agrees very well with the photometry. The second is overestimated by 15%. It is in fact quite surprising that we are able to find a decent agreement between photometry and spectral cubes in the red band, knowing that in the latter case the spatial sampling is worse.

Despite the higher uncertainty inherent to the fitting performed in spectral cubes, we found that the results agree quite well in the red band and according to this 20-target sample we found an average correction factor of 10% to apply to the FWHM derived from any spectral cubes to obtain the equivalent photometric FWHM. Note that there is some scatter in this statistic and that outliers should be treated carefully, such as the case of TX CAM. Bear in mind that we found that the FWHM derived from photometry maps might depend on the map-maker algorithm up to 6%.

In what regards the remaining stars in the sample, most of them were found to be point-like with the exception of 8 PN and 1 OH/IR star. The fit is completely bad[6] for about 30% of the sample, so these results are inconclusive. The extended sources identified in this work are: PN MZ3, NGC 6781, NGC 40, NGC 6543, NGC 6545, NGC 3242, NGC 6826 and IRAS 19312+1950. At least two sources, IC 418 and NGC 7026, are semi-extended, but still not properly sampled by PACS.

2.5 Summary

- We studied the spectrometer PSF by fitting a 2D-Gaussian model to Neptune mapping observations with the newest calibration files.
- We also fitted Vesta observations to measure the inner size of the photometer's PSF for several positions in the field-of-view.
- We used photometry maps to find extended sources. After excluding 8 planetary nebulae that show bright rings and other features we obtained the FWHM of 37 targets by fitting the same Gaussian model.
- We concluded that reliable and equivalent estimates of the FWHM can be obtained from HPF and Jscanam maps.
- We fitted two types of spectral cubes: rebinned and interpolated, and found that most targets in the THROES catalogue are point-like. In fact, only 9/72 appear to be extended sources. For the remaining 35 targets in the catalogue the fit is inconclusive.
- From the comparison of sizes derived from red band photometry and spectral cubes we concluded that the latter provide a FWHM 10% higher on average.

[6] Very high RMSE and a variation in the size of up to 10" in adjacent wavelength channels.

Chapter 3

CO and other spectral features in evolved stars

In this chapter we analyse the spectra of 107 stars in the THROES catalogue by identifying the most common spectral features[1], namely molecular and atomic/ionic (fine-structure) lines, while conducting a survey of CO emission. The main goal in this chapter is to fit CO lines that will be used to infer physical conditions of the CSE in chapter 4. PACS observations are best suited for tracing a warmer gas component in the circumstellar shells and outflows around evolved stars, usually missed in sub-mm/mm observations.

3.1 Features in PACS spectra

In general, PACS range spectra are crowded with prominent emission lines. Line emission occurs when atoms or ions make a transition from one bound electronic state to another bound state at a lower energy. Additionally, vibrational and rotational states of molecules can be excited either by collisions or by radiation, also giving rise to emission lines upon de-excitation. Because these 2 modes have much smaller energy separations than those of electronic states, the vibrational and rotational transitions occur from the infrared to the millimetre-wave regions of the electromagnetic spectrum instead of the visible and near-UV as in the case of electronic transitions.

The chemical species found in THROES targets and their relative line strengths are expected to vary according to the evolutionary stage and spectral type.

[1] We do not cover solid-state (dust) features in this thesis.

3.1.1 Molecular lines

In figure 3.1 we compare the continuum subtracted[2] spectrum of 3 C-rich stars in the THROES catalogue spanning different evolutionary stages from AGB to PN. Straightaway we see significant differences such as the richer molecular content in the youngest star (CIT 6) relatively to the PN IRAS 21282+5050 as expected. Noticeably, that is the main difference between the emission line spectra of AGBs and PNs with the latter being almost devoided of molecular lines and yet showing strong ionic emission.

Since molecules were not expected to survive in the hostile, ionised environment of PN, the first detection of CO in a PN (NGC 7027) was a surprising discovery (Mufson et al. 1975). In fact, in this case the amount of molecular gas mass inferred from the first CO transition appears to be about 10 times higher than the mass of ionised gas. Anyway, the presence of CO is probably the remnants of the molecular gas of the AGB phase.

The strongest molecular features in the AGB and PPN spectra in figure 3.1 belong to CO isotopologues and HCN. However, in the case of O-rich AGB stars there are number of brighter lines of different chemical species. In figure 3.2 we show 3 examples of O-rich stars (NML Tau, AFGL 6815 and NGC 7026) of different evolutionary stages. A number of strong lines in the spectrum of NML Tau (or IK Tau) appear to correspond to H_2O (both ortho- and para-water) and OH. Some fainter lines could be SiO, SO or SO_2 typically found in O-rich targets. Line identification is not an easy task since there are several hundred predicted lines in this wavelength range that frequently overlap. In the O-rich PPN AFGL 6815 (also known as Cotton Candy Nebula) CO is dominant, despite multiple weaker unidentified lines being present, whereas in NGC 7026 CO rotational lines do not exist in the PACS range.

3.1.2 Atomic/ionic lines

There are essentially two processes (besides cosmic rays) that can convert molecules back to atoms and ions: (1) - the stronger (UV) stellar radiation field that induces pho-

[2] This procedure is explained in the next section.

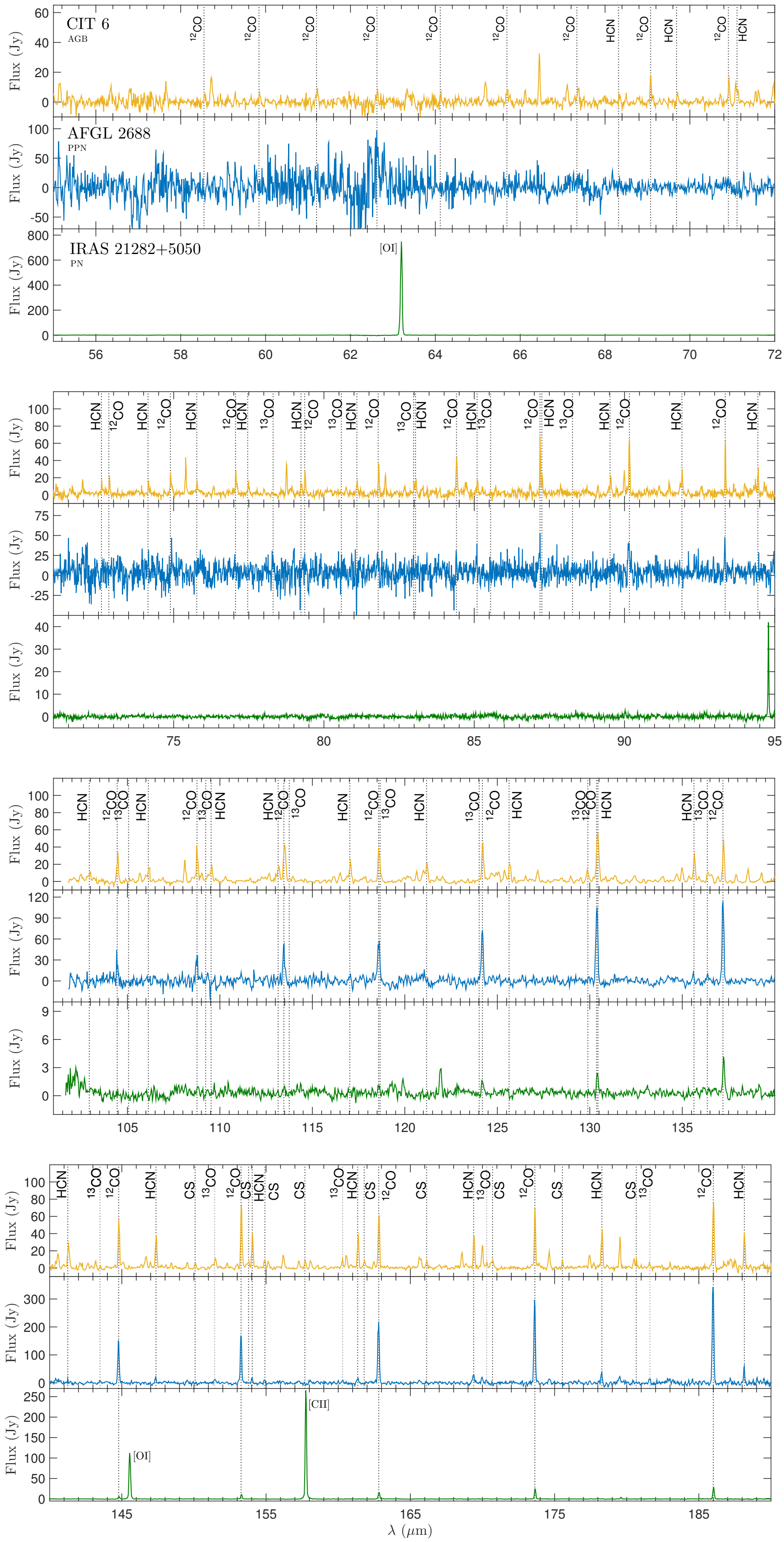

Fig. 3.1: PACS continuum subtracted spectra of 3 carbon-rich stars of different evolutionary stages.: CIT 6 (orange), AFGL 2688 (blue) and IRAS 21282+5050 (green).

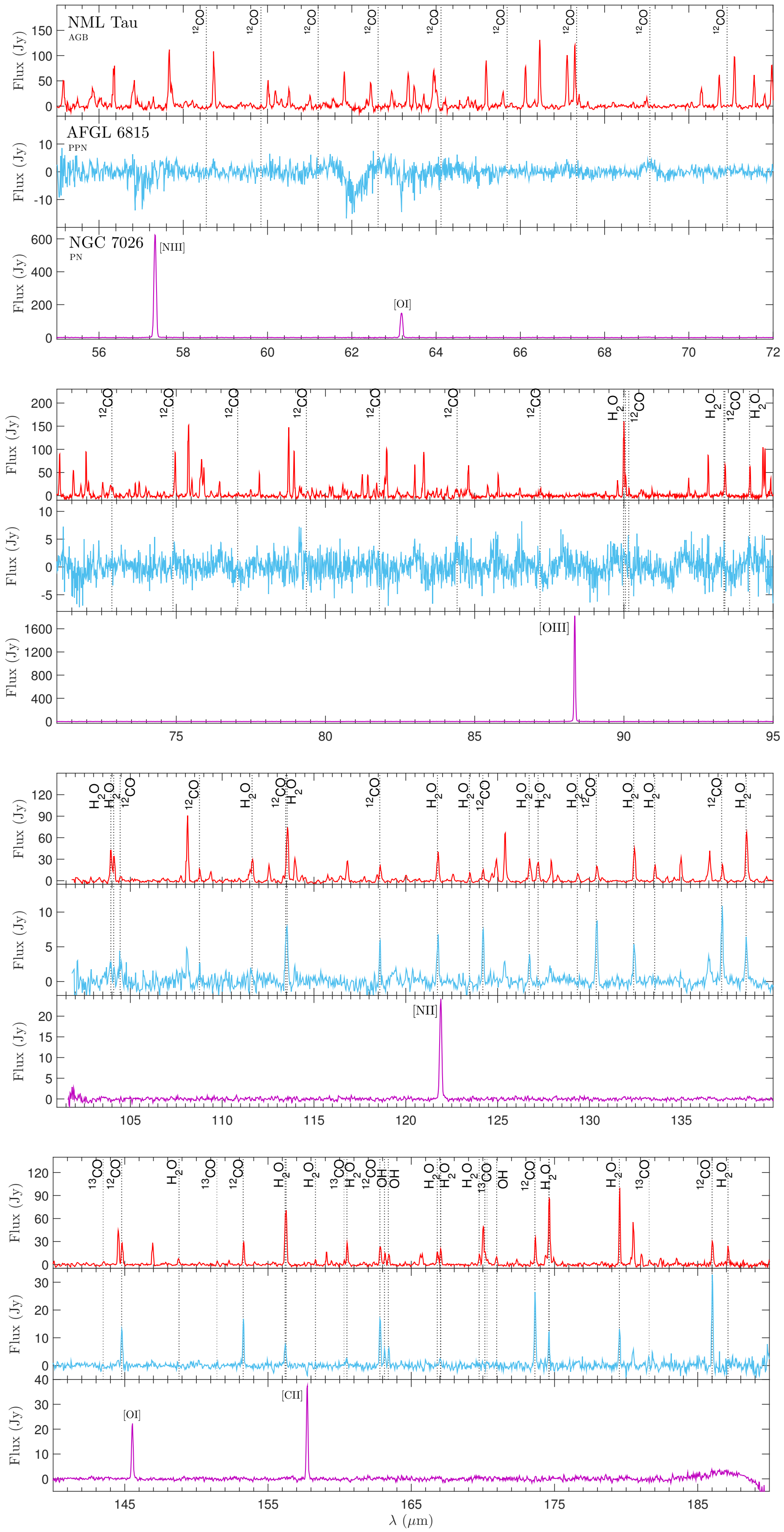

Fig. 3.2: PACS continuum subtracted spectra of 3 oxygen-rich stars of different evolutionary stages.: NML Tau (red), AFGL 6815 (blue) and NGC 7026 (purple).

Table 3.1: Atomic and ionic fine-structure lines in the far-infrared (Kwok 2000).

Ion	Wavelength (μm)	Energy (eV)
[SI]	56.311	0
[NIII]	57.317	29.60
[PII]	60.64	10.48
[OI]	63.184	0
[FII]	67.2	17.42
[SiI]	68.473	0
[OIII]	88.356	35.12
[AlI]	89.237	0
[FeIII]	105.37	16.19
[NII]	121.898	14.53
[SiI]	129.682	0
[OI]	145.525	0
[CII]	157.741	11.26

todissociation; (2) - shocks resulting from the interaction between slow and fast winds. In a simplified way, both mechanisms originate atoms, which can be further ionised giving rise to many permitted transitions in the NIR and strong forbidden lines like [OIII] at 88 μm and [CII] at 158 μm. The latter are example of fine-structure lines corresponding to transitions between states of the same multiplets (Kwok 2000). In table 3.1 we tabulate the most common lines in the far-infrared. Atomic and ionic lines are characteristic of PN and they do not show up in AGB's spectra.

The most prominent features in the spectra of IRAS 21282+5050 and CPD-568032 and other C-rich PN are [OI] and [CII], while in NGC 7026 (O-rich) we find even higher-degree ionised species, in particular [OIII] as shown in figure 3.2. From other studies in literature, the first two PN are known to be very compact, low-excitation PN (e.g. Kwok et al. 1993); Chesneau et al. 2006). In contrast, NGC 6537 (not displayed) is an extreme opposite case being a huge high-excitation, slightly O-rich PN (Lawrence et al. 1999; Edwards & Ziurys 2013). In its spectrum we found higher ionised species such as [NIII] and [OIII]. The FIR emission of NGC 7026 seems to be more compact (figure 2.12) than NGC 6537, but their spectra have some similarities namely the presence of a larger variety of lines compared to

IRAS 21282+5050.

In the two displayed PPN (AFGL 2688 and AFGL 6815) spectra in figures 3.1 and 3.2 we do not detect atomic/ionic lines which is an indication that the central star is not hot enough to ionise the bulk of the CSE. Further on we will study in greater detail another C-rich PPN named AFGL 618. The PACS spectra of AFGL 2688 and AFGL 618 are similar, being dominated by CO lines. Other molecules are visible such as HCN and CS amongst some other faint lines of unidentified species. However, there are already significant differences between these 2 PPN, namely the presence of ionised gas in the latter revealed by the [OI] lines at 63 μm and 146 μm. This is an indication that AFGL 618 is already entering the PN stage.

A more detailed view over the 3 C-rich targets plotted in figure 3.1 will be given in chapter 4. Note that the spectrum of every single star in the THROES catalogue cannot be displayed and studied here in detail, but can be accessed through the catalogue website.

3.2 Identifying and fitting CO lines

Carbon-monoxide is one of the most important molecules in astronomy.

Despite being the most common molecule in the Universe, H_2 is a homonuclear, linear molecule with no permanent dipole moment, thus all the low-lying energy levels are quadrupole transitions with small transition probabilities, but relatively high excitation energies. This means they are only excited in high temperatures or strong UV radiation fields conditions. Therefore, the most abundant molecule that carries most of the gas mass and plays a key role in the thermal balance and gas-phase chemistry, is practically invisible to direct observation. Consequently, we rely on the so-called "tracer" species, generally CO, to study CSE chemistry and ISM across the galaxy.

CO is a very stable molecule because it is held together by a triple (polar) covalent bound (figure 1.4). However, it can be excited to rotational levels above the ground state by radiation or collisions (namely with H_2). The energy levels[3] of the rotational states of a diatomic molecule (such as CO) are given by:

[3]Obtained (R_J) by solving the Schrödinger equation $\hat{H}\Psi = E\Psi$ of the rigid rotor.

$$E_J = \frac{\hbar}{2I}\ J(J+1) \tag{3.1}$$

where $J = 0, 1, 2...$ is the rotational quantum number, I is the moment of inertia and h is the Planck constant. In this case the lowest rotational transition, $J = 1 \rightarrow 0$, has a frequency of 115 GHz, or a wavelength of 2600 μm, which is well outside Herschel range. In fact, the first detectable CO transition falling within Herschel/PACS range is the $J = 14 \rightarrow 13$ at ~ 186 μm. The complete list of CO transitions in PACS range can be found in table A.9.

CO can be found in several isotopologue forms. The most common one is $^{12}C^{16}O$, while others such as $^{13}C^{16}O$, $^{12}C^{18}O$ or $^{12}C^{17}O$ are far less abundant. One of the most important observational quantities to measure is the $^{12}CO/^{13}CO$ ratio as it can be used to trace past star formation history. It is believed, for instance, that the $^{12}CO/^{13}CO$ ratio evolves as consequence of nucleosynthesis in AGB stars and there is observational evidence that the ejecta from AGB stars dominates the evolution of the isotopologue-ratio in the local ISM (Ramsted & Olofsson 2014, and references therein). This ratio derived for stars in different evolutionary stages is usually different. Although this ratio is not so well constrained for M-type stars (O-rich AGBs) and PN, it is well known for carbon AGB stars through measurements of photospheric molecular NIR lines (Lambert et al. 1986; Ohnaka & Tsuji 1996) and CO observations in the radio (e.g. Schöier & Olofsson 2000). While Lambert et al. (1986) found that the $^{12}CO/^{13}CO$ ratio is between 30-70, Schöier & Olofsson (2000) found lower ratios by a factor of 2 for the same targets. Based on optical data Abia & Isern (1997) estimated ratios in the range 20–35 for most carbon stars in their sample. In what regards OH/IR stars Delfosse et al. (1997) estimated much lower ratios (~ 4) suggesting these are massive stars where the hot bottom burning process has converted ^{12}C into ^{14}N. More recently, Ramsted & Olofsson (2014) consistently estimated the $^{12}CO/^{13}CO$ ratio in a relatively larger sample of stars of 3 spectral types (M, S and C) and derived a median ratio of 13, 26 and 34 respectively, while not finding any correlation whatsoever with mass-loss rate.

In this chapter we fitted the rotational line profiles of ^{12}CO and ^{13}CO isotopologues in the ground vibrational state. For that, the first step involves subtracting the continuum.

3.2.1 Continuum subtraction

No standard parametric function is able to accurately reproduce the shape of the continuum of most targets in the entire PACS/spectrometer range. While a simple degree-one or -two polynomial fits rather well the region above 100 μm, that is surely not the case of the bluest, bumpy part of the spectrum. A non-parametric method is then needed for this purpose. One of the most popular ways to do it is by using splines which are piecewise-defined polynomials. A drawback of this approach is that one has to choose the number of nodes where the pieces connect, i.e., a smoothing parameter that controls the appearance of the fit. So, if we want to process the entire sample of THROES targets this is definitely not the fastest or pratical way to do it.

Alternatively, we used local-regression which has been applied in a number of fields, but not so much in astronomy. For that we used a free R package called *locfit*[4] (Loader 1999). Basically the difference between local-regression and standard regression techniques is that instead of finding the parameters of a given model to minimise the squared sum of residuals of the entire data set, it computes a weighted least-squares in a sliding window using a polynomial (degree 2 by default) in a nearest-neighbours fashion. Note that a smoothing parameter ($0 < \alpha \leq 1$) also exists in local-regression and it is related with the proportion of data to use in each fit. To assess the performance of the fit we employed generalized cross-validation (GCV, Craven & Wahba 1979) and computed the GCV statistic defined as:

$$GCV = n \, \frac{\sum_{i=1}^{n} (Y_i - \hat{\mu}(x_i))^2}{(n - tr(H))^2} \tag{3.2}$$

where Y_i is the polynomial model, n is the number of models and $tr(H)$ is the trace of the hat matrix[5]. The denominator is called "equivalent degrees of freedom"[6]. The best smoothing parameter is the one that minimises the GCV statistic as depicted in figure 3.3.

[4]http://www.statistik.lmu.de/ leiten/Lehre/Material/GLM$_0$708/$Tutorium/locfit$.pdf

[5]The diagonal elements of the hat matrix are called "leverages" and describe the influence the response value on the fitted value.

[6]The concept of degrees of freedom for non-parametric models is complex, because there is not a number of parameters, so they are empirically determined and result in numbers that are not necessarily integers.

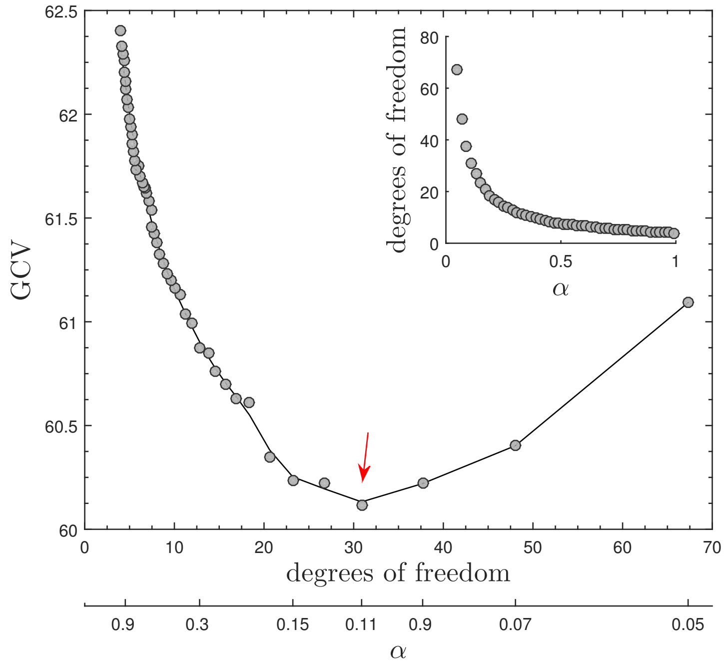

Fig. 3.3: Generalized-cross-validation statistic as a function of the degrees of freedom and smoothing parameter. The best α is the one that minimzes the GCV.

In this example, we are fitting a portion of the spectrum of the C-rich AGB CIT6.

We also used fitting weights inversely proportional to the variance, i.e., $w_i = 1/\sigma_i^2$ as well as robust bisquare weighting to reduce the effect of outliers. So in the end the method is best named as non-parametric-local-robust-regression. The smoothing degree α chosen by GCV, although mathematically valid, might still not be the one that best suits one's needs in reality, hence reflecting the difficulty of purely data-based bandwidth selection. For example, in some cases the GCV curve is flat beyond a certain degree of freedom. Fortunately we were able to quickly fit and subtract the continuum in a sample of 107 out of 113 stars[7] and over-fitting occurred in just few cases, which were properly identified and corrected by choosing by hand a different smoothing. Of course one could argue that one could choose the number of nodes in spline fitting with cross-validation as well, but local regression proved to be faster and more efficient.

An example of the continuum subtraction is shown in figure 3.4 for the AGB star CIT 6. This local fitting routine was important to correctly recover line profiles that sit on top of bumpy regions of the spectrum, especially in the range $55 - 75$ μm. The continuum

[7]The excluded OBSIDS are mispointing or off-center observations of extended PN.

models were used to obtain continuum fluxes at selected wavelengths to plot a colour-colour diagram while the continuum subtracted spectra were finally used to fit CO lines.

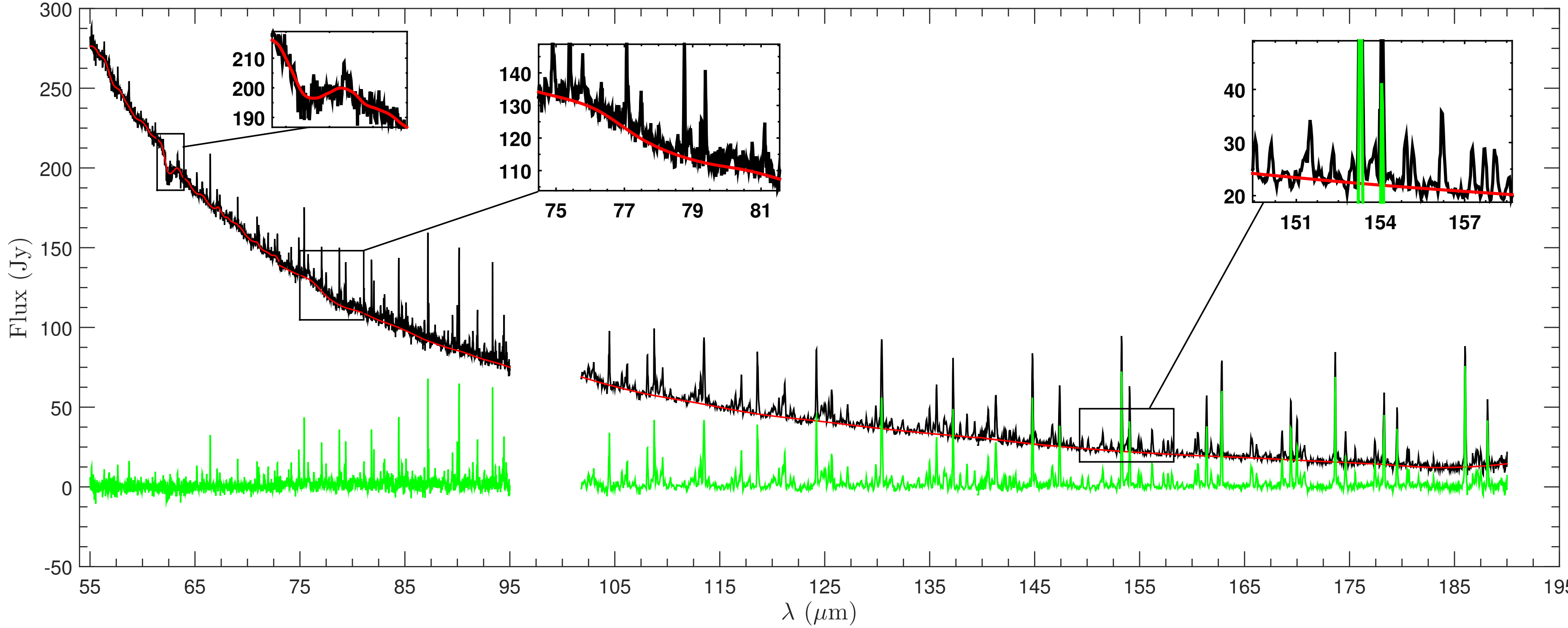

Fig. 3.4: Continuum subtraction of the spectrum of CIT 6 using a non-parametric method. This local-regression approach (red curve) enables a proper fit of the bumpy continuum under the lines in a fast, automatic way. The green line is the continuum subtracted spectrum. The feature around 62.5μm is interpreted as an instrumental artifact.

3.2.2 Line fitting

After subtracting the baseline from all spectra, we can proceed to line fitting. The molecular data, namely frequency and quantum numbers of each transition for any given species were taken from the CDMS database (Muller et al. 2001; 2005).

Spectral lines are usually not resolved with PACS, hence their shape is limited by the instrumental profile. A standard Gaussian function, $\Psi(\lambda)$, with 3 free-parameters is a good approximation of such profile:

$$\Psi(\lambda) = \alpha \ \exp\left[-\frac{(\lambda-\lambda_0)^2}{2\sigma^2}\right] \tag{3.3}$$

where α is the peak intensity, λ_0 is the central wavelength of the line and σ is the line width. The integrated flux under the line is given by:

$$F = \int \Psi(\lambda)\ d\lambda = \sqrt{2\pi}\ \alpha\sigma \ [\mathrm{Jy}\mu\mathrm{m}] \tag{3.4}$$

for which the uncertainty propagates approximately as follows:

$$\delta F = F\sqrt{\left(\frac{\delta\alpha}{\alpha}\right)^2 + \left(\frac{\delta\sigma}{\sigma}\right)^2} \tag{3.5}$$

To convert the integrated flux from [Jy.μm] to [W.m^{-2}] we used the following conversion formula:

$$F' = 2.99 \times 10^{-12} \times \frac{F}{\lambda_0^2}\ [\mathrm{Wm}^{-2}] \tag{3.6}$$

so that the uncertainty propagates as:

$$\delta F' = \sqrt{\left(\frac{F'}{F}\right)^2 (\delta F)^2 + \cancel{\left(\frac{4F'^2}{\lambda_0^2}\right)(\delta\lambda_0)^2}} \tag{3.7}$$

where the second term is canceled because it is much smaller (>10-100 times) than the first one. Lastly, the FWHM in velocity units and its correspondent uncertainty are given by:

$$FWHM = c\,\frac{2.355\;\sigma}{\lambda_0}\;[\mathrm{km\ s^{-1}}] \tag{3.8}$$

$$\delta FWHM = FWHM\,\sqrt{\left(\frac{\delta\sigma}{\sigma}\right)^2 + \left(\frac{\delta\lambda_0}{\lambda_0}\right)^2} \tag{3.9}$$

where c is the speed of light.

We primarily focused on ^{12}CO transitions[8] which were identified and fitted using the model 3.3. The fit was performed using the Levenberg-Marquardt method (e.g. Moré 1977) by making use of the function *fit* in MATLAB.

A search for CO transitions in the PACS range was performed in 72 out of 107 targets in the THROES catalogue for which there are PACS spectra in the full wavelength range ($55 - 190$ μm), except IRC+10216 which was observed only in the sub-ranges $70 - 100$ μm and $145 - 190$ μm. Among 35 excluded targets there are (inadvertent) mispointing cases such as NGC 6302, AFGL 5379, IRC-10259, IRAS 17347-3139, IRAS 16279-4757, IRAS 13428-6232 and OH 21.5+0.5, as well as observations with different pointings on planetary nebula (rims and off-center observations). The results obtained for the parameters of line fitting can be found in table A.11 in the appendix. Note that due to spectral leakage issues, spectral data between $95 - 102$ μm was deleted which means we were are not able to retrieve the transitions[9] $J_{\rm up} = 26$ and $J_{\rm up} = 27$.

When the fit was obviously wrong, for example, due to line blend, it was recomputed by choosing different parameter lower/upper bounds. But we noticed that constraining the fit too much to mitigate the effect of nearby lines causes it to fail to converge properly[10] and to print wrong confidence intervals. For this reason we decided to leave the results as they were, flagging particular transitions when we see an obvious blend. This being said, we caution the reader that due to insufficient spectral resolution the reported line strengths and integrated fluxes may be affected by line blend from nearby transitions.

CIT 6 is an example of a target with a wide range of CO transitions detected up to very high rotational numbers. However, this is certainly not the case of most stars in this

[8] Every time we simply refer CO lines we mean the ^{12}C^{16}O isotopologue.

[9] $J_{\rm up}$—Rotational quantum number of the upper level transition.

[10] It may converge to a local minimum that is not the absolute minimum.

sample of 72 targets. Figures B.4.1 in the appendix show an example of fitted CO line profiles in the case of AGB star CIT 6 from $J_{\rm up} = 14$ to $J_{\rm up} = 39$. Above that, the SNR is already on the detection limit ($\sim 5\sigma$). For completeness we provide in the appendix the remaining line fluxes up to $J_{\rm up} = 44$. Lines with SNR$<$5 were also not considered in the remaining targets.

As mentioned before, line profiles are not resolved, so line blend may be a serious issue, especially in strong molecular emitters. The profiles of the transitions $J_{\rm up} = 34$ and $J_{\rm up} = 35$ in CIT 6 are clearly blend with other unidentified species causing a severe line broadening, which translates into a large FWHM. The FWHM can be compared to the remaining lines in figure 3.5. As we move to higher wavelengths, line strengths increase, but the profiles become broader as they are limited by the lower spectral resolution[11]. Some known blends include CO transitions J = 30 $\rightarrow$ 29 and J = 20 $\rightarrow$ 19 with HCN J = 39 $\rightarrow$ 38 and J = 26 $\rightarrow$ 25 respectively. Another known blend occurs at $\lambda \sim 118.5$ with the transition J = 22 $\rightarrow$ 21 of ^{12}CO and J = 23 $\rightarrow$ 22 of ^{13}CO. We found a line blend at 113 μm in some stars (e.g. TX CAM, W Hya, WX PSC, etc.) which is yet to be understood. The fact that we cannot resolve spectral lines means we cannot extract any information regarding the kinematics of the gas.

3.3 Results and discussion

Here we present the results regarding the continuum subtraction and line fitting.

3.3.1 CO in the sample of stars

CO lines become weaker with increasing frequency. Table 3.2 shows some numbers for the percentage of stars within each evolutionary class that show the first CO transition in the PACS range ($J = 14 \rightarrow 13$), used to trace its overall presence. The AGB class is further divided into several chemical types. In fact, only half of the sample shows CO lines that become weaker as one moves to shorter wavelengths. This is shown, for example, by the number of targets that exhibit the CO transition ($J = 25 \rightarrow 24$) at ~ 105 μm which

[11] http://herschel.esac.esa.int/Docs/PACS/html/ch04s07.html

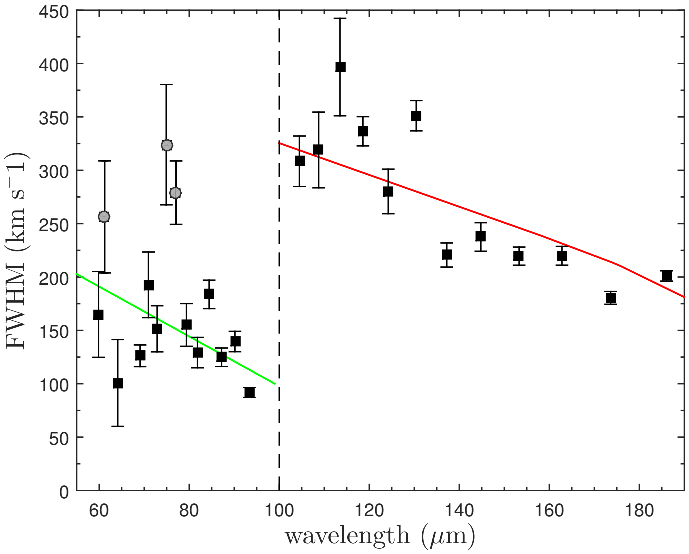

Fig. 3.5: Line full width at half maximum in velocity units of the fitted CO lines in the PACS spectrum of CIT 6. The coloured lines are the theoretical instrumental spectral resolution and the grey circles flag known line blends.

is only 31%. If we analyse any other higher J line, for example the ($J = 36 \rightarrow 35$), we find that only 9 targets have these very high J transitions in their spectrum. They are: V Hya, CIT 6, W Aql, PI GRU, AFGL 3116, AFGL 618, KHI CYG, IRAS 16594-4656 and IRC+10216, although in the case o W Aql it is already approaching the detection limit. We will study most of them in greater detail in chapter 4. Despite being stronger in C-rich AGBs than in O-rich AGBs, CO lines were still found in all but 2 oxygen stars. Nonetheless, the higher J lines are not so common in these targets. For example, the $J = 25 \rightarrow 24$ transition was only found in 5 out of 16 (31%) O-rich AGB stars. The C-rich AGBs that do not have CO features in their spectra are AQ Sgr and RT Cap which have a very faint (<10 Jy) and noisy spectrum in the entire wavelength range.

We also confirmed the scenario where molecular lines are expected to be much more common in earlier-stage stars than in PN since only 3 out of 17 (18%) PN show CO lines, whereas in the AGB group we found CO in 24 out of 28 stars (86%). The 3 PNs are NGC 6537 which is slighltу O-rich with C/O = 0.95 (Edwards & Ziurys 2013), IRAS 21282+5050 and CPD-568032, both C-rich (Meixner et al. 1993; de Marco et al. 1997).

In figure 3.6 we present 4 examples of the measured transition fluxes, namely the $J_{\rm up} = 14$, $J_{\rm up} = 16$, $J_{\rm up} = 28$ and $J_{\rm up} = 31$ flux versus the modelled continuum flux under each line. This line-to-continuum ratio gives a rough idea of the relative importance of the

Table 3.2: Number of targets with detected (SNR ≥ 5) $J_{\rm up} = 14$ (186 μm) and $J_{\rm up} = 25$ (105 μm) CO transitions in each class.

Class	$J = 14 \rightarrow 13$		$J = 25 \rightarrow 24$	
O-rich	14/16 (88%)	AGB 24/28 (86%)	5/16 (31%)	AGB 14/27 (52%)
C-rich	7/9 (78%)		6/8 (75%)	
S	3/3 (100/%)		3/3 (100/%)	
OH/IR	2/5 (40%)		0/5 (0%)	
PPN	9/22 (41%)		6/22 (27%)	
PN	3/17 (18%)		2/17 (12%)	
total	39/72 (54%)		22/71 (31%)	

dust and gas emission mechanisms. The strongest CO lines were found in 3 of the targets with the brightest continua: IRC+10216 (AGB star), AFGL 618 and AFGL 2688 (2 PPN), followed by the AGB stars IRAS 19312+1950 and CIT 6. This trend is not new. In fact, the strongest FIR sources are also the strongest CO emitters (e.g. Bujarrabal et al. 1992). AGBs are amongst the targets with the brightest continuum and the faintest. The 3 PNs were found to have $J_{\rm up} = 14$ and $J_{\rm up} = 16$ with approximately the same strength, but distinct continuum fluxes. However, in the case of PNs a smaller range of transitions was found relatively to the average of AGBs and PPN.

We found strong linear correlations[12] ($R^2 > 0.85$) between the measured line fluxes and continuum flux in AGB stars. The slope of the linear trend changes with wavelength in the following way:

$$F_{\rm J14} = 0.5^{0.6}_{0.4}\ F_{\rm cont}\ [\text{AGB}] \tag{3.10}$$

$$F_{\rm J16} = 0.3^{0.4}_{0.2}\ F_{\rm cont}\ [\text{AGB}] \tag{3.11}$$

$$F_{\rm J28} = 0.019^{0.022}_{0.017}\ F_{\rm cont}\ [\text{AGB}] \tag{3.12}$$

$$F_{\rm J31} = 0.0099^{0.011}_{0.0087}\ F_{\rm cont}\ [\text{AGB}] \tag{3.13}$$

where the lower and upper bounds on the slope are 95% CIs. The reason why there is such a deviation from the linear prediction could be due to the underestimation of line

[12] In regression analysis the square of Pearson's R (correlation coefficient) is the coefficient of determination that estimates the explained fraction of variance in the data.

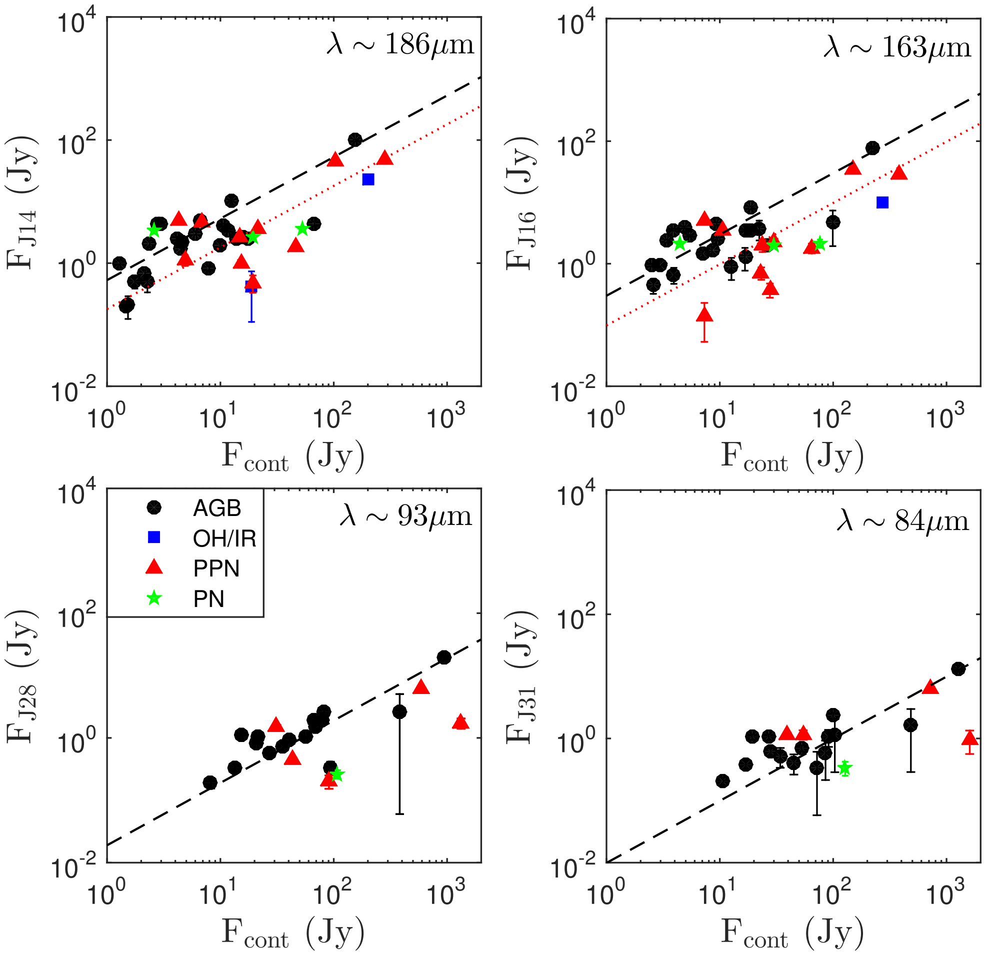

Fig. 3.6: CO $J_{\rm up}$ = 14, $J_{\rm up}$ = 16, $J_{\rm up}$ = 28 and $J_{\rm up}$ = 31 line flux versus continuum flux under the line peak. The black and red lines are least-squares fits to the AGBs and PPNs respectively.

fluxes because of opacity effects or there are simply different gas-to-dust ratios in different targets. In the case of PPNs, the correlations are weaker with $R^2 = 0.75$ and $R^2 = 0.65$ in $F_{\rm J14}$ and $F_{\rm J16}$ respectively. The linear models are given by:

$$F_{\rm J14} = 0.19^{0.26}_{0.12}\ F_{\rm cont}\ [\rm PPN] \tag{3.14}$$

$$F_{\rm J16} = 0.098^{0.14}_{0.05}\ F_{\rm cont}\ [\rm PPN] \tag{3.15}$$

In the bottom panels, due to the lack of points the fit is not good and the correlation coefficient is very low. We avoided the constant term in the linear regression because it is rather uncertain and it does not change the derived slope upon its exclusion. Also, its physical meaning is hard to interpret. To sum up, we conclude that CO rotational lines are stronger at longer wavelengths in absolute terms and relatively to the continuum.

IRAS 19312+1950 is an interesting case. This OH/IR star is one of the brightest targets in the catalogue, but in spite of showing the forth strongest $J_{\rm up} = 14$ CO line, we did not find a wide range of transitions. In fact, this particular transition is unusually strong with the subsequent quickly decaying in such way that in the bottom panels of figure 3.6 it does not appear. The last transition we found was the $J = 24 \rightarrow 23$. This raises the question if there is a line blend with some other species, greatly increasing the intensity of the feature at 186 μm, though we are not aware of known line at that wavelength. A more likely explanation could be the existence of a large amount of cold gas traced by lower J lines and very few hot gas in proportion.

IRC+10216 (or CW Leo) is, notably, the star that shows the strongest CO lines and the richer chemical content in this sample. In opposition, HD 235858 reveals only 4 faint transitions in an otherwise featureless spectrum.

Next, we fitted ^{13}CO rotational lines. Since this isotopologue is much less abundant than ^{12}CO and the latter is already scarce in most THROES targets in PACS range, we only found 13 stars (18% of the sample) with ^{13}CO transitions with SNR$\geq$5. A number of them are blended with known species such as HCN and ^{12}CO and other unidentified lines. This means that adding to their relatively smaller signal-to-noise ratio, their integrated fluxes have higher degree of uncertainty. From these 13 stars, 11 are AGB stars and 2 are PPN. As with ^{12}CO, IRC+10216 shows the strongest ^{13}CO lines. Figure 3.7 illustrates an example of fitted ^{13}CO profiles in the case of AFGL 2688, where we found isotopologue transitions from $J_{\rm up} = 15$ to $J_{\rm up} = 21$. The line fitting parameters of the remaining targets can be found in table A.11 in the appendices.

3.3.2 ^{12}CO/^{13}CO isotopologue ratio

Due to somewhat different molecular properties, the ^{13}CO probes regions slightly different from those sampled with ^{12}CO (De Beck et al. 2010). Furthermore, since ^{13}CO is less abundant than ^{12}CO, the CSE is optically thinner to those lines, meaning that ^{13}CO transitions can provide, in principle, a reliable diagnostic for the envelope's density structure. On the other hand, since they are fainter, their signal-to-noise ratio is much lower,

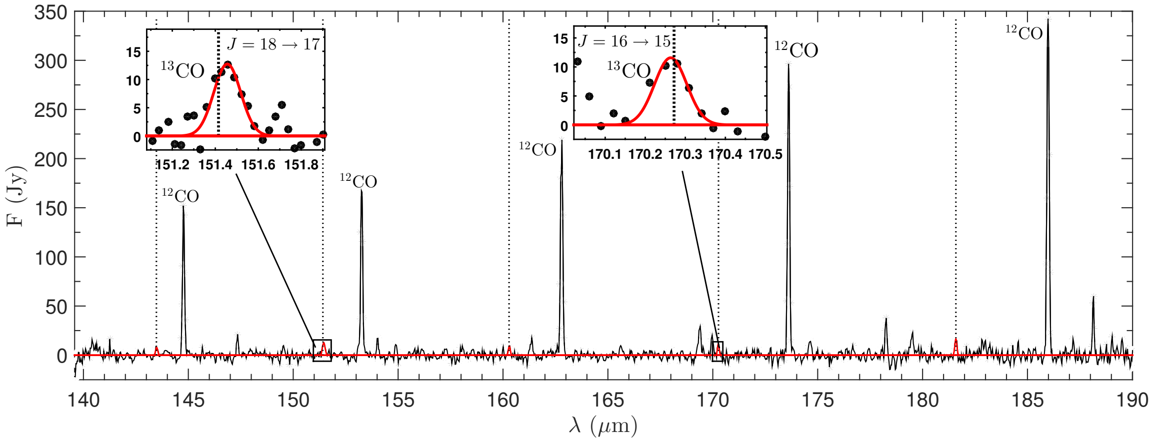

Fig. 3.7: Part of the PACS range spectrum (continuum subtracted) of AFGL 2688 showing the fitted ^{13}CO lines; ^{12}CO lines are labelled for comparison.

i.e., the relative uncertainty is much higher.

With the fluxes we derived by fitting both isotopologues, we can determine the isotopologue ratio ^{12}CO/^{13}CO in a straightforward way by simply dividing the measured line fluxes for the same transition in both species. This ratio is then corrected for the Einstein coefficient and frequency difference by a factor of ~ 0.92. For optically thin rotational lines the ^{12}CO/^{13}CO ratio should provide a good estimate of the abundance ratio. If we further assume that all carbon is locked in CO, then the ^{12}CO/^{13}CO can yield directly the ^{12}C/^{13}C isotopic ratio. Beware that any optical depth effects would decrease the ratio, i.e., the isotopic ratio would be underestimated. Schoier et al. (2000) argue that only detailed radiative transfer analysis is able to provide trustworthy abundance ratios, which is beyond the scope this thesis. Anyway, the very high J transitions should be less affected by optical depth effects.

The ^{12}CO/^{13}CO flux ratio was computed for 13 targets using the first 4 transitions of ^{13}CO within PACS range and the results are summarised in table 3.3. The uncertainty[13] results from the error propagation of the integrated flux and it is dominated by the flux uncertainty of ^{13}CO lines. Some scatter in the ratio for the same target as traced by different rotational transitions is visible. The targets with the highest ratios are, as expected (e.g. Milam et al. 2009), C-rich stars, namely AFGL 618, AFGL 2688 and CIT 6.

Estimates of this ratio can be found in literature, but this type of analysis is sensitive

[13]No flux calibration uncertainties were added (typically <20%).

Table 3.3: CO isotopologue ratio for several transitions in the PACS range. The ellipsis mark undetected ^{13}CO or bad fits.

	^{12}CO/^{13}CO				
Target Name	J = 15 → 14	J = 16 → 15	J = 17 → 16	J = 18 → 17	average
AFGL 2688	17±4	23±5	18±5	8±2	17
AFGL 3068	4±2	...	...	...	4
AFGL 3116	7±3	4±0.4	4.5±0.5	4±2	5
AFGL 618	19±3	21±2	29±8	16±3	21
CIT 6	9±1	9±1	7±1	3.7±0.5	7
EP Aqr	1.5±0.3	1.7±0.4	...	6±2	3
IRAS 15194-5115	2±1	5±2	2.2±0.2	2±1	3
IRC+10216	5±1	7.1±0.5	4±1	5±3	5
KHI CYG	...	6±1	6±1	8±2	7
NML TAU	5±1	...	...	...	5
OMI CET	2.5±0.5	3±1	5±1	6±2	4
R CAS	4±1	3±2	...	...	3
R DOR	2.3±0.4	1±1	...	...	2

to the particular transition studied or even telescope used (e.g. Schoier & Olofsson 2000). De Beck et al. (2010) used JCMT and APEX data observing from $J_{\rm up} = 2$ to $J_{\rm up} = 6$ to obtain the isotopologue ratio for a sample of AGB stars. Their uncertainties are of $\sim$ 28% and 42% depending on the spectral line. Using IRAM 30m, OSO, APEX and JCMT data Ramstedt & Olofsson (2014) computed ^{12}CO/^{13}CO flux ratios for the same transitions but in a larger set of AGB stars of the 3 main spectral types (M, S and C). The uncertainties should be of the same order. We conclude that our ratios are systematically smaller than the ones derived from low J observations, following the trend of decreasing ratios with decreasing wavelength. This could be due to optical depth effects are an actual ^{13}C enrichment due to a late ejection of material that is located closer to the central star in a region probed by these higher J CO lines.

3.3.3 PACS colour-colour diagram

As a sub-product of the line fitting we obtained useful information regarding the continuum of our targets. In the introduction we presented an IRAS two-colour diagram (figure

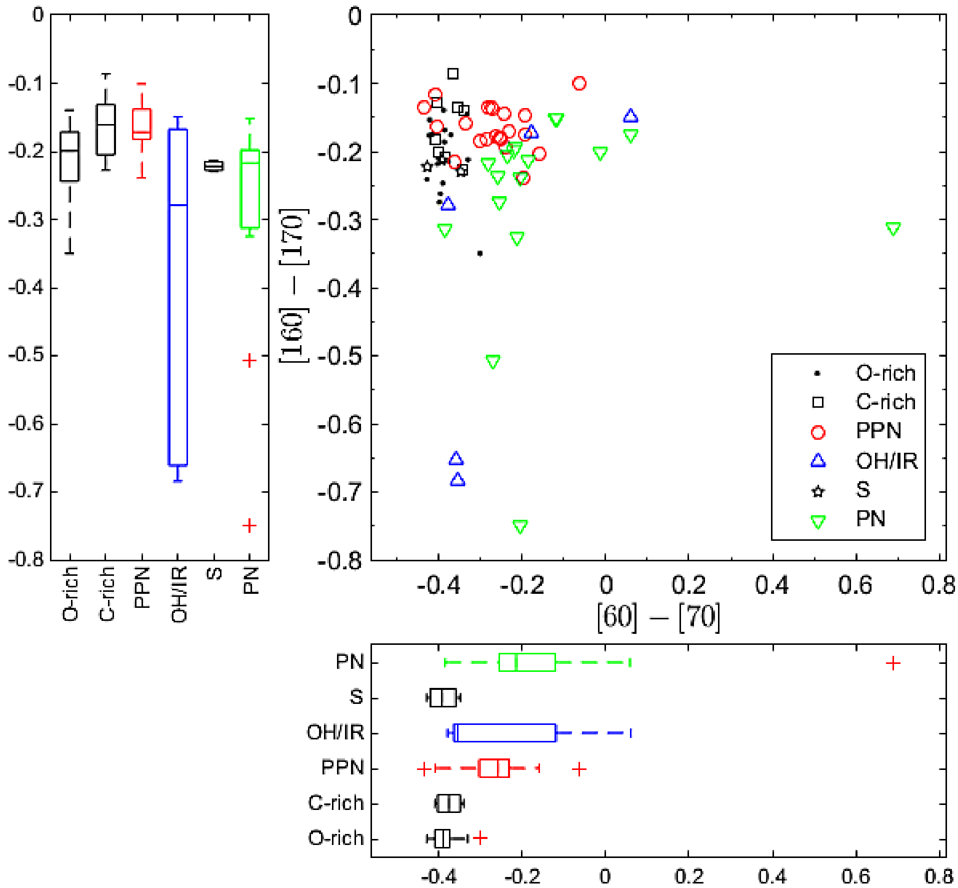

Fig. 3.8: A PACS-PACS color-color diagram. Points outside the whiskers in the box plot diagrams are regarded as outliers.

1.9) to characterise the sample of stars and we concluded that they can be distinguished in terms of IRAS colours as reflex of their MIR and FIR properties. Analogously, using the continuum models of PACS spectra we extracted fluxes at selected wavelengths: [60, 70, 160, 170] μm and we defined PACS colours in the following way:

$$[60] - [70] = -2.5 \ \log \left(\frac{F_\lambda(60)}{F_\lambda(70)} \right) \tag{3.16}$$

$$[160] - [170] = -2.5 \ \log \left(\frac{F_\lambda(160)}{F_\lambda(170)} \right) \tag{3.17}$$

We found that we are still able to separate the different types of stars with PACS colours (figure 3.8). Moreover, their location in the diagram provides important hints about the shape of their SED, hence the temperature of the dust-cooling continuum. AGB stars have the sharpest slopes between 60-70 μm ($< [60] - [70] > \sim -0.38$) meaning that they are in the Rayleigh Jeans limit and their SED peaks at shorter wavelengths compared to PPN and PN. The median colours of C-rich and O-rich stars are also different as depicted in the boxplot diagrams.

No excess at 170 μm relative to 160 μm was found in any class meaning that the flux in this wavelength region is steadily decreasing. However, we found an excess at 70 μm which translates into a $[60] - [70] > 0$ in 2 PN and 1 OH/IR star. This indicates that the peak of the SED is at longer wavelengths. These targets are NGC 6537, NGC 6781 and IRAS 19312+1950. For example, if we look at the spectrum of NGC 6537 (figure 3.9) we see that the flux increases from 55 μm until $\sim$ 65 μm from where it slightly decreases reaching a plateau just before further decreasing from 90 μm onwards. According to Wien's law[14] a peak between $60 - 70$ μm corresponds to a temperature of 40-50 K. So we conclude that probably NGC 6537 has a large amount of cold dust. Matsuura et al. (2005) drew the same conclusions using ISAAC, ISO/SWS and IRAS data.

At the bottom left corner of the diagram there are 3 targets (OH 32.8-0.3, IRAS 19067+0811 and NGC 3242) which show very blue colours. An inspection of their data reveals a nearly flat noisy spectrum in the longer wavelengths region.

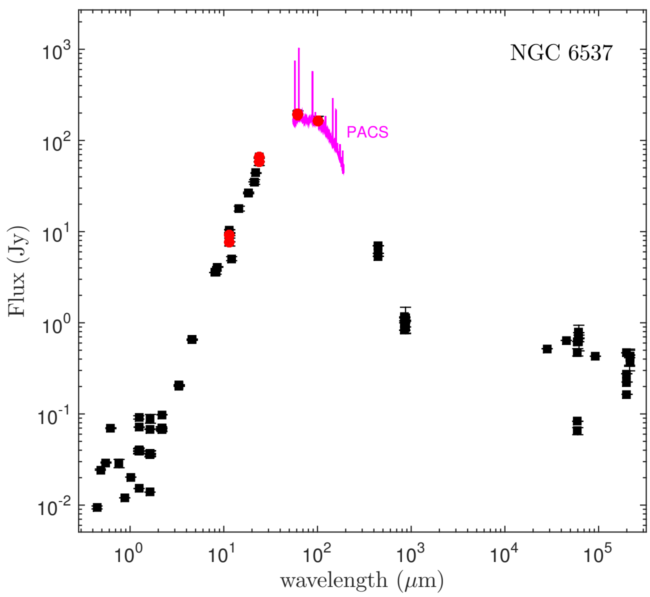

Fig. 3.9: Spectral energy distribution (SED) of NGC 6537 with PACS spectrum overlaid. The red points are IRAS fluxes and the black points are other photometry data such as 2MASS, AKARI, WISE, SDSS, VISTA, MSX and SCUBA (VizieR data).

[14]Wien's law: $\lambda_{\max} = \dfrac{2.8977729 \times 10^{-3}[\text{m.K}]}{\text{T[K]}}$

3.4 Summary

- We conducted a CO line survey on a sample of 72 evolved stars of different evolutionary stages from the THROES catalogue with the aim of deriving physical parameters of the molecular CSE.

- We confirmed that CO dominates the FIR spectra of carbon AGB stars, but in oxygen AGBs a number of comparably strong lines are seen. Some unidentified lines are probably OH, H_2O, SiO and SO among others.

- We identified atomic/ionic lines in the spectra of PN and concluded that the most common species are [NIII], [OI], [OIII], [NII] and [CII].

- We modelled the continuum spectra using a non-parametric method from where we obtained fluxes at selected wavelengths and drew a colour-colour diagram. PACS colours separate rather well targets in different evolutionary stages.

- After subtracting the continuum from our spectra we fitted ^{12}CO and ^{13}CO lines. The former isotopologue was found in about 54% of the sample, while the latter was found in just 18% of the stars. CO is rare in our sample of planetary nebulae and CO lines are relatively fainter in oxygen stars.

- Very high J rotational lines were found in 9 targets which is a probable indication of a significant amount of gas under relatively high temperature conditions.

- There is a correlation between line and continuum fluxes as showed in previous studies. The brightest FIR sources were found to be the strongest CO emitters. The scatter in these relations could be due to optical depth effects and/or very different gas-to-dust mass ratios.

- The ^{12}CO/^{13}CO ratio was computed for a smaller number of targets and it is lower than what is found in literature from low J CO observations.

- The SEDs of stars in different evolutionary stages have characteristic shapes as revealed by a PACS two-colour diagram plotted using continuum fluxes.

Chapter 4

Physical conditions in carbon-rich CSEs

In this chapter we estimate physical parameters of the CSE such as temperature and total gas mass using the rotational diagram. We focused in greater detail on a group of C-rich stars spanning different evolutionary stages from the sample of targets studied in chapter 3 for which we obtained CO line fluxes.

4.1 A sample of carbon-rich stars

From the sub-sample of 39 targets that show CO emission we selected all of the stars with carbon-dominated chemistry, i.e., not only C-rich AGBs but also PPN and PN known to be carbon enriched to study in greater detail. These targets are classified as 7 AGB stars, 5 PPN and 2 PN making a total of 14 stars. Their PACS range spectra can be found in the appendix in figure B.5.1. In this section we briefly review some of their properties in what regards their morphology and chemistry. Table 4.1 summarises some basic information with respect to the observations. In what follows we adopt the distances listed in table 4.2 taken from literature. The distance has great influence in some derived quantities so one has to be cautions when comparing results to research literature where consensus is not always achieved.

Table 4.1: Characterisation of the PACS spectrometer observations: evolutionary stage, coordinates (right ascension and declination), OBSID and observation date of a sample of carbon-rich stars.

Target name	Type	RA (J2000)	DEC (J2000)	OBSID	Obs. date
IRC+10216	AGB	$9^h47^m57^s.41$	13°16′43”.60	1342221889	2011-05-29
CIT 6	AGB	$10^h16^m2^s.28$	30°34′18”.48	1342197799 1342197800	2010-06-05
IRAS 15194-5115	AGB	$15^h23^m04^s.91$	−51°25′59”.0	1342215685 1342215686	2010-03-10
AFGL 2513	AGB	$20^h09^m14^s.25$	31°25′44”.9	1342270010 1342269936	2013-04-14 2013-04-12
V CYG	AGB	$20^h41^m18^s.27$	48°08′28”.8	1342208939 1342208940	2010-11-15
AFGL 3068	AGB	$23^h19^m12^s.39$	17°11′35”.4	1342199417 1342199418	2010-06-30
AFGL 3116	AGB	$23^h34^m27^s.67$	43°33′2”.52	1342212512 1342212513	2011-01-11
AFGL 618	PPN	$4^h42^m53^s.66$	36°6′53”.28	1342225838 1342225839	2011-08-07
HD 44179	PPN	$6^h19^m58^s.22$	−10°38′14”.7	1342220928 1342220929	2011-04-30
V HYA	PPN	$10^h51^m37^s.25$	21°15′00”.3	1342197790 1342197791	2010-06-05
IRAS 16594-4656	PPN	$17^h03^m10^s.03$	−47°00′27”.7	1342228414 1342228415	2011-09-10
AFGL 2688	PPN	$21^h2^m18^s.74$	36°41′37”.68	1342199233 1342199234	2010-06-26
CPD-56°8032	PN	$17^h7^m0^s.87$	−56°54′48”.0	1342228201 1342228202	2011-09-06
IRAS 21282+5050	PN	$21^h29^m58^s.42$	51°3′59”.76	1342220741 1342223375	2011-05-12 2011-06-30

4.1.1 IRC+10216

IRC+10216 (or CW Leonis) is the closest C-rich star and one of the most studied due to it's rich molecular content (e.g. Decin et al., 2010; Cernicharo et al., 1996). This source has been imaged by several authors using different methods. With an apparent size of $\sim 6''$, a inner core of $4''$ traced by SiS molecules, clumps and a probable bipolar structure at even smaller angular scales (Cernicharo et al., 2015, and references therein) it definitely contains a large diversity of temperature and density conditions.

Observations and models suggest a very cool (T $\sim$ 2000 K) star surrounded by an extended, roughly spherical CSE expanding at $\sim$ 14 km s^{-1} with a mass-loss rate $\dot{\rm M} \sim 1-4\times10^{-5}$ M$_\odot$ yr^{-1} (e.g. Sahai & Chronopoulos 2010; Cernicharo et al., 2015).

4.1.2 CIT 6

CIT 6 (or RW LMi) is a semi-regular variable star with a period of 640 days (de Beck et al. 2010) transiting from the asymptotic giant branch to the PPN phase. It is the seconds brightest C-rich late AGB star after IRC+10216. There is observational evidence for the presence of a binary companion (Monnier et al. 2000) that can explain the presence of a gas spiral structure, commonly seen in these objects. A spherical shell of $\sim 20''$, identified in molecular line mapping (Claussen et al. 2011), a bipolar structure observed in NIR and optical images and arcs at $1''-4''$ from the central star (Schmidt et al. 2002), are present in CIT 6.

This AGB star is known to contain a wealth of molecules in its CSE. For example, Zhang et al. (2009) used the Arizona Radio Observatory (ARO) and the Submillimeter Telescope (SMT) to find 29 chemical species such as SiO, SiC, CS and their isotopologues besides CO. Using the rotational diagram they estimated excitation temperatures in the range $\sim 30-58$ K. Chau et al. (2012) while studying the properties of cyanopolyynes (isotopologues of HCN), concluded that CIT 6 is probably older than IRC+10216 and built a 3D model to match observations which suggests that the CSE is asymmetric and composed of various incomplete shells.

De Beck et al. (2010) derived a mass-loss rate of $\dot{M} = 5.9 \times 10^{-6}$ $M_{\odot}$ yr^{-1} that can be variable in time. Recently, Hyosun et al. (2015) carried out high-resolution ^{12}CO J = 2 → 1 and ^{13}CO J = 2 → 1 observations and concluded that a mass-loss rate of $\dot{M} = 8 \times 10^{-6}$ $M_{\odot}$ yr^{-1} fits reasonably well the observed line profiles.

4.1.3 IRAS 15194-5115

IRAS 15194-5115 (or II Lup) was first identified as carbon star by Meadows et al. (1987) who compared it to the famous IRC+10216 in terms of brightness and NIR and MIR spectral features. This star is a long-period variable with a period of 575 days and a luminosity of 8900 $L_{\odot}$. Its CSE contains the typical carbon bearing molecules CO, CS, HCN, C_nH among others (e.g. Ali 2006).

Ryde et al. (1999) using ISO data modelled rotational CO isotopologues lines up to $J = 21 \rightarrow 20$ in the case of ^{12}CO and $J = 22 \rightarrow 21$ of ^{13}CO and derived a ^{12}CO/^{13}CO ratio of ∼ 5.5. The authors argue that the low ^{12}CO/^{13}CO ratio of ∼ 5.5 is very close to the ^{12}C/^{13}C isotope ratio in the stellar atmosphere which marks this star as a rather distinct case of C-rich sources, in particular the optically bright-ones, that have ^{12}C/^{13}C ratios above 30. They obtained a mass-loss rate of $\dot{M}10^{-5}$ $M_{\odot}$ yr^{-1} assuming a distance of 600 pc.

4.1.4 AFGL 2513

AFGL 2513 (or V1969 Cyg) is another Mira variable with $T_{\rm eff} \sim 2500$ K, mass-loss rate 2×10^{-5} $M_{\odot}$ yr^{-1} and an expansion velocity of 25.6 km s^{-1} (Groenewegen et al. 2002). Dedicated studies of this star were not found in literature.

4.1.5 V CYG

V Cyg is a Mira variable with a luminosity of ∼ 6200 $L_{\odot}$ and a relatively cold central star ($T_{\rm eff} \sim 2600$ K). Bujarrabal & Alcolea (1991) observed the CSE of V Cyg through CO $J = 1 \rightarrow 0$ and $J = 2 \rightarrow 1$ mapping observations and found an elongated nebula in the northeast-southwest direction with a size of $18'' \times 10''$.

V Cyg became the second AGB star with detected warm water vapour through the observation of orto- and para-water using Hershel/HIFI data (Neufeld et al. 2010). These authors also modelled high J CO transitions, namely $J_{\rm up} = 6$, $J_{\rm up} = 10$ and $J_{\rm up} = 16$ lines and derived a total mass-loss rate of 4.6×10^{-6} $M_{\odot}$ yr^{-1}. Previously, Schoier & Olofsson (2000) had presented a somewhat lower mass-loss rate of $\dot{M}1.6 \times 10^{-6}$ $M_{\odot}$ yr^{-1} for an expansion velocity of 11.5 km s^{-1}.

4.1.6 AFGL 3068

AFGL 3068 (or LL Peg) is a strong infrared source that shows an unusual Archimedean spiral traced up to 12" from the centre, thought to be originated by the gravitational interaction with a binary companion (Morris et al. 2006).

Zhang et al. (2009) conducted a molecular line survey in radio and sub-mm wavelengths and identified 23 molecular species and isotopologues, mainly carbon bearing molecules. They argue that this star has a larger C/O ratio than IRC+10216 and CIT 6, and it is in fact known as an "extreme carbon-star" with a thicker dust envelope. Zhang et al. (2009) also obtained rotational diagrams using line fluxes of SiC_2, SiS, C_4H and HC_3N and further assuming a size of 22" given by the known distribution of CO $J = 1 \rightarrow 0$ and $J = 2 \rightarrow 1$ from previous studies. They found temperatures in the range $36 - 78$ K. However, in this work we expect high rotational level CO transitions to come from a more compact and hotter region.

AFGL 3068 is a long-period variable ($\sim$ 700 days) and it is known to be one of the carbon stars with the highest mass-loss rate in the solar neighbourhood (e.g. Winters et al. 1997). Ramstedt & Olofsson (2014) report a mass-loss rate of $\dot{M}2.5 \times 10^{-5}$ $M_{\odot}$ yr^{-1}.

4.1.7 AFGL 3116

AFGL 3116 (or LP And) is a Mira variable with similar properties to CIT 6 being very dust-obscured by a thick CSE and it has very long period ($\sim$ 614 days, De Beck et al. 2010). De Beck et al. (2010) estimated a mass-loss rate of $\dot{M} = 4.6 \times 10^{-6}$ $M_{\odot}$ yr^{-1}, possibly variable, while Ramstedt & Olofsson (2014) derived $v_{\rm exp} = 14$ km s^{-1} and $\dot{M} =$

7×10^{-6} $M_{\odot}$ yr^{-1}.

4.1.8 AFGL 618 (The Westbrook Nebula)

AFGL 618 (or CRL 618) is a bipolar PPN, which evolved from the AGB about 200 years ago (Kwok & Bignell 1984) and it exhibits lobes expanding at ~ 200 km s^{-1} (Sánchez Contreras et al. 2002). Recent modelling suggest a total molecular mass of ~ 0.4 $M_{\odot}$ mostly contained in the halo and in the bipolar outflow (figure 1.3), approximately oriented in the E-W direction and carrying most of the momentum (Soria et al. 2013). The molecular envelope, which encloses most of the mass, contains an extended, round halo ($> 20''$) expanding more slowly and a CO core measured up to $\sim 7''$ from the centre (Sánchez Contreras et al. 2004). One of the most interesting findings was the discovery of warm H_2O vapor in the CSE of AFGL 618, which is also present in AFGL 2688 (Wesson et al. 2010, and references therein). Note that the origin of oxygen-bearing molecules in C-rich stars is not well understood (see introduction).

Huang et al. (2016) produced a 3D multidirectional-bullet model and derived a mass-loss rate for each component. For example it can be $\dot{M} = 1 - 4 \times 10^{-3}$ $M_{\odot}$ yr^{-1} in the outflows and about $\dot{M} = 5.5 \times 10^{-5}$ $M_{\odot}$ yr^{-1} in the halo that "slowly" expands at ~ 16 km s^{-1}. On the other hand, in the dense core (< 1500 au) the mass-loss can be up to 40 times higher.

4.1.9 HD 44179 (The Red Rectangle)

The Red Rectangle is also a bipolar nebula around a spectroscopy binary obscured by an optically thick torus (e.g. Men'shchikov et al. 2006). The X-shaped structure as shown in figure 4.1 extends over $\sim 40''$ and can be seen in a wide range of wavelengths from optical to mid-infrared. Using ALMA observations Bujarrabal et al. (2013) detected ^{12}CO and ^{13}CO emission coming from the X-structure and a rotating disk.

This PPN is known to be particularly rich in polycyclic aromatic hydrocarbons (PAHs) that are widely distributed in the nebula, while the CO emission is weak (Knapp et al. 2000). These authors found [CI] emission in HD 44179. Despite its carbon nature, O-rich

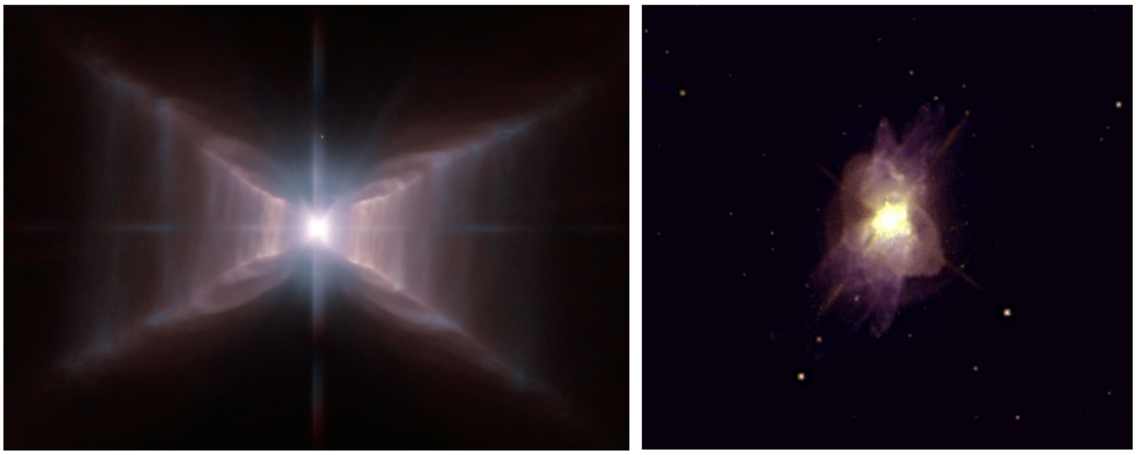

Fig. 4.1: HST images of 2 carbon pre-planetary nebulae; Left: the Red Rectangle on a $25'' \times 20''$ fov (credit: ESA/Hubble and NASA), right: Water Lily Nebula (credit: Sun Kwok, Bruce Hrivnak, and Kate Su).

material is also present in the torus. Miyata et al. (2004) observed the core ($\sim 0.09''$) in the MIR and concluded that the spectrum is well modelled by 358 K blackbody curve.

Men'shchikov et al. (2002) obtained a mass-loss history between $\dot{\mathrm{M}} \sim 10^{-8}$–$10^{-2}$ $\mathrm{M}_\odot$ yr^{-1} by studying the envelope's density distribution. Bujarrabal et al. (2016) obtained a total disk mass of ~ 0.01 $\mathrm{M}_\odot$ and a mass-loss for the keplerian disc component of $\dot{\mathrm{M}} \sim 10^{-6}$ $\mathrm{M}_\odot$ yr^{-1}.

4.1.10 V Hya

The semi-regular carbon star V Hya is very well known for its collimated, high-velocity ($\sim 70 - 120$ km s^{-1}) outflows, althought a more compact hot structure with $\sim 0.5''$ expanding at $10 - 15$ km s^{-1} is also observed (Sahai et al. 2009).

V Hya has a characteristic bright CO emission and unusual CO-line shapes, with two horns and Voigt-like profiles, in contrast to the parabolic line profile seen in almost all other AGB envelopes (Knapp et al. 2000). While studying atomic carbon emission, these authors derived a mass loss of 1.5×10^{-6} $\mathrm{M}_\odot$ yr^{-1} assuming a distance of 380 pc, and argue that since the central star of V Hya is cool, the [CI] emission should originate from shock dissociation of circumstellar CO and not from photodissociation. With slightly different assumptions, Sahai et al. (2009) used the fundamental vibration-rotation band of CO ($\nu = 1$, 4.7 μm) to find a range of temperatures in the lobes between $34 - 574$ K.

Daan Camps (MSc. thesis 2011) performed a detailed analysis of V Hya. In particular, he analysed its PACS spectrum[1] and identified spectral lines belonging to CO, HCN, CS, SiS and H_2O. Then he derived a mass-loss rate of $\dot{M} = 1.05 \times 10^{-6}$ $M_\odot$ yr^{-1} in good agreement with Knapp et al. (1997; 2000).

4.1.11 IRAS 16594-4656 (The Water Lily Nebula)

IRAS 16594-4656, also known as the Water Lily Nebula, hosts a central star with $T_{eff} \sim 10300$ K (Mishra et al. 2005). It was first identified as a PPN on the basis of its IRAS colours with its NIR/MIR emission being dominated by PAHs. These spectral features plus the detection of CO molecular emission in its envelope with velocity ~ 16 km s^{-1} confirmed its C-rich chemistry (García-Hernández et al. 2006, and references therein). These authors used the imaging mode of TIMMI2 installed on ESO 3.6m to obtaine MIR images of this source and found an elliptical nebula with its major axis oriented along the east-west direction at a P.A =80° and extending out to at least $3.5'' \times 2.1''$, coincident with the orientation of bipolar outflows identified in HST optical images.

In fact, while complex multilobe structure (figure 4.1) is seen in the optical V band and in the NIR H band, H_2 is traced in a clear bipolar, peanut-shaped outflow (Hrivnak et al. 2008).

A model with mass-loss of 1×10^{-5} $M_\odot$ yr^{-1} fits reasonably well CO $J = 1 \rightarrow 0$, $J = 2 \rightarrow 1$ and $J = 3 \rightarrow 2$ line profiles (Woods et al. 2005).

4.1.12 AFGL 2688 (The Egg Nebula)

AFGL 2688 (or CRL 2688) also known as the Egg Nebula, is a PPN who exhibits bipolar, optical lobes (figure 1.3) and multiple concentric arcs. The central star is completely obscured. (Sahai et al. 1998; Ishigaki et al. 2012). Jura et al. (2000) found an elongated structure ($5.6'' \times 1.9''$) at P.A $\sim 53°$ in cm-wavelength studies, while reporting that the visible outflows lies at P.A $\sim 15°$, resulting from scattered light. A compact CO core of $\sim 2''$ expanding at ≥ 10 km s^{-1} and shocked H_2 distributed orthogonally to the optical

[1]Actually we are using the same observation in this thesis, although it was reprocessed with more up-to-date calibration files.

lobes were reported by Cox et al. (2000) who used the IRAM interferometer.

Cox et al. (1996) presented the ISO LWS spectrum of AFGL 2688 and drew the same conclusions as we did in the previous chapter: the FIR spectrum of this PPN is dominated by CO lines and no atomic/ionised lines are yet seen, indicating that the central star is still not hot enough to ionise the gas envelope in preparation for the PN phase. The authors also argue that the molecular gas is heated by shocks and cools via NIR ro-vibrational H_2 and FIR CO lines. The mass of shocked H_2 gas was estimated to be $\sim 5 \times 10^{-3}$ $M_\odot$.

The dynamical age of the nebula and mass-loss rate were estimated to be ~ 350 yr and $\dot{M} = 3 \times 10^{-5}$ $M_\odot$ yr^{-1}, respectively (Ueta et al. 2006; Lo et al. 1976).

4.1.13 CPD-568032

CPD-56°8032 (or Hen 3-1333) is a young PN that hosts a Wolf-Rayet central star of the WC10 type. Moreover, there is evidence for dual-chemistry, namely carbon-rich and oxygen-rich dust grains in the CSE (Danehkar & Parker 2015, and references therein). Using the UCL echelle spectrograph De Marco et al. (1997) found a nebular expansion velocity of ~ 30 km s^{-1} by modelling Hα and Hβ lines and estimated a dynamical age of ~ 100 yr. These authors also used HST (Hβ band) images and found a nebular size of $\sim 2''$.

De Marco & Crowther (1998) found a mass-loss rate of $\dot{\mathrm{M}} = 4 \times 10^{-6}$ $M_\odot$ yr^{-1}.

4.1.14 IRAS 21282+5050

IRAS 21282+5050 is an unusual, young, low-excitation planetary nebula, that shows one of the highest IR excesses among it's class (Kwok et al. 1993). It was considered by (Cohen & Jones 1987) as a very compact source with a Wolf-Rayet central star of the spectral type O7-WC11. The first size estimate of IRAS 21282+5050 came from Likkel et al. (1988) who derived a diameter of $\sim 10''$ in CO ($J = 1 \to 0$ and $J = 2 \to 1$) observations. Using high resolution optical imaging Kwok et al. (1993) measured a size of approximately $\sim 7'' \times 5''$ oriented in the N-S direction, while Bregman et al. (1992) found a very compact nebula ($\sim 5''$) in the K band.

Table 4.2: Properties of the stars in the sample: distance, luminosity, effective temperature and mass-loss rate.

Target name	d (pc)	L ($L_\odot$)	T_{eff} (K)	$\dot{M}$ ($M_\odot$ yr^{-1})
IRC+10216	120[b]	9800[b]	2000[m]	1.5×10^{-5}
CIT 6	410[a]	8165[a]	2445[a]	6×10^{-6}
IRAS 15194-5115	500[b]	8900[b]	2400[m]	1.5×10^{-5}
AFGL 2513	1760[g]	8470[g]	2500[m]	2×10^{-5}
V CYG	366[b]	6000[b]	2581[m]	1.6×10^{-6}
AFGL 3068	1300[b]	10900[b]	2000[m]	2.5×10^{-5}
AFGL 3116	630[b]	9600[b]	2000[m]	7×10^{-6}
AFGL 618	900[d]	10000[d]	30000[d]	5.5×10^{-5}
HD 44179	710[h]	6050[h]	7750[h]	$10^{-8} - 10^{-2}$
V HYA	495[a]	17539[a]	2160[a]	1×10^{-6}
IRAS 16594-4656	1600[i]	6000[i]	10000[k]	1×10^{-5}
AFGL 2688	340[c]	5500[c]	7250[j]	3×10^{-5}
CPD-56°8032	1350[f]	5000[f]	30000[f]	4×10^{-6}
IRAS 21282+5050	2440[e]	4000[e]	30000[n]	6×10^{-5}

References: [(a)] Bergeat & Chevallier (2005), [(b)] Ramstedt et al. (2014), [(c)] Balick et al. (2012), [(d)] Sánchez Contreras et al. (2004), [(e)] Vickers et al. (2014), [(f)] Chesneau et al. (2006), [(g)] Guandalini et al. (2006), [(h)] Men'shchikov et al. (2006), [(i)] García-Hernández et al. (2006), [(j)] Ishigaki et al. (2012), [(k)] Mishra et al. (2015), [(l)] Sahai & Chronopoulos (2010), [(m)] De Beck et al. (2010), [(n)] Hasegawa & Kwok (2003); see text for $\dot{M}$

The mass-loss rate was first estimated by Likkel et al. (1988) in about $\dot{M} = 6 \times 10^{-5}$ $M_\odot$ yr^{-1} and later confirmed by Meixner et al. (1998) who assumed a distance of 2 kpc.

4.2 Rotational diagram analysis

We performed the rotational diagram (or population diagram) analysis whose details are well explained in Goldsmith & Langer (1999). Essentially, for a molecule in LTE, the population of each level N_u can be described by a single rotation temperature T_{rot} that matches the gas kinetic temperature as given by the Boltzmann distribution:

$$N_{\rm u} = \frac{N_{\rm tot}}{Z(T_{\rm rot})} g_u e^{-E_{\rm u}/kT_{\rm rot}} \tag{4.1}$$

where $N_{\rm tot}$ is the total number density of the species, $Z(T)$ is the partition function, $g_{\rm u}$ are the statistical weights and k is the Boltzmann constant. In the case of CO, the partition function can be approximate by:

$$Z(T) \approx \frac{T_{\rm rot}}{2.77} + 1/3 \tag{4.2}$$

The optical depth τ at the line centre of a given transition is defined by:

$$\tau = \frac{A_{\rm ij}\lambda^3 N_{\rm u}^{\rm col}}{8\pi V} \times (e^{(hc/(\lambda kT))} - 1) \tag{4.3}$$

where $V = v_{\rm exp}\sqrt{\pi}/(2\sqrt{\log 2})$ [km s^{-1}] with $v_{\rm exp}$ being the expansion velocity of the gas, $N_{\rm u}^{\rm col}$ is the column density of the upper level and $A_{\rm ij}$ is the Einstein A-coefficient for spontaneous emission. In the case of optically thick emission, an optical depth correction factor C_τ should be added. It can be defined as:

$$C_\tau = \frac{\tau}{1 - e^{-\tau}} \tag{4.4}$$

to be multiplied by the number of molecules and allowing us to rewrite equation 4.1 in the following way:

$$\ln\left(\frac{N_{\rm u}}{{\rm g_u}}\right) = \ln\left(\frac{N_{\rm tot}}{Z(T)}\right) - \frac{E_{\rm u}}{kT} - \ln C_\tau \tag{4.5}$$

where the left hand-side is proportional to the integrated line flux F as defined in equation 3.6 such that:

$$N_{\rm u} = \frac{4\pi F \lambda d^2}{A_{\rm ij} hc} \tag{4.6}$$

where d is the distance, h is the Planck constant and c is the speed of light. To the statistical uncertainty of the line flux computed using equation 3.7 (table A.11) we add in quadrature an average flux calibration uncertainty[2] (cal) of 15% so that the standard errors[3] are given by:

$$\delta N_{\mathrm{u}} = \sqrt{\left(\frac{\mathrm{cal}}{100} \times F\right)^2 + \left(\frac{\delta F}{F}\right)^2} \tag{4.7}$$

such that the error in the y-coordinate ($y \equiv \ln(N_{\mathrm{u}}/g_{\mathrm{u}})$) is simply:

$$\delta y = \frac{\delta N_{\mathrm{u}}}{N_{\mathrm{u}}} \tag{4.8}$$

After plotting the logarithm of the number of molecules per statistical weight (y) versus the energy of the upper transition divided by the Boltzmann constant $\left(\frac{E_{\mathrm{u}}}{k}\right)$, we fit a straight line whose slope and y-intercept are related to the temperature and number of gas molecules, respectively. To convert the latter to column density, an assumption of the size of the CSE is needed. For that we used data from literature and our own estimates of the first part of this work. The transition constants involved in these calculations, namely Einstein coefficients and statistical weights can be found in table A.9 in the appendices.

Note that this is a coupled problem because to correct the diagram for the opacity one has to calculate line optical depths τ that require an input temperature and column density. The approach we followed in this work was to compute a first guess of the temperature and column density using equation 4.5 without the opacity correction term, i.e. $\ln C_\tau = 0$. Then, after computing the opacity corrected line fluxes, we execute a second iteration and check the impact on the temperature and column density parameters. It keeps going iteratively until convergence is reached, which was defined in terms of a relative, maximum change of 30% in the derived parameters. Moreover, this has to be repeated for a range of different values of gas expansion velocity. If v_{exp} is too high, then the opacity correction might be unimportant. On the other hand, if v_{exp} is small (<20 km s^{-1}) the correction could be significant. Here we tried a range of expansion velocities: [10, 20, 30, 40] km s^{-1}.

The fit was performed by making use of the function *lm* in the R *stats* package[4]. We investigated the impact of fitting weights on the regression parameters. They are defined

[2] PACS Observer's Manual, v.2.5.1, 2013

[3] Note that the distance is a major source of uncertainty that cannot be accounted in most cases.

[4] https://stat.ethz.ch/R-manual/R-devel/library/stats/html/stats-package.html

as usually: $w_i = 1/\sigma_i^2$ where we devalue points with higher variance σ_i^2. Therefore, we perform the fit with and without fitting weights and both results ought to be reported. This is important when comparing results to literature.

At times, as we will present further on, a straight line does not quite properly fit the entire range of excitation temperatures. This could be an indication that lines are optically thick or that the LTE approximation is simply not valid. Alternatively, there could be, in fact, several temperature components corresponding to different regions of the CSE since our observations are not spatially resolved.

We convert the total number of CO molecules N to CO mass by simply multiplying it by the mass of a CO molecule ($m_{\mathrm{CO}} \sim 4.65 \times 10^{-23}$ g). To estimate the mass of molecular hydrogen, i.e., gas envelope mass, we adopted the fractional abundance relative to the CO of $f_{\mathrm{CO}} = 8 \times 10^{-4}$ (e.g. Teyssier et al. 2006) and used the following formula:

$$M_{\mathrm{H_2}} = \frac{N_{\mathrm{tot}}}{f_{\mathrm{CO}}}\, m_{\mathrm{H_2}} \tag{4.9}$$

such that the uncertainty propagates as:

$$\delta M_{\mathrm{H_2}} = \frac{\delta N}{N}\, M_{\mathrm{H_2}} \tag{4.10}$$

We obtained rotational diagrams for ^{12}CO and in some cases for ^{13}CO as well.

4.2.1 Code validation

The code was validated by reproducing the results of Justtanont et al. (2000) (hereafter J2000) who used ISO data to plot the rotational diagram (without opacity correction) of AFGL 618. In addition, since this target is also in our sample we compare our rotational diagram with J2000 in figure 4.2. Two points were excluded from their data[5] around 1800 K (at $\sim$ 100 μm) because we don't have PACS counterparts. Note that CO lines were previously detected only up to $J_{\mathrm{up}} = 37$, but here we find them until $J_{\mathrm{up}} = 45$. Adopting a distance of 1.8 kpc, J2000 derived a temperature of $T = 700$ K, a number of molecules

[5] The slight difference in the ISO temperature relative to the one reported in J2000 is probably due to the exclusion of 2 data points.

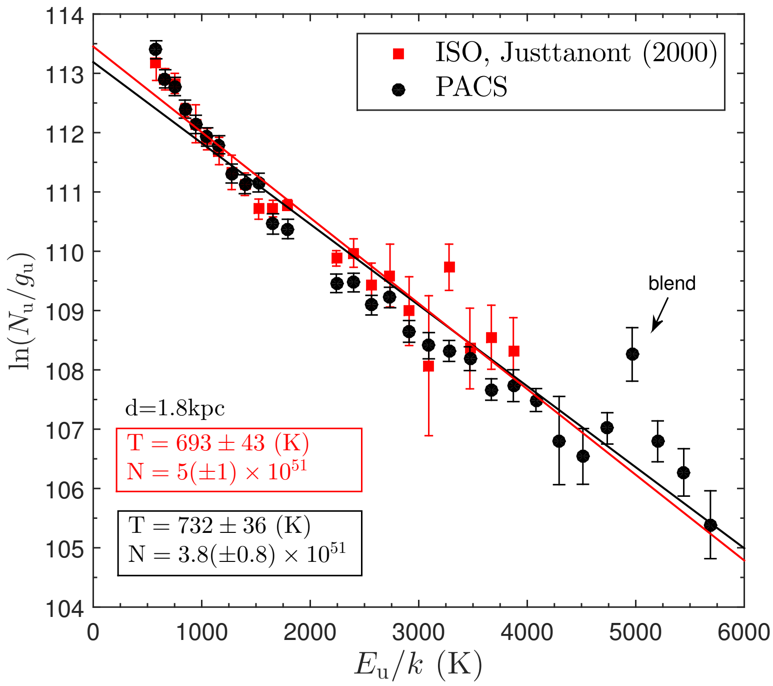

Fig. 4.2: ^{12}CO rotational diagram of AFGL 618 with ISO data (Justtanont et al. 2000) and with our PACS data. For this comparison (only) we adopted the distance d = 1.8 kpc.

of $N = 4.4 \times 10^{51}$, which implies a CO mass of $\sim 10^{-4}$ $M_\odot$ in good agreement with our PACS data.

4.2.2 A single temperature component

In a first approach we want to fit just one straight line to the data and compare the results with and without opacity correction.

To compute the column density we need to input a size. To decide on the size of the CO emitting region we take a look at the sizes we derived from photometry maps in the second chapter of this thesis (table A.6). For CIT 6, from both blue and red band photometry, we obtain a deconvolved size (equation 2.11) of $\sim 3''$ which agrees with the shells observed in the NIR up to $\sim 4''$. For AFGL 3116, we obtain a somewhat smaller size of $\sim 2.5''$, but essentially agrees with the PSF within 1σ. AFGL 618 was found to be point-like as well. Probably the FIR emission also arises from the dense core ($< 2''$) seen in other studies as mentioned before. AFGL 2688 is significantly larger than the photometer PSF in the blue band and we find a deconvolved size of $\sim 4''$. However, in the red band, it agrees with the beam size within the uncertainty. The size of $4''$ agrees with the elongated structure seen in radio wavelengths, but perhaps the CO region is even more compact since a CO core is known to exist at the scale of $\sim 2''$. In principle, the size of the CO emitting region could be smaller than what traced by the photometric bands which encloses both continuum and line emission within the bandwidth. IRC+10216 is also larger than the photometer PSF in both bands, but while in blue band we obtained a deconvolved size of $\sim 4''$, in the red band we get $\sim 5.8''$. It seems appropriate to adopt a larger size for this source relatively to the other AGBs. Regarding the remaining targets, AFGL 3068, HD 44179, IRAS 15194-5115, V Hya and IRAS 16594-4656 were all found to be point-like. Because these sizes are qualitatively not very different, we experiment in a first approach a reasonable size of $3''$ for all of them, and later we study the impact of this assumption on the derived quantities. In what regards the 2 PN, we do not have photometry data, but we know that the temperature conditions do not require a size as small as in AGB stars. Nevertheless, both IRAS 21282+5050 and CPD-568032 are known to be very compact nebulae so we set both sizes equal to $5''$. Furthermore, note that the size of the emitting region could be different for each transition, so in this approximation all observed CO lines are assumed to come from the same region. We also assume that the observed ^{12}CO and ^{13}CO lines come from a region with the same size.

Firstly, we study the rotational diagram of ^{12}CO. In figure 4.3 we present the rotational diagrams (without opacity correction) of the 14 targets where we see a range o ^{12}CO transitions following a linear trend under different temperature conditions. Qualitatively we found what is expected with PNs showing the coldest gas given the smaller number of detected CO lines, whereas AGBs and some PPNs possess the hottest gas.

To apply the opacity correction we used for AGB stars $v_{\rm exp} = 20$ km s^{-1}, for PPN we took $v_{\rm exp} = 40$ km s^{-1} and for PN we assumed $v_{\rm exp} = 30$ km s^{-1}. In table 4.3 we compile the rotational diagram results for the 14 targets with and without opacity correction. In the appendix (table A.12) we list the results of the linear regression without fitting weights which produces significant changes in some cases.

We conclude that for this choice of parameters, the opacity correction is small in this sample of stars and it has a negligible impact on the rotational diagram. However,

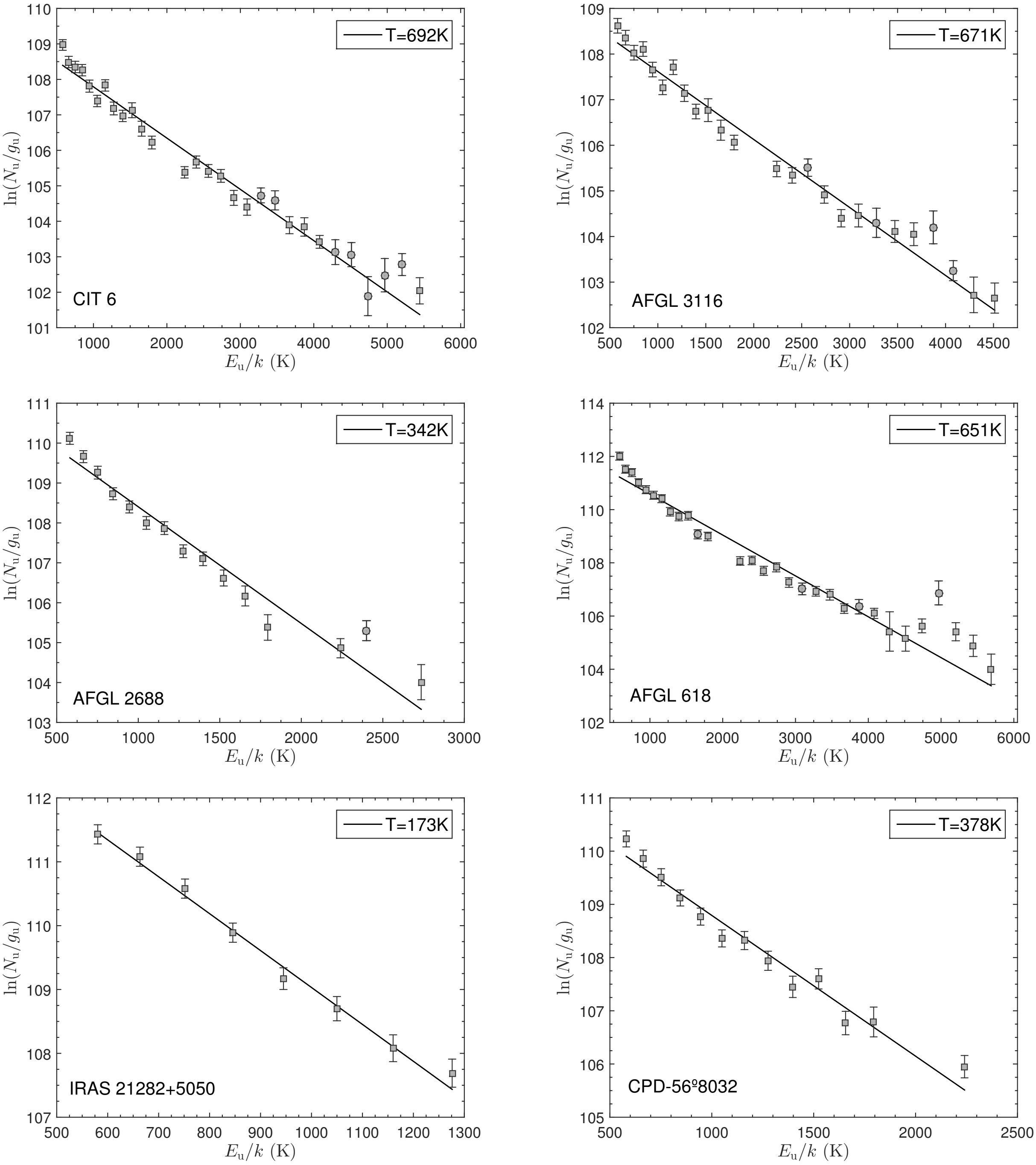

Fig. 4.3: Rotational diagrams for the sample of C-rich stars with a fitted, single temperature component. Circles mark known line blends.

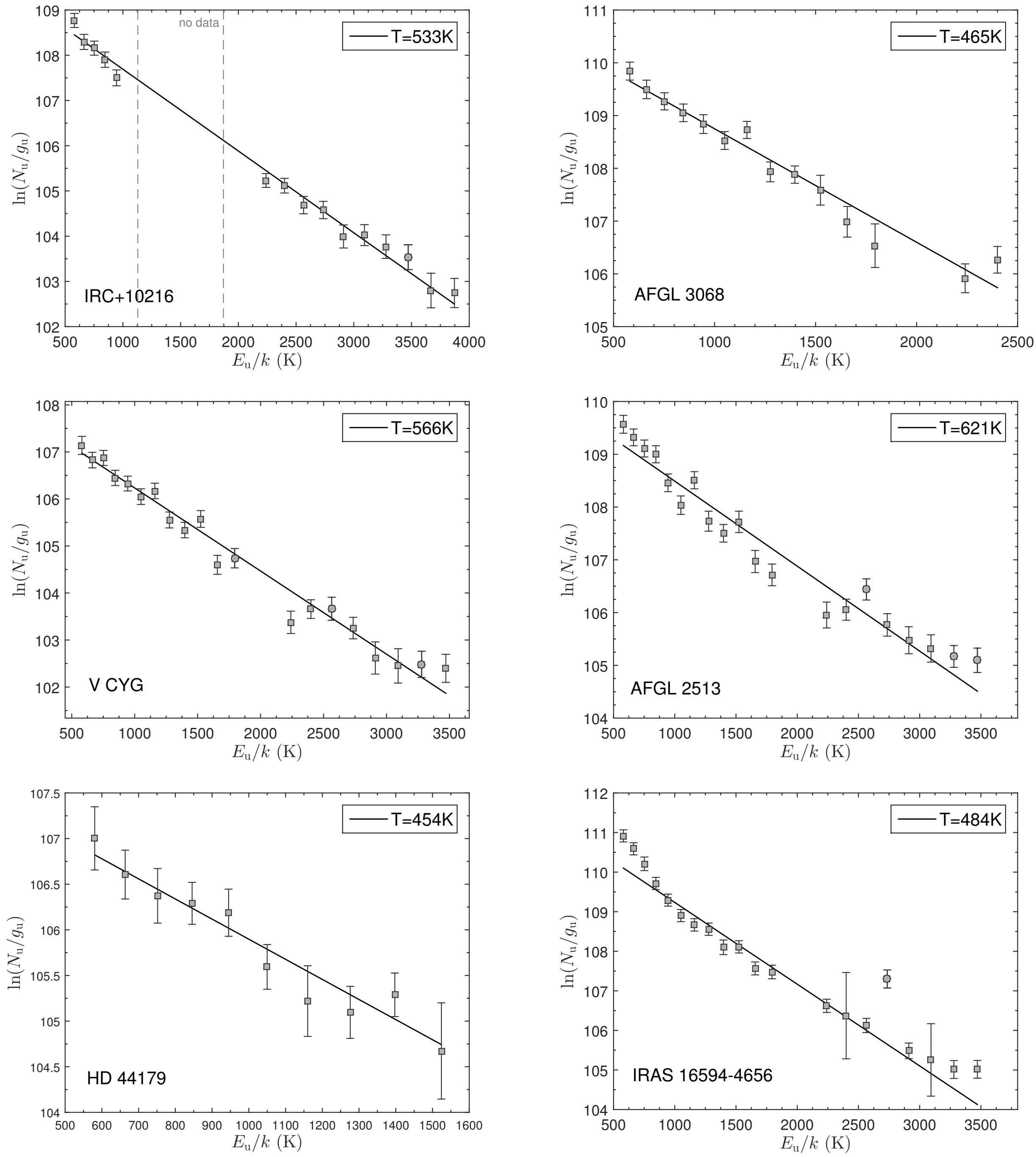

Fig. 4.3: Continued.

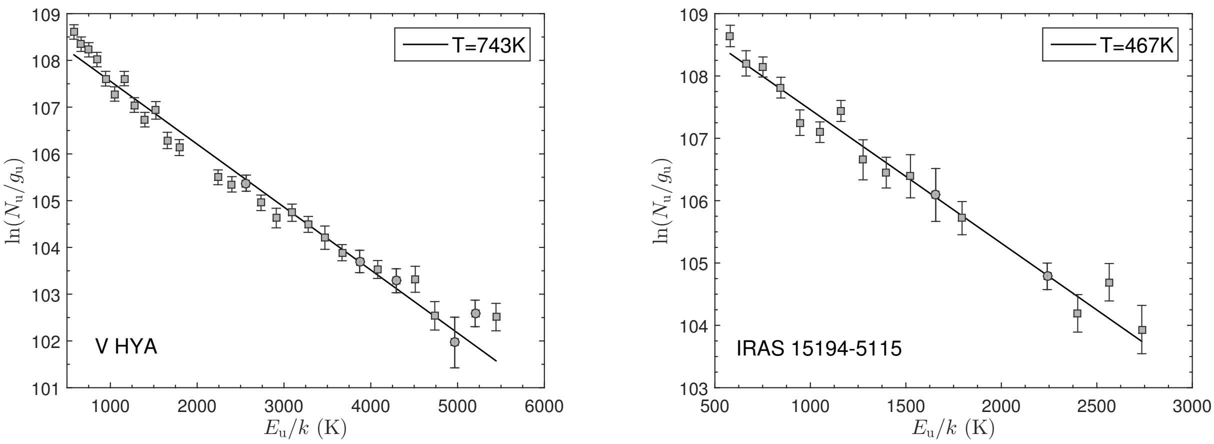

Fig. 4.3: Continued. Rotational diagrams for the sample of C-rich stars with a fitted single temperature component. Circles mark known line blends.

IRC+10216 may be an exception and deserves further attention.

The hottest gas was found in a young PPN, V Hya, followed by AFGL 618 and AGBs. AFGL 2688 has a relatively cold mass of gas comparable to CPD-568032. IRAS 21282+5050 is the target with the coldest gas ($T \sim 173$ K), but a gas mass of $\sim 10^{-2}$ $M_{\odot}$, the largest among these targets.

4.2.3 Parameter sensitivity and uncertainty

Although the choice of parameters, namely angular sizes and expansion velocities, seems reasonable, we want to evaluate how does our derived quantities from rotational diagrams depend on the uncertainty associated to those parameters.

a) Angular size

The size assumption largely influences the derived column density. It is hard to tell what is the region or physical origin of these high J, CO emission lines by just looking at the population diagrams, but these high temperatures probably require relative proximity to the star. This means that perhaps the true angular size of the emitting region could be smaller than what we assumed. A smaller size not only impacts directly the derived column density, but also affects the opacity correction, producing larger optical depths, hence a larger opacity correction for a given expansion velocity.

Figure 4.4 depicts the impact of the adopted size on the opacity correction and consequently on the temperature (T) and number of molecules ($N_{\rm tot}$). We studied the change

Table 4.3: Rotational diagram results (top: weighted least-squares, bottom: unweighted least-squares) for a given angular size and gas expansion velocity, with and without opacity correction C_τ.

Target Name	T (K)	N_{CO} (molecules)	N^{col} (cm^{-2})	M_{H_2} ($M_\odot$)	C_τ
IRC+10216	553±15	$7.1(\pm0.7)\times10^{49}$	$1.7(\pm0.2)\times10^{18}$	$1.5(\pm0.2)\times10^{-4}$	no
	530±14	$8.7(\pm0.7)\times10^{49}$	$2.1(\pm0.2)\times10^{18}$	$1.5(\pm0.2)\times10^{-4}$	yes
CIT 6	692±26	$6.9(\pm0.9)\times10^{49}$	$1.5(\pm0.2)\times10^{17}$	$1.4(\pm0.2)\times10^{-4}$	no
	690±26	$7.0(\pm0.9)\times10^{49}$	$1.5(\pm0.2)\times10^{17}$	$1.4(\pm0.2)\times10^{-4}$	yes
IRAS 15194-5115	467±24	$7(\pm1)\times10^{49}$	$1.8(\pm0.3)\times10^{17}$	$1.4(\pm0.2)\times10^{-4}$	no
	464±24	$7(\pm1)\times10^{49}$	$1.8(\pm0.3)\times10^{17}$	$1.5(\pm0.2)\times10^{-4}$	yes
AFGL 2513	621±35	$1.5(\pm0.3)\times10^{50}$	$3.0(\pm0.5)\times10^{16}$	$3.2(\pm0.5)\times10^{-4}$	no
	621±35	$1.5(\pm0.3)\times10^{50}$	$3.0(\pm0.5)\times10^{16}$	$3.2(\pm0.5)\times10^{-4}$	yes
V CYG	566±24	$1.6(\pm0.2)\times10^{49}$	$8(\pm1)\times10^{16}$	$3.4(\pm0.5)\times10^{-5}$	no
	564±24	$1.6(\pm0.2)\times10^{49}$	$8(\pm1)\times10^{16}$	$3.5(\pm0.5)\times10^{-5}$	yes
AFGL 3068	465±27	$2.5(\pm0.4)\times10^{50}$	$9(\pm1)\times10^{16}$	$5.3(\pm0.8)\times10^{-4}$	no
	464±27	$2.5(\pm0.4)\times10^{50}$	$9(\pm1)\times10^{16}$	$5.3(\pm0.8)\times10^{-4}$	yes
AFGL 3116	671± 24	$5.9(\pm0.7)\times10^{49}$	$9(\pm1)\times10^{16}$	$1.3(\pm0.2)\times10^{-4}$	no
	670± 24	$5.9(\pm0.7)\times10^{49}$	$9(\pm1)\times10^{16}$	$1.3(\pm0.2)\times10^{-4}$	yes
AFGL 618	651± 28	$1.2(\pm0.2)\times10^{51}$	$9(\pm1)\times10^{17}$	$2.5(\pm0.4)\times10^{-3}$	no
	646± 28	$1.2(\pm0.2)\times10^{51}$	$9(\pm1)\times10^{17}$	$2.6(\pm0.4)\times10^{-3}$	yes
HD 44179	454±47	$1.5(\pm0.4)\times10^{50}$	$1.8(\pm0.5)\times10^{16}$	$3.0(\pm0.8)\times10^{-5}$	no
	454±47	$1.5(\pm0.4)\times10^{50}$	$1.8(\pm0.5)\times10^{16}$	$3.0(\pm0.8)\times10^{-5}$	yes
V Hya	743±25	$5.3(\pm0.6)\times10^{49}$	$1.4(\pm0.2)\times10^{17}$	$1.1(\pm0.2)\times10^{-4}$	no
	742±25	$5.3(\pm0.6)\times10^{49}$	$1.4(\pm0.2)\times10^{17}$	$1.1(\pm0.2)\times10^{-4}$	yes
IRAS 16594-4656	484±26	$4.3(\pm0.8)\times10^{50}$	$1.1(\pm0.2)\times10^{17}$	$9(\pm2)\times10^{-4}$	no
	483±26	$4.3(\pm0.8)\times10^{50}$	$1.1(\pm0.2)\times10^{17}$	$9(\pm2)\times10^{-4}$	yes
AFGL 2688	342± 22	$2.8(\pm0.7)\times10^{50}$	$1.5(\pm0.4)\times10^{18}$	$6(\pm2)\times10^{-4}$	no
	333± 22	$3.1(\pm0.7)\times10^{50}$	$1.7(\pm0.4)\times10^{18}$	$7(\pm2)\times10^{-4}$	yes
CPD 568032	378± 22	$2.8(\pm0.5)\times10^{50}$	$3.5(\pm0.7)\times10^{16}$	$6(\pm1)\times10^{-4}$	no
	377± 22	$2.8(\pm0.5)\times10^{50}$	$3.5(\pm0.7)\times10^{16}$	$6(\pm1)\times10^{-4}$	yes
IRAS 21282+5050	173± 7	$4.6(\pm0.9)\times10^{51}$	$1.8(\pm0.3)\times10^{17}$	$9.8(\pm0.2)\times10^{-3}$	no
	173± 8	$4.7(\pm0.9)\times10^{51}$	$1.8(\pm0.3)\times10^{17}$	$9.8(\pm0.2)\times10^{-3}$	yes

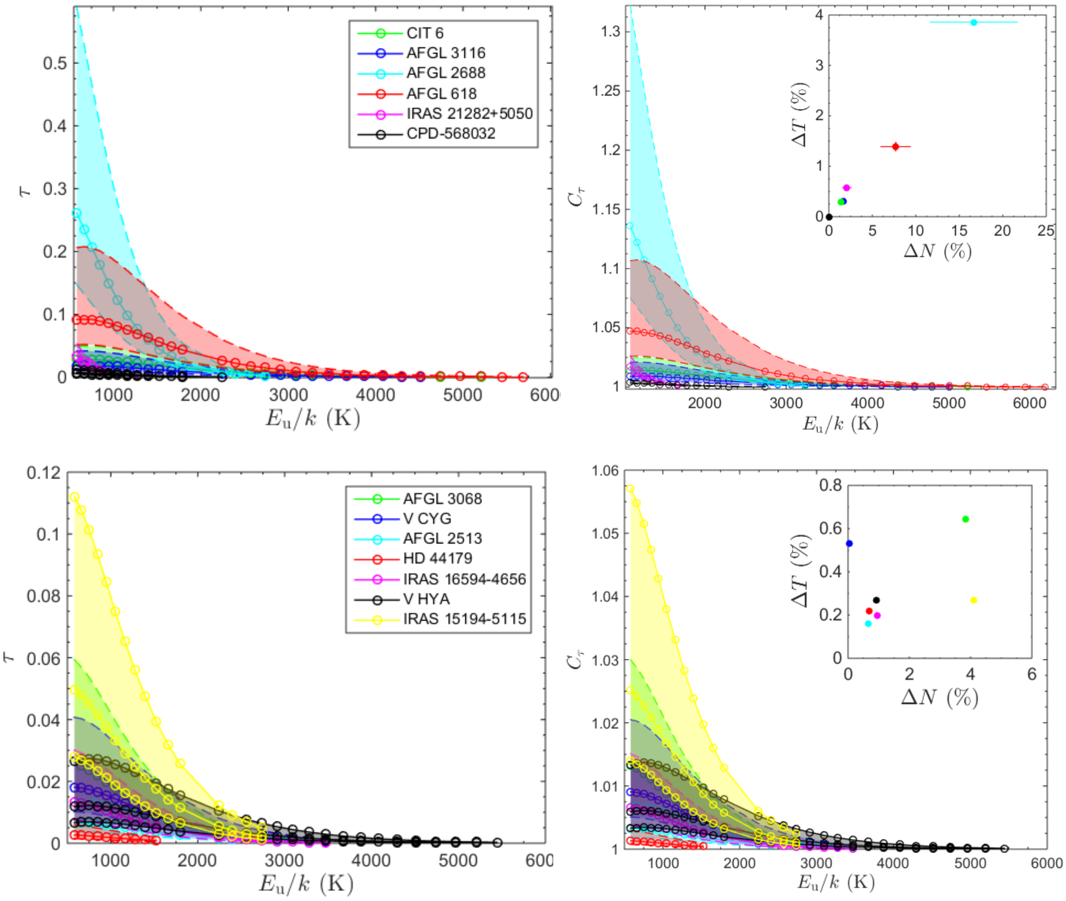

Fig. 4.4: Change in the opacity correction for a size variation of $\pm 1''$ and fixed expansion velocity. Variation of the optical depth (left) and opacity correction (right) with excitation temperature. The variation in temperature and number of molecules is also shown on the right side.

in line optical depth for a size variation of $\pm 1''$ from the assumed values and we concluded that, in this range, the optical depths are small ($\tau < 1$). In turn, the opacity correction is not very significant, hence T and $N_{\rm tot}$ change by less than 2% and 10%, respectively, in every star except AFGL 2688. In this case, the temperature changes by 4% and the number of molecules by 17%, which is still meaningless given the overall uncertainty inherent to the method. However, we note that if the true size of the CO emitting region is even more compact than $2''$, AFGL 2688 and AFGL 618 may suffer from moderate-to-high optical depth effects, at least in the lower J transitions.

This could also be the case of IRC+10216. In figure 4.5 we show the rotational diagram of IRC+10216 where we applied the opacity correction assuming an angular size of 3". We see that, despite visually producing a small correction, it changes the derived temperature by 8% and the number of CO molecules by 42%. This translates into a larger total mass of

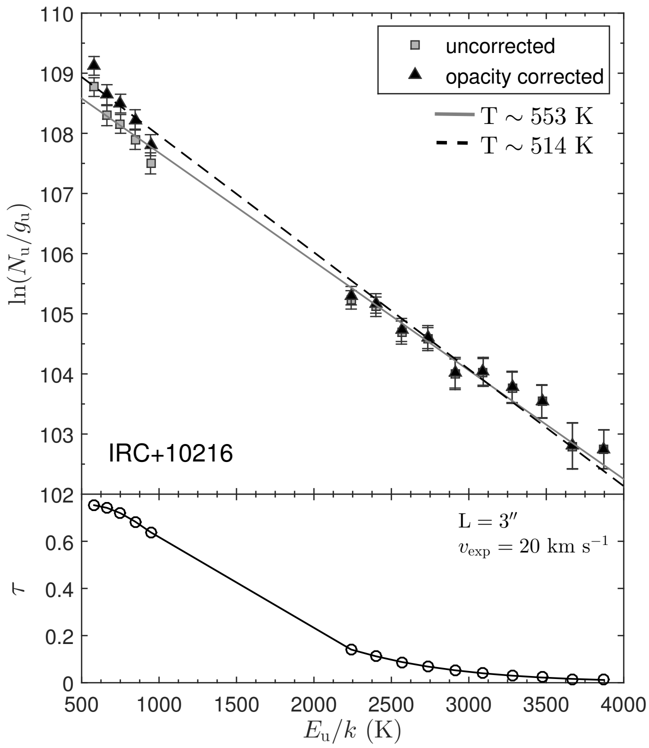

Fig. 4.5: The effect of the optical depth on the rotational diagram of IRC+10216.

gas by a factor of 1.5 approximately. We notice in the bottom plot that the optical depths are approaching unit for the lower J transitions, which means that there are important opacity effects. Adopting a smaller size will further increase the optical depths and the rotational diagram increasingly deviates from linear behaviour.

In what concerns the remaining targets, we tested smaller sizes down to only 2″ and we concluded that the opacity correction is still small ($C_\tau < 1.15$) in these circumstances as depicted in figure 4.4.

b) Expansion velocity

The gas expansion velocity varies from target to target and within the same target. For instance, in the same target a slow and a fast component may coexist as a reflex of changes in the mass-loss rate and the evolutionary stage of the central star. In the previous section we assumed rather average, representative velocities ranging from 20 to 40 km s^{-1}. The kinematics of the warm/hot CO gas component we are tracing here with PACS was never observed so there is not in literature a value we could adopt with confidence. So we are limited to an educated guess.

Mauron & Huggins (2006) reported an expansion velocity of 17 km s^{-1}, 15 km s^{-1} and

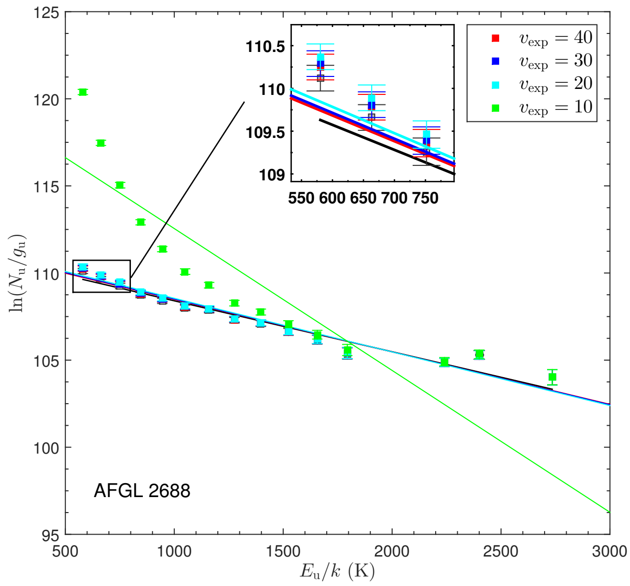

Fig. 4.6: Rotational diagram of AFGL 2688 for different expansion velocities. For $v_{\rm exp} \geq 20$ km s^{-1} convergence is attained in just 2 iterations, while for $v_{\rm exp} = 10$ km s^{-1} it takes 17 iterations and a severe deviation from linearity appears.

14 km s^{-1} of the gas envelope of CIT 6, AFGL 3116 and AFGL 3068 respectively. We tested these somewhat smaller values than our initial assumption and concluded that it has a negligible impact on the derived temperature and mass.

Using non-LTE modelling Ramstedt & Olofsson (2014) obtained $v_{\rm exp} = 22$ km s^{-1} in the case of IRAS 15194-5115, and a much lower velocity in the case of V Cyg of about ~ 12 km s^{-1}. Both values do not change the results here presented for the adopted sizes. The authors also obtained ~ 15 km s^{-1} in the case of IRC+10216, which is slightly smaller than what we assumed. We already know that IRC+10216 is problematic and convergence in the opacity correction is only attained for a large number of iterations according to our criteria. If the CO emission we are tracing with PACS comes from the same region with the same conditions or more extreme than the population studied in Ramstedt & Olofsson (2014), then IRC+10216 may suffer from moderate-to-high optical depth effects.

In what concerns the PPNs, Cox et al. (2000) found multiple molecular outflows in AFGL 2688 through CO ($J = 1 \rightarrow 0$) and continuum mapping observations, expanding at 22 km s^{-1} and 30 km s^{-1}, while in the centre a region of 2" is expanding at only ~ 10 km s^{-1} oriented along a P.A. of 54°. The direction of this elongation is in agreement with our photometry results (see chapter 2). Figure 4.6 shows the rotational diagram of

AFGL 2688 with opacity correction for different gas expansion velocities. For v_{exp} in range 20-40 km s^{-1} the opacity correction has little influence on the diagram. Consequently, the inferred temperature varies no more than 5% and the number of molecules changes up to 28%, which is within our convergence criterion achieved in just 2 iterations. However, for v_{exp} = 10 km s^{-1} the code converges in 17 iterations and produces severe opacity corrections in the lowest J transitions. In this case, the (green) straight line corresponds to a temperature and number of molecules that varied by 9% and 61%, respectively, relative to the uncorrected rotational diagram. These latter values are not even meaningful since there is a considerable departure from linear behaviour, which does not seem very realistic.

AFGL 618 is another source where different velocity components coexist. The fast, bipolar lobes outflow from the central star at velocities $\geq$ 250 km s^{-1}, whereas the spherical halo (>20") expands at $\sim$ 17 km s^{-1} (Sánchez Contreras et al. 2004b). A slow axial component expanding at $\sim$ 22 km s^{-1} and a dense, inner-torus that expands at $\leq$ 12 km s^{-1} are also reported. Huang et al. (2016) argue that this inner structure should have a size of 1500 au ($\sim$ 1.7″). We found a very compact nebula using PACS photometry (see table A.7), adding to the picture where the FIR emission comes from a relatively smaller and hotter region, close to the central star. Assuming a size of 3" we tested opacity corrections for a range of v_{exp} between 10-40 km s^{-1} and concluded that the temperature varies by a maximum of 3% and the number of molecules varies 18%. But if we lower the size to 2″ we find ourselves in an identical situation to AFGL 2688 with difficult convergence for v_{exp} = 10 km s^{-1}. So there is a trade-off between angular size and expansion velocity. If v_{exp} is much larger than what we assumed and the FIR CO emission is tracing one of the fast outflows, then the optical depths could be small.

Slow outflow velocities of $\sim$ 10 km s^{-1} in HD 44179 are reported in Bujarrabal et al. (2013). We tested a range of smaller velocities than what we had assumed and concluded that smaller values have negligible impact on the rotational diagram, at least down to a size of 1".

In the case of V Hya, if we take the expansion velocity of $\sim$ 10 km s^{-1} from Sahai et al. (2009) for the slow outflow observed in the NIR, we conclude that the opacity correction is still small for the adopted size of 3" and down to 1". For a size of 1" the maximum optical depth is ~ 0.43 and the temperature changes by 5% and the number of molecules varies by 21% relatively to the uncorrected rotational diagram. However, if the high J CO emission comes from an even more compact region, then significant optical depth effects are expected.

Finally, if we take the value of $v_{\rm exp} = 16$ km s^{-1} for the expanding envelope of IRAS 16594-4656 observed through low J CO transitions (García-Hernández et al. 2006) we draw the same type of conclusions, i.e., only a combination of low velocities and small sizes (<1") would produce large optical depths.

c) CO fractional abundance

The fractional abundance $f_{\rm CO}$ has no impact on the rotational diagram, it only influences the conversion from CO mass to H_2 mass. So to compare with literature, one simply scales the results with a different conversion ratio.

With these ideas in mind, we note that the derived gas temperature should be regarded as an upper limit, while the number of molecules/column density should be taken as a lower limit of the true temperature and density conditions of the gas in the CSE of these stars.

4.2.4 Significance of a multi-component fit

Despite being a good representation of the general trend in the data, a single straight line does not fit equally well the entire range of CO transitions in some targets. This deviation from prediction can have several origins as mentioned before. AFGL 618 is the target where that is more clearly visible. To demonstrate that, we can visualise the regression residuals as plotted below. The two charts in figure 4.7 are just different ways of showing the same issue: the residuals are not normally distributed, as they are not randomly distributed around zero on the leftmost chart and they deviate from the theoretical straight line on the normal Q-Q plot[6]. Moreover they seem to indicate a slope change at around $E_u/k \sim 2000$ K.

It is common in literature to split the rotational diagram in 2 or more segments corre-

[6]The Q-Q plot is used to compare quantiles of two distributions.

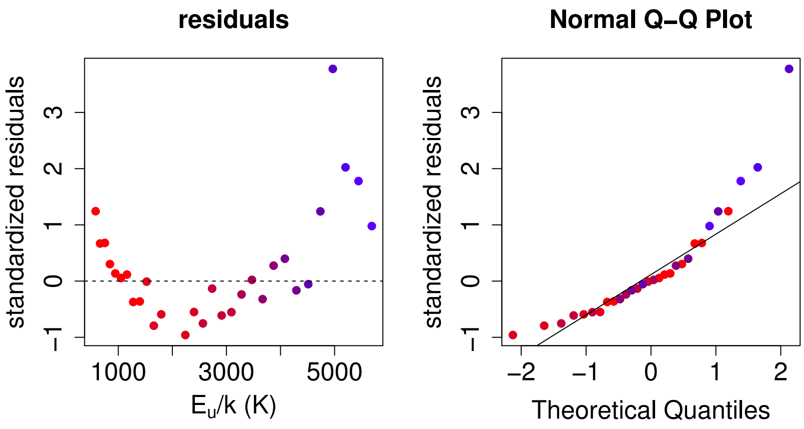

Fig. 4.7: Analysis of regression residuals in the rotational diagram of AFGL 618. The color code is related to the wavelength with red being longer wavelengths and blue corresponding to shorter ones.

sponding to several temperature components (e.g. Wesson et al. 2010; Zhang et al. 2013). However, it is not always clear by eye whether that slope change is present or not and where the breakpoint is located. For that reason we used statistical tests to automatically find structural changes in classical linear regression and assess their significance. To do so, we used *strucchange* package[7] (Zeileis et al. 2002) implemented in R. There is an extensive literature about this topic, namely about empirical fluctuation processes, but essentially the methods consist in minimising the residual sum of squares (RSS) by sectioning and fitting different portions of the data . Some of these tools are widely used in economy and medicine to look for changes in time series. In our case, it can be used to test the change in the slope of a straight line fitted to the data. Obviously, the more we split the data in segments the smaller the sum of residuals will be. However, that would lead to an undesired over-fit that really does not represent the data. To overcome that, one can use the Bayesian information criteria (BIC) or even Akaike's Information Criteria (AIC) to obtain an optimal number of breakpoints, as they will penalize model complexity. These quantities are defined as follows:

$$\mathrm{BIC} = -2\ln(\hat{L}) + k.\ln(n) \tag{4.11}$$

$$\mathrm{AIC} = -2\ln(\hat{L}) + 2k \tag{4.12}$$

where $\hat{L}$ is the maximum of the Likelihood function, k is the number of parameters and n

[7] https://www.jstatsoft.org/article/view/v007i02

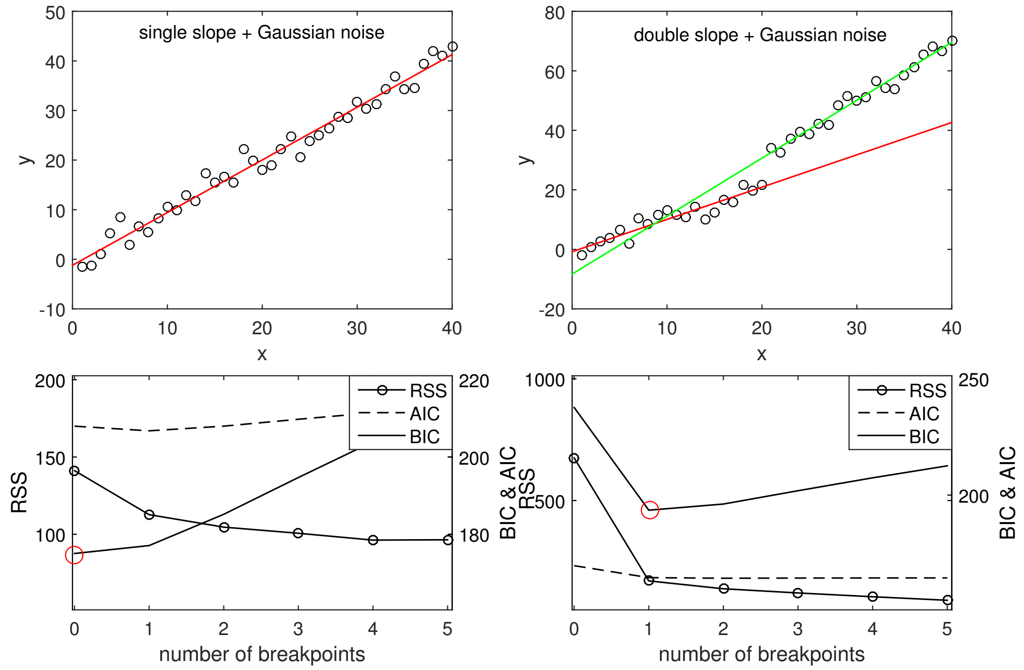

Fig. 4.8: Testing BIC and AIC for model selection with mock data. The number of breakpoints in the data is given by the minimum of BIC and AIC.

is the sample size. So we see that due to the term $k.\ln(n)$ BIC will penalize complicated models more severely than AIC. Under the assumption that errors are independent and normally distributed, BIC and AIC can be rewritten as function of the RSS as follows (Maindonald & Braun 2010):

$$\mathrm{BIC} = n\ln(\mathrm{RSS}/n) + k\ln(n) \tag{4.13}$$

$$\mathrm{AIC} = n\ln(\mathrm{RSS}/n) + 2k \tag{4.14}$$

Another approach is to use F-statistic[8] maximum (Andrews & Ploberger 1994), which is designed to test against a single structural change in the data. The F-statistic is basically the ratio of explained variance to the unexplained variance and it will produce an equivalent result to BIC if a 2-segment partition is assumed.

The best way to visualise the applicability of the criteria aforementioned is by plotting the RSS for a range of breakpoints, while looking for a minimum in the BIC (or AIC) curve. We have tested some these methods by generating mock data of straight lines plus some random Gaussian noise as exemplified in figure 4.8. Usually BIC and AIC agree in

[8]The F-test is used to test if two populations variance are equal.

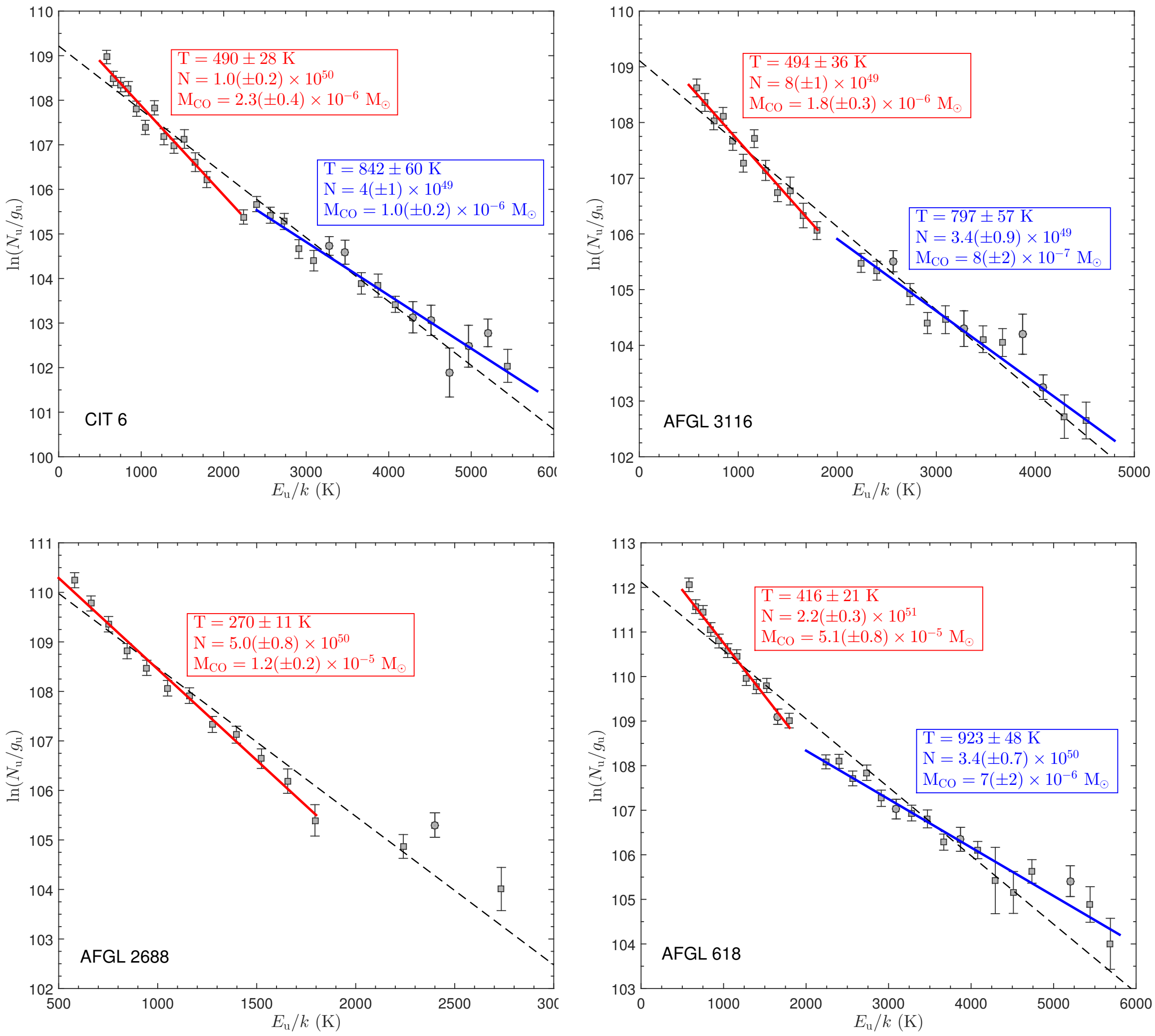

Fig. 4.9: Rotational diagrams with 2 temperature components (coloured lines) and single temperature fit (dashed line). Circles mark known line blends which were excluded from the fit.

the number of breakpoints, but in this case, for this level of noise, AIC incorrectly states that there must be a breakpoint on the simple straight line, while in the other situation where a change in the slope was introduced, it finds that any number of breakpoints larger than 1 would equally well represent the data. This is, as expected, a consequence of the much more permissive nature of AIC. On the other hand, the minimum of BIC on the left side is correctly at null number of breakpoints, whereas on the right side it suggests the existence of 1 breakpoint.

Hereinafter we only use BIC, but note that BIC is not immune to over-fitting, hence supervision is required. Given the small number of points we are not interested in splitting the diagram too much as it would, in fact, violate one of the conditions upon derivation of

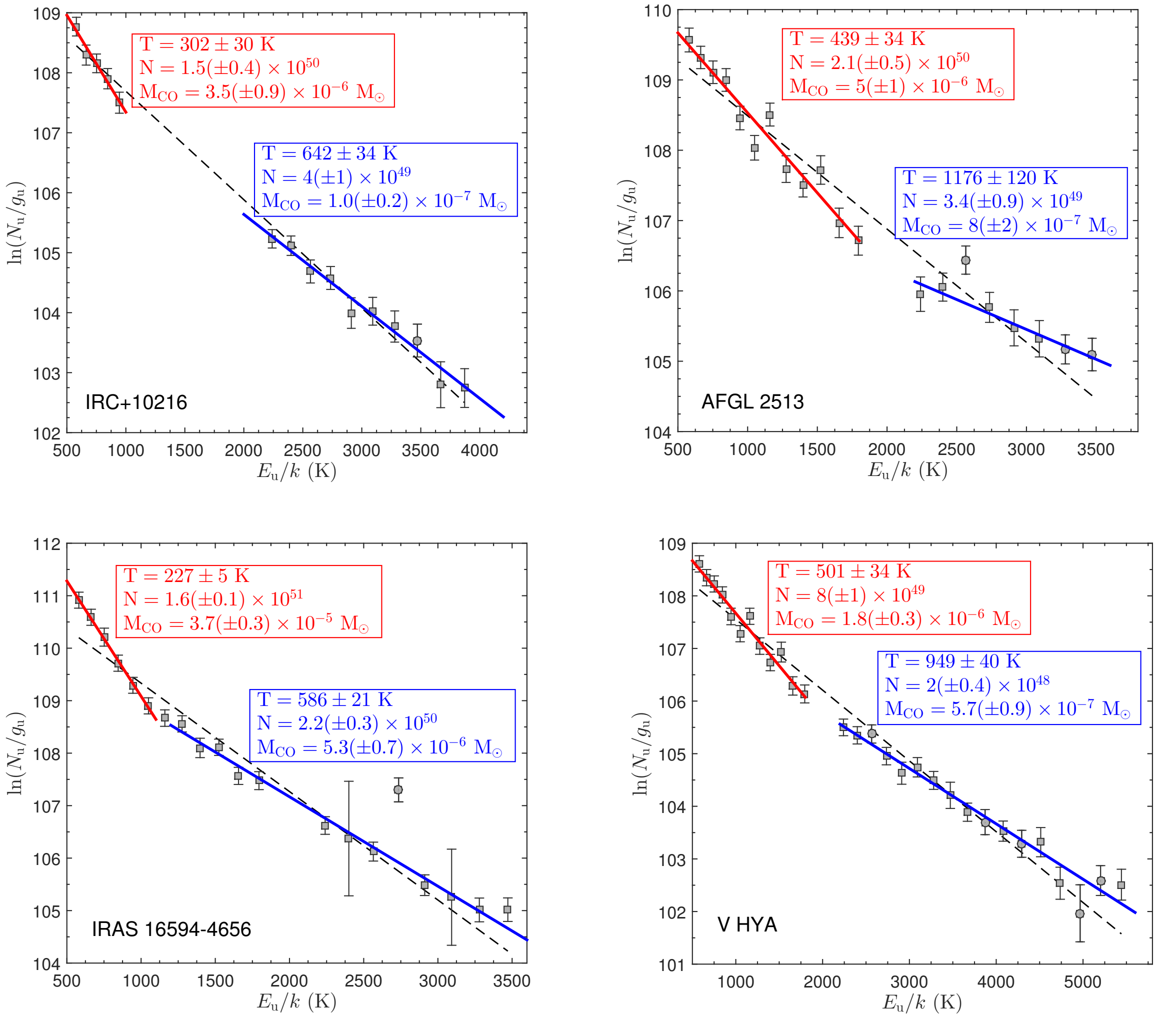

Fig. 4.10: Rotational diagrams of ^{12}CO with 2 temperature components (coloured lines) and single temperature fit (dashed line). Circles mark known line blends which were excluded from the fit.

equation 4.11 that $n \gg k$. This means we will not apply this statistical test to targets with only a few transitions detected (e.g. PNs). Because this method is sensitive to outliers, it is important to exclude points affected by line blend that clearly deviate from the linear trend. Lastly, beware that the BIC criteria does not prove that more than a different temperature component exists, it only highlights hidden patterns in the residuals which could be originated simply by heteroskedasticity in the data. Nevertheless, this approach is still useful to process a large set of observations in an automatic way, liberating the observer from deciding where to split the diagram. The F-statistic is then used to confirm BIC and quantify significance with a p-value. The significance level was set to $\alpha = 0.01$.

Finally, we present the results of the rotational diagram with 2 temperature components in figures 4.9 and 4.10. CIT 6 and AFGL 3116 share very similar conditions with a warm component of around ~ 500 K and a hot component[9] of ≥ 800 K. AFGL 618 has a colder warm component of 416 K and a hot component of more than 900 K. For AFGL 2688 the BIC criterion found an obvious breakpoint but we decided not to to fit the second component for $E_{\rm u}/k > 2000$ K because of the lack of points. In this case there is mass of CO gas of $\sim 10^{-5}$ $M_\odot$ at relatively cold (< 300 K) temperatures. In IRC+10216, although BIC clearly suggests a slope change[10], the F-test says it is not particularly significant with a p-value of 0.009, just marginally below a 1% significance cutoff. The inclusion of missing data in the range of excitation temperatures $1000 - 1500$ K would clarify this conclusion. IRAS 16594-4656 is an interesting case because the breakpoint was found at much smaller excitation temperature producing a much colder (~ 230 K) first-temperature-component than any other target. Concerning V Cyg, the F-test fails to reject the null hypothesis which means that the slope change is unlikely. A visual inspection of the rotational diagram helps confirming that.

Figure 4.11 shows the temperature histograms for the single components and split temperature components. The single least-squares fit corresponds to a sort of average temperature between low and high rotational levels. When we split the diagram in 2 components we see a bi-modal distribution of temperatures around ~ 400 K and ~ 850 K which we call "warm" and "hot". On the right side, we compare the temperature and mass derived from the 2 fitted lines in some targets. The warm component is up to ~ 7 times more massive than the hot component which can be hotter by a factor of nearly 3. If we assume that the temperature profile is given by a power-law of the type $T \propto r^{-\alpha}$ where r is the radial distance (e.g. Teyssier et al. 2006) and that the mass-loss rate and expansion velocity are constant, we find a direct power-law relation between temperature and mass with $\alpha \approx 0.5$ which fits the data quite well. Note that a large difference in the temperature between the warm and hot components can thus be an indication of very different radial distances of the emission which goes against our initial assumption that every transition comes from a region with the same size. Nevertheless, to obtain an accurate density law

[9] We call the cold component the one usually traced in radio observations T<100K.

[10] rotational diagram without opacity correction

Table 4.4: Rotational diagram results for a double component fit.

Target Name	T (K)	N_{CO} (molecules)	N^{col} (cm^{-2})	M_{H_2} ($M_{\odot}$)
IRC+10216	302±30	$1.5(\pm0.4) \times 10^{50}$	$4(\pm1) \times 10^{18}$	$3.2(\pm0.8) \times 10^{-4}$
	642±34	$4(\pm1) \times 10^{49}$	$1.0(\pm0.2) \times 10^{18}$	$9.0(\pm2) \times 10^{-5}$
CIT 6	490±28	$1.0(\pm0.2) \times 10^{50}$	$3.7(\pm0.6) \times 10^{17}$	$2.0(\pm0.3) \times 10^{-4}$
	842±60	$4(\pm1) \times 10^{49}$	$1.4(\pm0.4) \times 10^{17}$	$8(\pm2) \times 10^{-5}$
AFGL 3116	494±36	$8(\pm1) \times 10^{49}$	$1.2(\pm0.2) \times 10^{17}$	$1.7(\pm0.3) \times 10^{-4}$
	797±57	$3.4(\pm0.9) \times 10^{49}$	$5(\pm2) \times 10^{16}$	$7(\pm2) \times 10^{-5}$
AFGL 2688	270± 11	$5.0(\pm0.8) \times 10^{50}$	$2.7(\pm0.4) \times 10^{18}$	$1.1(\pm0.2) \times 10^{-3}$
	...	...	...	...
AFGL 618	416±21	$2.2(\pm0.3) \times 10^{51}$	$1.7(\pm0.3) \times 10^{18}$	$4.6(\pm0.7) \times 10^{-3}$
	923±48	$3.4(\pm0.7) \times 10^{50}$	$2.6(\pm0.5) \times 10^{17}$	$8(\pm2) \times 10^{-4}$
AFGL 2513	439±34	$2.1(\pm0.5) \times 10^{50}$	$4.3(\pm0.9) \times 10^{16}$	$4.5(\pm0.8) \times 10^{-4}$
	1176±120	$3.4(\pm0.9) \times 10^{49}$	$7(\pm1) \times 10^{15}$	$8(\pm2) \times 10^{-5}$
IRAS 16594	227±5	$1.6(\pm0.1) \times 10^{51}$	$3.9(\pm0.3) \times 10^{17}$	$3.4(\pm0.3) \times 10^{-3}$
	586±21	$2.2(\pm0.3) \times 10^{50}$	$5.6(\pm0.7) \times 10^{16}$	$4.7(\pm0.6) \times 10^{-4}$
V Hya	501±34	$8(\pm1) \times 10^{49}$	$2.0(\pm0.3) \times 10^{17}$	$1.7(\pm0.3) \times 10^{-4}$
	949±40	$2(\pm0.4) \times 10^{48}$	$6(\pm1) \times 10^{16}$	$5.3(\pm0.8) \times 10^{-5}$

in the envelope of these objects, detailed radiative transfer models are needed.

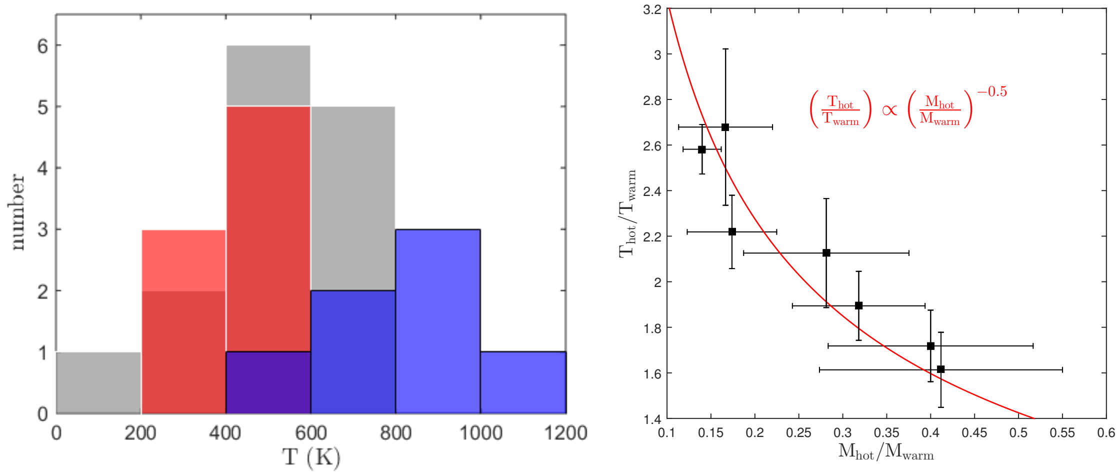

Fig. 4.11: Results of rotational diagrams. Left: Histograms of derived temperatures: single components (grey) and double components (red and blue for the coldest and hottest respectively); Right: temperature ratio versus mass ratio of the 2 fitted components. The red curve is the least-squares power-law fit.

4.2.5 The optically thinner ^{13}CO

Because ^{13}CO emission is optically thinner, the opacity correction is not as important as in the previous ^{12}CO rotational diagrams. Therefore, physical parameters derived from ^{13}CO lines are somewhat more reliable. However, this isotopologue produces very faint, i.e., low SNR lines in PACS range and their flux is more severely affected by line blend as explained in the previous chapter. These drawbacks cancel out the advantages of performing similar analysis using ^{13}CO rotational lines. In addition, only a few transitions were detected in a small number of stars.

For completeness, we present in figure 4.12 rotational diagrams of ^{13}CO in the sample of carbon stars. The constants used in this calculation are listed in table A.10 in the appendix. The regression parameters have associated a much larger uncertainty than before, preventing us from taking robust conclusions. However, in the case of IRC+10216 we found a good agreement between temperatures derived from ^{12}CO and ^{13}CO.

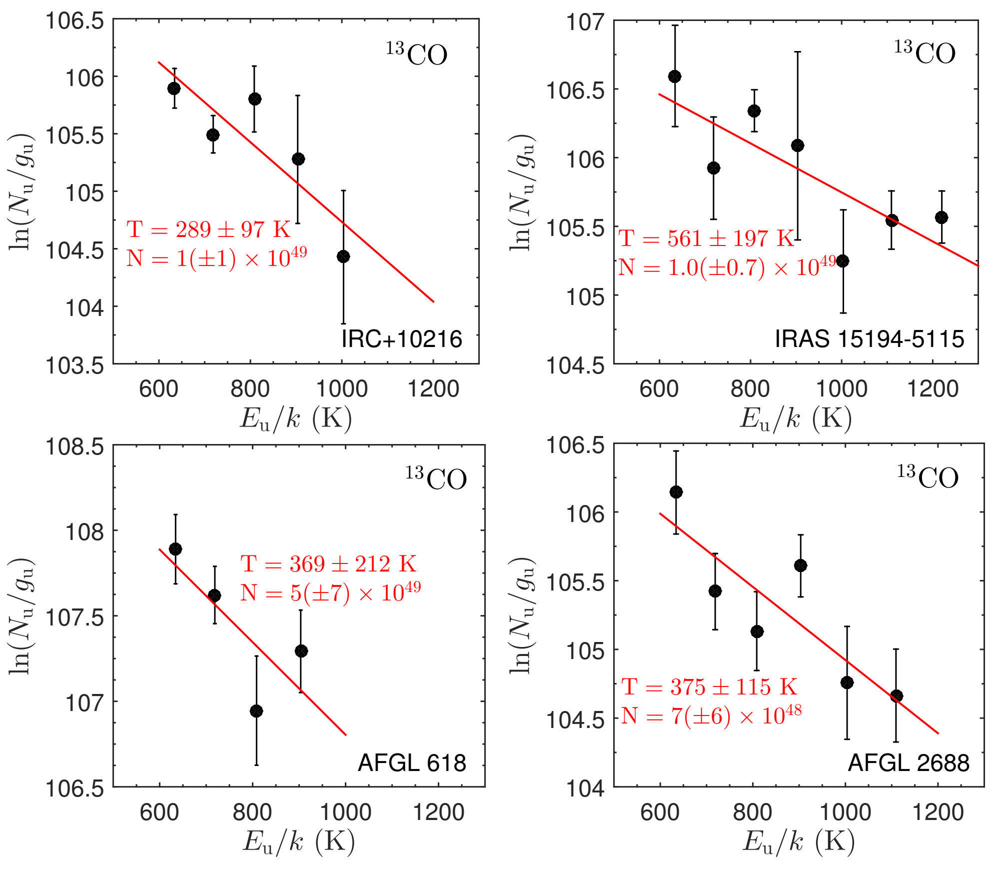

Fig. 4.12: Rotational diagrams of ^{13}CO in a sample of carbon stars.

4.3 Mass-loss rate in evolved stars

The mass-loss rate in AGB stars ranges between $10^{-8} - 10^{-5}$ $M_\odot$ yr^{-1} (De Beck et al. 2010), mainly in semi-regular variables and Miras, while OH/IR have optically opaque envelopes formed by intense mass loss that can reach up to $\sim 10^{-4}$ $M_\odot$ yr^{1}. In theory, the mass-loss should be lower in PN.

We can estimate the mass-loss rate in a straightforward way using the gas mass we derived from the rotational diagram and an assumption on the expansion velocity and size of the emitting region. If we further assume (for simplicity) that the mass-loss is spherically symmetric and that the density is uniform, then the amount of mass crossing the surface of radius r in an amount of time t is given by:

$$\begin{aligned} dM &= \rho dV = \rho\ 4\pi r^2 v_{\rm exp} dt \\ \frac{dM}{dt} &\equiv \dot{M} = 3 M_{\rm H_2}\ \frac{v_{\rm exp}}{r} \end{aligned} \tag{4.15}$$

Using the parameters listed in table 4.3, we computed the mass-loss rate for the 14 stars. Then, using the gas mass derived from the diagram splitting in two different temperature components, we recompute different estimates corresponding to the hottest temperature and the coldest temperature of the gas, which then yield a minimum and maximum mass-loss rate. The results can be found in table 4.5.

Overall, our results agree with the literature. For example, De Beck et al. (2010) derived a mass-loss rate of 5.9×10^{-6} $M_\odot$ yr^{-1} and 4.6×10^{-6} $M_\odot$ yr^{-1} for CIT 6 and AFGL 3116 respectively. The mass-loss rate of AFGL 2688 and AFGL 618 are known from previous studies to be 1.7×10^{-4} $M_\odot$ yr^{-1} and $2 \times 10^{-4} M_\odot$ yr^{-1} respectively (e.g. Milam et al. 2009, and references therein). However, the authors adopted different distances for the 2 PPN, but if we scale our values with their distances we obtain similar results. In the case of CPD-568032, De Marco & Crowther (1998) found $\dot{M} = 4 \times 10^{-6}$ $M_\odot$ yr^{-1}. Meixner et al. (1998) obtained 6×10^{-5} $M_\odot$ yr^{-1} for IRAS 21282+5050, in good agreement with our results. Ramstedt & Olofsson (2014) found a mass-loss rate for IRC+10216 of 1.5×10^{-5} $M_\odot$ yr^{-1} in good agreement with ours. These authors present a similar value

Table 4.5: Mass-loss rate in a sample of carbon stars. The average value corresponds to the parameters obtained from the single temperature fit, while the upper and lower bounds correspond to the split temperature components for the same expansion velocity and size.

Target Name	$\dot{M}$ ($M_\odot$ yr^{-1})	$\dot{M}$ ($M_\odot$ yr^{-1}) (literature)	ref.
IRC+10216	$1.0^{1.7}_{0.5} \times 10^{-5}$	1.5×10^{-5}	e
CIT 6	$2.9^{4.1}_{1.6} \times 10^{-6}$	5.9×10^{-6}	a
IRAS 15194-5115	2.5×10^{-6}	1.5×10^{-5}	e
AFGL 2513	$1.5^{2.2}_{0.4} \times 10^{-6}$	2×10^{-5}	f
V CYG	8×10^{-7}	1.6×10^{-6}	e
AFGL 3068	3.4×10^{-6}	2.5×10^{-5}	e
AFGL 3116	$1.7^{2.3}_{0.9} \times 10^{-6}$	4.6×10^{-6}	a
AFGL 618	$4.8^{8.6}_{1.5} \times 10^{-5}$	2×10^{-4}	b
HD 44179	7.1×10^{-7}	$10^{-8} - 10^{-2}$	i
V HYA	$3.8^{5.6}_{1.8} \times 10^{-6}$	1×10^{-6}	g
IRAS 16594-4656	$1^{3.6}_{0.5} \times 10^{-5}$	1×10^{-5}	h
AFGL 2688	$3.4^{5.5} \times 10^{-5}$	1.7×10^{-4}	b
CPD-568032	3.8×10^{-6}	4×10^{-6}	c
IRAS 21282+5050	3.0×10^{-5}	6×10^{-5}	d

References: (see text for comments) [(a)] De Beck et al. (2010), [(b)] Milam et al. (2009), [(c)] De Marco & Crowther (1998), [(d)] Meixneir et al. (1998), [(e)] Ramstedt & Olofsson (2014), [(f)] Groenewegen et al. (2002), [(g)] Camps (2011), [(h)] Woods et al. (2005)

for IRAS 15195-5115, but we found a much smaller value. A smaller value was also found in AFGL 3068 compared to 2.5×10^{-5} $M_\odot$ yr^{-1} in Ramstedt & Olofsson (2014), though we agree that the mass-loss rate should be higher in AFGL 3068 than in IRAS 15194-5115. The authors present a value for V Cyg of 1.6×10^{-6} $M_\odot$ yr^{-1}, which is larger than ours by a factor of 2. The mass-loss rate obtained in this work for HD 44179 fits within the broad range of mass-losses inferred from the multiple outflows in the Red Rectangle (Men'shchikov et al. 2002). Our mass-loss rate estimate for V Hya also agrees with literature (e.g. Knapp et al. 1997; Camps 2011) despite being slightly larger than in previous works. Changing the expansion velocity to a smaller value matching the rate of expansion of the compact core brings the results closer together.

Naturally, the mass-loss rate values could be tuned to better match previous obser-

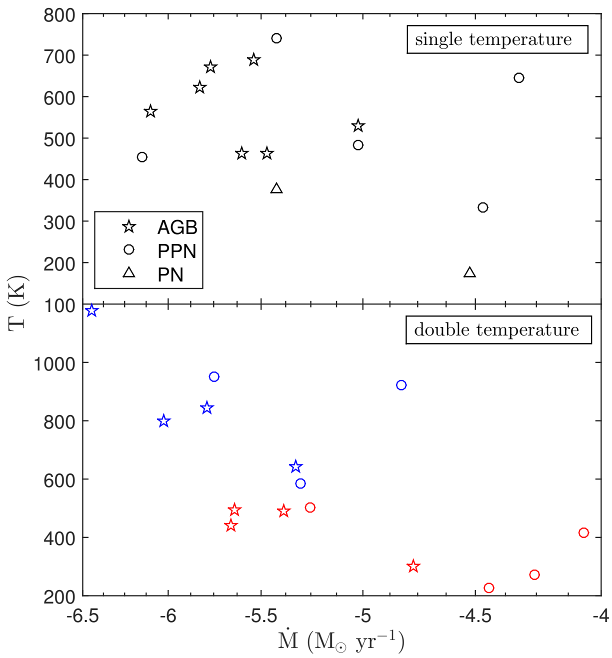

Fig. 4.13: Temperature versus the logarithm of the mass-loss rate. Top: Single temperature components; Bottom: two temperature components (blue - high J, red - low J).

vations with different input parameters such as the radius and expansion velocity of the gas mass. What is interesting is that we were able to find a good qualitative agreement between the properties of the molecular CSE derived using high J rotational transitions and the parameters found in literature for lower J CO lines.

In figure 4.13 we plot temperature against mass-loss rate. In the top chart we see no correlation between these two quantities while in the bottom one we conclude that the coldest component (red points) is associated to an higher mass-loss rate on average. Because we are assuming the same size and expansion velocity in both components, this trend is just a consequence of different masses. However, if the hottest (and youngest) component is indeed more compact than the coldest and if we further assume a radial temperature power-law with exponent $\alpha = 0.5$ as explained in section 4.2.4, we find a correction factor between ~3-7 to apply to the mass-loss rate of the hottest component. This factor brings the mass-loss rate of both temperature components closer together so we conclude that the mass-loss rate is constant within the uncertainties.

We also investigated the relation between mass-loss rate and luminosity and no correlation was found. The small number of data-points prevents us from studying the relation between mass-loss and pulsation period (variability).

4.4 Summary

- From the rotational diagram we inferred temperature and mass of molecular gas in 14 C-rich stars. For most targets the average temperatures are in range $\sim 400 - 900$ K and the mass of gas was found between $\sim 10^{-3} - 10^{-5}$ $M_{\odot}$.
- We applied statistical methods to automatically find breakpoints in linear regression and used them to split the rotational diagram in 2 components in some cases. On a number of targets we identified two temperature components: warm (~ 450 K) and hot (~ 750 K).
- We estimated the mass-loss rate and compared ours values to literature. A good agreement was found in most cases. Assuming the same size and expansion velocity of the gas, the mass-loss of the hottest component is always larger than the warm component. However, if we the size of the hot region is much smaller than what we assumed it can be showed that a correction to the mass-loss of the hot component essentially yields a constant mass-loss history.
- If the line emission is optically thick and/or the sizes of the emitting regions are much smaller than what we have assumed then the reported temperatures could be overestimated and the gas mass could be underestimated. Anyway, the order of magnitude of these quantities should remained unaltered which means that a warmer population of gas is being traced with these very high J CO observations.

Chapter 5

Conclusion

In this thesis we studied the CSE of evolved stars across several evolutionary stages using Herschel/PACS photometry and spectroscopy.

We obtained an estimate of size of the far-infrared emitting region of a sample of stars and concluded that most sources in the THROES catalogue are unresolved by PACS. We also obtained new measurements for the PSF FWHM of the photometer and spectrometer by fitting Vesta and Neptune observations.

In the second part we were mostly interested in measuring the flux of CO rotational transitions in our spectra. Very briefly we mentioned other spectral features, namely molecular and atomic/ionic lines and compared the chemical content of targets of different spectral types and evolutionary stages. For completeness we computed ^{12}CO/^{13}CO ratios and concluded that they are systematically lower than the values reported in literature using low J CO observations. As a sub-product of the line fitting we obtained continuum fluxes at selected wavelengths that we used to plot a colour-colour diagram. Stars in different locations in the diagram reflect different dust properties.

Finally we focused on carbon-rich sources from AGBs to PNs and performed the rotational diagram analysis using CO line fluxes. PACS allows to study multiple rotational lines of the ground vibrational state of the ^{12}CO isotopologue from $J = 14 \rightarrow 13$ to $J = 45 \rightarrow 44$ thanks to its large wavelength coverage. This method depends on the assumption of thermalisation of the transitions which proved to be a good premise since we found a range of points lying in a single straight line. We also obtained rotational diagrams for the ^{13}CO isotopologue, but the results are inconclusive due to the much lower SNR and number of detected transitions. This molecule has very weak lines in the PACS range and it was only found in a small fraction of our sample. We derived rotational temperature, column density, gas mass and mass-loss rate and studied the impact of the optical depth on the derived quantities. We concluded that for our choice of parameters the opacity correction is small, but if the size of the far-infrared emitting region is much smaller ($\ll 1''$) than what we assumed, then some targets may have moderate-to-high optical depth effects. This directly impacts the derived temperature and gas mass that should be regarded as a upper limit and a lower limit, respectively, of the true average conditions in the inner CSE.

There is certainly a lot more to do in the future. In what regards line identification the analysis could be extended to a larger number of molecules which were only mentioned briefly. Moreover, solid-state (dust) spectral features were completely disregarded in this work, but their identification in our sample is also of great scientific interest. This would help building a library with all chemical species found in each target of the catalogue and their measured fluxes. The CO rotational diagram analysis could be extended to the remaining targets in the sample, namely oxygen-rich stars and S stars. This would allow to study an eventual correlation between physical conditions, spectral type and evolutionary stage. The rotational diagram can also be extended to other molecules to derive the mass of other gas components and check if they trace the same temperature as CO. For example, HCN is another molecule that is commonly observed in a large range of transitions, at least in carbon rich targets.

This thesis opens the door to more sophisticated analysis such as radiative transfer (including non-LTE) that could be capable of obtaining a more accurate description of the density and chemical structure of the CSE, and it would also help us constraining the size of the emitting regions. Even so, using relatively simple considerations and fair assumptions we have given the first step towards a systematic characterization of the FIR properties of evolved stars and we obtained important insights into the very nature of their circumstellar envelopes.

Bibliography

[1] Abia, C. & Isern, J. 1997, MNRAS, 289L, 11A

[2] Agúndez, M. Cernicharo, J. & Guélin, M. 2014, A&A 570, A45

[3] Ali, A. 2006, A&A, 27, 399–409

[4] Amblard, A., Cooray, A., Serra, P. & Altieri, B. et al. 2011, Nature, 470, 510A

[5] Andrews, D. & Ploberger, W. 1994, Econometrica, 62, 1383–1414

[6] Balick, B. Gomez, T. Vinković, D., Alcolea, J., & et al, 2012, ApJ, 745, 188B

[7] Balog, Z.; Müller, T.; Nielbock, M. & Altieri, B. et al. 2013, *The Herschel-PACS photometer calibration: Point-source flux calibration for scan maps*, arXiv:1309.6099

[8] Balser, D. S., McMullin, J. P. & Wilson, T. L., 2002, ApJ, 572, 326B

[9] Bergeat, J., & Chevallier, L., 2005, A&A, 429, 235B

[10] Bieging J.H. & Nguyen-Quang-Rieu 1996, AJ 112, 706

[11] Blommaert, J. A. D. L., de Vries, B. L., Waters, L. B. F. M., & Waelkens, C. et al. 2014, A&A, 565A, 109B

[12] Bocchio, M., Bianchi, S. & Abergel, A. 2016, arXiv:1605.03587

[13] Bockelee-Morvan, D., Swinyard, B., Vandenbussche, B., & Hartogh, P. et al. 2014, 2011, epsc.conf, 231B

[14] Bregman, J. D., Booth, J. & Gilmore, D. K. et al. 1992, ApJ, 396, 120

[15] Bujarrabal, V., Alcolea, J. & Planesas, P. 1992, A&A, 257, 701-714

[16] Bujarrabal, V., Alcolea, J., Soria-Ruiz, R. & Planesas, P., et al. 2010, A&A, 521, L3

[17] Bujarrabal, V., Alcolea, J., Soria-Ruiz, R. & Planesas, P. et al. 2012, A&A, 537A, 8B

[18] Bujarrabal, V., Castro-Carrizo, A., Alcolea, J. & Van Winckel, H. et al. 2013, A&A, 557L, 11B

[19] Bujarrabal, V., Castro-Carrizo, A., Alcolea, J. & Santander-Garcia, M. 2016, arXiv:1606.07238

[20] Camps, D. 2011, *Unravelling the physical and chemical structures of winds in AGB stars*, MSc. thesis, KU Leuven

[21] Cernicharo, J., Barlow, M. J., Gonzalez-Alfonso, E., et al. 1996, A&A, 315, L201

[22] Cernicharo, J., Guélin, M., & Kahane, C. 2000, A&AS, 142, 181C

[23] Cernicharo, J., Marcelino, N., Agúndez, M. & Guélin, M. 2015, A&A, 575A, 91C

[24] Chesneau, O. 2006, ASPC, 355, 117C

[25] Chow, G. C. 1960, Econometrica, 28:591–605

[26] Chau, W., Zhang, Y. & Nakashima, J.I, et al. 2012, ApJ, 760, 66

[27] Claussen, M. J., Sjouwerman, L. O. & Rupen, M. P., et al. 2011, ApJ, 739, L5

[28] Cohen, M. & Jones, B. F. 1987, ApJ, 321L, 151C

[29] Cortese, L., Fritz, J., Bianchi, S. & Boselli, A. 2014, MNRAS, 440, 942C

[30] Cox, P., Gonzalez-Alfonso, E., Barlow, M. J. & Liu, X.-W. et al 1996, A&A, 315L, 265C

[31] Cox, P., Lucas, R., Huggins, P. J. & Forveille, T., et al. 2000, A&A, 353, L25

[32] Cox, N. L. J., Kerschbaum, F., Van Marle, A.J., & Decin, L., et al. 2012, A&A 537, A35

[33] Crampton, D., Cowley, A.P, & Humphreys, R.M. 1975, ApJ, 198L, 135C

[34] Danehkar, A. & Parker, Q. A. 2015, MNRAS, 449L, 56D

[35] Danilovich, T., Bergman, P., Justtanont, K. & Lombaert, R., 2014, A&A, 569A, 76D

[36] De Beck, E., Decin, L., De Koter, A. & Justtanont, K., et al. 2010, A&A 523, A18

[37] Decin, L. 2012, *Late Stages of Stellar Evolution - Herschel's contributions*, arXiv:1212.4861

[38] Decin, L., Cernicharo, J., Barlow, M. J. & Royer, P. 2010, A&A, 518L, 143D

[39] Delfosse, X., Kahane, C. & Forveille, T. 1997, A&A, 320, 249D

[40] De Marco, O., Barlow, M. J. & Storey, P. J. 1997, MNRAS, 292, 86D

[41] De Marco, O., & Crowther, P. A. 1998, MNRAS, 296, 419

[42] Duari, D., Cherchneff, I., & Willacy, K. 1999, A&A, 341, L47

[43] Edwards, J. L., & Ziurys, L. M. 2013, ApJ, 770L, 5E

[44] García-Hernández, D. A., Manchado, A., García-Lario, P. & Cañete, A. B. et al. 2006, ApJ, 640, 829G

[45] García-Lario, P. 2012, IAUS, 283, 33G

[46] Goodrich, R. W. 1991, ApJ, 376, 654G

[47] Goldsmith, P.F, & Langer, W.D. 1999, ApJ, 517, 209

[48] Goto, M., Kobayashi, N., Terada, H., & Tokunaga, A. T. 2002, ApJ, 572, 276G

[49] Graciá-Carpio, J., Wetzstein, M. & Roussel, H. et al. 2015, arXiv:1512.03252

[50] Groenewegen, M. A. T., van der Veen, W. E. C. J., & Matthews, H. E. 1998, A&A, 338, 491G

[51] Groenewegen, M. A. T., Sevenster, M., Spoon, H. W. W. & Pérez, I. 2002, A&A, 390, 511G

[52] Groenewegen, M. A. T., Waelkens, C., Barlow, M. J., et al. 2011, AA, 526, A162

[53] Guandalini, R., Busso, M., Ciprini, S., Silvestro, G. & Persi, P. 2006,A&A, 445, 1069G

[54] Hasegawa, T. I. & Kwok, S. 2003, ApJ, 585, 475H

[55] Herpin, F. & Cernicharo, J. 2000, ApJ, 530, 129

[56] Herwig, F. 2005, *Evolution of asymptotic giant branch stars*, Annu. Rev. Astron. Astrophys, 43: 435-479

[57] Hrivnak, B. J., Smith, N., Su, Kate Y. L. & Sahai, R. 2008, ApJ, 688, 327H

[58] Huang, P.S., Lee, C.F., Moraghan, A. & Smith, M. 2016, ApJ, 820, 134

[59] Hyosun, K., Sheng-Yuan, L., Naomi, H. & Ronny, Z.G, et al. 2015, ApJ, 814, 61K

[60] Ishigaki, M. N., Parthasarathy, M., & Reddy, B. E. et al. 2012, MNRAS, 425, 997

[61] Jorissen, A., Mayer, A., van Eck, S., & Ottensamer, R., et al. 2011, A&A, 532A, 135J

[62] Jura, M., Turner, J. L., Van Dyk, S., & Knapp, G. R. 2000, ApJ, 528, L105

[63] Justtanont,K., Barlow M.J., Tielens , A.G.G.M., & Hollenbach, D.. et al. 2000, A&A, 360, 1117–1125

[64] Justtanont, K., Khouri, T., Maercker, M., & Alcolea, J. et al. 2012, A&A, 537A, 144J

[65] Kim, H., Liu, S., Hirano, N. & Zhao-Geisler, R. et al. 2015, ApJ, 814, 61K

[66] Knapp, G. R., Jorissen, A. & Young, K. 1997, A&A, 326, 318–328

[67] Knapp, G. R., Crosas, M., Young, K. & Ivezić, Ž. 2000, ApJ, 534, 324K

[68] Könyves, V., André, P., Men'shchikov, A. & Palmeirim, P. et al. 2015, A&A, 584A, 91K

[69] Kwok, S., Hrivnak, B. J., & Geballe, T. R. 1995, ApJ, 454, 394

[70] Kwok, S., 2000, *The Origin and Evolution of Planetary Nebulae*, Cambridge University Press

[71] Lacey, C. G., Baugh, C. M., Frenk, C. S. & Benson, A. J. et al. 2014, MNRAS, 440, 2013D

[72] Ladjal, D. 2011, *The Herschel - PACS guaranteed time key programme on evolved stars: its preparation, execution and initial data exploitation*, PhD Thesis, KU Leuven, Belgium

[73] Lambert, D. L., Gustafsson, B., Eriksson, K. & Hinkle, K.H. 1986, ApJS, 62, 373L

[74] Lawrence, H.A., Siek, H. & Feibelman, W.A. 1999, PNAS, 96, 5366A

[75] Likkel, L., Morris, M., Forveille, T. & Omont, A. 1988, A&A, 198, 1L

[76] Lo, K. Y., & Bechis, K. P. 1976, ApJ, 205, L21

[77] Loader, C. 1999, *Local Regression and Likelihood*, Springer,

[78] Lombaert, R., Decin, L., Royer, P. & de Koter, A. et al., 2016, A&A, 588A, 124L

[79] Lutz, D. 2015, *PACS photometer point spread function*, V2.2, `http://herschel.esac.esa.int/twiki/pub/Public/PacsCalibrationWeb/bolopsf_22.pdf`

[80] Matsuura, M., Zijlstra, A.A, Gray, M.D, et al. 2005, MNRAS, 363, 628M

[81] Maindonald, J. & Braun, W. J. 2010, *Data analysis and graphics using R: An example-based approach*, Cambridge University Press, chp.6, p. 187

[82] Mayer, A., Jorissen, A., Kerschbaum, F., & Ottensamer, R. et al. 2013, A&A, 549A, 69M

[83] Mayer, A., Jorissen, A., Paladini, C., & Kerschbaum, F. et al. 2014, A&A, 570A, 113M

[84] Mauron, N. & Huggins, P. J. 2006, A&A, 452, 257M

[85] Meadows, P. J., Good, A. R. & Wolstencroft, R. D. 1987, MNRAS, 225P, 43M

[86] Men'shchikov, A. B., Schertl, D., Tuthill, P. G., Weigelt, G. & Yungelson, L. R. 2002, A&A, 393, 867M

[87] Meixner, M., Skinner, C. J., Temi, P. & Rank, D. 1993, ApJ, 411, 266M

[88] Milam, S. N., Woolf, N. J. & Ziurys, L. M. 2009, ApJ, 690, 837

[89] Millar, T.J., 2016, arXiv: 1605.03365v1

[90] Mishra, A., Li, A. & Jiang, B. W. 2015, ApJ, 802, 39M

[91] Miyata, T., Kataza, H., Okamoto, Y. K. & Onaka, T. 2004, A&A 415, 179-187

[92] Molinari, S., Swinyard, B., Bally, J. & Barlow, M. et al. 2010, A&A, 518, L100

[93] Monnier, J. D., Tuthill, P. G., & Danchi, W. C. 2000, ApJ, 545, 957

[94] Moré, J.J., *The Levenberg-Marquardt Algorithm: Implementation and Theory," Numerical Analysis*, Lecture Notes in Mathematics 630, Springer Verlag, pp 105–116

[95] Morris, M., Sahai, R., Matthews, K. & Cheng, J. et al. 2006, IAUS, 234, 469M

[96] Müller, T. G., Balog, Z., Nielbock, M., & Moreno, R. et al. 2016, A&A, 588A, 109M

[97] Müller, H. S. P., Schlöder, F.; Stutzki, J. & Winnewisser, G. 2005, J. Mol. Struct., 742, 215–227

[98] Müller, H. S. P., Thorwirth, S., Roth, D. A. & Winnewisser, G. 2001, A&A 370, L49–L52

[99] Mufson, S. L., Lyon, J. & Marionni, P. A. 1975, ApJ, 201L, 85M

[100] Neufeld, D. A., González-Alfonso, E., Melnick, G. & Pułecka, M. et al. 2010, A&A 521, L5

[101] Ohnaka, K. & Tsuji, T., 1998, A&A, 335, 1018O

[102] Omont, A., 1987, IAUS, 120, 3570

[103] Ott, S. 2010, ASP Conference Series, 434, 139

[104] Palmeirim, P., André, Ph., Kirk, J., & Ward-Thompson, D. et al. 2013, A&A, 550A, 38P

[105] Philippe A., 2013, *The Herschel View of Star Formation*, arXiv:1309.7762

[106] Pilbratt, G. L., Riedinger, J. R., & Passvogel, t., et al. 2010, A&A 518, L1

[107] Poglitsch, A., Waelkens, C. & Geis, N., et al. 2010, A&A 518, L2

[108] Pollaco, D.L, Kilkenny, D., Marang, F., et al. 1992, MNRAS, 256, 669

[109] Popesso, P., Magnelli, B., & Buttiglione, S., et al. 2012, arXiv:1211.4257

[110] Ramstedt, S., Schöier, F. L., Olofsson, H. & Lundgren, A. A. 2008, A&A, 487, 645R

[111] Ramstedt, S. & Olofsson, H. 2014, A&A, 566A, 145R

[112] Regibo, S., 2012, *Data Reduction and Analysis Algorithms for the Herschel Space Observatory*, PhD thesis, KU Leuven, Belgium

[113] Ryde, N., Schöier, F. L. & Olofsson, 1999, A&A, 345, 841R

[114] Sahai, R., Trauger, J. T., & Watson, A. M. et al. 1998, ApJ, 493, 301

[115] Sahai, R., Sugerman, B.E.K. & Hinkle, K. 2009, ApJ, 699, 1015–1023

[116] Sahai, R, & Chronopoulos, C.K, 2010, ApJ, 711L, 53S

[117] Sánchez Contreras, C., Sahai, R., & Gil de Paz, A. 2002, ApJ, 578, 269S

[118] Sánchez Contreras, C., Bujarrabal, A. & Castro-Carrizo, J. et al. 2004b, ApJ, 617, 1142S

[119] Sánchez Contreras, C. & Sahai, R. 2004a, ApJ, 602, 960S

[120] Schöier, F. L. & Olofsson, H. 2000, A&A, 359, 586S

[121] Smith, C. L., Zijlstra, A. A. & Fuller, G. A. 2015, MNRAS, 454, 177S

[122] Solomon, P., Jefferts, K. B., Penzias, A. A., & Wilson, R. W. 1971, ApJ, 163, L53

[123] Soria-Ruiz, R., Bujarrabal, V., & Alcolea, J. 2013, A&A, 559, A45

[124] Suh, K.W. 2015, arXiv:1506.05176

[125] Teyssier, D., Hernandez, R., Bujarrabal, V. & Yoshida, H. et al. 2006, A&A, 450, 167T

[126] Ueta, T., Murakawa, K., & Meixner, M. 2006, ApJ, 641, 1113

[127] van der Veen, W. E. C. J. & Habing, H. J. 1988, A&A, 194, 125V

[128] Vickers, S. B., Frew, D. J., Parker, Q. A. & Bojičić, I. S., 2014, arXiv:1403.7230

[129] Wesson, R., Cernicharo, J., Barlow, M.J. & Matsuura, M. et al. 2010, A&A, 518, L144

[130] Westbrook, W. E., Gezari, D. Y. et al. 1976, ApJ, 209, 94W

[131] Winckel, H.V., 2003, *Post-AGB stars*, Annu. Rev. Astron. Astrophys, 41: 391-427

[132] Winters, J. M., Fleischer, A. J., Le Bertre, T. & Sedlmayr, E. et al. 1997, A&A, 326, 305W

[133] Woods, P. M., Nyman, L.-A. & Schöier, F. L., et al. 2005, A&A, 429, 977

[134] Yuan, Y. 2015, *Recent Advances in Trust Region Algorithms*, Mathematical Programming

[135] Zhang, Y., Kwok, S. & Nakashima, J. 2009, ApJ, 700, 1262–1281

[136] Zeileis, A. Leisch, F. Hornik, K. & Kleiber, C. 2002, JSS, 7(2), 1-38

[137] Zeileis, A., Kleiber, C., Kraemer, W. & Hornik, K. 2003, Computational Statistics & Data Analysis, 44, 109-123

Appendices

Chapter A

Appendice of tables

A.1 Stars in the THROES catalogue

Table A.1: Stars in the THROES catalogue: name, coordinates, classification and variability (if applied) of 107 stars. Targets marked with "x" are not variable stars or that information is unknown.

Target name	R.A (deg)	DEC (deg)	Class	Variability
AC Her	277.5676	21.8668	PPN	RV Tau variable
AFGL 2019	268.3282	-26.9436	O-rich AGB	Semi-regular
AFGL 2403	292.6228	19.8447	OH/IR	x
AFGL 2513	302.3093	31.4291	C-rich AGB	Mira Cet
AFGL 2688	315.5781	36.6938	PPN	x
AFGL 3068	349.8016	17.1931	C-rich AGB	Mira Cet
AFGL 3116	353.6152	43.5506	C-rich AGB	Mira Cet
AFGL 4106	155.8311	-59.5346	PPN	x
AFGL 4202	223.1012	-62.0721	C-rich AGB	x
AFGL 4259	301.5947	27.0362	OH/IR	x
AFGL 618	70.7236	36.1147	PPN	x
AFGL 6815	259.583	-32.4556	PPN	x
AQ Sgr	293.5791	-16.3741	C-rich AGB	Semi-regular
BD +303639	293.6884	30.5163	PN	x
CIT 6	154.0094	30.5718	C-rich AGB	Semi-regular
CPD-568032	257.2536	-56.9133	PN	x
CPD-642939	219.292	-64.8013	PPN	x
EP Aqr	326.6327	-2.2127	O-rich AGB	Semi-regular
g her	247.1606	41.8816	O-rich AGB	Semi-regular

HD 161796	266.2311	50.0443	PPN	Semi-regular
HD 2385858	37.2932	54.8517	PPN	x
HD 331319	297.3731	31.4545	PPN	x
HD 44179	94.9925	-10.6374	PPN	x
HD 56126	109.0427	9.9966	PPN	Semi-regular
HDE 269006	75.5307	-71.3369	unclassified	unclassified
HEN2-113	224.973	-54.302	PPN	x
Hen2-90	197.4009	-61.3266	PN	x
HEN3-1475	266.309	-17.9462	PPN	x
HEN3-401	154.8852	-60.2248	PN	x
IC 418	81.8675	-12.6973	PN	x
IRAS 07027-7934	104.8599	-79.6463	PN	x
iras 08011-3627	120.7568	-36.5966	PPN	RV Tau variable
iras 08544-4431	134.0591	-44.7196	PPN	RV Tau variable
iras 09256-6324	141.722	-63.6302	PPN	RV Tau variable
iras 09371+1212	144.9749	11.9814	PPN	RV Tau variable
IRAS 09425-6040	146.0066	-60.9072	PPN	x
iras 10456-5712	161.91	-57.4674	PPN	x
IRAS 15194-5115	230.7704	-51.433	C-rich AGB	x
IRAS 16342-3814	249.417	-38.338	PPN	x
IRAS 16594-4656	255.7917	-47.0076	PPN	x
IRAS 17010-3840	256.1179	-38.7396	OH/IR	x
IRAS 17251-2821-1	262.077	-28.3991	OH/IR	x
IRAS 17276-2846-1	262.7012	-28.8172	OH/IR	x
IRAS 17323-2424-1	263.8583	-24.4422	OH/IR	x
IRAS 18488-0107	282.8592	-1.0645	O-rich AGB	Mira Cet
IRAS 19067+0811	287.2845	8.277	OH/IR	Mira Cet
IRAS 19306+1407	293.2295	14.2269	PPN	x
IRAS 19312+1950	293.3512	19.9486	OH/IR	x
IRAS 19474-0744	297.5264	-7.6145	O-rich AGB	Semi-regular
IRAS 20000+3239	300.498	32.7924	PPN	x
IRAS 20038-2722	301.7301	-27.2249	O-rich AGB	long-period
IRAS 20248-2825	306.9799	-28.261	O-rich AGB	Semi-regular
IRAS 21282+5050	322.4934	51.0666	PN	x
IRAS 21554+6204	329.2424	62.3121	OH/IR	x
IRAS 22036+5306	331.3761	53.3591	PPN	x

irc+10216	146.9892	13.2787	C-rich AGB	Mira Cet
IRC+50137	77.831	52.8758	OH/IR	Mira Cet
J 175521.7-293912	268.8404	-29.6536	OH/IR	x
KHI CYG	297.6413	32.914	S	x
MGE 3222	281.48	-2.4189	PN	x
MGE 4218	244.019	-51.5989	C/S AGB	x
MWC 922	275.3162	-13.0241	PN	x
NGC 3242	156.192	-18.6411	PN	x
NGC 40	3.2542	72.5219	PN	x
NGC 6445	267.3133	-20.0095	PN	x
NGC 6537	271.3045	-19.843	PN	x
NGC 6543	269.6392	66.6331	PN	x
NGC 6781	289.617	6.5386	PN	x
NGC 6826	296.2006	50.525	PN	x
NGC 7009	316.045	-11.3635	PN	x
NGC 7026	316.5773	47.8519	PN	x
NML CYG	311.606	40.1165	O-rich AGB	Semi-regular
NML TAU	58.3701	11.4062	O-rich AGB	Mira Cet
OH 104.91+2.41	334.8645	59.856	OH/IR	x
OH 231.8+4.2	115.5701	-14.7144	OH/IR	x
OH 26.5+0.6	279.3852	-5.3998	OH/IR	Mira Cet
OH 30.1-0.7	282.1746	-2.8411	O-rich AGB	Mira Cet
OH 30.7+0.4	281.5241	-1.9881	PPN	x
OH 32.8-0.3	283.0924	-0.2371	OH/IR	Mira Cet
OMI CET	34.8366	-2.9776	O-rich AGB	Mira Cet
PI GRU	335.6842	-45.9479	S	x
PNMz3	244.3058	-51.9862	PN	x
r aql	286.5927	8.2	O-rich AGB	Mira Cet
R CAS	359.6036	51.3888	O-rich AGB	Mira Cet
R DOR	69.1899	-62.0771	O-rich AGB	Semi-regular
R Lep	74.9014	-14.8062	C-rich AGB	Mira Cet
RAFGL 2374	290.4021	9.4656	O-rich AGB	x
RAFGL 4205	224.9728	-54.302	PPN	x
RR Aql	299.4002	-1.8864	O-rich AGB	Mira Cet
RT Cap	304.2772	-21.3179	C-rich AGB	Semi-regular
S Aur	81.781	34.1496	C-rich AGB	Semi-regular

s ther	237.6942	48.483	S	x
Tc1	266.397	-46.0899	PN	x
TX CAM	75.2099	56.1812	O-rich AGB	Mira Cet
U Hya	159.3886	-13.3845	C-rich AGB	Semi-regular
U Mon	112.6977	-9.7768	PPN	RV Tau variable
V CYG	310.3261	48.1413	C-rich AGB	Mira
V HYA	162.9052	-21.25	PPN	Semi-regular
V1300 Aql	302.6161	-6.2704	O-rich AGB	Mira Cet
V384 Per	51.6229	47.5301	C-rich AGB	Semi-regular
v438 oph	258.6657	11.0694	O-rich AGB	Semi-regular
W AQL	288.8476	-7.0471	S	x
W HYA	207.2583	-28.3676	O-rich AGB	Semi-regular
W Ori	76.3488	1.1776	C-rich AGB	Semi-regular
WX PSC	16.6082	12.598	O-rich AGB	Mira Cet
X HER	240.6632	47.2403	O-rich AGB	Semi-regular
Y CVn	191.2826	45.4402	C-rich AGB	Semi-regular

A.2 IRAS colours in THROES

Table A.2: IRAS fluxes in 4 bands (12, 25, 60 and 100 μm) and 2 colours (see text) for the stars in the THROES catalogue. AFGL 2688 and NML CYG have no IRAS data.

Target name	$F_\lambda(12)$	$F_\lambda(25)$	$F_\lambda(60)$	$F_\lambda(100)$	[12]-[25]	[25]-[60]
AC Her	41.43	65.33	21.37	8.04	0.494	-1.213
AFGL 2019	243.6	195.5	61.12	227.4	-0.239	-1.262
AFGL 2403	88.5	178.8	88.2	31.31	0.764	-0.767
AFGL 2513	172.9	95.57	24.4	20.8	-0.644	-1.482
AFGL 2688	—	—	—	—	—	—
AFGL 3068	706.7	775.6	248.5	73.7	0.101	-1.236
AFGL 3116	959.1	469.1	111.6	35.45	-0.776	-1.559
AFGL 4106	200.8	1755	851.8	181.1	2.354	-0.785
AFGL 4202	667.4	234	63.95	75.34	-1.138	-1.408
AFGL 4259	17.89	41.95	20.31	7.48	0.925	-0.788
AFGL 618	470.8	1106	1036	339.9	0.927	-0.071
AFGL 6815	57.92	322.3	268.3	82.41	1.864	-0.199
AQ Sgr	56.64	18.73	5.69	5.88	-1.201	-1.294
BD +303639	89.39	234.5	161.7	70.08	1.047	-0.404

CIT 6	3319	1219	273.6	86.12	-1.088	-1.622
CPD-568032	143.7	257.2	199.1	91.69	0.632	-0.278
CPD-642939	4.04	108.7	70.71	20.61	3.575	-0.467
EP Aqr	637.4	320.7	47.13	16.39	-0.746	-2.082
g her	437.6	148.8	23.63	6.6	-1.171	-1.998
HD 161796	6.12	183.5	151.7	48.67	3.692	-0.207
HD 2385858	73.88	302.4	96.59	40.97	1.530	-1.239
HD 331319	0.54	37.99	55.83	14.76	4.618	0.418
HD 44179	421.6	456.1	173.1	66.19	0.085	-1.052
HD 56126	24.51	116.7	50.13	18.72	1.694	-0.917
HDE 269006	0.95	11.84	3.86	21.01	2.739	-1.217
HEN2-113	92.41	310.5	176.6	71.3	1.316	-0.613
Hen2-90	49.4	83.76	19.76	50.15	0.573	-1.568
HEN3-1475	7.05	28.31	63.68	33.43	1.509	0.880
HEN3-401	4.12	38.33	76.14	41.49	2.422	0.745
IC 418	38.27	199.2	103.6	31.24	1.791	-0.710
IRAS 07027-7934	22.69	81.96	41.97	13.57	1.394	-0.727
iras 08011-3627	131.3	94.32	26.12	11.96	-0.359	-1.394
iras 08544-4431	180.3	158.8	56.25	28.43	-0.138	-1.127
iras 09256-6324	101	96.24	34.52	13.46	-0.052	-1.113
iras 09371+1212	0.27	4.59	70.7	28.21	3.076	2.969
IRAS 09425-6040	26.82	55.53	21.18	5.05	0.790	-1.047
iras 10456-5712	189.1	115.5	30.86	10.89	-0.535	-1.433
IRAS 15194-5115	1321	565.3	145.1	50.98	-0.922	-1.477
IRAS 16342-3814	16.2	199.8	290.2	139.4	2.728	0.405
IRAS 16594-4656	44.92	298	131.4	34.36	2.054	-0.889
IRAS 17010-3840	57.77	100.4	52.23	50.06	0.600	-0.710
IRAS 17251-2821-1	3.57	8.51	4.25	19.91	0.943	-0.754
IRAS 17276-2846-1	2.5	7.91	7.07	30.01	1.251	-0.122
IRAS 17323-2424-1	3.44	8.53	4.35	13.52	0.986	-0.731
IRAS 18488-0107	16.45	42.98	44.03	72.8	1.043	0.026
IRAS 19067+0811	24.63	72.05	38.9	91.1	1.165	-0.669
IRAS 19306+1407	3.58	58.65	31.83	10.03	3.036	-0.664
IRAS 19312+1950	22.47	70.6	366.1	423.1	1.243	1.787
IRAS 19474-0744	460.6	271.5	47.31	17.22	-0.574	-1.897
IRAS 20000+3239	15.03	70.97	29.99	43.1	1.685	-0.935

IRAS 20038-2722	394.7	152.4	28.41	13.65	-1.033	-1.824
IRAS 20248-2825	493.8	192	32.59	12.69	-1.026	-1.926
IRAS 21282+5050	50.99	74.36	33.43	14.99	0.410	-0.868
IRAS 21554+6204	62.94	138.2	52.13	15.59	0.854	-1.059
IRAS 22036+5306	8.43	46.28	107.2	50.7	1.849	0.912
irc+10216	47530	23070	5652	922	-0.785	-1.527
IRC+50137	226.9	274.2	72.39	23.01	0.206	-1.446
J 175521.7-293912	3.06	8.21	7.05	109.7	1.072	-0.165
KHI CYG	1688	459	80.67	17.72	-1.414	-1.888
MGE 3222	4.43	8.52	19.88	239.7	0.710	0.920
MGE 4218	154.6	15	39.92	386.6	-2.533	1.063
MWC 922	336	597.5	253.2	436	0.625	-0.932
NGC 3242	4.5	35.58	53.38	29.61	2.245	0.440
NGC 40	14.49	71.9	64.76	27.51	1.739	-0.114
NGC 6445	1.5	15.01	44.44	43.23	2.501	1.178
NGC 6537	7.72	58.3	189.9	166.1	2.195	1.282
NGC 6543	7.51	113.5	133.3	62.68	2.948	0.175
NGC 6781	0.31	2.56	44.56	76.99	2.292	3.102
NGC 6826	4.93	39.33	46.79	21.32	2.255	0.189
NGC 7009	6.33	56.7	91.1	48.06	2.380	0.515
NGC 7026	2.39	18.35	42.74	30.91	2.213	0.918
NML CYG	—	—	—	—	—	—
NML TAU	4634	2377	332.1	102.8	-0.725	-2.137
OH 104.91+2.41	123.2	228.9	90.65	34.96	0.673	-1.006
OH 231.8+4.2	18.98	226.3	548.3	294	2.691	0.961
OH 26.5+0.6	359.8	633.8	463	310.7	0.615	-0.341
OH 30.1-0.7	111.1	279.9	237	806.9	1.003	-0.181
OH 30.7+0.4	13.93	19.75	61.53	289.9	0.379	1.234
OH 32.8-0.3	22.85	65.75	364.5	583.2	1.148	1.860
OMI CET	4881	2261	300.8	88.44	-0.836	-2.190
PI GRU	908.5	437.3	77.3	23.28	-0.794	-1.881
PNMz3	88.76	343.4	277	112.6	1.469	-0.233
r aql	401.7	244.6	139.7	83.06	-0.539	-0.608
R CAS	1341	554.6	102.8	38.85	-0.959	-1.830
R DOR	5157	1594	243.5	83.45	-1.275	-2.040
R Lep	379.5	116.3	26.19	9.14	-1.284	-1.619

RAFGL 2374	127.2	155	41.42	9.78	0.215	-1.433
RAFGL 4205	92.41	310.5	176.6	71.3	1.316	-0.613
RR Aql	332.2	150.9	27.47	10.13	-0.857	-1.850
RT Cap	72.93	20.74	4.41	3.61	-1.365	-1.681
S Aur	161.9	41.3	9.57	11.59	-1.483	-1.588
s ther	199.3	97.09	16.7	5.97	-0.781	-1.911
Tc1	2.02	11.88	13.38	4.72	1.924	0.129
TX CAM	1640	634.7	134.3	38.56	-1.031	-1.686
U Hya	205.5	72.37	17.23	14.46	-1.133	-1.558
U Mon	124.3	88.43	26.59	9.54	-0.370	-1.305
V CYG	665.1	234.2	49.15	17.25	-1.133	-1.695
V HYA	1107	459.6	98.87	29.89	-0.954	-1.668
V1300 Aql	1255	1061	215.5	63.65	-0.182	-1.731
V384 Per	535.2	198.7	39.95	11.94	-1.076	-1.742
v438 oph	61.56	26.69	4.45	3.72	-0.907	-1.945
W AQL	1575	669.6	111.7	35.99	-0.929	-1.944
W HYA	4200	1189	195	72.25	-1.370	-1.963
W Ori	183.8	51.69	14.25	6.27	-1.377	-1.399
WX PSC	1155	967.6	215.2	72.08	-0.192	-1.632
X HER	484.5	241.4	39.37	18.29	-0.756	-1.969
Y CVn	276.3	70.32	17.25	7.82	-1.486	-1.526

A.3 PACS/Spectrometer PSF

The following table contains the spectrometer Gaussian parameters derived for raster observations of Neptune at selected wavelengths, across the field-of-view.

Table A.3: Spectrometer beam size as a function of wavelength; a is the major axis, b is the minor axis and $\Phi_{\rm PSF}$ $(arcsec) = \sqrt{a.b} = FWHM$.

Target	λ (μm)	a (arcsec)	b (arcsec)	$\Phi_{\rm PSF}$ $(arcsec)$
neptune	55	9.22 ±0.02	8.31 ±0.02	8.75 ±0.03
neptune	55	9.23 ±0.03	8.19 ±0.02	8.7 ±0.03
neptune	55	8.94 ±0.02	8.24 ±0.02	8.58 ±0.03
neptune	55	8.92 ±0.02	8.4 ±0.02	8.66 ±0.03
neptune	55	10.04 ±0.02	8.47 ±0.02	9.22 ±0.03
neptune	55	9.61 ±0.02	8.51 ±0.02	9.04 ±0.03
neptune	55	9.38 ±0.02	8.55 ±0.02	8.96 ±0.03

neptune	55	9.37 ±0.02	8.49 ±0.02	8.92 ±0.03
neptune	55	9.33 ±0.02	8.63 ±0.02	8.97 ±0.03
neptune	55	9.01 ±0.02	8.54 ±0.02	8.77 ±0.03
neptune	55	9.02 ±0.02	8.51 ±0.02	8.76 ±0.03
neptune	62	9 ±0.02	8.54 ±0.02	8.77 ±0.03
neptune	62	9.16 ±0.02	8.57 ±0.02	8.86 ±0.03
neptune	62	8.74 ±0.02	8.61 ±0.02	8.67 ±0.03
neptune	62	8.99 ±0.02	8.49 ±0.02	8.74 ±0.03
neptune	62	9.69 ±0.02	8.8 ±0.02	9.23 ±0.03
neptune	62	9.45 ±0.02	8.62 ±0.02	9.02 ±0.03
neptune	62	9.34 ±0.02	8.55 ±0.02	8.93 ±0.03
neptune	62	9.45 ±0.02	8.81 ±0.02	9.12 ±0.03
neptune	62	9.33 ±0.02	8.52 ±0.02	8.91 ±0.03
neptune	62	9.15 ±0.02	8.3 ±0.02	8.71 ±0.03
neptune	62	9.57 ±0.02	8.36 ±0.02	8.94 ±0.03
neptune	68	8.87 ±0.02	8.56 ±0.02	8.72 ±0.02
neptune	68	8.74 ±0.02	8.48 ±0.02	8.61 ±0.02
neptune	68	8.55 ±0.02	8.31 ±0.02	8.43 ±0.03
neptune	68	8.51 ±0.02	8.22 ±0.02	8.37 ±0.03
neptune	68	9.45 ±0.02	8.67 ±0.02	9.05 ±0.03
neptune	68	9.07 ±0.02	8.44 ±0.02	8.75 ±0.03
neptune	68	9.05 ±0.02	8.32 ±0.02	8.67 ±0.03
neptune	68	9.35 ±0.02	8.66 ±0.02	9 ±0.03
neptune	68	8.94 ±0.02	8.4 ±0.02	8.67 ±0.03
neptune	68	8.84 ±0.02	8.24 ±0.02	8.54 ±0.03
neptune	68	9.16 ±0.02	8.24 ±0.02	8.69 ±0.03
neptune	73	8.63 ±0.02	8.32 ±0.02	8.48 ±0.03
neptune	73	8.59 ±0.02	8.25 ±0.02	8.42 ±0.02
neptune	73	8.56 ±0.02	8.21 ±0.02	8.38 ±0.03
neptune	73	8.49 ±0.02	8.22 ±0.02	8.35 ±0.03
neptune	73	9.25 ±0.02	8.52 ±0.02	8.88 ±0.03
neptune	73	9.04 ±0.02	8.4 ±0.02	8.71 ±0.03
neptune	73	8.97 ±0.02	8.24 ±0.02	8.6 ±0.03
neptune	73	9.06 ±0.02	8.38 ±0.02	8.71 ±0.03
neptune	73	9.01 ±0.02	8.29 ±0.02	8.64 ±0.03
neptune	73	8.73 ±0.02	8.12 ±0.02	8.42 ±0.03

neptune	73	9.09 ±0.02	8.35 ±0.02	8.71 ±0.03
neptune	75	9.11 ±0.02	8.4 ±0.02	8.75 ±0.02
neptune	75	8.74 ±0.02	8.35 ±0.02	8.54 ±0.03
neptune	75	8.8 ±0.02	8.57 ±0.02	8.69 ±0.03
neptune	75	8.95 ±0.02	8.63 ±0.02	8.79 ±0.03
neptune	75	9.27 ±0.02	8.63 ±0.02	8.94 ±0.03
neptune	75	9.27 ±0.02	8.69 ±0.02	8.97 ±0.03
neptune	75	9.35 ±0.02	8.66 ±0.02	9 ±0.03
neptune	75	9.1 ±0.02	8.64 ±0.02	8.86 ±0.03
neptune	75	8.81 ±0.02	8.66 ±0.02	8.73 ±0.03
neptune	75	8.9 ±0.02	8.63 ±0.02	8.77 ±0.03
neptune	75	9.56 ±0.02	8.76 ±0.02	9.15 ±0.03
neptune	84	8.85 ±0.02	8.4 ±0.02	8.62 ±0.03
neptune	84	8.81 ±0.02	8.34 ±0.02	8.57 ±0.03
neptune	84	8.91 ±0.02	8.29 ±0.02	8.59 ±0.03
neptune	84	8.79 ±0.02	8.27 ±0.02	8.53 ±0.03
neptune	84	9.46 ±0.02	8.58 ±0.02	9.01 ±0.03
neptune	84	9.13 ±0.02	8.45 ±0.02	8.78 ±0.03
neptune	84	9.22 ±0.02	8.37 ±0.02	8.79 ±0.03
neptune	84	9.22 ±0.02	8.49 ±0.02	8.85 ±0.03
neptune	84	9.17 ±0.02	8.3 ±0.02	8.72 ±0.03
neptune	84	9.1 ±0.02	8.33 ±0.02	8.71 ±0.03
neptune	84	9.59 ±0.02	8.49 ±0.02	9.02 ±0.03
neptune	94	9.08 ±0.02	8.46 ±0.02	8.77 ±0.03
neptune	94	9.1 ±0.02	8.48 ±0.02	8.79 ±0.03
neptune	94	9.12 ±0.02	8.58 ±0.02	8.84 ±0.03
neptune	94	9.21 ±0.02	8.67 ±0.02	8.94 ±0.03
neptune	94	9.38 ±0.02	8.63 ±0.02	9 ±0.03
neptune	94	9.29 ±0.02	8.46 ±0.02	8.87 ±0.03
neptune	94	9.44 ±0.02	8.45 ±0.02	8.94 ±0.03
neptune	94	9.23 ±0.02	8.59 ±0.02	8.91 ±0.03
neptune	94	9.17 ±0.02	8.44 ±0.02	8.8 ±0.03
neptune	94	9.13 ±0.02	8.42 ±0.02	8.77 ±0.03
neptune	94	9.79 ±0.02	8.6 ±0.02	9.17 ±0.03
neptune	110	10.29 ±0.02	8.92 ±0.02	9.58 ±0.03
neptune	110	9.86 ±0.02	8.79 ±0.02	9.31 ±0.02

neptune	110	9.61 ±0.02	8.98 ±0.02	9.29 ±0.03
neptune	110	9.72 ±0.02	8.93 ±0.02	9.32 ±0.02
neptune	110	10.5 ±0.02	8.9 ±0.02	9.67 ±0.03
neptune	110	10.01 ±0.02	8.9 ±0.02	9.44 ±0.03
neptune	110	9.89 ±0.02	8.91 ±0.02	9.39 ±0.03
neptune	110	9.89 ±0.02	8.88 ±0.02	9.37 ±0.03
neptune	110	9.98 ±0.02	8.96 ±0.02	9.45 ±0.03
neptune	110	9.87 ±0.02	8.8 ±0.02	9.32 ±0.03
neptune	110	10.09 ±0.02	8.87 ±0.02	9.46 ±0.03
neptune	125	10.81 ±0.02	9.36 ±0.01	10.06 ±0.02
neptune	125	10.74 ±0.01	9.46 ±0.01	10.08 ±0.02
neptune	125	10.32 ±0.02	9.36 ±0.01	9.83 ±0.02
neptune	125	10.6 ±0.02	9.31 ±0.01	9.93 ±0.02
neptune	125	10.94 ±0.02	9.67 ±0.01	10.28 ±0.02
neptune	125	10.83 ±0.02	9.55 ±0.02	10.17 ±0.02
neptune	125	10.38 ±0.02	9.31 ±0.02	9.83 ±0.02
neptune	125	10.73 ±0.02	9.52 ±0.02	10.1 ±0.02
neptune	125	10.48 ±0.02	9.35 ±0.01	9.9 ±0.02
neptune	125	10.51 ±0.02	9.28 ±0.02	9.88 ±0.02
neptune	136	11.14 ±0.01	9.63 ±0.01	10.36 ±0.02
neptune	136	10.51 ±0.01	9.41 ±0.01	9.94 ±0.02
neptune	136	10.4 ±0.02	9.49 ±0.01	9.94 ±0.02
neptune	136	10.28 ±0.02	9.48 ±0.01	9.87 ±0.02
neptune	136	10.92 ±0.01	9.76 ±0.01	10.32 ±0.02
neptune	136	10.5 ±0.02	9.51 ±0.01	9.99 ±0.02
neptune	136	10.47 ±0.02	9.48 ±0.01	9.96 ±0.02
neptune	136	11.05 ±0.02	9.83 ±0.01	10.42 ±0.02
neptune	136	10.43 ±0.01	9.57 ±0.01	9.99 ±0.02
neptune	136	10.27 ±0.01	9.38 ±0.01	9.81 ±0.02
neptune	136	10.86 ±0.01	9.47 ±0.01	10.14 ±0.02
neptune	145	11.2 ±0.01	9.73 ±0.01	10.44 ±0.02
neptune	145	10.58 ±0.01	9.49 ±0.01	10.02 ±0.02
neptune	145	10.66 ±0.01	9.67 ±0.01	10.15 ±0.02
neptune	145	10.8 ±0.01	9.83 ±0.01	10.3 ±0.02
neptune	145	10.98 ±0.01	9.85 ±0.01	10.4 ±0.02
neptune	145	10.59 ±0.01	9.75 ±0.01	10.16 ±0.02

neptune	145	10.68 ±0.01	9.76 ±0.01	10.21 ±0.02
neptune	145	10.98 ±0.01	9.88 ±0.01	10.42 ±0.02
neptune	145	10.75 ±0.01	9.87 ±0.01	10.3 ±0.02
neptune	145	10.56 ±0.01	9.78 ±0.01	10.16 ±0.02
neptune	145	10.76 ±0.01	9.78 ±0.01	10.26 ±0.02
neptune	150	11.29 ±0.01	10.34 ±0.01	10.81 ±0.02
neptune	150	10.62 ±0.01	10.2 ±0.01	10.41 ±0.02
neptune	150	10.92 ±0.01	10.5 ±0.01	10.71 ±0.02
neptune	150	11.46 ±0.01	10.45 ±0.01	10.94 ±0.02
neptune	150	10.95 ±0.01	10.41 ±0.01	10.68 ±0.02
neptune	150	10.78 ±0.01	10.42 ±0.01	10.6 ±0.02
neptune	150	11.14 ±0.01	10.67 ±0.01	10.9 ±0.02
neptune	150	10.88 ±0.01	10.51 ±0.01	10.69 ±0.02
neptune	150	10.71 ±0.01	10.56 ±0.01	10.63 ±0.02
neptune	150	10.99 ±0.01	10.68 ±0.01	10.83 ±0.02
neptune	150	11.57 ±0.01	10.51 ±0.01	11.03 ±0.02
neptune	168	12.06 ±0.01	10.67 ±0.01	11.34 ±0.02
neptune	168	11.44 ±0.01	10.45 ±0.01	10.93 ±0.01
neptune	168	11.72 ±0.01	10.81 ±0.01	11.26 ±0.02
neptune	168	11.98 ±0.01	10.9 ±0.01	11.43 ±0.02
neptune	168	11.8 ±0.01	10.74 ±0.01	11.26 ±0.02
neptune	168	11.52 ±0.01	10.88 ±0.01	11.19 ±0.02
neptune	168	11.69 ±0.01	10.95 ±0.01	11.31 ±0.02
neptune	168	11.83 ±0.01	10.89 ±0.01	11.35 ±0.02
neptune	168	11.58 ±0.01	10.89 ±0.01	11.23 ±0.01
neptune	168	11.51 ±0.01	10.99 ±0.01	11.25 ±0.01
neptune	168	11.74 ±0.01	10.96 ±0.01	11.34 ±0.02
neptune	187	13.21 ±0.02	11.66 ±0.01	12.41 ±0.02
neptune	187	12.51 ±0.01	11.4 ±0.01	11.94 ±0.02
neptune	187	12.89 ±0.01	12.19 ±0.01	12.54 ±0.02
neptune	187	13.51 ±0.02	12.4 ±0.01	12.94 ±0.02
neptune	187	12.99 ±0.01	11.54 ±0.01	12.24 ±0.02
neptune	187	13.02 ±0.01	12.09 ±0.01	12.55 ±0.02
neptune	187	12.68 ±0.01	11.9 ±0.01	12.28 ±0.02
neptune	187	12.92 ±0.01	11.61 ±0.01	12.25 ±0.02
neptune	187	12.6 ±0.01	11.8 ±0.01	12.19 ±0.02

neptune	187	12.64 ±0.01	12.1 ±0.01	12.37 ±0.02
neptune	187	12.65 ±0.02	11.83 ±0.01	12.23 ±0.02

A.4 PACS/Photometer PSF

Table A.4: Photometer beam size in two bands; a is the major axis, b is the minor axis, $\Phi_{\mathrm{PSF}}\ (arcsec) = \sqrt{a.b} = FWHM$ and angle is the array-to-map angle.

Target	Band	a (arcsec)	b (arcsec)	$\Phi_{\mathrm{PSF}}\ (arcsec)$	angle	note
Vesta	Blue	5.53±0.02	5.1±0.02	5.31±0.03	+63	
Vesta	Blue	5.31±0.02	5.0±0.02	5.15±0.03	+63	recentered
Vesta	Blue	5.74±0.02	5.43±0.02	5.58±0.03	+63	recentered
Vesta	Blue	6.29±0.02	5.49±0.02	5.88±0.03	+42	
Vesta	Blue	5.89±0.02	5.05±0.02	5.46±0.03	+42	
Vesta	Blue	5.6±0.02	4.91±0.02	5.25±0.03	+42	recentered
Vesta	Blue	6.0±0.02	5.34±0.02	5.66±0.03	+42	recentered
Vesta	Blue	6.4±0.02	5.56±0.02	5.96±0.03	-42	
Vesta	Blue	6.01±0.02	5.12±0.02	5.55±0.03	-42	
Vesta	Blue	5.77±0.02	4.8±0.02	5.26±0.03	-42	recentered
Vesta	Blue	6.16±0.02	5.24±0.02	5.68±0.03	-42	recentered
Vesta	Red	12.12±0.03	10.73±0.03	11.41±0.04	+63	
Vesta	Red	11.29±0.03	9.87±0.03	10.56±0.04	+63	
Vesta	Red	11.27±0.03	9.72±0.03	10.47±0.04	+63	recentered
Vesta	Red	12.13±0.03	10.59±0.03	11.33±0.05	+63	recentered
Vesta	Red	12.35±0.03	10.44±0.03	11.35±0.04	+42	
Vesta	Red	11.51±0.03	9.59±0.03	10.5±0.04	+42	
Vesta	Red	11.41±0.03	9.47±0.03	10.4±0.05	+42	recentered
Vesta	Red	12.28±0.03	10.35±0.03	11.27±0.05	+42	recentered
Vesta	Red	12.37±0.03	10.48±0.03	11.39±0.04	-42	
Vesta	Red	11.53±0.03	9.64±0.03	10.54±0.04	-42	
Vesta	Red	11.47±0.03	9.56±0.03	10.47±0.05	-42	recentered
Vesta	Red	12.31±0.04	10.41±0.03	11.32±0.05	-42	recentered

A.5 Photometry fitting

The next tables contain information relative to the fit parameters obtained from photometry maps (HPF and JScanam) for our targets. The data was obtained from the HSA. Note that U Mon and IRAS 10178-5958 were not observed in the blue (70μm)band, so we only provide the results in the red band.

The reported standard errors correspond to the propagated statistical uncertainties only, i.e, they do not include absolute flux calibration errors.

Figures 2.9 and 2.10 were generated using tables A.5 and A.6.

Table A.5: Fitting parameters from HPF photometry maps in the red and blue bands: peak intensity (P), flux (F) and FWHM (Φ).

		HPF					
Target	OBSID	P_{70} (Jy/px)	F_{70} (Jy)	Φ_{70} ($''$)	P_{160} (Jy/px)	F_{160} (Jy)	Φ_{160} ($''$)
AFGL2688	1342195837	72.3±0.3	383±3	6.89±0.05	24.06±0.04	338±1	11.27±0.04
AFGL3068	1342188378	7.79±0.01	28.2±0.1	5.72±0.02	1.302±0.002	18.85±0.05	11.44±0.03
AFGL3116	1342188490	2.267±0.004	9.88±0.04	6.28±0.02	0.409±0.001	7.3±0.03	12.69±0.05
AFGL618	1342193132	48.4±0.1	163±1	5.52±0.03	10.407±0.02	132.0±0.6	10.71±0.04
CIT6	1342210620	4.89±0.01	20.9±0.1	6.2±0.03	0.938±0.003	16.7±0.1	12.67±0.09
IRC+10216	1342186298	65.2±0.2	351±2	6.99±0.04	12.75±0.03	218±1	12.42±0.06
EPAQR	1342195460	0.868±0.002	3.45±0.02	5.99±0.03	0.1711±0.004	2.55±0.01	11.61±0.06
HD235858	1342196757	2.459±0.005	9.38±0.05	5.87±0.03	0.355±0.001	5.36±0.03	11.68±0.05
HD44179	1342185549	6.49±0.007	21.80±0.06	5.51±0.01	1.618±0.001	22.07±0.05	11.1±0.02
HD56126	1342207151	1.578±0.004	6.59±0.04	6.15±0.04	0.257±0.001	3.671±0.03	11.36±0.09
HD 161796	1342183565	4.949±0.007	16.93±0.05	5.56±0.02	0.745±0.001	9.78±0.02	10.89±0.02
IRAS15194-5115	1342190247	3.303±0.007	13.45±0.06	6.07±0.03	0.615±0.001	10.33±0.06	12.32±0.06
IRAS16342-3814	1342216493	14.66±0.02	47.4±0.2	5.41±0.02	3.957±0.005	52.6±0.1	10.96±0.03
IRAS16594-4656	1342193052	2.954±0.004	13.09±0.04	6.33±0.02	0.598±0.001	9.26±0.03	11.84±0.04
IRAS17347-3139	1342241406	5.222±0.006	17.14±0.05	5.45±0.01	1.34±0.005	19.3±0.2	11.41±0.1
IRAS22036+5306	1342198911	5.077±0.007	16.47±0.05	5.41±0.02	1.415±0.002	19.22±0.05	11.08±0.03
KHICYG	1342188320	1.568±0.003	6.336±0.03	6.04±0.03	0.3346±0.0005	5.1±0.02	11.74±0.03
NGC6302	1342250872	12.44±0.02	140.7±0.6	10.11±0.04	7.27±0.02	192.3±0.9	15.46±0.07
NMLCYG	1342195485	30.81±0.06	108.1±0.5	5.63±0.02	5.73±0.02	80.5±0.6	11.26±0.08

NMLTAU	1342190343	6.26±0.01	25.9±0.1	6.12±0.02	0.867±0.002	14.40±0.06	12.25±0.05
OMICET	1342190335	6.01±0.01	23.2±0.1	5.9±0.03	1.084±0.002	15.67±0.07	11.43±0.05
PIGRU	1342196799	1.109±0.003	4.774±0.03	6.24±0.04	0.236±0.001	3.52±0.03	11.6±0.08
RCAS	1342222422	2.518±0.006	9.85±0.06	5.95±0.03	0.522±0.001	8.03±0.04	11.79±0.06
RLEP	1342190304	0.538±0.001	2.145±0.011	6±0.03	0.1190±0.0003	1.74±0.01	11.5±0.06
RTCAP	1342231102	0.1210±0.0003	0.398±0.002	5.45±0.03	0.0258±0.0001	0.328±0.002	10.74±0.05
STHER	1342188324	0.236±0.001	1.209±0.007	6.81±0.03	0.0511±0.0001	0.849±0.004	12.25±0.05
TXCAM	1342217395	2.151±0.006	10.02±0.07	6.49±0.04	0.422±0.001	6.02±0.04	11.36±0.06
UHYA	1342212001	0.319±0.001	1.167±0.009	5.75±0.04	0.0678±0.0003	0.861±0.008	10.71±0.09
V1943SGR	1342208468	0.604±0.001	2.019±0.01	5.5±0.02	0.1279±0.0003	1.677±0.009	10.88±0.06
VCYG	1342188462	0.924±0.002	3.55±0.02	5.89±0.03	0.1821±0.0005	2.975±0.017	12.15±0.07
VHYA	1342211997	2.393±0.005	8.69±0.04	5.73±0.02	0.453±0.001	6.411±0.029	11.3±0.05
WORI	1342229983	0.338±0.001	1.181±0.006	5.62±0.02	0.0751±0.0001	1.008±0.004	11.02±0.04
WXPSC	1342188486	3.522±0.007	14.53±0.06	6.11±0.02	0.56±0.001	9.919±0.047	12.66±0.06
XHER	1342188322	0.702±0.001	2.62±0.01	5.81±0.02	0.1303±0.0002	2.002±0.009	11.79±0.05
YCVN	1342188330	0.418±0.001	1.486±0.006	5.67±0.02	0.09989±0.0001	1.378±0.005	11.22±0.04
IRAS10178-5958	1342237204	—	—	—	0.813±0.001	12.847±0.024	11.95±0.02
UMon	1342243117	—	—	—	0.242±0	3.003±0.006	10.59±0.02

Table A.6: Fitting parameters from JScanam photometry maps in the blue and red bands: peak intensity (P), flux (F) and FWHM (Φ).

	JScanam					
Target	P_{70} (Jy/px)	F_{70} (Jy)	Φ_{70} ($''$)	P_{160} (Jy/px)	F_{160} (Jy)	Φ_{160} ($''$)
AFGL2688	69.4±0.2	371±2	6.95±0.04	24.44±0.03	337.4±0.8	11.17±0.03
AFGL3068	8.46±0.02	27.7±0.1	5.44±0.02	1.393±0.002	18.93±0.06	11.08±0.03
AFGL3116	2.47±0.005	9.67±0.05	5.95±0.03	0.443±0.001	7.29±0.04	12.2±0.05
AFGL618	46.8±0.1	160±1	5.56±0.03	10.52±0.02	132.0±0.5	10.65±0.03
CIT6	4.91±0.01	20.8±0.1	6.19±0.03	0.951±0.002	15.96±0.09	12.32±0.06
IRC+10216	67.9±0.2	350±2	6.83±0.04	12.73±0.03	219±1	12.46±0.06
EPAQR	0.919±0.002	3.41±0.02	5.79±0.03	0.1827±0.0004	2.57±0.01	11.27±0.05
HD235858	2.58±0.004	9.29±0.04	5.71±0.02	0.401±0.002	6.14±0.09	11.77±0.2
HD44179	7.026±0.008	21.58±0.06	5.27±0.01	1.708±0.001	22.01±0.05	10.79±0.02
HD56126	1.575±0.003	6.58±0.03	6.14±0.02	0.254±0.001	3.60±0.02	11.32±0.06
HD 161796	4.767±0.009	17.62±0.08	5.8±0.03	0.753±0.001	9.82±0.03	10.86±0.06
IRAS15194-5115	3.551±0.008	13.20±0.07	5.27±0.02	0.642±0.002	10.58±0.07	12.2±0.07
IRAS16342-3814	15.57±0.02	47.8±0.2	6.1±0.02	4.219±0.007	54.0±0.2	10.75±0.04
IRAS16594-4656	3.162±0.005	13.01±0.05	5.26±0.01	0.652±0.001	9.20±0.04	11.29±0.04
IRAS17347-3139	5.585±0.007	17.08±0.05	5.34±0.02	1.448±0.008	18.8±0.2	10.83±0.12
IRAS22036+5306	5.23±0.01	16.51±0.07	5.75±0.03	1.511±0.002	19.08±0.06	10.69±0.03
KHICYG	1.698±0.004	6.22±0.03	9.9±0.05	0.361±0.001	5.191±0.02	11.4±0.04
NGC6302	12.85±0.03	139.3±0.7	5.59±0.02	7.624±0.018	191±1	15.05±0.08
NMLCYG	31.02±0.05	107.2±0.4	5.74±0.03	5.778±0.01	80.8±0.4	11.24±0.05

NMLTAU	6.96±0.02	25.4±0.1	5.95±0.03	0.941±0.002	14.27±0.06	11.7±0.04
OMICET	5.95±0.01	23.3±0.1	6.18±0.03	1.085±0.002	15.90±0.07	11.51±0.05
PIGRU	1.129±0.003	4.77±0.03	5.88±0.03	0.2411±0.0004	3.58±0.02	11.59±0.05
RCAS	1.895±0.004	7.24±0.04	6.11±0.03	0.43±0.001	6.14±0.02	11.36±0.04
RLEP	0.53±0.001	2.192±0.012	5.5±0.02	0.1207±0.0003	1.769±0.01	11.51±0.06
RTCAP	0.1193±0.003	0.400±0.002	6.63±0.04	0.0258±0.0001	0.328±0.002	10.74±0.05
STHER	0.253±0.001	1.23±0.008	6.4±0.03	0.0556±0.0002	0.909±0.006	12.15±0.07
TXCAM	2.159±0.004	9.79±0.04	5.66±0.03	0.416±0.001	6.15±0.03	11.56±0.05
UHYA	0.329±0.001	1.165±0.007	5.55±0.02	0.0658±0.0004	1.046±0.013	12.0±0.1
V1943SGR	0.59±0.001	2.009±0.009	5.78±0.02	0.1291±0.0003	1.728±0.01	11±0.06
VCYG	0.952±0.002	3.542±0.02	5.8±0.03	0.199±0.001	3.21±0.03	12.1±0.1
VHYA	2.347±0.004	8.73±0.04	5.8±0.02	0.448±0.001	6.66±0.03	11.6±0.05
WORI	0.334±0.001	1.173±0.006	5.63±0.02	0.0752±0.0001	0.993±0.004	10.92±0.04
WXPSC	3.848±0.008	14.15±0.07	5.76±0.03	0.602±0.001	9.86±0.05	12.16±0.06
XHER	0.759±0.002	2.59±0.01	5.54±0.02	0.1474±0.0004	2.05±0.01	11.22±0.06
YCVN	0.44±0.001	1.506±0.007	5.56±0.02	0.1109±0.0003	1.357±0.007	10.51±0.05
IRAS10178-5958	—	—	—	0.887±0.001	12.83±0.03	11.43±0.02
UMon	—	—	—	0.2444±0.0004	3.183±0.013	10.85±0.04

Table A.7: Major axis, minor axis, position angle and FWHM (Φ") derived from photometry Jscanam maps.

Target Name	Blue Camera				Red Camera			
	a (")	b (")	P.A. (deg)	Φ (")	a (")	b (")	P.A. (deg)	Φ (")
AFGL 2688	7.42±0.03	6.52±0.03	58±1	6.95±0.04	11.79±0.02	10.59±0.02	73±1	11.17±0.03
AFGL 3068	5.6±0.02	5.28±0.01	51±2	5.44±0.02	11.72±0.02	10.48±0.02	68±1	11.08±0.03
AFGL 3116	6.13±0.02	5.78±0.02	61±2	5.95±0.03	13.02±0.04	11.43±0.04	69±1	12.2±0.05
AFGL 618	5.91±0.02	5.23±0.02	59±1	5.56±0.03	11.37±0.02	9.97±0.02	81±1	10.65±0.03
CIT 6	6.35±0.02	6.03±0.02	106±3	6.19±0.03	12.99±0.04	11.67±0.04	103±1	12.32±0.06
CW LEO	6.95±0.03	6.7±0.03	97±5	6.83±0.04	13.06±0.04	11.89±0.04	112±1	12.46±0.06
EP AQR	6.06±0.02	5.54±0.02	76±2	5.79±0.03	12.11±0.04	10.49±0.03	80±1	11.27±0.05
HD 161796	5.88±0.02	5.69±0.02	66±3	5.78±0.02	11.55±0.02	10.21±0.02	118±1	10.86±0.03
HD 235858	5.87±0.01	5.55±0.01	79±2	5.71±0.02	12.5±0.1	11.09±0.1	93±3	11.77±0.15
HD 44179	5.44±0.01	5.1±0.01	90±1	5.27±0.01	11.56±0.01	10.07±0.01	101.1±0.4	10.79±0.02
HD 56126	6.31±0.02	5.99±0.01	90±2	6.14±0.02	12.09±0.05	10.61±0.04	95±1	11.32±0.06
IRAS 10178-5958	...	...	...	...	11.83±0.01	11.05±0.01	106±1	11.43±0.02
IRAS 15194-5115	5.98±0.02	5.62±0.02	85±2	5.8±0.03	13.07±0.05	11.38±0.05	104±1	12.2±0.07
IRAS 16342-3814-1	5.44±0.01	5.1±0.01	86±2	5.27±0.02	11.51±0.03	10.04±0.03	98±1	10.75±0.04
IRAS 16594-4656	6.59±0.02	5.65±0.01	86±1	6.1±0.02	12.2±0.03	10.45±0.03	108±1	11.29±0.04
IRAS 17347-3139	5.3±0.01	5.21±0.01	38±4	5.26±0.01	11.44±0.09	10.24±0.08	98±3	10.83±0.12
IRAS 22036+5306	5.59±0.02	5.1±0.01	59±1	5.34±0.02	11.27±0.02	10.13±0.02	48±1	10.69±0.03
KHI CYG	5.91±0.02	5.6±0.02	12±2	5.75±0.03	12.41±0.03	10.48±0.03	33±1	11.4±0.04
NGC 6302	11.58±0.04	8.47±0.03	173.3±0.4	9.9±0.05	15.92±0.06	14.23±0.05	4±1	15.05±0.08

NML CYG	5.79±0.02	5.4±0.01	88±2	5.59±0.02	12.02±0.04	10.51±0.03	89±1	11.24±0.05
NML TAU	5.95±0.02	5.54±0.02	85±2	5.74±0.03	12.53±0.03	10.93±0.03	78±1	11.7±0.04
OMI CET	6.22±0.02	5.69±0.02	68±1	5.95±0.03	12.2±0.04	10.85±0.03	80±1	11.51±0.05
PI GRU	6.43±0.02	5.94±0.02	83±2	6.18±0.03	12.48±0.03	10.76±0.03	73±1	11.59±0.05
R CAS	6.05±0.02	5.72±0.02	69±2	5.88±0.03	12.07±0.03	10.7±0.03	76±1	11.36±0.04
R LEP	6.39±0.02	5.85±0.02	57±2	6.11±0.03	12.21±0.04	10.85±0.04	72±1	11.51±0.06
RT CAP	5.76±0.02	5.26±0.02	61±1	5.5±0.02	11.4±0.03	10.11±0.03	72±1	10.74±0.05
ST HER	6.95±0.03	6.32±0.03	15±2	6.63±0.04	12.45±0.05	11.85±0.05	2±3	12.15±0.07
TX CAM	6.56±0.02	6.25±0.02	63±2	6.4±0.03	12.19±0.03	10.96±0.03	84±1	11.56±0.05
U Mon	...	...	...	...	11.42±0.03	10.3±0.03	91±1	10.85±0.04
U HYA	5.82±0.02	5.51±0.02	111±3	5.66±0.03	12.5±0.1	11.45±0.09	121±4	12±0.1
V CYG	6.07±0.02	5.54±0.02	35±2	5.8±0.03	12.6±0.08	11.56±0.07	48±3	12.1±0.1
V HYA	5.87±0.02	5.73±0.02	96±5	5.8±0.02	12.42±0.04	10.83±0.03	127±1	11.6±0.05
V1943 SGR	5.8±0.02	5.31±0.02	74±1	5.55±0.02	11.74±0.04	10.3±0.04	80±1	11±0.06
W ORI	5.83±0.02	5.44±0.02	89±2	5.63±0.02	11.63±0.03	10.26±0.03	88±1	10.92±0.04
WX PSC	5.93±0.02	5.6±0.02	69±2	5.76±0.03	12.97±0.04	11.41±0.04	69±1	12.16±0.06
X HER	5.73±0.02	5.36±0.02	160±2	5.54±0.02	12.06±0.04	10.44±0.04	160±1	11.22±0.06
Y CVN	5.82±0.02	5.31±0.01	114±1	5.56±0.02	10.53±0.03	10.5±0.04	100±50	10.51±0.05

A.6 Continuum fluxes

Table A.8: Continuum fluxes at selected wavelengths of 107 targets in the THROES catalogue. The statistical uncertainties of the continuum estimate are not provided since they are very small.

Target Name	F(60)	F(70)	F(80)	F(90)	F(100)[1]	F(110)	F(120)	F(130)	F(140)	F(150)	F(160)	F(170)	F(180)
ACHer	—	17.89	—	—	—	—	—	—	5.13	—	—	—	—
AFGL2019	—	35.68	—	—	—	—	—	—	14.64	—	—	—	—
AFGL2403	—	73.71	—	—	—	—	—	—	12.21	—	—	—	—
AFGL2513	21.57	15.76	11.51	8.97	7.71	6.18	5.00	4.17	3.47	3.10	2.62	2.30	1.98
AFGL2688	2922.34	2272.71	1778.45	1457.49	1156.01	925.94	794.84	662.10	537.53	450.19	386.02	340.89	291.58
AFGL3068	250.03	175.36	129.13	101.11	87.77	68.50	57.50	48.27	39.88	32.66	27.52	22.70	18.51
AFGL3116	119.91	82.80	60.16	44.80	37.78	29.70	23.84	19.69	16.25	12.85	11.00	9.14	7.41
AFGL4106	—	591.35	—	—	—	—	—	—	99.54	—	—	—	—
AFGL4202	—	—	—	17.00	—	—	—	—	6.92	—	—	—	2.96
AFGL4259	—	17.23	—	—	—	—	—	—	3.75	—	—	—	—
AFGL618	1273.78	1012.35	793.69	650.03	516.44	409.08	338.87	273.40	224.27	186.30	156.82	132.61	113.83
AFGL6815	248.87	191.09	144.01	122.37	97.12	75.35	63.32	53.06	44.78	37.34	31.85	26.93	22.76
AQSgr	3.26	2.32	1.47	1.33	1.31	0.90	0.67	0.55	0.59	0.26	0.20	0.18	0.09
BD+303639	144.85	118.70	90.36	75.57	66.29	55.15	46.79	39.10	32.33	26.66	22.38	18.71	15.43
CIT6	228.70	156.87	112.98	87.52	72.21	57.54	45.98	38.15	31.97	23.60	19.46	16.46	12.95
CPD-568032	212.40	173.13	137.08	115.98	97.77	80.06	66.69	55.10	45.10	37.20	31.18	25.95	21.92
CPD-642939	—	50.98	—	—	—	—	—	—	11.15	—	—	—	—
EPAqr	33.00	22.38	15.20	11.90	10.19	8.23	6.82	5.56	4.66	3.83	3.39	2.95	2.53

[1]The flux at 100μm is extrapolated.

gher	17.21	12.33	—	—	6.08	5.16	4.20	3.43	2.84	—	—	—	—
HD161796	149.15	107.01	74.18	57.83	48.45	36.20	28.54	23.25	18.94	15.07	12.33	10.11	8.16
HD235858	83.77	57.69	39.89	30.71	26.33	20.55	16.38	13.40	11.42	9.24	7.68	6.61	5.61
HD331319	—	38.08	—	—	—	—	—	—	7.86	—	—	—	—
HD44179	169.08	136.67	105.48	88.87	78.13	63.03	53.41	45.50	38.96	33.24	28.95	24.75	21.85
HD56126	58.26	39.06	27.68	19.77	18.08	13.49	10.70	8.48	6.69	5.05	4.07	3.59	2.76
HDE269006	—	1.80	—	—	—	—	—	—	0.18	—	—	—	—
HEN2-113	193.38	153.12	118.78	98.33	83.07	65.39	54.84	43.87	36.07	29.03	24.60	20.85	17.66
Hen2-90	—	12.51	—	—	—	—	—	—	2.97	—	—	—	—
HEN3-1475	64.21	55.46	45.83	39.12	35.28	29.06	24.72	20.90	17.64	14.67	12.83	10.64	8.86
HEN3-401	70.00	62.65	54.76	48.57	42.26	36.94	31.99	27.26	23.25	19.50	16.58	14.42	12.38
IC418	59.69	41.90	30.76	24.02	18.26	15.22	12.82	10.72	8.83	7.75	7.13	5.34	3.88
IRAS07027-7934	—	28.44	—	—	—	—	—	—	6.33	—	—	—	—
iras08011-3627	23.26	17.93	13.86	11.68	10.05	8.19	6.63	5.92	5.22	4.60	3.83	3.38	2.84
iras08544-4431	53.59	43.04	33.92	28.55	25.23	20.91	17.07	14.80	12.82	10.60	9.70	8.12	7.40
iras09256-6324	31.46	24.56	20.08	17.32	14.04	12.06	9.94	9.00	7.77	6.86	6.04	5.32	4.88
iras09371+1212	77.98	61.27	39.64	29.13	27.53	26.19	23.69	20.62	18.06	14.64	12.52	10.64	8.63
IRAS09425-6040	18.00	15.02	10.10	8.06	6.94	5.61	4.56	3.75	3.24	2.47	1.97	1.58	1.14
iras10456-5712	28.45	22.60	18.02	14.52	13.73	10.96	9.26	7.91	6.69	5.70	5.08	4.31	3.36
IRAS15194-5115	94.25	68.07	49.53	38.83	31.64	26.06	21.29	17.71	14.84	12.10	10.46	9.23	7.61
IRAS16342-3814	361.91	303.42	252.90	212.14	181.90	149.32	125.02	105.98	90.57	77.44	67.10	58.63	51.07
IRAS16594-4656	106.87	80.89	60.58	47.60	41.17	31.73	25.63	20.45	16.63	12.91	10.77	9.09	7.47

IRAS17010-3840	—	23.37	—	—	—	—	—	—	7.71	—	—	—	—
IRAS17251-2821	—	2.57	—	—	—	—	—	—	0.66	—	—	—	—
IRAS17276-2846	—	5.16	—	—	—	—	—	—	0.73	—	—	—	—
IRAS17323-2424	—	2.45	—	—	—	—	—	—	-0.02	—	—	—	—
IRAS18488-0107	47.03	34.62	24.47	18.63	15.32	12.57	10.58	8.84	7.59	6.57	5.67	4.96	4.14
IRAS19067+0811	31.26	22.47	15.10	11.30	9.16	6.84	5.02	3.87	2.81	2.11	1.68	0.92	0.61
IRAS19306+1407	—	20.99	—	—	—	—	—	—	4.17	—	—	—	—
IRAS19312+1950	411.05	434.55	428.86	422.66	429.47	428.18	412.43	382.61	348.72	318.06	282.52	246.27	219.05
IRAS19474-0744	46.00	31.01	21.85	16.07	13.42	10.53	8.53	6.77	5.68	4.58	4.18	3.35	2.81
IRAS20000+3239	27.32	20.10	13.29	10.40	9.83	7.27	5.87	4.73	3.81	2.97	2.57	2.22	1.70
IRAS20038-2722	17.63	12.33	9.06	6.77	5.87	4.82	3.98	3.28	2.82	2.34	1.96	1.72	1.65
IRAS20248-2825	21.56	14.71	10.97	8.51	7.15	5.65	4.80	3.89	3.34	2.88	2.45	2.09	1.87
IRAS21282+5050	29.09	23.88	20.05	16.15	14.63	11.32	10.08	8.34	7.16	5.54	5.06	3.75	2.78
IRAS21554+6204	—	28.89	—	—	—	—	—	—	6.29	—	—	—	—
IRAS22036+5306	126.75	106.05	81.89	68.46	59.55	54.05	46.75	39.92	34.22	28.34	24.36	20.75	17.03
IRC+10216	—	—	1417.77	1050.87	—	—	—	—	—	277.74	240.54	202.60	166.28
IRC+50137	—	38.34	—	—	—	—	—	—	8.00	—	—	—	—
J175521.7-293912	—	4.26	—	—	—	—	—	—	0.75	—	—	—	—
KHICYG	60.31	42.03	30.27	23.47	19.10	15.48	12.37	10.27	8.29	6.69	5.72	4.70	3.90
MGE_3222	17.58	14.23	—	—	6.87	5.82	4.74	3.71	3.04	—	—	—	—
MGE_4218	20.43	14.75	—	—	6.76	5.35	4.61	3.78	3.09	—	—	—	—
MWC922	165.19	136.63	84.68	66.81	54.91	43.03	35.39	29.84	24.53	20.50	17.34	13.90	11.97

NGC3242	18.71	14.61	11.59	10.59	9.49	7.34	6.15	5.31	4.65	3.75	2.67	1.68	1.21
NGC40	22.58	17.82	13.63	11.75	9.68	8.23	6.68	5.85	4.84	4.32	3.82	3.08	2.10
NGC6445	14.50	14.32	13.86	11.88	13.32	11.16	10.84	9.47	8.20	7.47	6.71	5.57	4.13
NGC6537	170.44	179.82	163.64	165.81	156.69	144.14	133.01	117.19	103.61	91.12	79.85	67.98	58.15
NGC6543	91.56	73.70	56.31	48.46	42.76	33.31	28.15	23.68	19.49	15.59	12.94	10.71	8.63
NGC6781	0.40	0.75	0.52	0.39	2.03	1.66	1.68	1.72	1.80	1.47	0.90	0.67	1.11
NGC6826	19.54	15.46	12.03	10.56	9.22	6.72	5.59	4.76	3.93	3.24	2.72	2.11	1.37
NGC7009	55.68	46.88	35.91	32.84	28.04	21.94	18.48	15.61	12.86	10.56	8.64	7.10	5.76
NGC7026	27.35	24.54	19.96	18.76	17.66	13.80	12.32	10.57	9.09	7.73	6.55	5.69	4.54
NMLCYG	989.81	730.48	533.98	419.44	345.99	271.93	221.25	177.52	147.39	119.40	104.42	85.85	74.37
NMLTAU	239.01	165.64	116.49	86.13	69.41	53.86	42.67	33.28	27.37	20.90	17.87	13.88	11.54
OH104.91+2.41	—	87.77	—	—	—	—	—	—	13.85	—	—	—	—
OH231.8+4.2	1115.29	946.14	730.27	624.37	530.60	437.94	384.67	324.63	270.26	233.11	200.76	171.09	150.62
OH26.5+0.6	548.32	386.73	251.79	186.50	140.27	111.70	87.85	69.16	54.97	42.87	34.87	26.97	20.26
OH30.1-0.7	190.12	144.15	103.32	78.82	64.01	46.69	35.59	27.34	20.95	15.79	12.70	9.20	7.18
OH30.7+0.4	7.31	6.90	7.05	7.55	8.98	10.82	11.83	12.49	12.81	13.10	13.04	11.88	11.52
OH32.8-0.3	193.94	139.97	89.32	64.47	48.68	35.92	27.45	20.07	14.58	10.24	7.30	3.89	1.27
OMICET	208.59	141.28	100.68	77.73	63.13	49.12	41.21	33.11	27.44	22.38	19.56	16.62	14.98
PIGRU	45.09	30.38	21.46	16.41	13.39	10.82	8.90	7.37	6.00	5.13	4.18	3.41	2.53
PNMz3	163.70	126.40	95.76	76.29	68.15	53.74	45.52	37.45	30.56	25.51	20.70	16.95	13.86
RAFGL2374	—	17.99	—	—	—	—	—	—	4.34	—	—	—	—
RAFGL4205	—	148.56	—	—	—	—	—	—	36.42	—	—	—	—

raql	33.19	24.97	—	—	11.89	9.80	8.06	6.54	5.42	—	—	—	—
RCAS	72.08	50.49	37.76	29.42	24.27	19.54	16.04	13.37	11.12	8.68	7.51	6.33	5.53
RDOR	211.99	150.63	113.16	87.23	74.93	59.53	50.36	40.87	34.67	27.39	23.83	20.27	17.06
RLep	—	—	—	8.78	—	—	—	—	2.95	—	—	—	1.46
RRAql	21.81	15.35	—	—	7.06	5.73	4.91	3.85	3.09	—	—	—	—
RTCap	3.58	2.47	2.14	1.68	1.39	1.16	0.84	0.72	0.60	0.54	0.45	0.40	0.28
SAur	—	—	—	3.42	—	—	—	—	1.52	—	—	—	0.17
sther	11.75	7.87	—	—	3.34	2.76	2.28	1.70	1.43	—	—	—	—
Tc1	6.21	5.15	3.80	2.59	2.75	2.18	1.93	1.54	1.17	0.93	0.52	0.26	0.17
TXCAM	93.91	64.78	44.35	33.66	27.22	21.99	19.18	16.26	13.36	10.60	9.10	7.44	5.94
UHya	—	—	—	3.87	—	—	—	—	1.44	—	—	—	0.37
UMon	22.07	17.66	13.27	11.31	10.13	8.43	7.12	6.24	5.58	4.74	4.48	3.93	3.12
V1300Aql	153.77	107.38	80.67	61.68	45.13	35.47	28.39	22.75	18.76	15.46	13.22	10.53	8.96
V384Per	—	—	—	12.14	—	—	—	—	4.15	—	—	—	2.35
v438oph	2.52	2.32	—	—	1.06	0.89	0.81	0.66	0.38	—	—	—	—
VCYG	35.57	25.94	19.44	14.37	12.10	9.78	7.90	6.82	6.10	4.30	3.63	2.94	2.59
VHYA	88.40	60.67	44.00	34.75	27.66	22.46	18.24	14.97	12.80	9.56	7.75	6.96	5.03
WAQL	59.24	42.99	29.33	23.72	19.30	15.15	12.20	9.95	8.10	6.29	5.12	4.15	3.54
WHYA	143.97	100.95	92.57	73.69	49.85	41.93	36.08	30.80	26.96	23.84	20.84	17.84	15.10
WOri	—	—	—	5.12	—	—	—	—	1.83	—	—	—	0.43
WXPSC	213.87	151.16	107.05	80.14	65.01	49.93	40.39	32.32	26.94	21.43	17.57	14.41	11.74
XHER	21.58	14.99	12.36	9.85	7.64	6.17	5.44	4.61	3.76	3.11	2.81	2.21	1.58

YCVn	—	—	—	6.73	—	—	—	—	2.56	—	—	—	1.09

A.7 CO transitions in the PACS range

Table A.9: ^{12}CO rotational transitions in the PACS/spectrometer range.

λ (μm)	Quantum numbers	E_u/k (K)	A_{ij}(s^{-1})	g_u
185.98	$J = 14 \rightarrow 13$	580.4965	0.00027	29
173.62	$J = 15 \rightarrow 14$	663.3613	0.00034	31
162.8	$J = 16 \rightarrow 15$	751.7329	0.00041	33
153.26	$J = 17 \rightarrow 16$	845.6078	0.00048	35
144.77	$J = 18 \rightarrow 17$	944.9828	0.00057	37
137.2	$J = 19 \rightarrow 18$	1049.8537	0.00067	39
130.38	$J = 20 \rightarrow 19$	1160.2167	0.00077	41
124.19	$J = 21 \rightarrow 20$	1276.0677	0.00088	43
118.59	$J = 22 \rightarrow 21$	1397.402	0.00101	45
113.45	$J = 23 \rightarrow 22$	1524.2152	0.00114	47
108.75	$J = 24 \rightarrow 23$	1656.5023	0.00128	49
104.43	$J = 25 \rightarrow 24$	1794.2582	0.00143	51
—	—	—	—	—
—	—	—	—	—
93.35	$J = 28 \rightarrow 27$	2240.2858	0.00194	57
90.16	$J = 29 \rightarrow 28$	2399.8625	0.00213	59
87.19	$J = 30 \rightarrow 29$	2564.8796	0.00232	61
84.41	$J = 31 \rightarrow 30$	2735.3308	0.00252	63
81.81	$J = 32 \rightarrow 31$	2911.2098	0.00274	65
79.36	$J = 33 \rightarrow 32$	3092.5095	0.00295	67
77.06	$J = 34 \rightarrow 33$	3279.2233	0.00318	69
74.89	$J = 35 \rightarrow 34$	3471.3438	0.0034	71
72.84	$J = 36 \rightarrow 35$	3668.8636	0.00364	73
70.91	$J = 37 \rightarrow 36$	3871.7755	0.00388	75
69.06	$J = 38 \rightarrow 37$	4080.0714	0.00412	77
67.35	$J = 39 \rightarrow 38$	4293.7434	0.00437	79
65.68	$J = 40 \rightarrow 39$	4512.7833	0.00461	81
64.12	$J = 41 \rightarrow 40$	4737.1828	0.00486	83
62.62	$J = 42 \rightarrow 41$	4966.9333	0.00511	85
62.62	$J = 43 \rightarrow 42$	5202.0258	0.00536	87
59.85	$J = 44 \rightarrow 43$	5442.4516	0.00561	89
58.54	$J = 45 \rightarrow 44$	5688.2012	0.00585	91

Table A.10: Parameters of the detected ^{13}CO rotational transitions.

λ (μm)	Quantum numbers	E_u/k (K)	$A_{ij}(s^{-1})$	g_u
181.608	$J = 15 \rightarrow 14$	634.21	0.000296	62
170.29	$J = 16 \rightarrow 15$	718.70	0.000357	66
160.305	$J = 17 \rightarrow 16$	808.45	0.000426	70
151.431	$J = 18 \rightarrow 17$	903.46	0.000502	74
143.494	$J = 19 \rightarrow 18$	1003.73	0.000587	78
143.494	$J = 20 \rightarrow 19$	1003.73	0.000587	78
136.351	$J = 21 \rightarrow 20$	1109.25	0.000679	82

A.8 CO in the THROES catalogue

Table A.11: Fitted CO (^{12}CO and ^{13}CO isotopologue) lines in the THROES targets: line flux (F), FWHM and continuum flux under the line.

Target Name	Molecule	Transition	F (Jy.μm)	FWHM (km s^{-1})	F_{cont} (Jy)	comment
AFGL2513	^{12}CO					
		$J = 14 \rightarrow 13$	1.02±0.08	208±12	1.3	
		$J = 15 \rightarrow 14$	0.97±0.05	194±8	2.22	
		$J = 16 \rightarrow 15$	0.95±0.05	231±10	2.51	
		$J = 17 \rightarrow 16$	1.01±0.06	220±10	2.95	
		$J = 18 \rightarrow 17$	0.69±0.05	242±14	3.37	
		$J = 19 \rightarrow 18$	0.53±0.05	221±15	3.72	
		$J = 20 \rightarrow 19$	0.98±0.06	350±17	4.14	
		$J = 21 \rightarrow 20$	0.52±0.06	270±24	4.57	
		$J = 22 \rightarrow 21$	0.47±0.03	315±17	5.21	
		$J = 23 \rightarrow 22$	0.66±0.09	371±38	5.76	
		$J = 24 \rightarrow 23$	0.35±0.05	292±33	6.34	
		$J = 25 \rightarrow 24$	0.3±0.04	322±34	7.11	
		$J = 28 \rightarrow 27$	0.19±0.04	103±15	8.24	overestimated continuum
		$J = 29 \rightarrow 28$	0.23±0.03	107±11	8.91	
		$J = 30 \rightarrow 29$	0.37±0.05	284±29	9.99	blend
		$J = 31 \rightarrow 30$	0.21±0.03	129±15	10.71	
		$J = 32 \rightarrow 31$	0.17±0.03	182±29	11.04	
		$J = 33 \rightarrow 32$	0.15±0.03	210±33	11.72	
		$J = 34 \rightarrow 33$	0.14±0.02	165±18	12.73	blend

		$J = 35 \rightarrow 34$	0.14±0.02	340±45	13.5	blend
AFGL2688	^{12}CO					
		$J = 14 \rightarrow 13$	47±1	199±4	286.7	
		$J = 15 \rightarrow 14$	36.5±0.8	196±3	316.06	
		$J = 16 \rightarrow 15$	29±1	232±7	375.33	
		$J = 17 \rightarrow 16$	20.6±0.7	210±6	435.36	
		$J = 18 \rightarrow 17$	17.6±0.5	225±5	498.06	
		$J = 19 \rightarrow 18$	13.7±0.7	237±9	566.96	
		$J = 20 \rightarrow 19$	13.9±0.7	279±10	656.39	
		$J = 21 \rightarrow 20$	8.9±0.6	270±13	736.31	
		$J = 22 \rightarrow 21$	8.4±0.7	359±22	809.42	
		$J = 23 \rightarrow 22$	5.9±0.8	284±28	876.44	
		$J = 24 \rightarrow 23$	4.2±0.8	329±49	940.46	
		$J = 25 \rightarrow 24$	2.1±0.6	124±25	1025.4	
		$J = 28 \rightarrow 27$	1.7±0.3	114±16	1329.3	
		$J = 29 \rightarrow 28$	2.9±0.6	237±35	1452.1	blend
		$J = 30 \rightarrow 29$	—	—	—	bad fit
		$J = 31 \rightarrow 30$	0.95±0.4	97±30	1601.5	
	^{13}CO					
		$J = 15 \rightarrow 14$	2±0.5	186±36	292.33	
		$J = 16 \rightarrow 15$	1.2±0.3	167±29	337.44	
		$J = 17 \rightarrow 16$	1.1±0.3	195±37	383.58	

		$J = 18 \rightarrow 17$	1.9±0.3	292±38	444.49	
		$J = 19 \rightarrow 18$	0.9±0.4	247±70	509.8	blend
		$J = 20 \rightarrow 19$	1.04±0.32	227±52	577.66	blend
AFGL3068	^{12}CO					
		$J = 14 \rightarrow 13$	2.5±0.2	199±11	17.33	
		$J = 15 \rightarrow 14$	2.1±0.1	168±8	21.76	
		$J = 16 \rightarrow 15$	2.0±0.1	226±9	25.76	
		$J = 17 \rightarrow 16$	1.9±0.1	194±12	30.81	
		$J = 18 \rightarrow 17$	1.9±0.1	254±10	36.52	
		$J = 19 \rightarrow 18$	1.6±0.1	265±16	41.92	
		$J = 20 \rightarrow 19$	2.2±0.1	337±16	47.73	
		$J = 21 \rightarrow 20$	1.2±0.1	256±22	53.58	
		$J = 22 \rightarrow 21$	1.26±0.08	332±16	58.21	
		$J = 23 \rightarrow 22$	1.1±0.3	292±52	65.23	
		$J = 24 \rightarrow 23$	0.7±0.2	271±52	72.32	
		$J = 25 \rightarrow 24$	0.5±0.2	276±78	77.08	overestimated continuum
		$J = 28 \rightarrow 27$	0.34±0.08	114±20	93.65	
		$J = 29 \rightarrow 28$	0.5±0.1	167±26	100.86	
	^{13}CO					
		$J = 15 \rightarrow 14$	0.5±0.2	101±28	18.11	
AFGL3116	^{12}CO					
		$J = 14 \rightarrow 13$	3.1±0.2	197±10	6.08	

$J = 15 \rightarrow 14$	2.9±0.2	185±9	7.78	
$J = 16 \rightarrow 15$	2.5±0.1	215±8	9.47	
$J = 17 \rightarrow 16$	3.3±0.2	226±11	11.84	
$J = 18 \rightarrow 17$	2.4±0.7	257±13	14.07	
$J = 19 \rightarrow 18$	1.9±0.1	238±9	16.6	
$J = 20 \rightarrow 19$	3.5±0.2	368±17	18.91	
$J = 21 \rightarrow 20$	2.2±0.2	335±26	21.51	
$J = 22 \rightarrow 21$	1.72±0.09	332±14	23.76	
$J = 23 \rightarrow 22$	1.9±0.4	369±57	26.85	
$J = 24 \rightarrow 23$	1.5±0.2	364±47	29.79	
$J = 25 \rightarrow 24$	1.22±0.07	320±14	32.9	
$J = 28 \rightarrow 27$	0.93±0.07	120±7	40.63	
$J = 29 \rightarrow 28$	0.89±0.08	137±9	43.64	
$J = 30 \rightarrow 29$	1.1±0.1	219±20	48.2	blend
$J = 31 \rightarrow 30$	0.69±0.08	172±15	52.57	
$J = 32 \rightarrow 31$	0.44±0.05	162±15	55.1	
$J = 33 \rightarrow 32$	0.5±0.1	174±26	59.86	
$J = 34 \rightarrow 33$	0.5±0.1	212±46	64.56	blend
$J = 35 \rightarrow 34$	0.41±0.08	212±31	69.65	
$J = 36 \rightarrow 35$	0.42±0.08	247±37	72.61	
$J = 37 \rightarrow 36$	0.5±0.2	351±87	75.48	blend
$J = 38 \rightarrow 37$	0.21±0.04	153±19	43.67	blend

		$J = 39 \rightarrow 38$	0.13±0.05	163±45	46.4	
		$J = 40 \rightarrow 39$	0.13±0.04	126±28	49.26	
	^{13}CO					
		$J = 15 \rightarrow 14$	0.4±0.2	200±63	6.44	blend
		$J = 16 \rightarrow 15$	0.57±0.04	342±17	—	blend
		$J = 17 \rightarrow 16$	0.68±0.06	228±14	10.27	
		$J = 18 \rightarrow 17$	0.7±0.4	887±486	12.12	blend
		$J = 19 \rightarrow 18$	0.29±0.06	212±33	14.48	
AFGL618	^{12}CO					
		$J = 14 \rightarrow 13$	44.82±1.1	232±4	104.25	
		$J = 15 \rightarrow 14$	33.5±1.06	205±5	123.27	
		$J = 16 \rightarrow 15$	35.53±1.3	254±7	150.63	
		$J = 17 \rightarrow 16$	28.89±0.8	235±5	178.39	
		$J = 18 \rightarrow 17$	26±1	244±7	207.77	
		$J = 19 \rightarrow 18$	25±1	268±8	238.26	
		$J = 20 \rightarrow 19$	25.18±0.65	288±6	270.43	
		$J = 21 \rightarrow 20$	18±1	252±11	308.31	
		$J = 22 \rightarrow 21$	16.9±0.9	241±10	347.16	
		$J = 23 \rightarrow 22$	19.64±1	362±14	381.98	
		$J = 24 \rightarrow 23$	11±1	308±20	418.04	blend
		$J = 25 \rightarrow 24$	11.3±0.8	332±16	456.1	
		$J = 28 \rightarrow 27$	6.1±0.3	123±4	595.16	

	$J = 29 \rightarrow 28$	6.8±0.3	146±5	648.84	
	$J = 30 \rightarrow 29$	5.0±0.4	146±8	676.29	
	$J = 31 \rightarrow 30$	6.2±0.5	174±11	724.13	
	$J = 32 \rightarrow 31$	3.8±0.4	168±13	767.98	
	$J = 33 \rightarrow 32$	3.2±0.5	160±20	800.69	blend
	$J = 34 \rightarrow 33$	3.2±0.3	178±13	868.22	
	$J = 35 \rightarrow 34$	3±0.4	226±23	917.8	
	$J = 36 \rightarrow 35$	1.9±0.2	157±12	939.72	
	$J = 37 \rightarrow 36$	2.2±0.5	252±42	955.79	blend
	$J = 38 \rightarrow 37$	1.8±0.2	227±21	1047.6	
	$J = 39 \rightarrow 38$	1.4±0.3	225±34	1090.2	
	$J = 40 \rightarrow 39$	0.8±0.4	134±45	1133.5	
	$J = 41 \rightarrow 40$	1.3±0.3	167±27	1187.4	
	$J = 42 \rightarrow 41$	4.85±2.06	709±228	1206.2	blend
	$J = 43 \rightarrow 42$	1.2±0.4	186±43	1260.5	
	$J = 44 \rightarrow 43$	0.7±0.3	148±41	1276.8	
	$J = 45 \rightarrow 44$	0.3±0.2	72±30	1319.9	
^{13}CO					
	$J = 15 \rightarrow 14$	1.6±0.2	153±15	111.08	
	$J = 16 \rightarrow 15$	1.5±0.1	229±13	131.35	
	$J = 17 \rightarrow 16$	0.9±0.3	185±40	155.99	

		$J = 18 \rightarrow 17$	1.5±0.3	288±43	183.39	
AFGL6815	^{12}CO					
		$J = 14 \rightarrow 13$	3.62±0.2	168±7	21.42	
		$J = 15 \rightarrow 14$	3.15±0.1	197±7	25.41	
		$J = 16 \rightarrow 15$	2.29±0.28	218±19	30.38	
		$J = 17 \rightarrow 16$	1.73±0.09	182±7	35.41	
		$J = 18 \rightarrow 17$	1.7±0.15	248±17	40.88	
		$J = 19 \rightarrow 18$	1.3±0.09	268±14	48.13	
		$J = 20 \rightarrow 19$	1.16±0.08	281±15	52.73	
		$J = 21 \rightarrow 20$	0.8±0.07	227±15	58.78	
		$J = 22 \rightarrow 21$	0.49±0.09	181±24	64.27	
		$J = 23 \rightarrow 22$	1.09±0.09	379±24	72.51	
		$J = 24 \rightarrow 23$	0.2±0.2	88±59	77.5	bad fit
		$J = 25 \rightarrow 24$	0.2±0.1	126±46	87.78	
CIT6	^{12}CO					
		$J = 14 \rightarrow 13$	10.3±0.3	201±5	12.45	
		$J = 15 \rightarrow 14$	7.8±0.3	180±6	15.57	
		$J = 16 \rightarrow 15$	8.2±0.4	220±9	18.99	
		$J = 17 \rightarrow 16$	8.9±0.45	220±8	22.3	
		$J = 18 \rightarrow 17$	6.7±0.5	238±13	27.02	
		$J = 19 \rightarrow 18$	5.13±0.35	221±11	32.16	
		$J = 20 \rightarrow 19$	9.2±0.5	351±14	36.54	

$J = 21 \rightarrow 20$	5.5±0.5	280±21	41.4	
$J = 22 \rightarrow 21$	5.1±0.3	337±14	45.73	
$J = 23 \rightarrow 22$	7±1	397±46	51.82	
$J = 24 \rightarrow 23$	4.5±0.7	319±35	57.3	
$J = 25 \rightarrow 24$	3.4±0.4	308±24	63.83	
$J = 28 \rightarrow 27$	2.0±0.1	92±5	78.42	
$J = 29 \rightarrow 28$	2.9±0.3	140±10	85.23	
$J = 30 \rightarrow 29$	2.5±0.2	125±9	91.54	
$J = 31 \rightarrow 30$	2.3±0.2	184±13	99.83	
$J = 32 \rightarrow 31$	1.4±0.2	129±14	106.52	
$J = 33 \rightarrow 32$	1.1±0.2	155±20	112.35	
$J = 34 \rightarrow 33$	1.7±0.2	279±30	122.64	
$J = 35 \rightarrow 34$	1.6±0.4	324±56	133.01	blend
$J = 36 \rightarrow 35$	0.8±0.2	151±22	139.47	blend
$J = 37 \rightarrow 36$	0.9±0.2	193±31	144.97	
$J = 38 \rightarrow 37$	0.6±0.06	126±10	164.23	
$J = 39 \rightarrow 38$	0.5±0.2	218±52	174.15	
$J = 40 \rightarrow 39$	0.5±0.1	249±55	182.85	blend
$J = 41 \rightarrow 40$	0.15±0.08	101±41	192.63	blend
$J = 42 \rightarrow 41$	0.3±0.1	165±55	196.52	blend
$J = 43 \rightarrow 42$	0.4±0.1	256±52	219.05	blend
$J = 44 \rightarrow 43$	0.2±0.07	165±40	229.47	blend

	^{13}CO					
		$J = 15 \rightarrow 14$	0.8±0.1	230±22	12.57	
		$J = 16 \rightarrow 15$	0.9±0.1	234±30	16.65	
		$J = 17 \rightarrow 16$	1.2±0.2	223±22	19.68	
		$J = 18 \rightarrow 17$	1.7±0.2	301±25	23.15	blend
CPD-568032	^{12}CO					
		$J = 14 \rightarrow 13$	2.7±0.1	199±6	19.37	
		$J = 15 \rightarrow 14$	2.3±0.1	200±8	25.02	
		$J = 16 \rightarrow 15$	1.9±0.1	231±12	29.94	
		$J = 17 \rightarrow 16$	1.57±0.05	202±5	35.02	
		$J = 18 \rightarrow 17$	1.31±0.06	232±9	41.23	
		$J = 19 \rightarrow 18$	1±0.06	231±11	47.85	
		$J = 20 \rightarrow 19$	1.12±0.09	266±16	54.69	
		$J = 21 \rightarrow 20$	0.88±0.08	236±17	61.39	
		$J = 22 \rightarrow 21$	0.61±0.08	250±25	68.25	
		$J = 23 \rightarrow 22$	0.81±0.09	355±30	75.03	
		$J = 24 \rightarrow 23$	0.4±0.07	303±39	82.57	
		$J = 25 \rightarrow 24$	0.5±0.1	338±61	88.95	
		$J = 28 \rightarrow 27$	0.26±0.04	115±13	108.58	
EPAqr	^{12}CO					
		$J = 14 \rightarrow 13$	0.69±0.05	216±13	2.16	
		$J = 15 \rightarrow 14$	0.61±0.04	197±9	2.61	

		$J = 16 \rightarrow 15$	1.0±0.1	388±33	2.92	blend
		$J = 17 \rightarrow 16$	0.65±0.04	254±11	3.28	
		$J = 18 \rightarrow 17$	0.9±0.3	287±62	3.86	blend
		$J = 19 \rightarrow 18$	0.72±0.06	423±27	4.36	
		$J = 20 \rightarrow 19$	0.74±0.1	739±75	5.02	blend
		$J = 21 \rightarrow 20$	0.6±0.06	639±52	5.68	blend
		$J = 22 \rightarrow 21$	1.6±0.2	331±26	6.56	
		$J = 23 \rightarrow 22$	2.6±0.3	304±25	7.26	blend
	^{13}CO					
		$J = 15 \rightarrow 14$	0.39±0.07	328±50	2.36	
		$J = 16 \rightarrow 15$	0.5±0.1	361±58	2.82	
		$J = 17 \rightarrow 16$	—	—	—	
		$J = 18 \rightarrow 17$	0.14±0.04	220±47	3.25	
		$J = 19 \rightarrow 18$	0.4±0.1	624±197	4	
		$J = 20 \rightarrow 19$	—	—	—	
		$J = 21 \rightarrow 20$	0.22±0.04	433±57	5.09	
HD235858	^{12}CO					
		$J = 14 \rightarrow 13$	1.1±0.2	190±28	4.87	
		$J = 15 \rightarrow 14$	0.9±0.1	201±25	6.26	
		$J = 16 \rightarrow 15$	0.14±0.09	163±78	7.31	overestimated continuum
		$J = 17 \rightarrow 16$	0.46±0.08	208±29	8.75	
HD44179	^{12}CO					

		$J=14 \rightarrow 13$	0.5±0.2	119±28	19.32	
		$J=15 \rightarrow 14$	0.39±0.09	139±23	24.25	
		$J=16 \rightarrow 15$	0.38±0.1	224±43	27.65	
		$J=17 \rightarrow 16$	0.41±0.07	209±28	31.92	
		$J=18 \rightarrow 17$	0.44±0.09	335±54	35.83	
		$J=19 \rightarrow 18$	0.28±0.05	192±28	40.83	
		$J=20 \rightarrow 19$	0.23±0.08	221±60	45.26	
		$J=21 \rightarrow 20$	0.23±0.06	221±41	50.21	
		$J=22 \rightarrow 21$	0.32±0.06	324±45	54.63	
		$J=23 \rightarrow 22$	0.2±0.1	238±91	59.49	
HEN2-113	^{12}CO					
		$J=14 \rightarrow 13$	2.6±0.1	197±6	15.01	
		$J=15 \rightarrow 14$	2.17±0.07	183±4	20.06	
		$J=16 \rightarrow 15$	2.0±0.5	223±38	23.8	
		$J=17 \rightarrow 16$	1.8±0.07	215±6	27.5	
		$J=18 \rightarrow 17$	1.5±0.07	222±7	32.84	
		$J=19 \rightarrow 18$	1.25±0.08	255±13	38.21	
		$J=20 \rightarrow 19$	1.26±0.08	243±11	43.55	
		$J=21 \rightarrow 20$	1.05±0.07	254±13	49.47	
		$J=22 \rightarrow 21$	1.1±0.2	450±45	55.99	blend
		$J=23 \rightarrow 22$	1.0±0.1	342±34	61.33	
		$J=24 \rightarrow 23$	0.47±0.08	266±35	67.25	

		$J = 25 \rightarrow 24$	0.58±0.08	324±35	73.5	
		$J = 28 \rightarrow 27$	0.2±0.05	115±21	90.7	
		$J = 29 \rightarrow 28$	0.12±0.01	147±6	98.4	blend
		$J = 30 \rightarrow 29$	0.11±0.04	95±28	104.48	
IRAS15194-5115	^{12}CO					
		$J = 14 \rightarrow 13$	5.0±0.4	212±13	6.69	
		$J = 15 \rightarrow 14$	3.9±0.5	184±19	8.22	
		$J = 16 \rightarrow 15$	4.5±0.2	236±7	9.38	
		$J = 17 \rightarrow 16$	3.8±0.3	220±12	11.1	
		$J = 18 \rightarrow 17$	2.6±0.4	219±23	12.59	
		$J = 19 \rightarrow 18$	2.6±0.2	242±13	14.65	
		$J = 20 \rightarrow 19$	4.2±0.3	368±22	16.6	
		$J = 21 \rightarrow 20$	2.2±0.6	302±65	18.7	
		$J = 22 \rightarrow 21$	2.04±0.4	280±41	20.88	
		$J = 23 \rightarrow 22$	2.2±0.7	355±83	23.32	
		$J = 24 \rightarrow 23$	1.8±0.7	558±171	25.68	blend
		$J = 25 \rightarrow 24$	1.39±0.3	371±61	28.23	
		$J = 28 \rightarrow 27$	0.7±0.1	91±10	35.87	blend
		$J = 29 \rightarrow 28$	0.45±0.12	126±25	38.6	
		$J = 30 \rightarrow 29$	0.8±0.21	349±69	41.94	
		$J = 31 \rightarrow 30$	0.41±0.15	180±49	45.01	
	^{13}CO					

		$J = 15 \rightarrow 14$	1.5±0.5	202±51	6.73	
		$J = 16 \rightarrow 15$	0.9±0.3	170±47	8.72	
		$J = 17 \rightarrow 16$	1.62±0.04	265±5	9.88	
		$J = 18 \rightarrow 17$	1±1	391±206	11.4	blend
		$J = 19 \rightarrow 18$	0.7±0.3	188±47	13	
		$J = 20 \rightarrow 19$	1.2±0.2	339±39	14.89	blend
		$J = 21 \rightarrow 20$	1.4±0.2	321±28	16.75	
		$J = 22 \rightarrow 21$	—	—	—	bad fit
IRAS16342-3814	^{12}CO					
		$J = 14 \rightarrow 13$	1.8±0.3	337±35	46.45	
		$J = 15 \rightarrow 14$	2.1±0.3	404±39	55.97	
		$J = 16 \rightarrow 15$	1.8±0.3	916±135	64.72	blend
		$J = 17 \rightarrow 16$	2.0±0.1	433±21	73.84	
		$J = 18 \rightarrow 17$	2.0±0.3	732±78	84.33	blend
		$J = 19 \rightarrow 18$	1.6±0.1	531±26	94.62	blend
		$J = 20 \rightarrow 19$	1.4±0.2	447±38	104.69	blend
		$J = 21 \rightarrow 20$	1.3±0.2	691±67	116.3	blend
		$J = 22 \rightarrow 21$	0.9±0.2	523±83	128.85	blend
		$J = 23 \rightarrow 22$	2.9±0.4	492±58	139.89	blend
IRAS16594-4656	^{12}CO					
		$J = 14 \rightarrow 13$	4.7±0.1	189±4	6.86	
		$J = 15 \rightarrow 14$	4.2±0.1	187±4	8.47	

		$J = 16 \rightarrow 15$	3.5±0.3	247±15	10.54	
		$J = 17 \rightarrow 16$	2.5±0.08	216±5	12.34	
		$J = 18 \rightarrow 17$	1.93±0.04	226±4	14.71	
		$J = 19 \rightarrow 18$	1.52±0.05	241±6	17.8	
		$J = 20 \rightarrow 19$	1.4±0.06	238±8	20.37	
		$J = 21 \rightarrow 20$	1.43±0.05	289±8	23.31	
		$J = 22 \rightarrow 21$	1.0±0.1	285±23	27.24	
		$J = 23 \rightarrow 22$	1.18±0.05	301±9	29.45	
		$J = 24 \rightarrow 23$	0.77±0.05	291±14	32.75	
		$J = 25 \rightarrow 24$	0.78±0.06	338±21	36.07	
		$J = 28 \rightarrow 27$	0.45±0.03	134±8	43.53	
		$J = 29 \rightarrow 28$	0.39±0.42	121±99	46.98	bad fit
		$J = 30 \rightarrow 29$	0.33±0.03	157±12	50.57	
		$J = 31 \rightarrow 30$	1.16±0.2	144±19	54.31	blend
		$J = 32 \rightarrow 31$	0.2±0.03	160±15	58.27	
		$J = 33 \rightarrow 32$	0.2±0.2	179±122	61.49	bad fit
		$J = 34 \rightarrow 33$	0.15±0.03	168±22	66.04	
		$J = 35 \rightarrow 34$	0.16±0.03	245±31	71.33	blend
IRAS19312+1950	^{12}CO					
		$J = 14 \rightarrow 13$	23±1	173±6	203.1	
		$J = 15 \rightarrow 14$	15.4±0.8	211±8	233.24	
		$J = 16 \rightarrow 15$	9.9±0.6	233±11	271.78	

		$J = 17 \rightarrow 16$	6.0±0.5	191±12	307.99	
		$J = 18 \rightarrow 17$	6.1±0.6	249±18	337.15	
		$J = 19 \rightarrow 18$	3.0±0.3	228±16	361.07	
		$J = 20 \rightarrow 19$	2.9±0.3	237±15	381.21	
		$J = 21 \rightarrow 20$	1.8±0.2	220±18	402.7	
		$J = 22 \rightarrow 21$	1.0±0.3	198±37	415.88	
		$J = 23 \rightarrow 22$	3.2±0.3	390±23	425.23	
		$J = 24 \rightarrow 23$	1.3±0.3	433±66	430.04	blend
IRAS19474-0744	^{12}CO					
		$J = 14 \rightarrow 13$	0.5±0.2	149±34	2.27	
		$J = 15 \rightarrow 14$	0.52±0.08	198±22	3.01	
		$J = 16 \rightarrow 15$	0.7±0.2	265±57	3.93	
		$J = 17 \rightarrow 16$	0.52±0.06	212±18	4.32	
		$J = 18 \rightarrow 17$	0.5±0.5	222±207	5.13	bad fit
		$J = 19 \rightarrow 18$	0.36±0.08	285±48	6.06	
		$J = 20 \rightarrow 19$	0.35±0.06	262±34	6.71	
		$J = 21 \rightarrow 20$	0.29±0.06	269±39	7.8	
		$J = 22 \rightarrow 21$	1.94±0.14	287±15	8.8	blend
		$J = 23 \rightarrow 22$	1.79±0.19	278±23	9.8	blend
		$J = 24 \rightarrow 23$	0.28±0.08	355±76	10.8	overestimated continuum
IRAS20038-2722	^{12}CO					
		$J = 14 \rightarrow 13$	0.21±0.08	154±45	1.53	

		$J = 15 \rightarrow 14$	0.33±0.1	196±47	1.46	
		$J = 16 \rightarrow 15$	—	—	—	blend
		$J = 17 \rightarrow 16$	0.26±0.06	258±49	1.98	
		$J = 18 \rightarrow 17$	0.3±0.37	253±240	2.43	
		$J = 19 \rightarrow 18$	0.31±0.07	613±106	2.57	blend
		$J = 20 \rightarrow 19$	0.40±0.13	945±247	2.96	blend
		$J = 21 \rightarrow 20$	0.21±0.08	445±122	3.33	blend
		$J = 22 \rightarrow 21$	0.78±0.15	520±74	3.8	blend
		$J = 23 \rightarrow 22$	0.9±0.1	262±27	4.2	blend
IRAS20248-2825	^{12}CO					
		$J = 14 \rightarrow 13$	0.2±0.04	128±18	1.47	
		$J = 15 \rightarrow 14$	0.35±0.07	170±25	1.82	
		$J = 16 \rightarrow 15$	0.37±0.07	285±42	2.08	blend
		$J = 17 \rightarrow 16$	0.37±0.04	231±20	2.57	
		$J = 18 \rightarrow 17$	0.31±0.26	247±159	2.85	
		$J = 19 \rightarrow 18$	0.25±0.05	304±43	3.58	
		$J = 20 \rightarrow 19$	0.27±0.05	361±49	3.88	
		$J = 21 \rightarrow 20$	0.18±0.03	272±33	4.37	
		$J = 22 \rightarrow 21$	0.89±0.08	303±21	4.97	blend
		$J = 23 \rightarrow 22$	0.49±0.04	291±17	5.47	blend
		$J = 24 \rightarrow 23$	0.17±0.04	286±51	5.76	

		$J = 25 \rightarrow 24$	0.1±0.2	564±646	6.61	blend
IRAS21282+5050	^{12}CO					
		$J = 14 \rightarrow 13$	3.43±0.07	182±3	2.63	
		$J = 15 \rightarrow 14$	2.94±0.05	188±2	3.58	
		$J = 16 \rightarrow 15$	2.14±0.05	228±4	4.39	
		$J = 17 \rightarrow 16$	1.28±0.04	207±5	5.25	
		$J = 18 \rightarrow 17$	0.73±0.05	228±12	6.27	
		$J = 19 \rightarrow 18$	0.54±0.06	277±24	7.14	
		$J = 20 \rightarrow 19$	0.33±0.05	292±33	7.98	
		$J = 21 \rightarrow 20$	0.26±0.04	375±44	9.19	
IRAS22036+5306	^{12}CO					
		$J = 14 \rightarrow 13$	1±0.12	350±33	15.14	blend
		$J = 15 \rightarrow 14$	0.9±0.1	487±40	20.18	blend
		$J = 16 \rightarrow 15$	0.71±0.16	961±172	23.24	blend
		$J = 17 \rightarrow 16$	0.73±0.07	466±36	27.14	blend
		$J = 18 \rightarrow 17$	0.72±0.08	523±45	31.43	blend
irc+10216	^{12}CO					
		$J = 14 \rightarrow 13$	99±4	184±6	156.65	
		$J = 15 \rightarrow 14$	75±6	174±10	179.31	
		$J = 16 \rightarrow 15$	79±2	226±4	220.68	
		$J = 17 \rightarrow 16$	73±4	203±7	263.07	
		$J = 18 \rightarrow 17$	57±5	180±13	313.71	

		—				
		$J = 28 \rightarrow 27$	20.01±0.62	91±2	955.73	
		$J = 29 \rightarrow 28$	20±1	110±5	1043.6	
		$J = 30 \rightarrow 29$	14±2	98±9	1152.2	
		$J = 31 \rightarrow 30$	14±2	143±13	1252.9	
		$J = 32 \rightarrow 31$	8±2	111±18	1344.2	
		$J = 33 \rightarrow 32$	9±2	164±22	1436.7	
		$J = 34 \rightarrow 33$	8±2	166±27	1570.2	
		$J = 35 \rightarrow 34$	6±1	155±27	1702.8	blend
		$J = 36 \rightarrow 35$	3±1	160±42	1833.8	
		$J = 37 \rightarrow 36$	3±1	131±28	1883.5	
	^{13}CO					
		$J = 15 \rightarrow 14$	13±1	197±12	159.77	
		$J = 16 \rightarrow 15$	10.1±0.6	209±10	191.06	
		$J = 17 \rightarrow 16$	16±4	245±44	230.54	
		$J = 18 \rightarrow 17$	11±6	358±153	273.26	
		$J = 19 \rightarrow 18$	6±3	197±80	323.52	
KHICYG	^{12}CO					
		$J = 14 \rightarrow 13$	2.5±0.2	162±8	4.11	
		$J = 15 \rightarrow 14$	2.9±0.2	194±11	4.4	
		$J = 16 \rightarrow 15$	2.9±0.1	220±6	5.43	
		$J = 17 \rightarrow 16$	2.42±0.08	204±5	6.3	

$J = 18 \rightarrow 17$	2.59±0.4	237±28	7.5	
$J = 19 \rightarrow 18$	2.1±0.07	250±6	8.64	
$J = 20 \rightarrow 19$	2.5±0.1	290±10	10.21	
$J = 21 \rightarrow 20$	1.7±0.1	266±13	11.37	
$J = 22 \rightarrow 21$	1.93±0.06	300±7	12.66	
$J = 23 \rightarrow 22$	4.6±0.2	390±13	14.11	
$J = 24 \rightarrow 23$	1.6±0.1	286±15	16.02	
$J = 25 \rightarrow 24$	1.4±0.2	356±29	17.5	
$J = 28 \rightarrow 27$	1.02±0.07	126±6	21.68	
$J = 29 \rightarrow 28$	1.0±0.2	113±20	23.36	
$J = 30 \rightarrow 29$	0.71±0.06	130±8	24.63	
$J = 31 \rightarrow 30$	1.0±0.1	149±13	27.03	
$J = 32 \rightarrow 31$	0.5±0.3	126±52	28.8	
$J = 33 \rightarrow 32$	0.5±0.15	142±31	30.69	
$J = 34 \rightarrow 33$	0.5±0.05	171±12	32.78	
$J = 35 \rightarrow 34$	1.4±0.4	339±72	36.08	
$J = 36 \rightarrow 35$	0.44±0.09	194±31	37.34	
$J = 37 \rightarrow 36$	0.3±0.1	110±49	37.82	
$J = 38 \rightarrow 37$	0.23±0.05	178±27	43.67	
$J = 39 \rightarrow 38$	1.1±0.3	499±106	46.4	blend
$J = 40 \rightarrow 39$	0.13±0.17	149±144	49.26	
$J = 41 \rightarrow 40$	0.06±0.09	87±89	51.59	

	^{13}CO					
		$J = 15 \rightarrow 14$	0.2±0.1	88±48	3.74	bad fit
		$J = 16 \rightarrow 15$	0.45±0.06	269±29	4.67	blend
		$J = 17 \rightarrow 16$	0.35±0.04	187±17	5.69	
		$J = 18 \rightarrow 17$	0.28±0.04	173±21	6.5	
		$J = 19 \rightarrow 18$	0.28±0.04	363±39	7.76	blend
NGC6537	^{12}CO					
		$J = 14 \rightarrow 13$	3.6±0.32	197±13	52.06	
		$J = 15 \rightarrow 14$	3.54±0.33	208±15	64.03	
		$J = 16 \rightarrow 15$	2.15±0.32	198±22	76.52	
		$J = 17 \rightarrow 16$	2.39±0.27	266±23	86.87	
		$J = 18 \rightarrow 17$	1.41±0.14	236±18	97.89	
		$J = 19 \rightarrow 18$	0.82±0.1	234±22	107.65	
		$J = 20 \rightarrow 19$	0.77±0.14	253±35	116.5	
		$J = 21 \rightarrow 20$	0.38±0.09	172±30	126.1	
NMLCYG	^{12}CO					
		$J = 14 \rightarrow 13$	4.4±0.4	173±10	67.61	
		$J = 15 \rightarrow 14$	4.3±0.3	178±8	81.15	
		$J = 16 \rightarrow 15$	4.6±0.4	230±13	99.19	
		$J = 17 \rightarrow 16$	4.1±0.2	186±8	113.54	
		$J = 18 \rightarrow 17$	5.4±0.6	253±23	132.24	
		$J = 19 \rightarrow 18$	2.8±0.3	234±22	154.97	

		$J = 20 \rightarrow 19$	3.6±0.6	265±34	176.34	
		$J = 21 \rightarrow 20$	2.2±0.7	208±52	208.58	
		$J = 22 \rightarrow 21$	4.5±0.9	726±112	227.61	blend
		$J = 23 \rightarrow 22$	14.02±3.23	313±55	257.36	blend
		$J = 24 \rightarrow 23$	2.15±0.32	168±19	278.48	
		$J = 25 \rightarrow 24$	—	—	—	blend; bad fit
		$J = 28 \rightarrow 27$	3±2	503±371	382	blend
		$J = 29 \rightarrow 28$	1±2	122±207	419.13	
		$J = 30 \rightarrow 29$	0.46±0.15	60±15	448	
		$J = 31 \rightarrow 30$	1.63±1.35	110±69	484.94	
		$J = 32 \rightarrow 31$	0.28±2	65±261	509.97	bad fit
		$J = 33 \rightarrow 32$	1±2	158±250	542.22	
		$J = 34 \rightarrow 33$	0.23±0.3	90±91	574.28	
		$J = 35 \rightarrow 34$	9±2	176±33	618.08	blend
		$J = 36 \rightarrow 35$	6±1	1482±265	650.23	blend
NMLTAU	^{12}CO					
		$J = 14 \rightarrow 13$	4.1±0.3	201±9	10.43	
		$J = 15 \rightarrow 14$	3.8±0.2	175±8	13.85	
		$J = 16 \rightarrow 15$	3.6±0.2	254±11	16.71	
		$J = 17 \rightarrow 16$	3.4±0.1	203±7	19.34	
		$J = 18 \rightarrow 17$	3.9±0.4	266±21	23.7	
		$J = 19 \rightarrow 18$	2.4±0.2	228±14	28.43	

		$J = 20 \rightarrow 19$	2.7±0.3	288±21	32.86	
		$J = 21 \rightarrow 20$	1.8±0.4	258±43	38.5	
		$J = 22 \rightarrow 21$	2.5±0.4	302±34	43.95	
		$J = 23 \rightarrow 22$	3.4±0.2	336±13	50.32	blend
		$J = 24 \rightarrow 23$	1.4±0.2	224±22	55.23	
		$J = 25 \rightarrow 24$	0.8±1.4	326±460	62.48	overestimated continuum
		$J = 28 \rightarrow 27$	0.1±0.6	64±212	77.64	bad fit
		$J = 29 \rightarrow 28$	0.5±1	80±134	85.73	bad fit
		$J = 30 \rightarrow 29$	0.73±0.1	181±21	93.39	
		$J = 31 \rightarrow 30$	1.17±0.88	319±182	103.41	blend
		$J = 32 \rightarrow 31$	0.3±1	146±434	110.04	bad fit
		$J = 33 \rightarrow 32$	0.49±0.9	190±256	118.87	bad fit
		$J = 34 \rightarrow 33$	0.2±0.1	122±52	127.32	
		$J = 35 \rightarrow 34$	3.9±1.35	160±42	139.93	blend
		$J = 36 \rightarrow 35$	2.5±0.5	473±69	147.72	blend
	^{13}CO					
		$J = 15 \rightarrow 14$	0.8±0.2	203±41	11.38	
		$J = 16 \rightarrow 15$	—	—	—	blend; bad fit
		$J = 17 \rightarrow 16$	0.5±0.3	135±62	18.1	bad fit
		$J = 18 \rightarrow 17$	0.4±0.1	168±34	20.05	
		$J = 19 \rightarrow 18$	0.5±0.1	274±41	24.41	
PIGRU	^{12}CO					

$J = 14 \rightarrow 13$	4.3±0.1	184±5	2.99	
$J = 15 \rightarrow 14$	3.7±0.2	187±6	3.12	
$J = 16 \rightarrow 15$	3.6±0.1	241±7	3.84	
$J = 17 \rightarrow 16$	3.4±0.08	215±4	4.88	
$J = 18 \rightarrow 17$	3.1±0.2	235±11	5.52	
$J = 19 \rightarrow 18$	2.74±0.07	250±5	6.44	
$J = 20 \rightarrow 19$	2.7±0.1	261±8	7.37	
$J = 21 \rightarrow 20$	2.46±0.1	290±9	8.1	
$J = 22 \rightarrow 21$	2.23±0.06	290±6	9.18	
$J = 23 \rightarrow 22$	3.89±0.15	380±11	10.4	
$J = 24 \rightarrow 23$	1.9±0.1	309±13	11.11	
$J = 25 \rightarrow 24$	1.74±0.12	304±15	12.2	
$J = 28 \rightarrow 27$	1.12±0.05	112±4	15.22	
$J = 29 \rightarrow 28$	0.9±0.1	120±13	16.27	
$J = 30 \rightarrow 29$	1.01±0.06	139±6	18.06	
$J = 31 \rightarrow 30$	1.05±0.1	139±10	19.24	
$J = 32 \rightarrow 31$	0.7±0.2	139±30	20.69	
$J = 33 \rightarrow 32$	0.61±0.1	145±19	21.7	
$J = 34 \rightarrow 33$	0.53±0.04	150±8	23.95	
$J = 35 \rightarrow 34$	1.2±0.3	382±71	25.85	blend
$J = 36 \rightarrow 35$	0.46±0.05	167±15	27.39	
$J = 37 \rightarrow 36$	0.2±0.1	138±65	29.77	

		$J = 38 \rightarrow 37$	0.31±0.03	177±14	31.66	
		$J = 39 \rightarrow 38$	—	—	—	blend; bad fit
		$J = 40 \rightarrow 39$	0.2±0.2	233±128	35.62	
		$J = 41 \rightarrow 40$	0.17±0.08	172±61	37.58	
		$J = 42 \rightarrow 41$	0.05±0.1	74±107	39.12	overestimated continuum
		$J = 43 \rightarrow 42$	0.21±0.06	197±47	43.18	overestimated continuum
		$J = 44 \rightarrow 43$	0.13±0.08	186±80	45.23	
OH26.5+0.6	^{12}CO					
		$J = 14 \rightarrow 13$	0.42±0.31	213±119	18.82	blend
		$J = 15 \rightarrow 14$	0.63±0.15	245±43	25.67	
		$J = 16 \rightarrow 15$	—	—	—	blend; bad fit
		$J = 17 \rightarrow 16$	0.8±0.1	203±23	40.16	
		$J = 18 \rightarrow 17$	1.±0.7	284±117	48.19	
		$J = 19 \rightarrow 18$	0.1±0.5	134±388	59.32	overestimated continuum
		$J = 20 \rightarrow 19$	0.3±0.2	172±73	68.59	
		$J = 21 \rightarrow 20$	—	—	—	blend; bad fit
		$J = 22 \rightarrow 21$	0.2±0.2	137±86	91.04	overestimated continuum
		$J = 23 \rightarrow 22$	2.0±1	284±135	103.01	blend
		$J = 24 \rightarrow 23$	0.5±0.1	203±41	114.83	
OMICET	^{12}CO					
		$J = 14 \rightarrow 13$	3.4±0.2	180±8	11.68	
		$J = 15 \rightarrow 14$	3.2±0.3	183±11	15.7	

	$J = 16 \rightarrow 15$	3.5±0.4	245±22	18.54	
	$J = 17 \rightarrow 16$	2.8±0.2	200±8	21.15	
	$J = 18 \rightarrow 17$	2.7±0.5	226±28	24.88	
	$J = 19 \rightarrow 18$	2.0±0.2	253±21	29.36	
	$J = 20 \rightarrow 19$	2.3±0.2	309±20	32.78	
	$J = 21 \rightarrow 20$	1.5±0.2	256±24	36.93	
	$J = 22 \rightarrow 21$	8.7±0.6	313±15	42.58	blend
	$J = 23 \rightarrow 22$	2.6±0.5	355±49	46.95	
	$J = 24 \rightarrow 23$	1.7±0.2	322±35	50.47	overestimated continuum
	$J = 25 \rightarrow 24$	0.6±0.4	328±159	57.14	overestimated continuum
	$J = 28 \rightarrow 27$	1.5±0.2	162±17	68.76	
	$J = 29 \rightarrow 28$	0.7±1	105±141	77.6	bad fit
	$J = 30 \rightarrow 29$	0.5±0.2	147±47	85.1	
	$J = 31 \rightarrow 30$	1.0±0.3	142±33	91.05	
	$J = 32 \rightarrow 31$	0.4±0.4	136±98	97.44	
	$J = 33 \rightarrow 32$	0.5±0.5	128±95	103.41	
	$J = 34 \rightarrow 33$	0.5±0.2	142±54	109.48	
^{13}CO					
	$J = 15 \rightarrow 14$	1.18±0.22	191±26	14.51	blend
	$J = 16 \rightarrow 15$	0.9±0.1	182±17	16.77	
	$J = 17 \rightarrow 16$	0.5±0.1	152±24	19.55	
	$J = 18 \rightarrow 17$	0.5±0.1	151±29	21.37	overestimated continuum

		$J = 19 \rightarrow 18$	0.61±0.07	353±32	25.33	
		$J = 20 \rightarrow 19$	1.5±0.3	599±87	30.05	blend
		$J = 21 \rightarrow 20$	0.3±0.1	215±85	33.12	
RCAS	^{12}CO					
		$J = 14 \rightarrow 13$	1.7±0.1	195±13	4.51	
		$J = 15 \rightarrow 14$	1.5±0.07	176±6	5.93	
		$J = 16 \rightarrow 15$	1.46±0.08	243±10	7.01	
		$J = 17 \rightarrow 16$	1.24±0.09	206±12	8.48	
		$J = 18 \rightarrow 17$	1.3±0.1	264±19	10.04	
		$J = 19 \rightarrow 18$	0.87±0.07	244±15	11.84	
		$J = 20 \rightarrow 19$	0.97±0.09	308±22	13.24	
		$J = 21 \rightarrow 20$	0.68±0.07	292±22	14.61	
		$J = 22 \rightarrow 21$	1.4±0.1	307±16	16.47	
		$J = 23 \rightarrow 22$	5.3±0.3	303±13	18.11	blend
		$J = 24 \rightarrow 23$	0.41±0.06	244±28	20.18	
		$J = 25 \rightarrow 24$	0.31±0.3	466±340	21.86	bad fit
		$J = 28 \rightarrow 27$	0.58±0.06	175±14	26.78	
		$J = 29 \rightarrow 28$	0.1±0.5	99±273	29.27	
		$J = 30 \rightarrow 29$	0.19±0.05	118±25	32.01	
		$J = 31 \rightarrow 30$	0.5±0.2	350±93	34.12	blend
	^{13}CO					
		$J = 15 \rightarrow 14$	0.4±0.1	165±43	5.09	

		$J=16\rightarrow15$	0.4±0.3	551±311	6.28	blend
RDOR	^{12}CO					
		$J=14\rightarrow13$	2.7±0.15	181±8	15.68	
		$J=15\rightarrow14$	3.3±0.2	225±11	19.29	
		$J=16\rightarrow15$	3.5±0.9	290±55	22.28	
		$J=17\rightarrow16$	3.3±0.5	236±27	26.06	
		$J=18\rightarrow17$	3.5±0.3	261±9	31.31	blend; bad fit
		$J=19\rightarrow18$	3.01±0.59	352±53	34.82	
		$J=20\rightarrow19$	3.45±0.98	414±90	38.66	blend
		$J=21\rightarrow20$	2.6±0.5	367±55	44.22	
		$J=22\rightarrow21$	7±2	288±60	50.12	
		$J=23\rightarrow22$	14±2	308±30	54.8	blend
		$J=24\rightarrow23$	2.7±0.5	366±49	59.86	
		$J=25\rightarrow24$	—	—	—	bad fit
		$J=28\rightarrow27$	2.6±0.5	179±26	82.17	
		$J=29\rightarrow28$	—	—	—	bad fit
	^{13}CO					
		$J=15\rightarrow14$	1.4±0.2	314±33	16.47	blend
		$J=16\rightarrow15$	2±1	693±366	20.22	blend
		$J=17\rightarrow16$	—	—	—	blend
		$J=18\rightarrow17$	—	—	—	bad fit

		$J = 19 \rightarrow 18$	1.1±0.3	412±92	31	blend
TXCAM	^{12}CO					
		$J = 14 \rightarrow 13$	2.3±0.2	198±15	4.54	
		$J = 15 \rightarrow 14$	2.2±0.2	174±15	6.87	
		$J = 16 \rightarrow 15$	1.6±0.3	257±32	8.54	blend
		$J = 17 \rightarrow 16$	1.6±0.2	208±14	10	
		$J = 18 \rightarrow 17$	2±1	267±131	11.49	
		$J = 19 \rightarrow 18$	0.9±0.2	245±29	14.26	
		$J = 20 \rightarrow 19$	0.9±0.15	329±42	15.82	
		$J = 21 \rightarrow 20$	—	—	—	blend; bad fit
		$J = 22 \rightarrow 21$	1.6±0.2	309±24	19.15	
		$J = 23 \rightarrow 22$	3.2±0.4	247±21	20.49	blend
VCYG	^{12}CO					
		$J = 14 \rightarrow 13$	2.1±0.3	159±15	2.38	
		$J = 15 \rightarrow 14$	1.9±0.1	169±9	2.49	
		$J = 16 \rightarrow 15$	2.3±0.1	212±9	3.43	
		$J = 17 \rightarrow 16$	1.8±0.1	175±8	4.06	
		$J = 18 \rightarrow 17$	1.9±0.09	234±9	4.71	
		$J = 19 \rightarrow 18$	1.68±0.1	231±12	6.11	
		$J = 20 \rightarrow 19$	2.19±0.15	299±15	6.72	
		$J = 21 \rightarrow 20$	1.4±0.1	254±15	7.58	
		$J = 22 \rightarrow 21$	1.25±0.09	259±13	7.9	

		$J = 23 \rightarrow 22$	1.8±0.2	406±29	9.06	
		$J = 24 \rightarrow 23$	0.8±0.1	194±20	10.16	
		$J = 25 \rightarrow 24$	0.9±0.1	312±33	11.23	blend
		$J = 28 \rightarrow 27$	0.34±0.06	104±14	13.46	
		$J = 29 \rightarrow 28$	0.49±0.06	103±10	14.74	
		$J = 30 \rightarrow 29$	0.5±0.1	269±39	16.35	blend
		$J = 31 \rightarrow 30$	0.39±0.07	122±16	16.95	
		$J = 32 \rightarrow 31$	0.22±0.07	96±22	18.15	
		$J = 33 \rightarrow 32$	0.2±0.07	161±41	19.47	
		$J = 34 \rightarrow 33$	0.23±0.05	290±52	20.74	blend
		$J = 35 \rightarrow 34$	0.22±0.06	206±40	21.97	
VHYA	^{12}CO					
		$J = 14 \rightarrow 13$	4.9±0.2	222±6	4.22	
		$J = 15 \rightarrow 14$	4.6±0.1	204±4	6.34	
		$J = 16 \rightarrow 15$	4.93±0.09	267±4	7.36	
		$J = 17 \rightarrow 16$	4.8±0.2	238±7	8.94	
		$J = 18 \rightarrow 17$	3.7±0.1	263±8	11.07	
		$J = 19 \rightarrow 18$	3.1±0.1	246±6	13.5	
		$J = 20 \rightarrow 19$	5.1±0.2	356±9	14.84	
		$J = 21 \rightarrow 20$	3.3±0.15	316±11	17.02	
		$J = 22 \rightarrow 21$	2.8±0.1	315±10	18.82	
		$J = 23 \rightarrow 22$	3.8±0.4	403±35	20.75	

		$J = 24 \rightarrow 23$	2.2±0.2	333±23	23	
		$J = 25 \rightarrow 24$	2.1±0.2	374±23	25.31	
		$J = 28 \rightarrow 27$	1.54±0.08	158±6	31.46	
		$J = 29 \rightarrow 28$	1.5±0.1	168±9	34.59	
		$J = 30 \rightarrow 29$	1.6±0.1	231±15	36.38	blend
		$J = 31 \rightarrow 30$	1.16±0.08	206±11	39.25	
		$J = 32 \rightarrow 31$	0.9±0.1	171±19	42.13	
		$J = 33 \rightarrow 32$	1.1±0.1	238±19	44.98	
		$J = 34 \rightarrow 33$	0.92±0.07	262±16	47.69	
		$J = 35 \rightarrow 34$	0.74±0.15	266±40	52.31	
		$J = 36 \rightarrow 35$	0.58±0.05	205±13	54.1	
		$J = 37 \rightarrow 36$	0.51±0.09	253±36	56.44	blend
		$J = 38 \rightarrow 37$	0.45±0.05	236±21	63.92	
		$J = 39 \rightarrow 38$	0.38±0.08	240±38	67.59	blend
		$J = 40 \rightarrow 39$	0.41±0.1	271±48	70.34	
		$J = 41 \rightarrow 40$	0.2±0.05	175±35	74.41	
		$J = 42 \rightarrow 41$	0.12±0.06	120±47	75.48	blend
		$J = 43 \rightarrow 42$	0.23±0.06	264±48	85.15	blend
		$J = 44 \rightarrow 43$	0.22±0.06	280±53	88.46	
V1300Aql	^{12}CO					
		$J = 14 \rightarrow 13$	0.82±0.07	177±12	7.95	
		$J = 15 \rightarrow 14$	1.01±0.07	195±11	9.89	

		$J = 16 \rightarrow 15$	0.89±0.35	250±73	12.66	
		$J = 17 \rightarrow 16$	0.81±0.04	210±8	14.3	
		$J = 18 \rightarrow 17$	1±0.5	248±96	17.12	
		$J = 19 \rightarrow 18$	0.49±0.04	260±15	19.81	
		$J = 20 \rightarrow 19$	0.56±0.05	303±21	22.56	
		$J = 21 \rightarrow 20$	0.4±0.05	262±27	26.15	overestimated continuum
		$J = 22 \rightarrow 21$	0.49±0.09	307±44	29.3	overestimated continuum
		$J = 23 \rightarrow 22$	1.88±0.46	294±55	33.11	blend
		$J = 24 \rightarrow 23$	0.59±0.04	259±15	36.41	
		$J = 25 \rightarrow 24$	0.03±0.01	852±178	39.98	blend
		$J = 28 \rightarrow 27$	1.04±0.05	162±5	56.19	blend
		$J = 29 \rightarrow 28$	0.15±0.3	124±189	61.47	
		$J = 30 \rightarrow 29$	0.13±0.03	93±14	66.57	
		$J = 31 \rightarrow 30$	0.3±0.3	344±215	71.99	blend
WAQL	^{12}CO					
		$J = 14 \rightarrow 13$	4.27±0.19	195±7	2.82	
		$J = 15 \rightarrow 14$	3.4±0.1	191±4	3.86	
		$J = 16 \rightarrow 15$	3.9±0.16	223±7	4.89	
		$J = 17 \rightarrow 16$	3.6±0.1	207±6	5.88	
		$J = 18 \rightarrow 17$	3.09±0.19	237±11	7.25	
		$J = 19 \rightarrow 18$	2.72±0.08	245±5	8.56	
		$J = 20 \rightarrow 19$	3.2±0.1	289±8	9.86	

		$J = 21 \rightarrow 20$	2.8±0.2	303±17	11.26	
		$J = 22 \rightarrow 21$	2.3±0.08	277±8	12.61	
		$J = 23 \rightarrow 22$	3.4±0.1	394±12	14.03	
		$J = 24 \rightarrow 23$	1.59±0.08	275±11	15.62	
		$J = 25 \rightarrow 24$	1.49±0.1	307±15	17.04	
		$J = 28 \rightarrow 27$	0.85±0.05	113±5	20.51	
		$J = 29 \rightarrow 28$	0.9±0.2	122±15	23.47	
		$J = 30 \rightarrow 29$	0.74±0.06	159±10	25.64	
		$J = 31 \rightarrow 30$	0.61±0.08	126±13	28.15	
		$J = 32 \rightarrow 31$	0.4±0.1	139±32	28.88	
		$J = 33 \rightarrow 32$	0.36±0.06	155±20	29.58	
		$J = 34 \rightarrow 33$	0.31±0.04	151±13	32.11	
		$J = 35 \rightarrow 34$	0.5±0.3	340±138	35.98	blend
		$J = 36 \rightarrow 35$	0.19±0.06	191±42	38.63	
		$J = 37 \rightarrow 36$	0.11±0.08	87±45	37.9	
		$J = 38 \rightarrow 37$	0.13±0.03	200±39	43.33	
WHYA	^{12}CO					
		$J = 14 \rightarrow 13$	2.55±0.3	197±15	14.07	
		$J = 15 \rightarrow 14$	3.05±0.3	230±17	16.81	
		$J = 16 \rightarrow 15$	—	—	—	blend; bad fit
		$J = 17 \rightarrow 16$	2.44±0.2	217±15	22.68	
		$J = 18 \rightarrow 17$	3.0±2	273±159	26	

		$J = 19 \rightarrow 18$	1.9±0.3	356±37	26.69	blend
		$J = 20 \rightarrow 19$	3.4±0.4	809±73	29.1	blend
		$J = 21 \rightarrow 20$	1.5±0.2	478±56	31.93	
		$J = 22 \rightarrow 21$	4.7±0.6	320±29	35.58	blend
		$J = 23 \rightarrow 22$	7.1±0.7	333±25	38.28	blend
		$J = 24 \rightarrow 23$	1.4±0.2	495±62	41.33	
		$J = 25 \rightarrow 24$	0.2±0.2	132±94	44.63	blend
		$J = 28 \rightarrow 27$	2.0±0.3	182±19	66.79	
		$J = 29 \rightarrow 28$	1±2	146±321	73.19	bad fit
		$J = 30 \rightarrow 29$	0.4±0.2	123±39	79.17	
		$J = 31 \rightarrow 30$	0.6±0.4	109±51	85.61	
		$J = 32 \rightarrow 31$	0.5±1	130±225	90.43	bad fit
		$J = 33 \rightarrow 32$	0.7±0.7	146±108	93.53	
		$J = 34 \rightarrow 33$	0.2±0.2	109±72	100.37	
WXPSC	^{12}CO					
		$J = 14 \rightarrow 13$	2±0.23	197±17	9.94	
		$J = 15 \rightarrow 14$	1.25±0.11	156±10	13.83	
		$J = 16 \rightarrow 15$	1.29±0.52	234±70	16.67	
		$J = 17 \rightarrow 16$	1.26±0.12	216±16	19.5	
		$J = 18 \rightarrow 17$	1.17±0.97	205±130	24.18	
		$J = 19 \rightarrow 18$	1.05±0.13	305±30	27.24	
		$J = 20 \rightarrow 19$	1.29±0.21	337±42	31.04	

		$J = 21 \rightarrow 20$	0.8±0.19	264±48	35.91	
		$J = 22 \rightarrow 21$	1.54±0.32	757±120	40.94	blend
		$J = 23 \rightarrow 22$	2.69±0.23	332±22	45.85	blend
		$J = 24 \rightarrow 23$	0.95±0.12	337±33	50.24	
		$J = 25 \rightarrow 24$	0.25±0.35	126±131	56.44	blend; bad fit
XHER	^{12}CO					
		$J = 14 \rightarrow 13$	0.5±0.1	136±24	1.76	
		$J = 15 \rightarrow 14$	0.3±0.1	160±39	1.93	
		$J = 16 \rightarrow 15$	0.4±0.1	273±56	2.59	
		$J = 17 \rightarrow 16$	0.39±0.09	159±27	3.09	
		$J = 18 \rightarrow 17$	0.6±0.4	248±122	3.02	blend
		$J = 19 \rightarrow 18$	0.33±0.07	303±50	4.14	blend
		$J = 20 \rightarrow 19$	0.3±0.1	501±157	4.59	
		$J = 21 \rightarrow 20$	0.2±0.1	103±37	4.82	blend

A.9 Rotational diagram results

Table A.12: Results of the rotational diagram using least-squares without weights and no opacity correction.

unweighted least-squares					
Target Name	T (K)	N (molecules)	N^{col} (cm^{-2})	M_{H_2} ($M_\odot$)	C_τ
CIT 6	723±26	$6.3(\pm0.9)\times10^{49}$	$1.3(\pm0.2)\times10^{17}$	$1.4(\pm0.2)\times10^{-4}$	no
AFGL 3116	699± 23	$5.6(\pm0.7)\times10^{49}$	$9(\pm1)\times10^{16}$	$1.2(\pm0.2)\times10^{-4}$	no
AFGL 2688	367± 25	$2.3(\pm0.6)\times10^{50}$	$1.3(\pm0.3)\times10^{18}$	$5(\pm2)\times10^{-4}$	no
AFGL 618	732± 36	$1.0(\pm0.2)\times10^{51}$	$7(\pm2)\times10^{17}$	$2.0(\pm0.5)\times10^{-3}$	no
IRAS 21282+5050	176± 7	$4.3(\pm0.9)\times10^{51}$	$1.7(\pm0.3)\times10^{17}$	$9(\pm2)\times10^{-3}$	no
CPD 568032	387± 22	$2.6(\pm0.5)\times10^{50}$	$3.3(\pm0.7)\times10^{16}$	$6(\pm1)\times10^{-4}$	no
IRC+10216	564±14	$6.8(\pm0.8)\times10^{49}$	$1.7(\pm0.2)\times10^{18}$	$1.4(\pm0.2)\times10^{-4}$	no
AFGL 3068	460±28	$2.4(\pm0.5)\times10^{50}$	$9(\pm2)\times10^{16}$	$5.3(\pm0.8)\times10^{-4}$	no
V CYG	580±24	$1.5(\pm0.2)\times10^{49}$	$7(\pm1)\times10^{16}$	$3.2(\pm0.5)\times10^{-5}$	no
AFGL 2513	641±35	$1.4(\pm0.3)\times10^{50}$	$2.8(\pm0.5)\times10^{16}$	$2.9(\pm0.5)\times10^{-4}$	no
HD 44179	431±38	$1.5(\pm0.4)\times10^{49}$	$1.9(\pm0.5)\times10^{16}$	$3(\pm0.8)\times10^{-5}$	no
IRAS 16594	503±24	$4.0(\pm0.8)\times10^{50}$	$1.0(\pm0.2)\times10^{17}$	$8.3(\pm2)\times10^{-4}$	no
V Hya	774±25	$5.0(\pm0.6)\times10^{49}$	$1.3(\pm0.2)\times10^{17}$	$1.1(\pm0.2)\times10^{-4}$	no
IRAS 15194	481±21	$6(\pm1)\times10^{49}$	$1.6(\pm0.3)\times10^{17}$	$1.4(\pm0.2)\times10^{-4}$	no

Chapter B

Appendice of figures

B.1 PACS/spectrometer PSF version 3

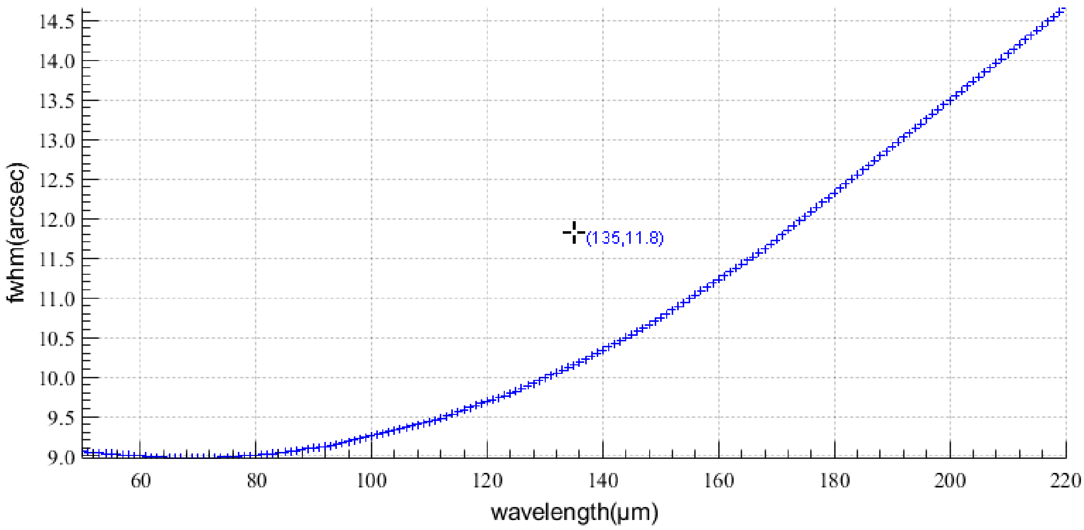

Fig. B.1: PACS spectrometer FWHM as a function of the wavelength, derived for a previous version of the calibration files and obtained from the HSA.

B.2 Photometry maps fitting

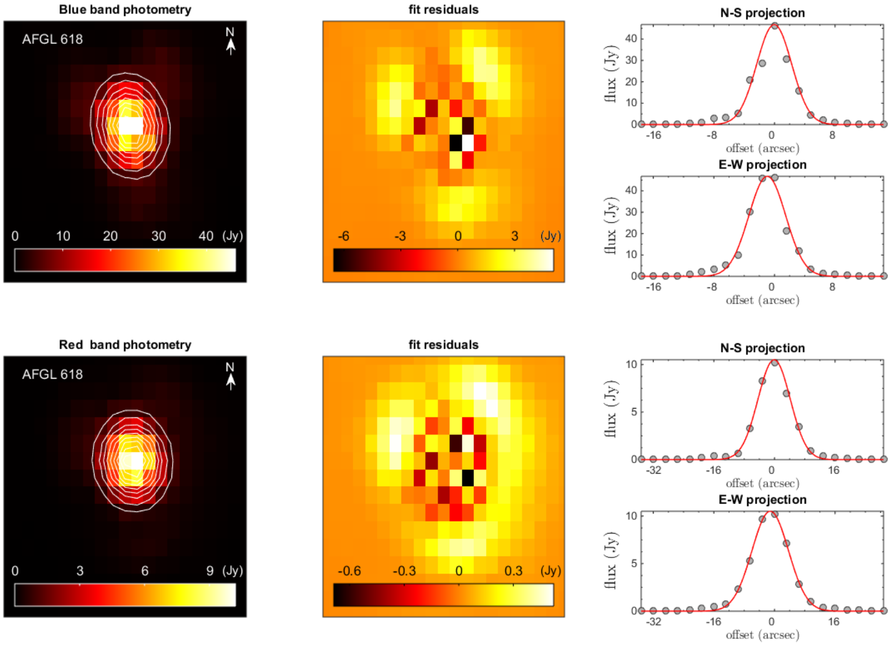

Fig. B.2.2: 2D-Gaussian model of AFGL 618 in the blue and red bands.

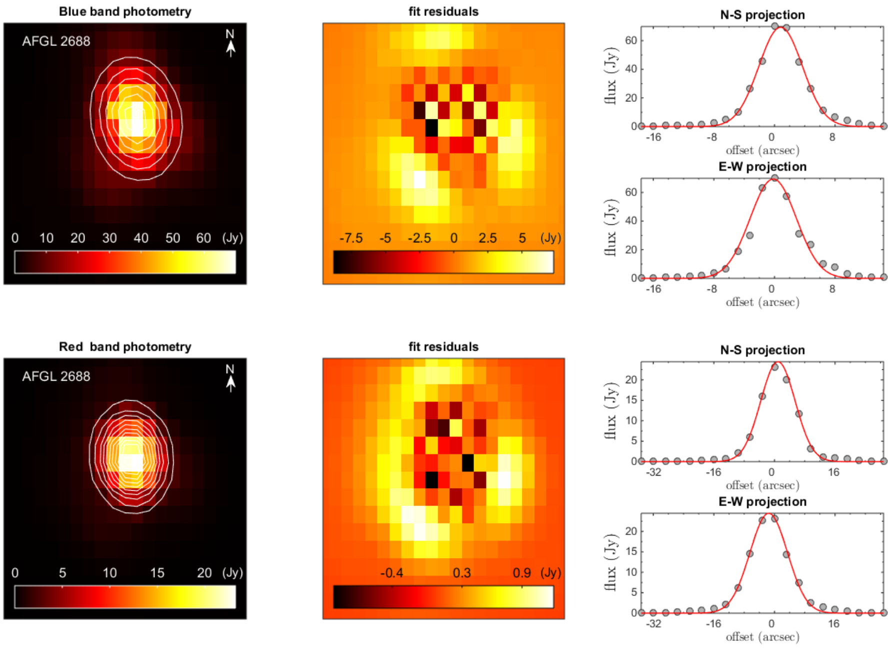

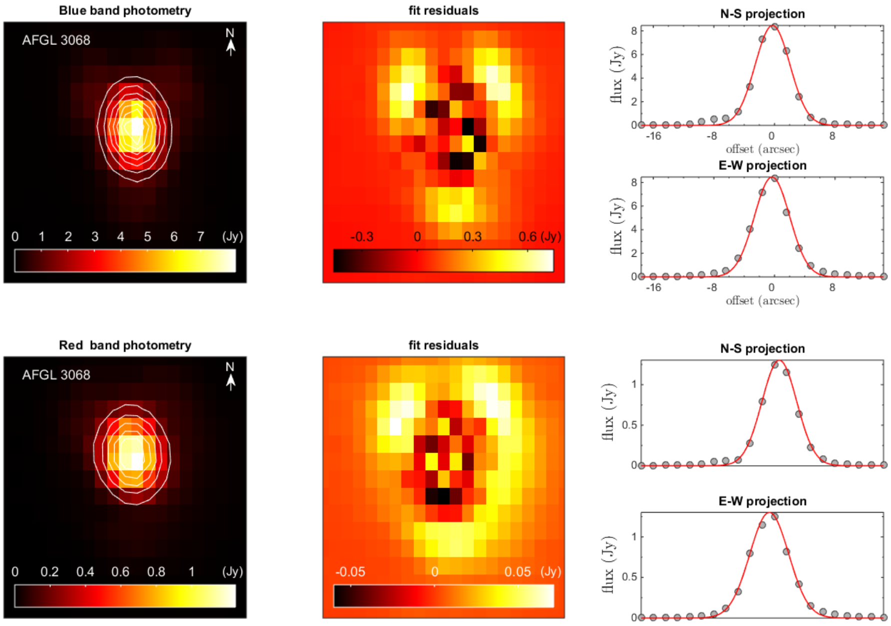
Blue band photometry
AFGL 3068
N
0 1 2 3 4 5 6 7 (Jy)
fit residuals
-0.3 0 0.3 0.6 (Jy)
N-S projection
flux (Jy)
offset (arcsec)
E-W projection
flux (Jy)
offset (arcsec)
Red band photometry
AFGL 3068
N
0 0.2 0.4 0.6 0.8 1 (Jy)
fit residuals
-0.05 0 0.05 (Jy)
N-S projection
flux (Jy)
E-W projection
flux (Jy)

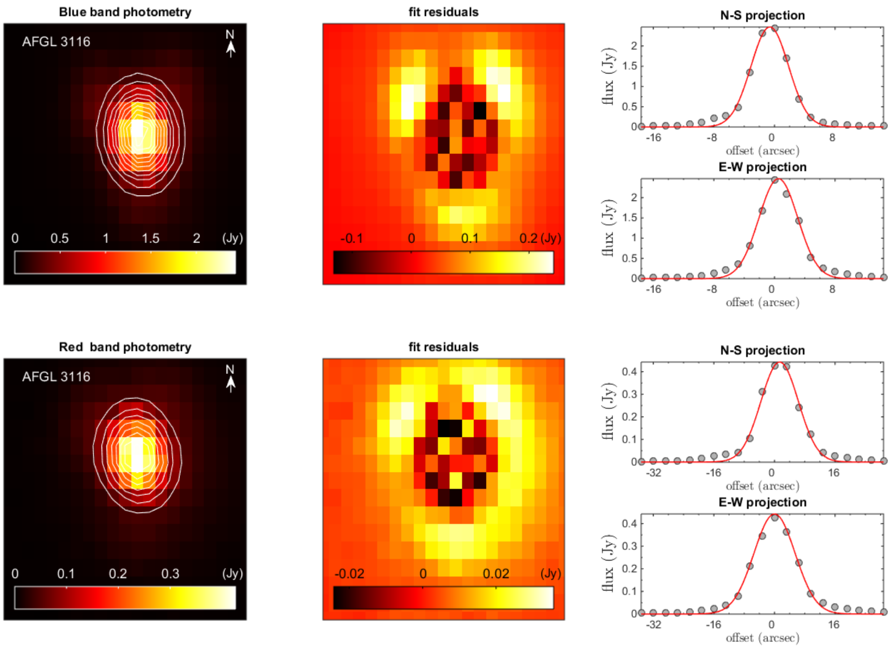
Blue band photometry
AFGL 3116
N
0 0.5 1 1.5 2 (Jy)
fit residuals
-0.1 0 0.1 0.2 (Jy)
N-S projection
flux (Jy)
offset (arcsec)
E-W projection
flux (Jy)
offset (arcsec)
Red band photometry
AFGL 3116
N
0 0.1 0.2 0.3 (Jy)
fit residuals
-0.02 0 0.02 (Jy)
N-S projection
flux (Jy)
offset (arcsec)
E-W projection
flux (Jy)
offset (arcsec)

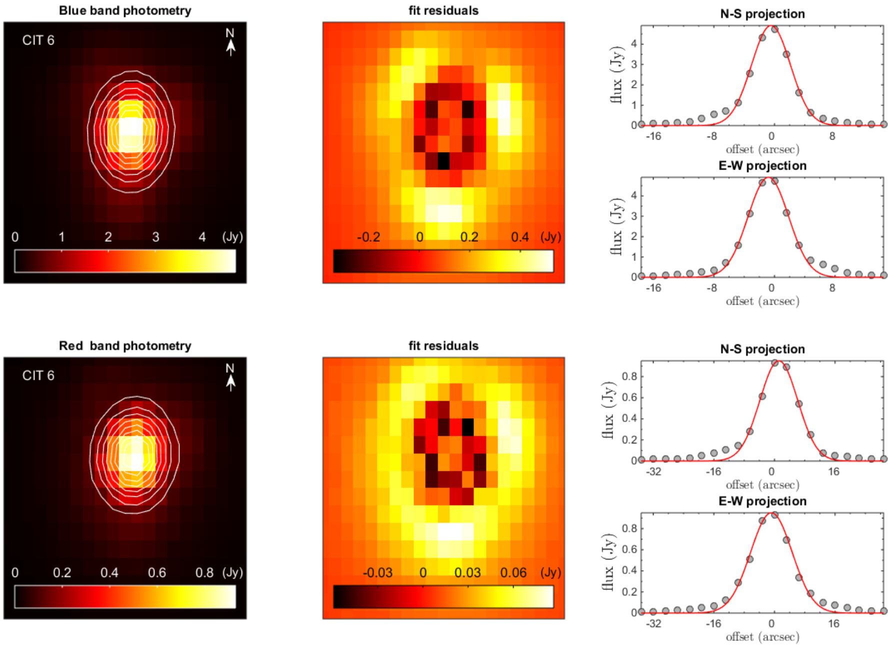
Blue band photometry
CIT 6
N
0 1 2 3 4 (Jy)
fit residuals
-0.2 0 0.2 0.4 (Jy)
N-S projection
E-W projection
flux (Jy)
offset (arcsec)
Red band photometry
CIT 6
0 0.2 0.4 0.6 0.8 (Jy)
fit residuals
-0.03 0 0.03 0.06 (Jy)

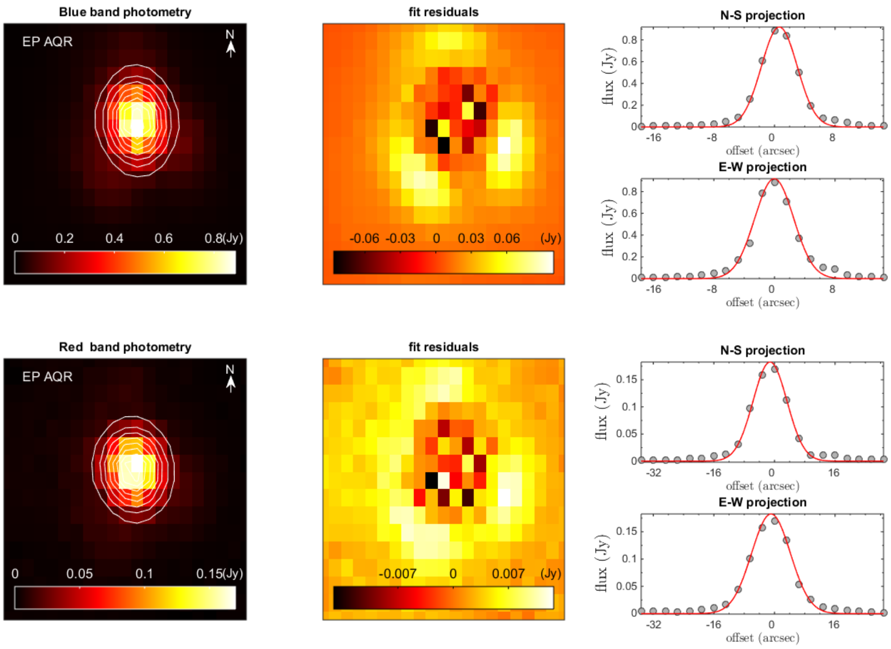
Blue band photometry
EP AQR
N
0 0.2 0.4 0.6 0.8(Jy)
fit residuals
-0.06 -0.03 0 0.03 0.06 (Jy)
N-S projection
E-W projection
flux (Jy)
offset (arcsec)
Red band photometry
EP AQR
0 0.05 0.1 0.15(Jy)
fit residuals
-0.007 0 0.007 (Jy)

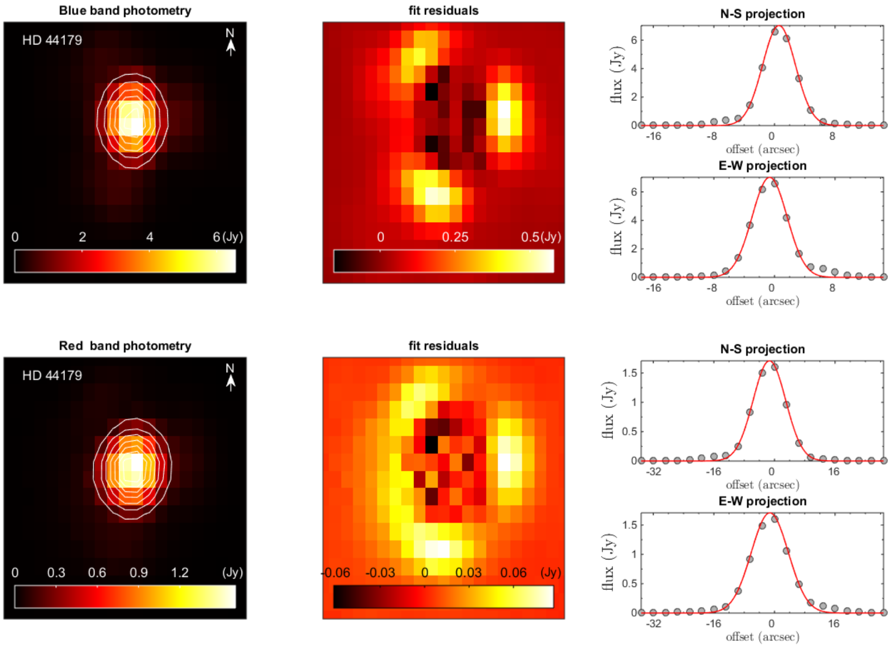
Blue band photometry
HD 44179
N
0 2 4 6 (Jy)
fit residuals
0 0.25 0.5(Jy)
N-S projection
E-W projection
flux (Jy)
offset (arcsec)
Red band photometry
HD 44179
0 0.3 0.6 0.9 1.2 (Jy)
-0.06 -0.03 0 0.03 0.06 (Jy)

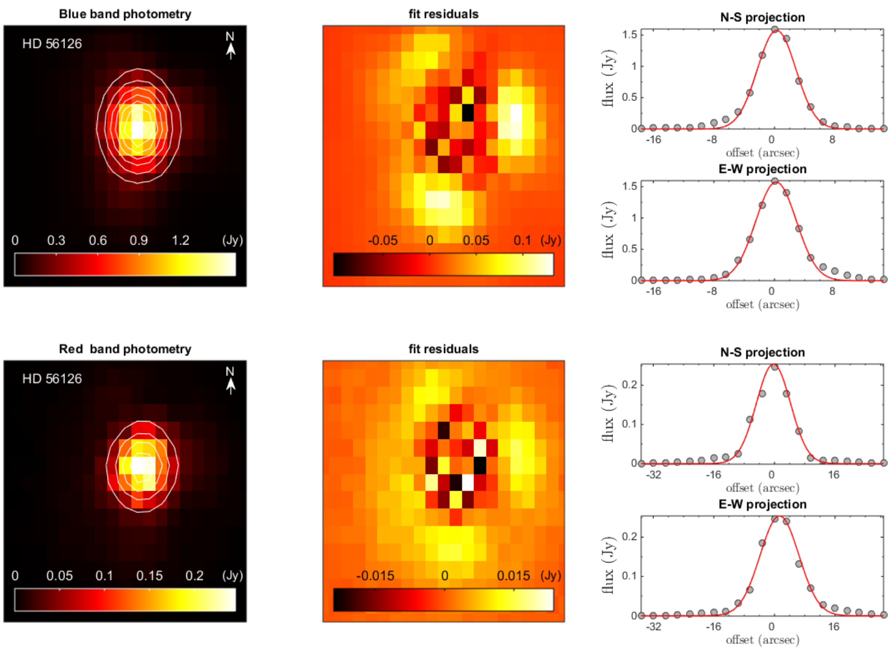
Blue band photometry
HD 56126
N
0 0.3 0.6 0.9 1.2 (Jy)
fit residuals
-0.05 0 0.05 0.1 (Jy)
N-S projection
E-W projection
flux (Jy)
offset (arcsec)
Red band photometry
HD 56126
0 0.05 0.1 0.15 0.2 (Jy)
-0.015 0 0.015 (Jy)

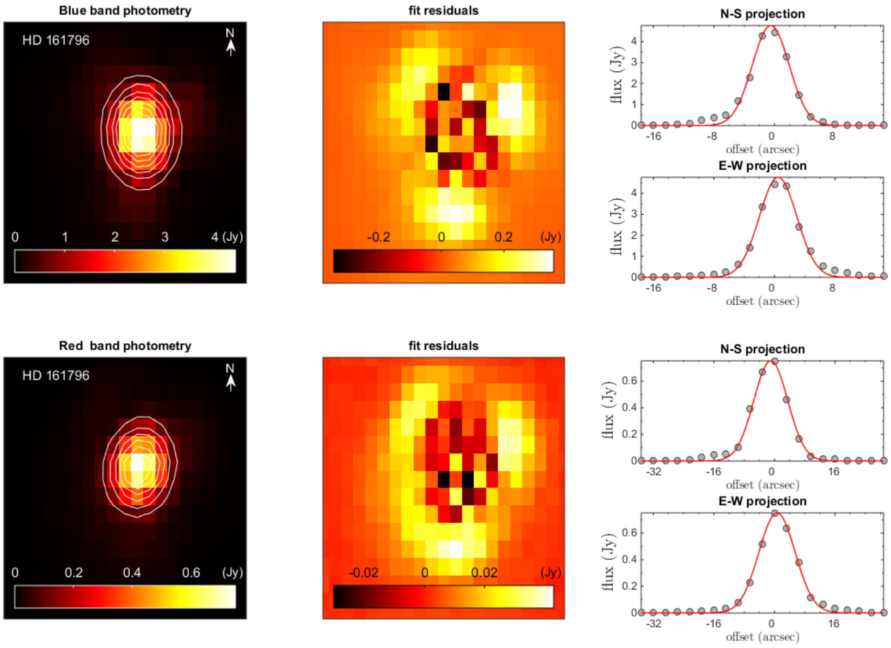
Blue band photometry
HD 161796
N
0 1 2 3 4 (Jy)
fit residuals
-0.2 0 0.2 (Jy)
N-S projection
E-W projection
flux (Jy)
offset (arcsec)
Red band photometry
HD 161796
0 0.2 0.4 0.6 (Jy)
-0.02 0 0.02 (Jy)

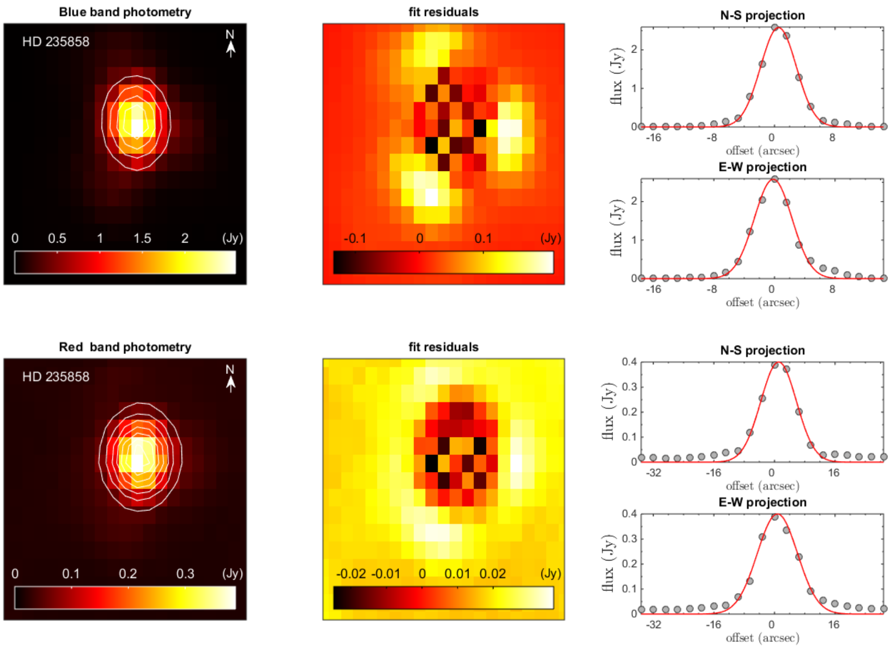
Blue band photometry
HD 235858
N
0 0.5 1 1.5 2 (Jy)
fit residuals
-0.1 0 0.1 (Jy)
N-S projection
E-W projection
flux (Jy)
offset (arcsec)
Red band photometry
HD 235858
0 0.1 0.2 0.3 (Jy)
-0.02 -0.01 0 0.01 0.02 (Jy)

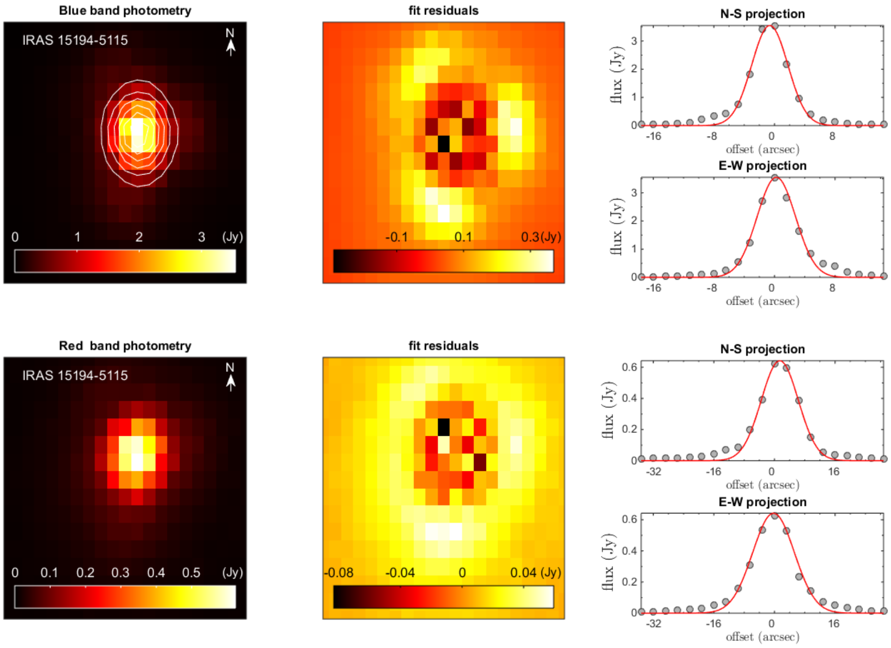
Blue band photometry
IRAS 15194-5115
N
0 1 2 3 (Jy)
fit residuals
-0.1 0.1 0.3(Jy)
N-S projection
flux (Jy)
offset (arcsec)
E-W projection
Red band photometry
IRAS 15194-5115
0 0.1 0.2 0.3 0.4 0.5 (Jy)
-0.08 -0.04 0 0.04 (Jy)

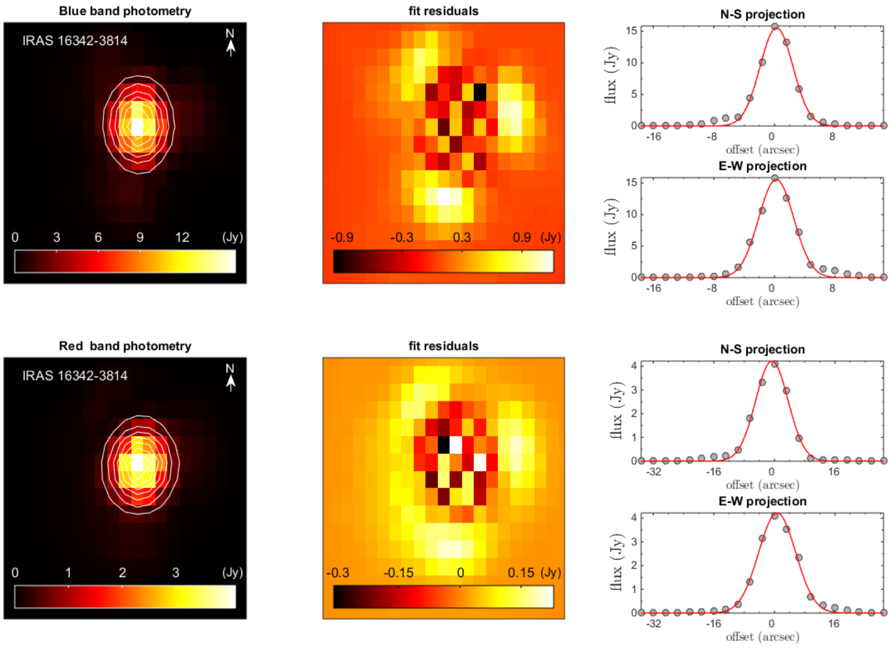
Blue band photometry
IRAS 16342-3814
N
0 3 6 9 12 (Jy)
fit residuals
-0.9 -0.3 0.3 0.9 (Jy)
N-S projection
flux (Jy)
offset (arcsec)
E-W projection
Red band photometry
IRAS 16342-3814
0 1 2 3 (Jy)
-0.3 -0.15 0 0.15 (Jy)

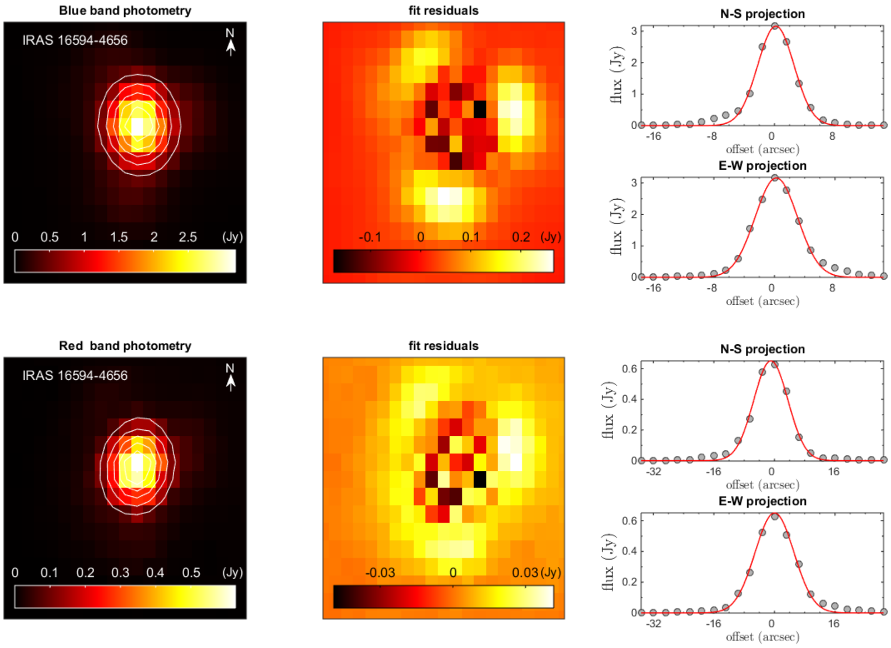
Blue band photometry
IRAS 16594-4656
N
fit residuals
N-S projection
E-W projection
flux (Jy)
offset (arcsec)
Red band photometry
IRAS 16594-4656

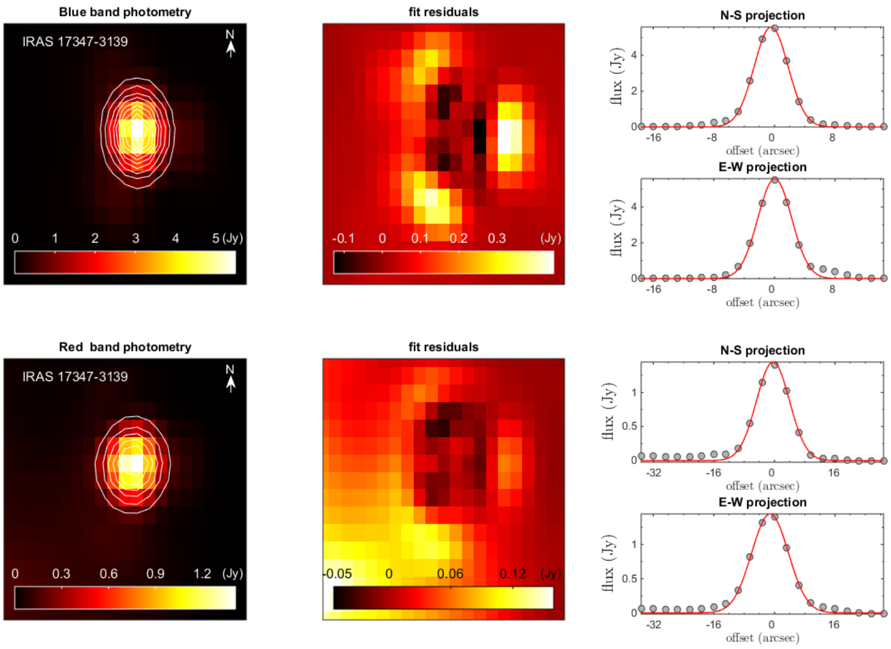
Blue band photometry
IRAS 17347-3139
N
fit residuals
N-S projection
E-W projection
flux (Jy)
offset (arcsec)
Red band photometry
IRAS 17347-3139

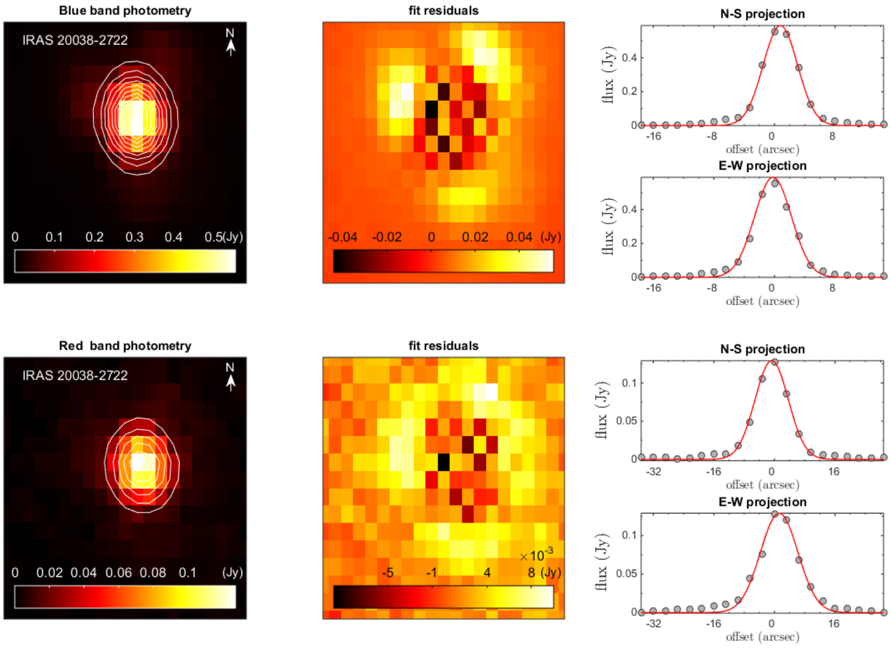
Blue band photometry
IRAS 20038-2722
N
0 0.1 0.2 0.3 0.4 0.5(Jy)
fit residuals
-0.04 -0.02 0 0.02 0.04 (Jy)
N-S projection
flux (Jy)
offset (arcsec)
E-W projection
Red band photometry
IRAS 20038-2722
0 0.02 0.04 0.06 0.08 0.1 (Jy)
×10^-3
-5 -1 4 8 (Jy)

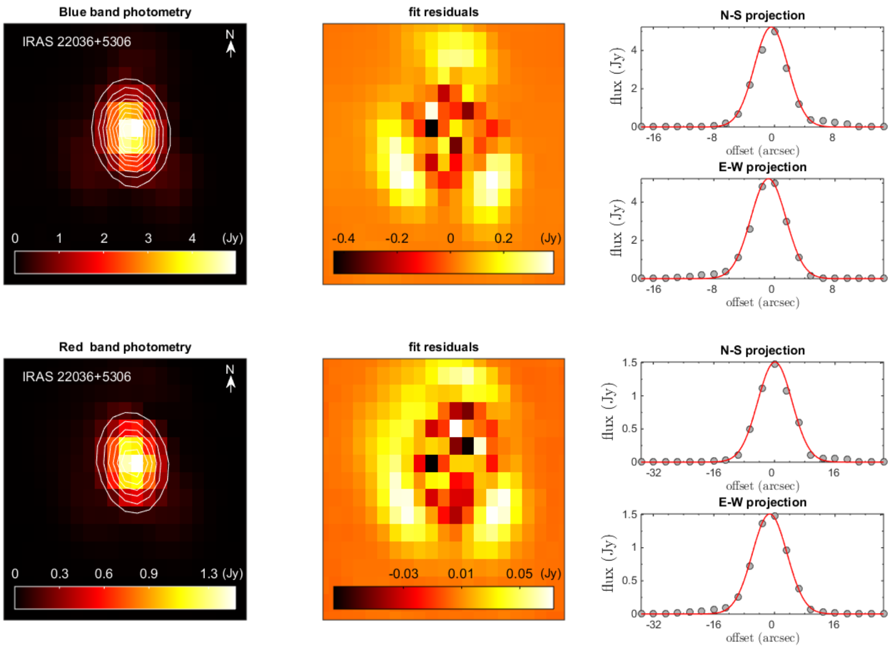
Blue band photometry
IRAS 22036+5306
N
0 1 2 3 4 (Jy)
fit residuals
-0.4 -0.2 0 0.2 (Jy)
N-S projection
flux (Jy)
offset (arcsec)
E-W projection
Red band photometry
IRAS 22036+5306
0 0.3 0.6 0.9 1.3 (Jy)
-0.03 0.01 0.05 (Jy)

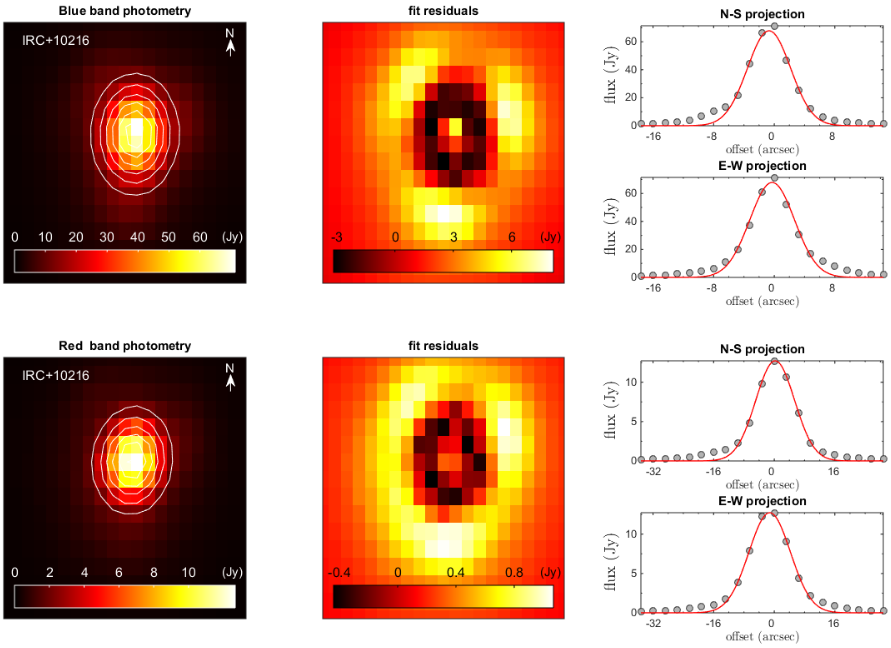
Blue band photometry
IRC+10216
N
0 10 20 30 40 50 60 (Jy)
fit residuals
-3 0 3 6 (Jy)
N-S projection
E-W projection
flux (Jy)
offset (arcsec)
Red band photometry
IRC+10216
0 2 4 6 8 10 (Jy)
-0.4 0 0.4 0.8 (Jy)

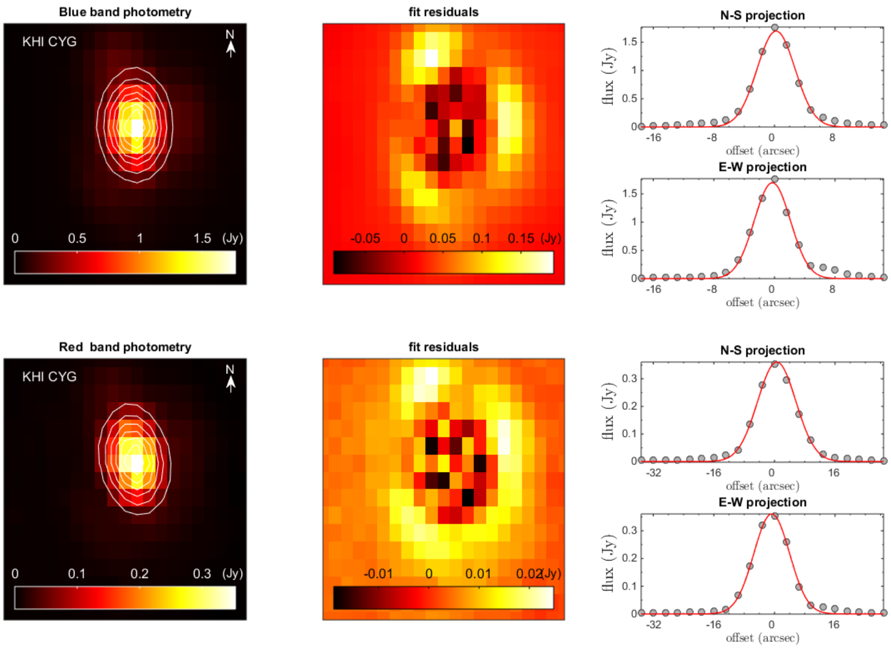
Blue band photometry
KHI CYG
N
0 0.5 1 1.5 (Jy)
fit residuals
-0.05 0 0.05 0.1 0.15 (Jy)
N-S projection
E-W projection
flux (Jy)
offset (arcsec)
Red band photometry
KHI CYG
0 0.1 0.2 0.3 (Jy)
-0.01 0 0.01 0.02 (Jy)

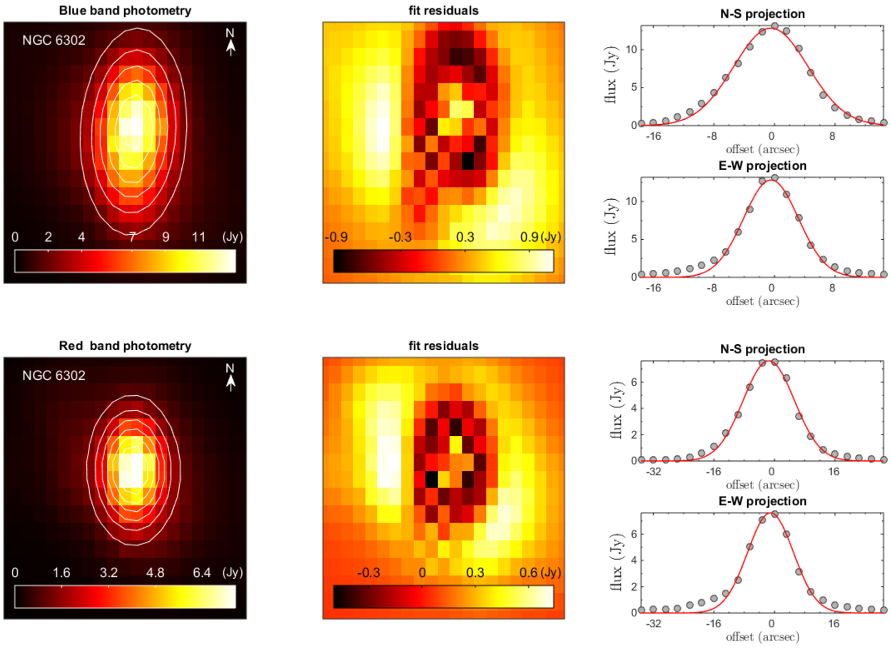
Blue band photometry
NGC 6302
fit residuals
N-S projection
E-W projection
Red band photometry
NGC 6302
fit residuals
N-S projection
E-W projection

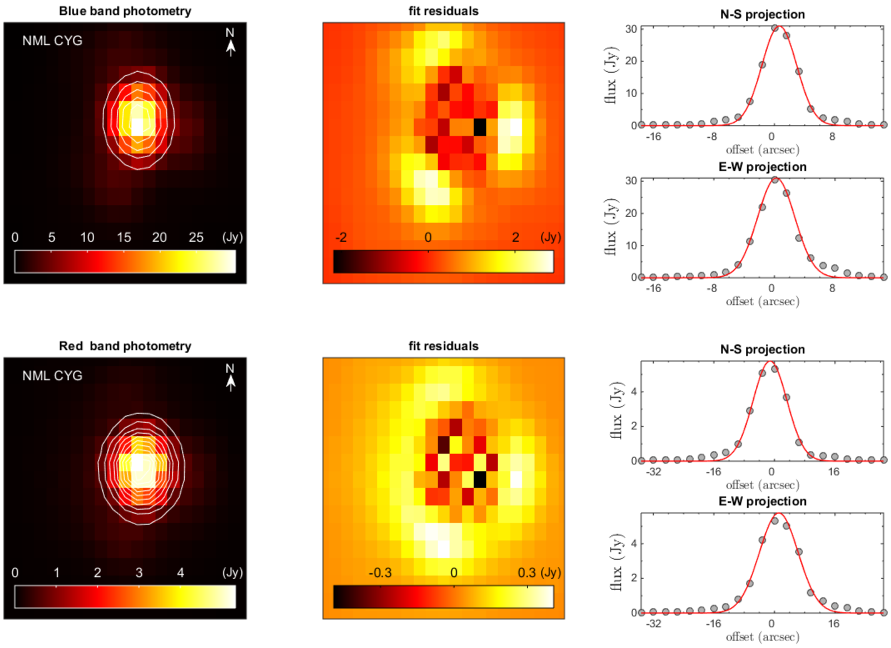
Blue band photometry
NML CYG
fit residuals
N-S projection
E-W projection
Red band photometry
NML CYG
fit residuals
N-S projection
E-W projection

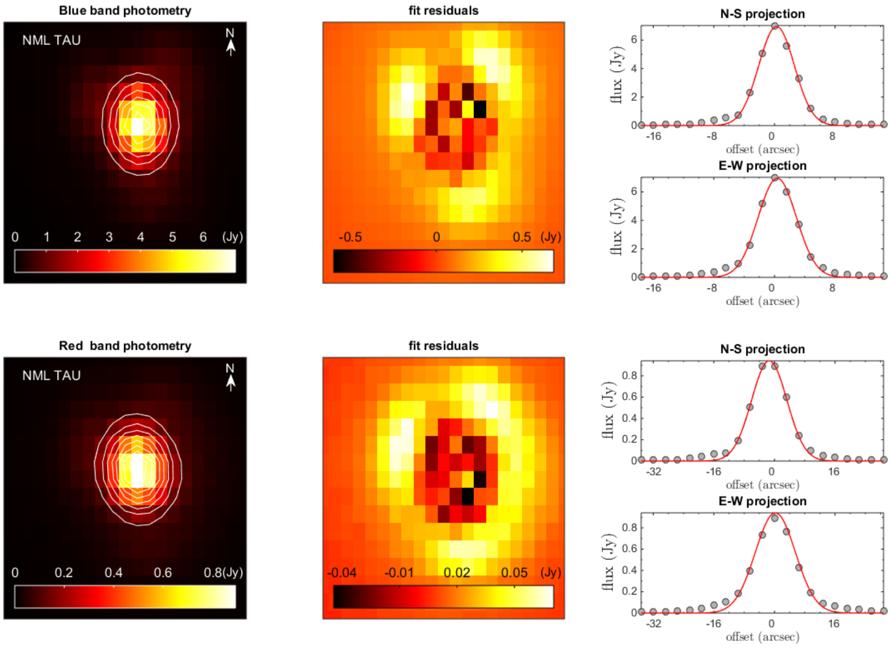
Blue band photometry
NML TAU
N
0 1 2 3 4 5 6 (Jy)
fit residuals
-0.5 0 0.5 (Jy)
N-S projection
E-W projection
flux (Jy)
offset (arcsec)
Red band photometry
NML TAU
0 0.2 0.4 0.6 0.8(Jy)
-0.04 -0.01 0.02 0.05 (Jy)

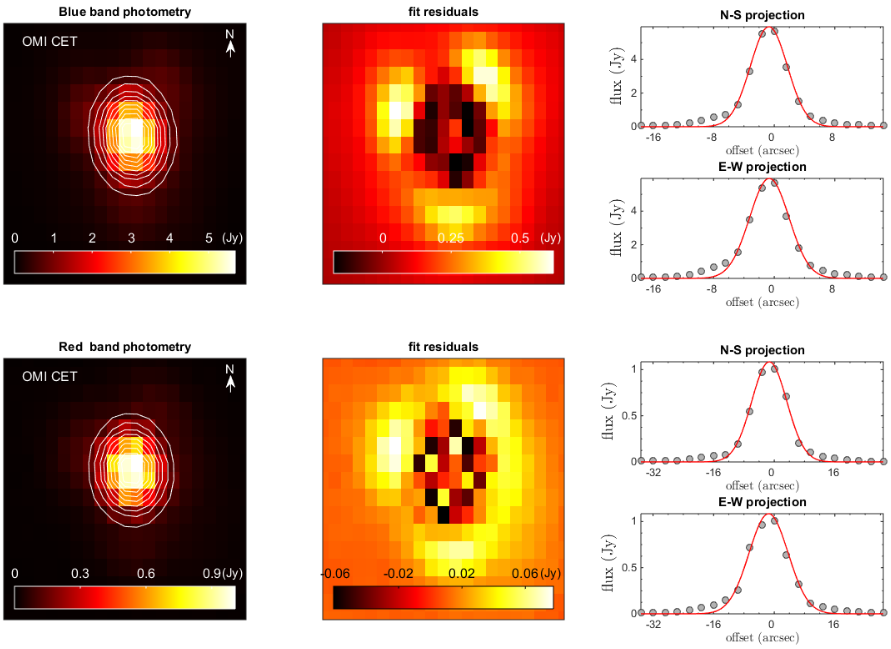
Blue band photometry
OMI CET
N
0 1 2 3 4 5 (Jy)
fit residuals
0 0.25 0.5 (Jy)
N-S projection
E-W projection
flux (Jy)
offset (arcsec)
Red band photometry
OMI CET
0 0.3 0.6 0.9(Jy)
-0.06 -0.02 0.02 0.06(Jy)

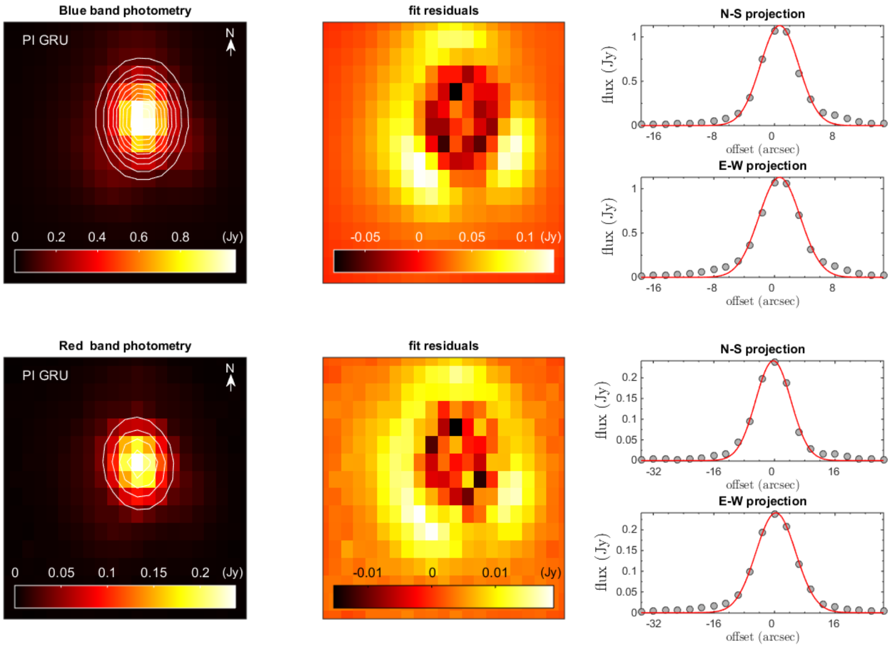
Blue band photometry
PI GRU
N
0 0.2 0.4 0.6 0.8 (Jy)
fit residuals
-0.05 0 0.05 0.1 (Jy)
N-S projection
flux (Jy)
offset (arcsec)
E-W projection
Red band photometry
0 0.05 0.1 0.15 0.2 (Jy)
-0.01 0 0.01 (Jy)

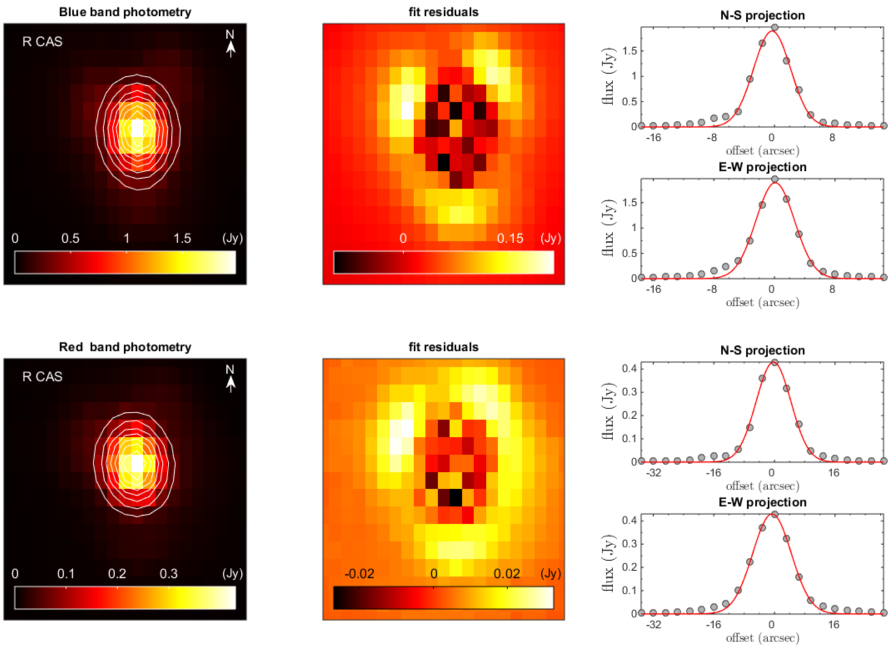
Blue band photometry
R CAS
N
0 0.5 1 1.5 (Jy)
fit residuals
0 0.15 (Jy)
N-S projection
flux (Jy)
offset (arcsec)
E-W projection
Red band photometry
0 0.1 0.2 0.3 (Jy)
-0.02 0 0.02 (Jy)

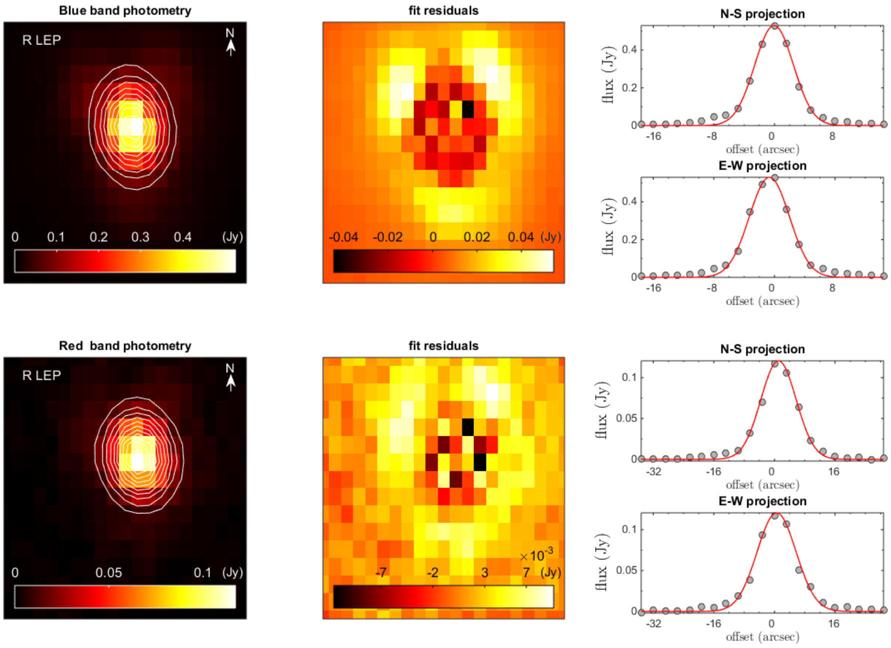
Blue band photometry
R LEP
N
0 0.1 0.2 0.3 0.4 (Jy)
fit residuals
-0.04 -0.02 0 0.02 0.04 (Jy)
N-S projection
E-W projection
flux (Jy)
offset (arcsec)
Red band photometry
R LEP
0 0.05 0.1 (Jy)
fit residuals
×10^-3
-7 -2 3 7 (Jy)

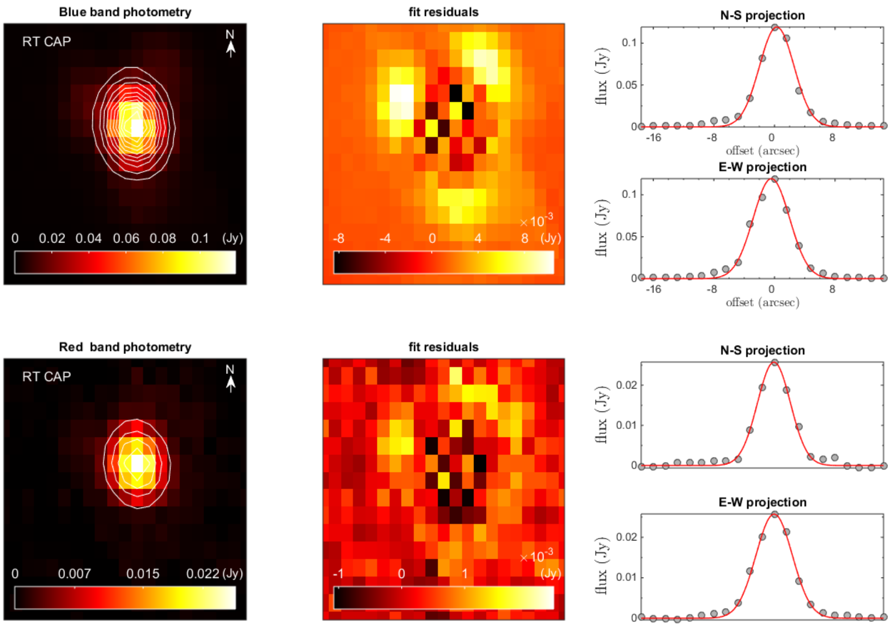
Blue band photometry
RT CAP
N
0 0.02 0.04 0.06 0.08 0.1 (Jy)
fit residuals
×10^-3
-8 -4 0 4 8 (Jy)
N-S projection
E-W projection
flux (Jy)
offset (arcsec)
Red band photometry
RT CAP
0 0.007 0.015 0.022 (Jy)
fit residuals
×10^-3
-1 0 1 (Jy)

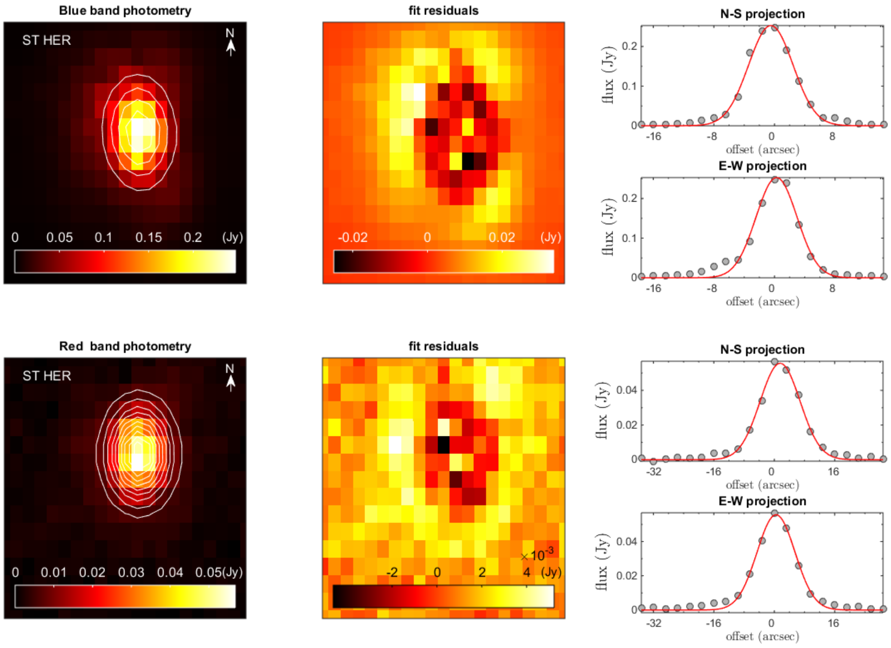
Blue band photometry
ST HER
N
0 0.05 0.1 0.15 0.2 (Jy)
fit residuals
-0.02 0 0.02 (Jy)
N-S projection
flux (Jy)
offset (arcsec)
E-W projection
Red band photometry
0 0.01 0.02 0.03 0.04 0.05(Jy)
×10-3
-2 0 2 4 (Jy)

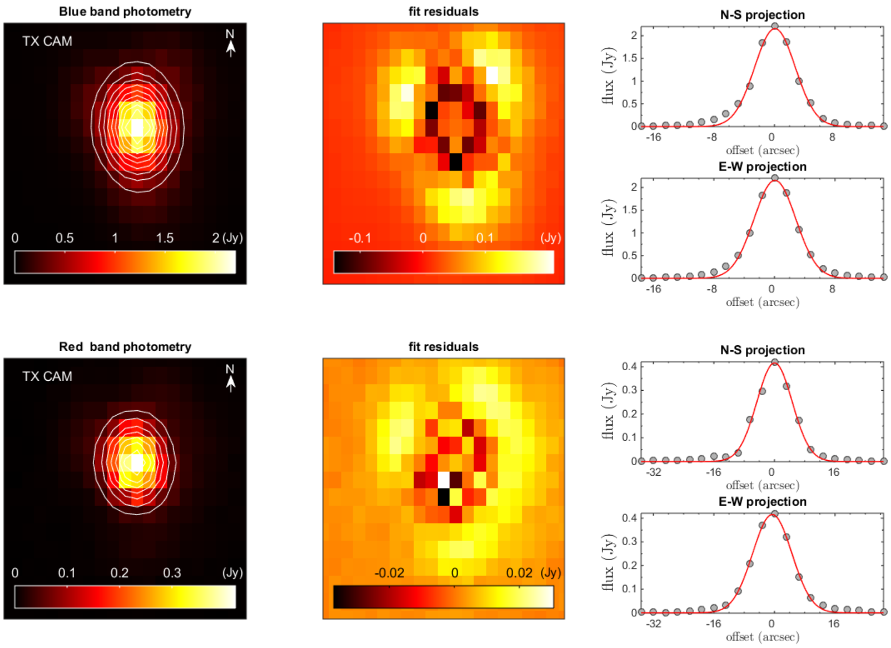
Blue band photometry
TX CAM
N
0 0.5 1 1.5 2 (Jy)
fit residuals
-0.1 0 0.1 (Jy)
N-S projection
flux (Jy)
offset (arcsec)
E-W projection
Red band photometry
0 0.1 0.2 0.3 (Jy)
-0.02 0 0.02 (Jy)

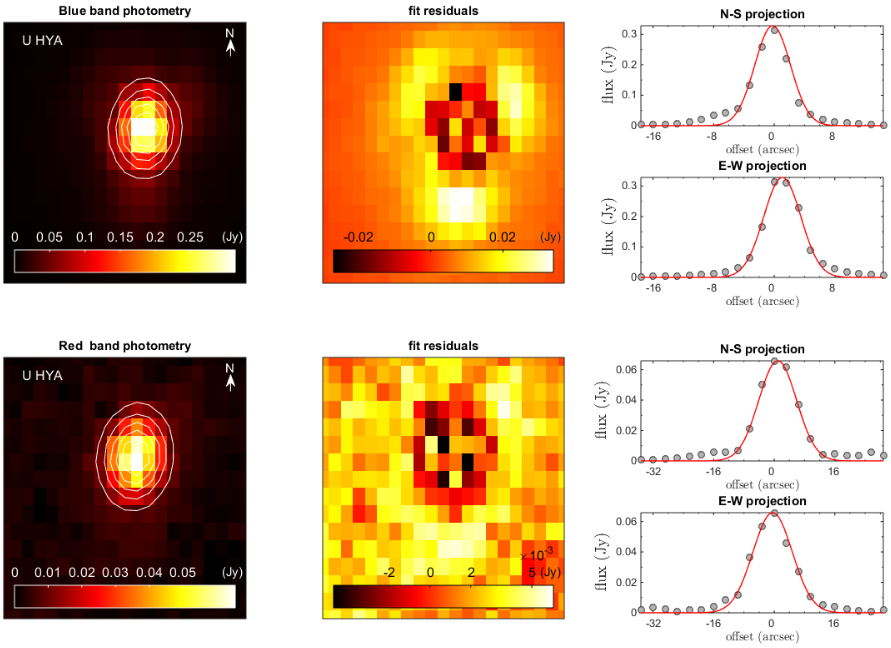
Blue band photometry
U HYA
N
0 0.05 0.1 0.15 0.2 0.25 (Jy)
fit residuals
-0.02 0 0.02 (Jy)
N-S projection
E-W projection
flux (Jy)
offset (arcsec)
Red band photometry
U HYA
0 0.01 0.02 0.03 0.04 0.05 (Jy)
fit residuals
×10-3
-2 0 2 5 (Jy)

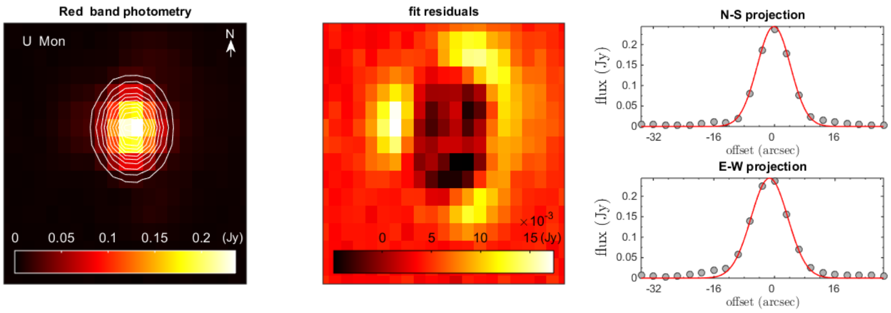
Red band photometry
U Mon
N
0 0.05 0.1 0.15 0.2 (Jy)
fit residuals
×10-3
0 5 10 15 (Jy)
N-S projection
E-W projection
flux (Jy)
offset (arcsec)

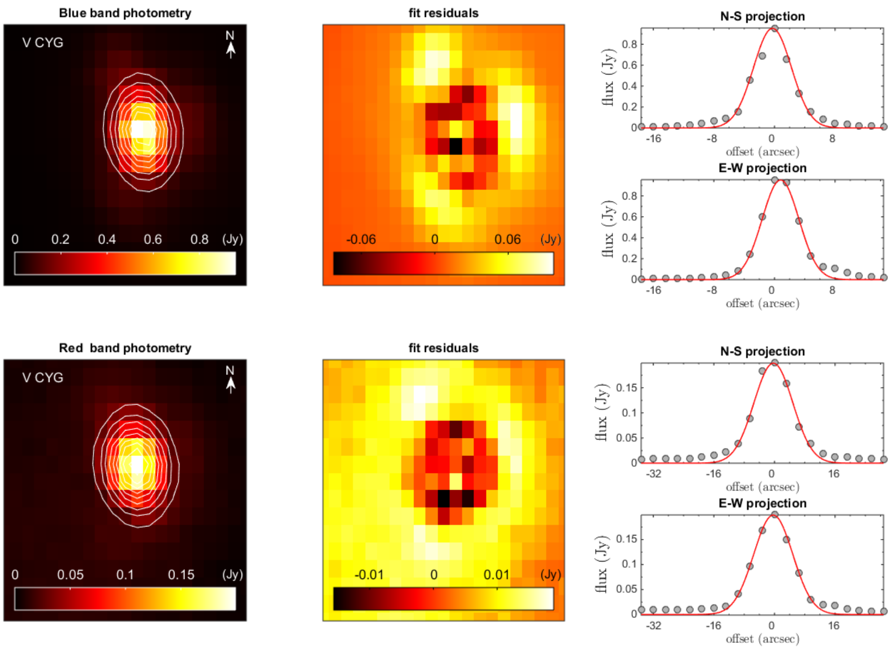
Blue band photometry
V CYG
N
0 0.2 0.4 0.6 0.8 (Jy)
fit residuals
-0.06 0 0.06 (Jy)
N-S projection
E-W projection
flux (Jy)
offset (arcsec)
Red band photometry
V CYG
0 0.05 0.1 0.15 (Jy)
fit residuals
-0.01 0 0.01 (Jy)

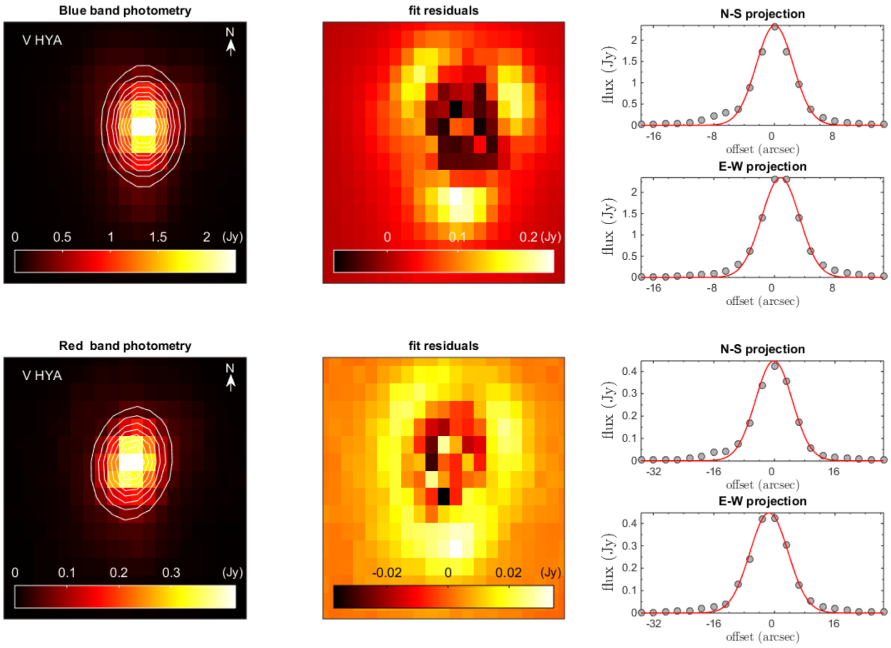
Blue band photometry
V HYA
N
0 0.5 1 1.5 2 (Jy)
fit residuals
0 0.1 0.2 (Jy)
N-S projection
flux (Jy)
offset (arcsec)
E-W projection
Red band photometry
V HYA
0 0.1 0.2 0.3 (Jy)
fit residuals
-0.02 0 0.02 (Jy)
N-S projection
E-W projection

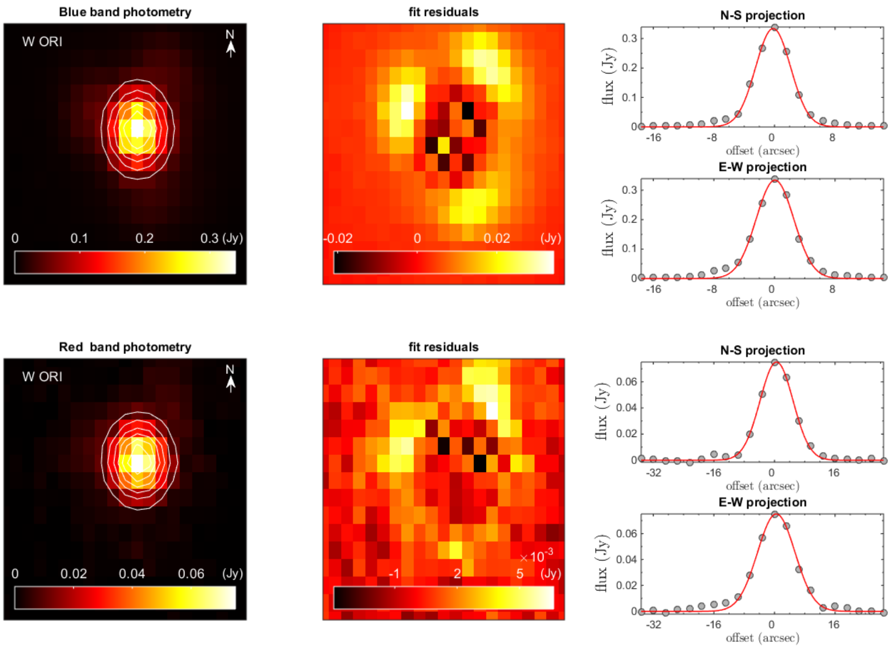
Blue band photometry
W ORI
N
0 0.1 0.2 0.3 (Jy)
fit residuals
-0.02 0 0.02 (Jy)
N-S projection
flux (Jy)
offset (arcsec)
E-W projection
Red band photometry
W ORI
0 0.02 0.04 0.06 (Jy)
fit residuals
$\times 10^{-3}$
-1 2 5 (Jy)
N-S projection
E-W projection

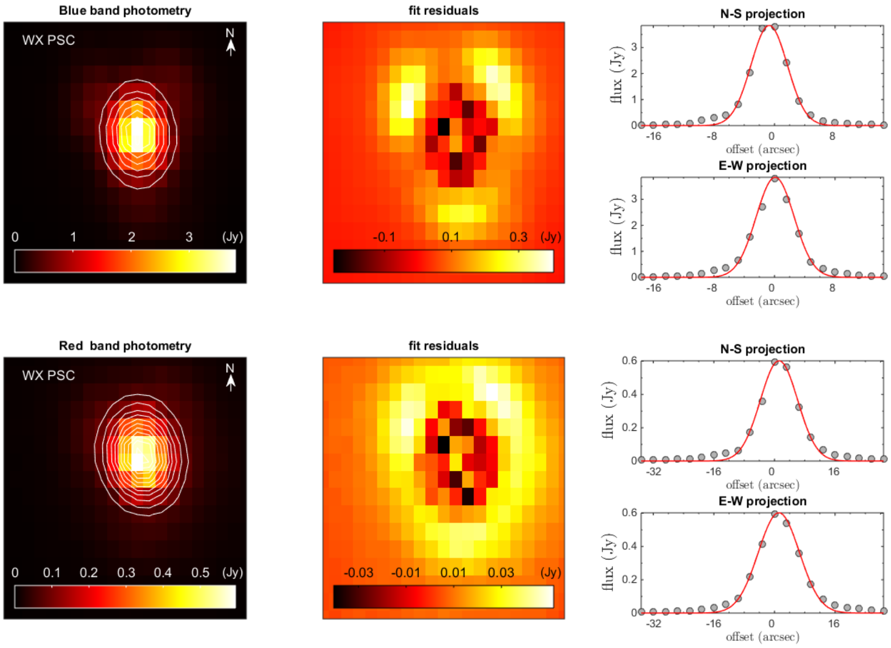
Blue band photometry
WX PSC
N
0 1 2 3 (Jy)
fit residuals
-0.1 0.1 0.3 (Jy)
N-S projection
E-W projection
flux (Jy)
offset (arcsec)
Red band photometry
WX PSC
0 0.1 0.2 0.3 0.4 0.5 (Jy)
fit residuals
-0.03 -0.01 0.01 0.03 (Jy)

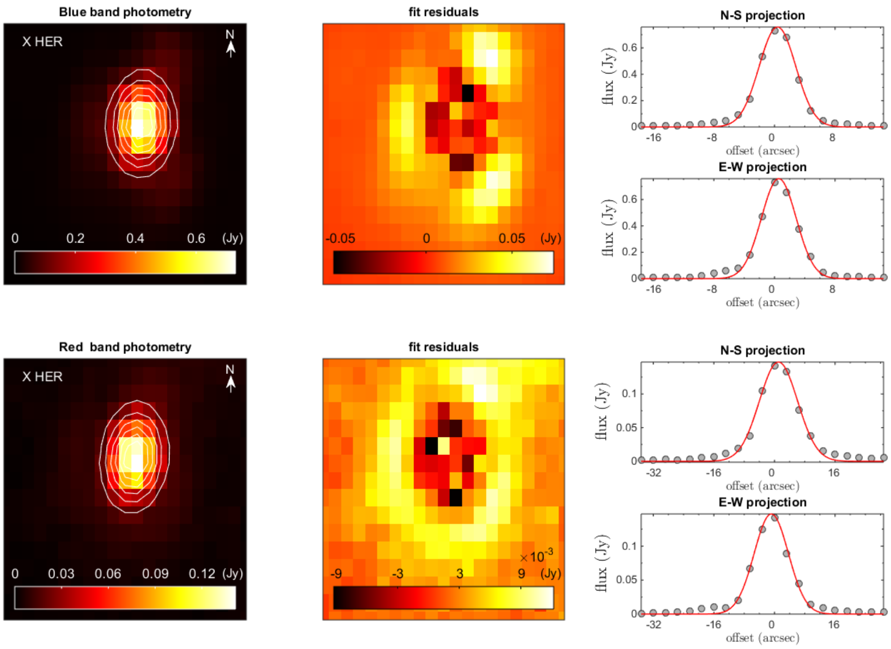
Blue band photometry
X HER
N
0 0.2 0.4 0.6 (Jy)
fit residuals
-0.05 0 0.05 (Jy)
N-S projection
E-W projection
flux (Jy)
offset (arcsec)
Red band photometry
X HER
0 0.03 0.06 0.09 0.12 (Jy)
fit residuals
×10^-3
-9 -3 3 9 (Jy)

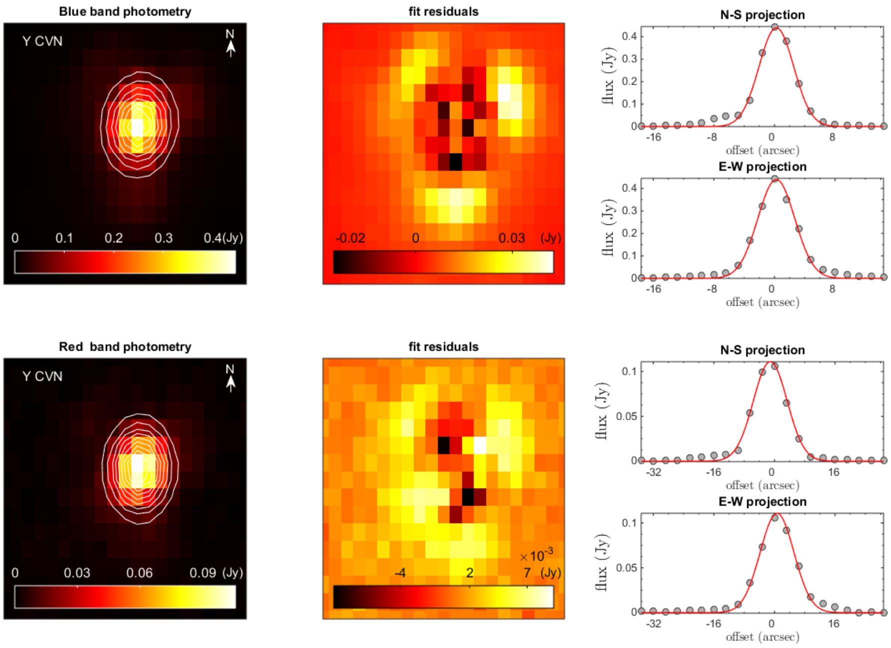
Blue band photometry
Y CVN
N
0 0.1 0.2 0.3 0.4(Jy)
fit residuals
-0.02 0 0.03 (Jy)
N-S projection
flux (Jy)
offset (arcsec)
E-W projection
Red band photometry
Y CVN
N
0 0.03 0.06 0.09 (Jy)
fit residuals
×10^-3
-4 2 7 (Jy)
N-S projection
E-W projection

B.3 Extended sources

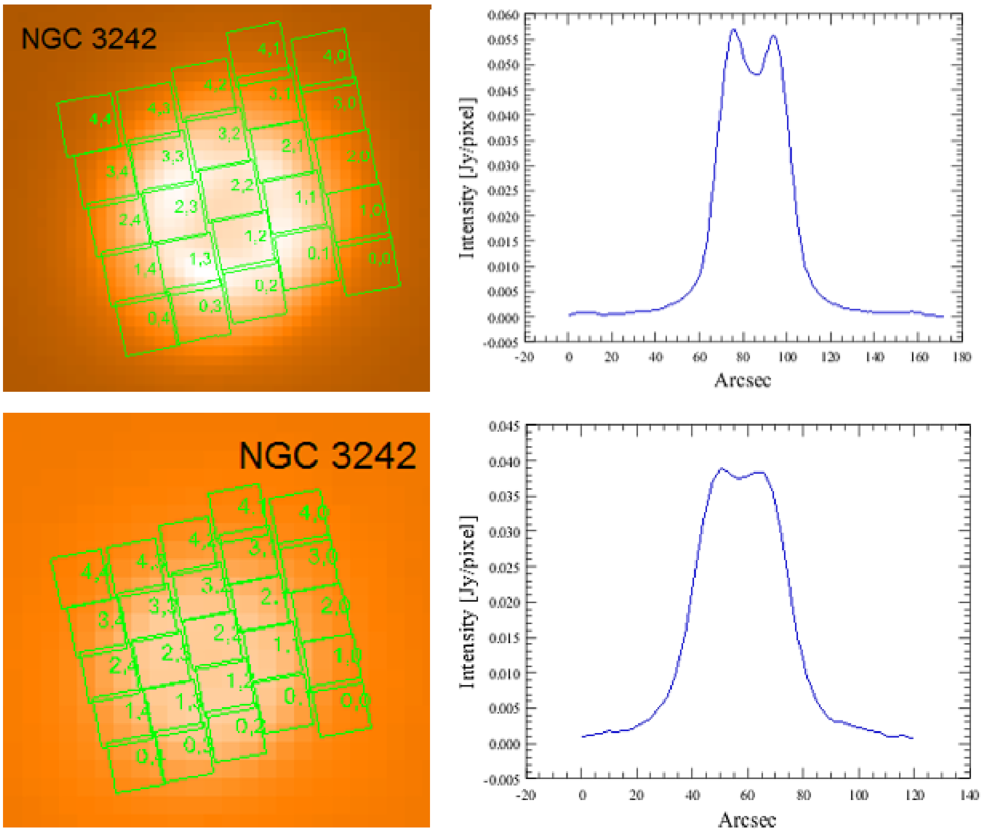

Fig. B.3.1: Photometry maps (blue and red bands) of extended sources with PACS spectrometer footprint overlaid. The plots on the right side are intensity profiles.

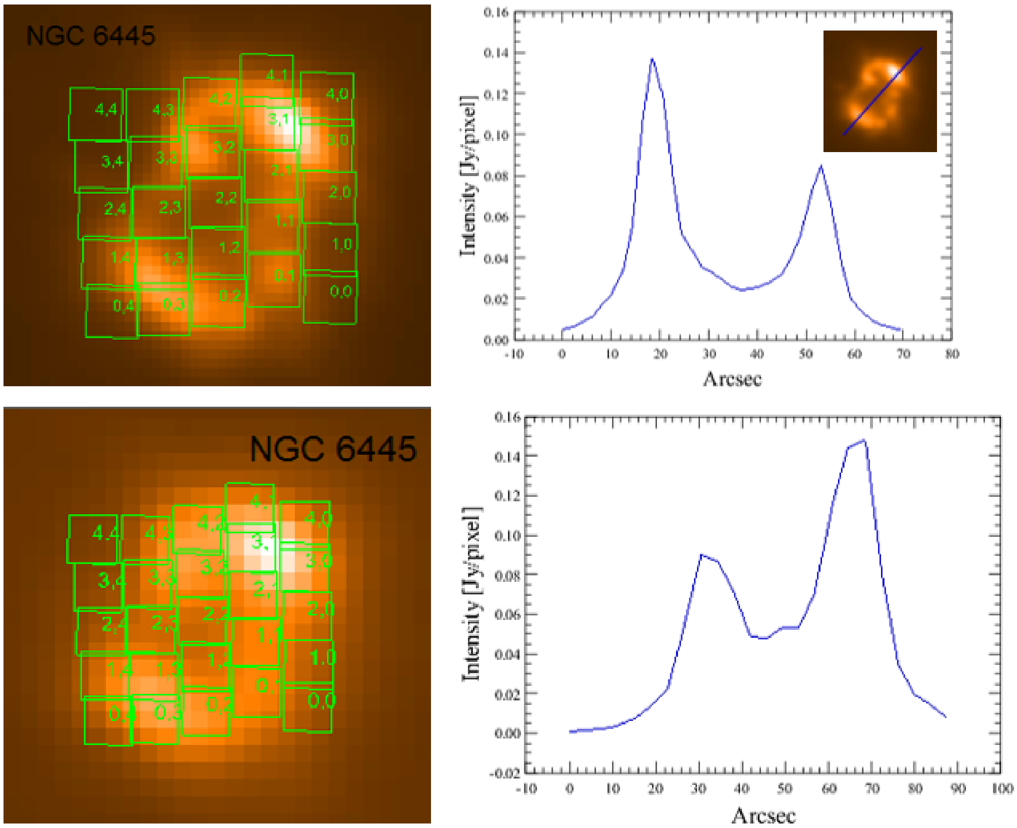
NGC 6445
Intensity [Jy/pixel]
Arcsec
NGC 6445
Intensity [Jy/pixel]
Arcsec

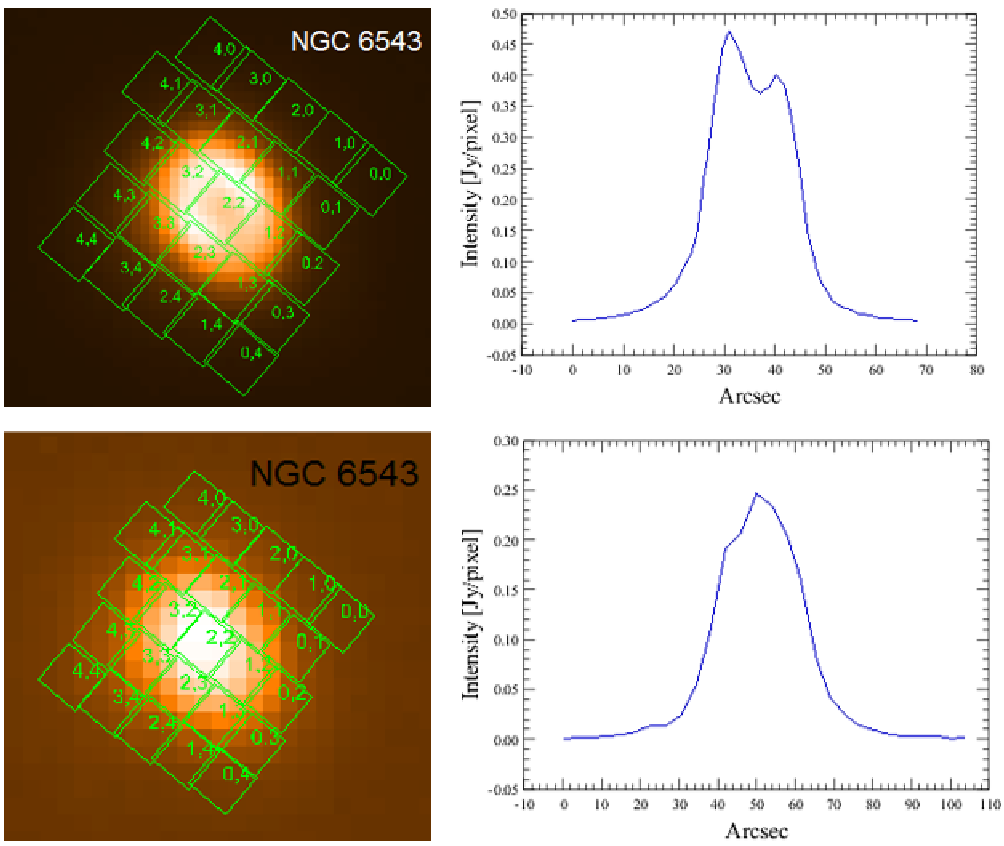
NGC 6543
Intensity [Jy/pixel]
Arcsec
NGC 6543
Intensity [Jy/pixel]
Arcsec

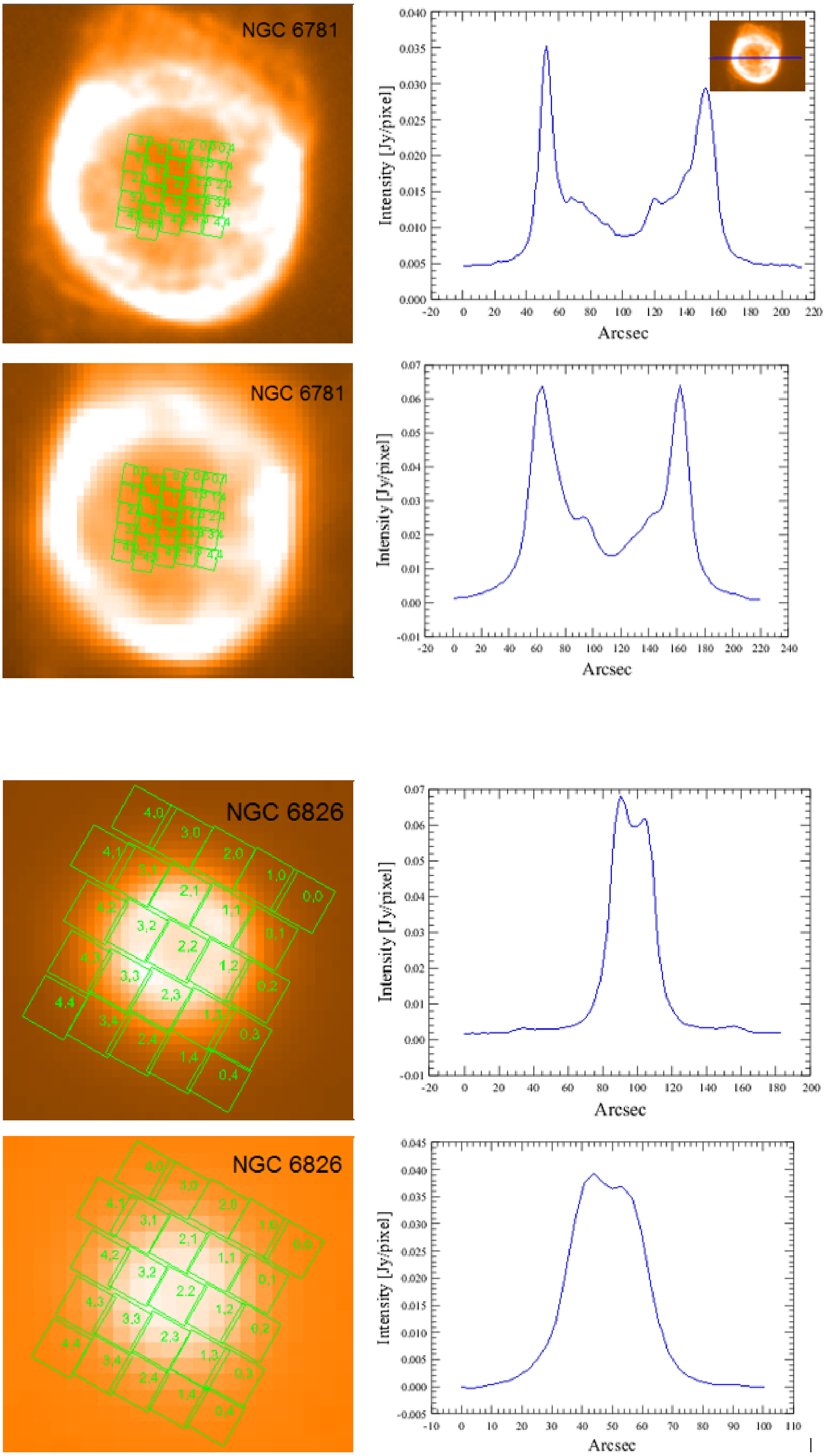
NGC 6781
Intensity [Jy/pixel]
Arcsec
NGC 6781
Intensity [Jy/pixel]
Arcsec
NGC 6826
Intensity [Jy/pixel]
Arcsec
NGC 6826
Intensity [Jy/pixel]
Arcsec

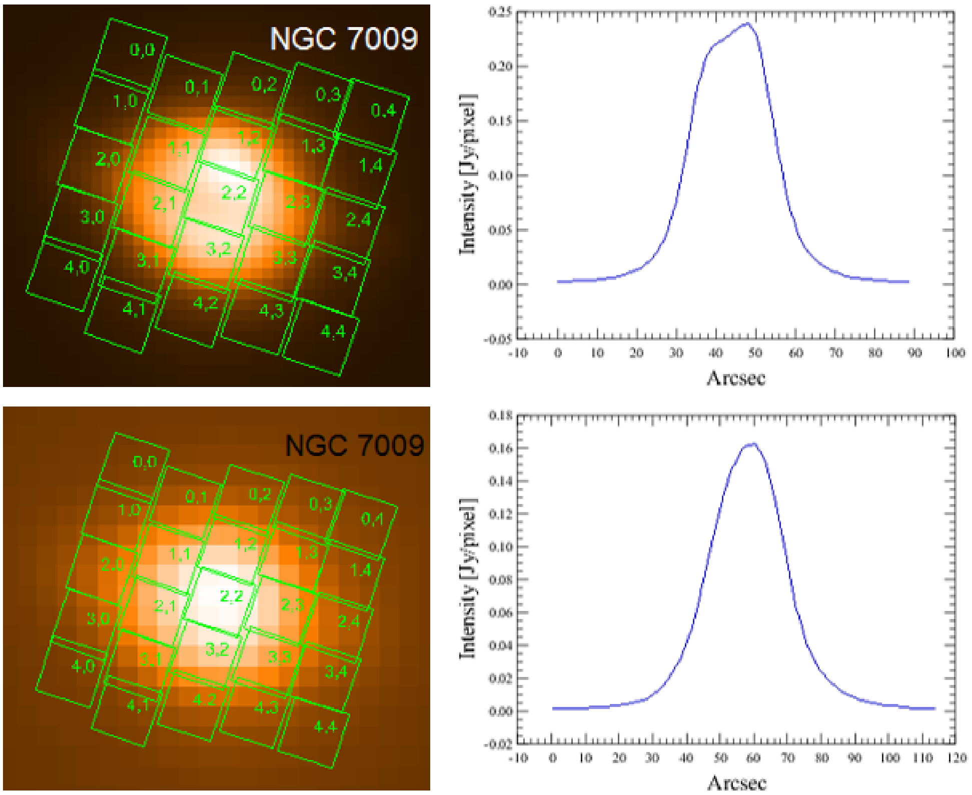
NGC 7009
NGC 7009
Intensity [Jy/pixel]
Arcsec
Intensity [Jy/pixel]
Arcsec

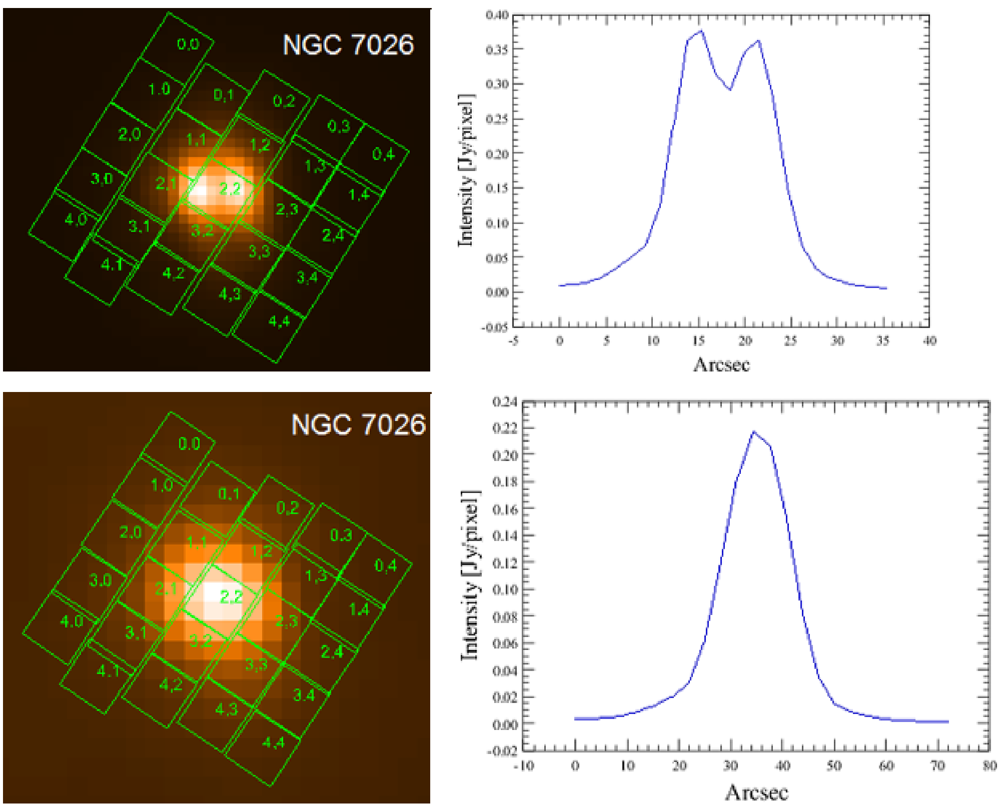
NGC 7026
NGC 7026
Intensity [Jy/pixel]
Arcsec
Intensity [Jy/pixel]
Arcsec

B.4 CO line profiles in a sample of C-rich stars

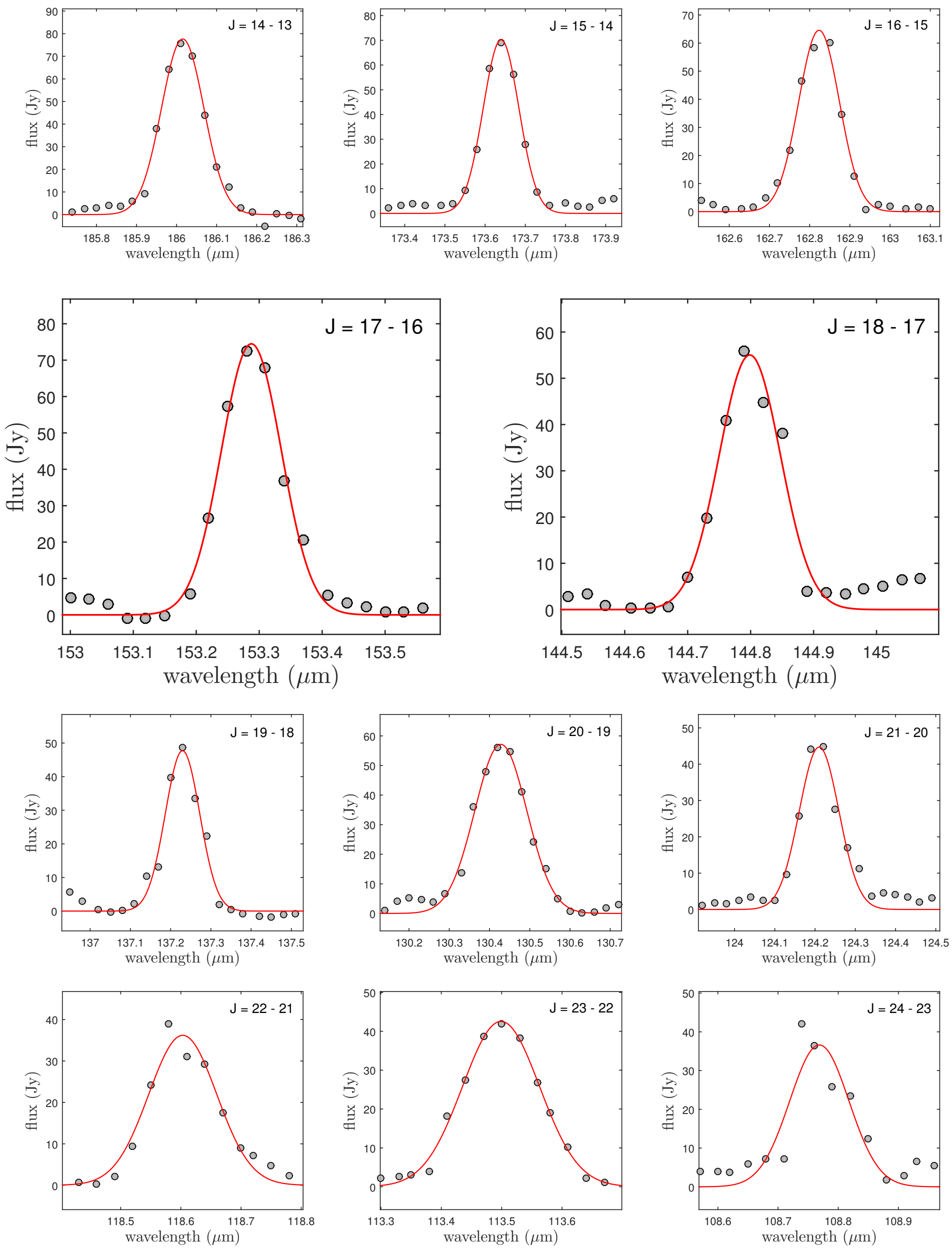

Fig. B.4.1: Fitting ^{12}CO spectral lines in the carbon-rich AGB CIT 6.

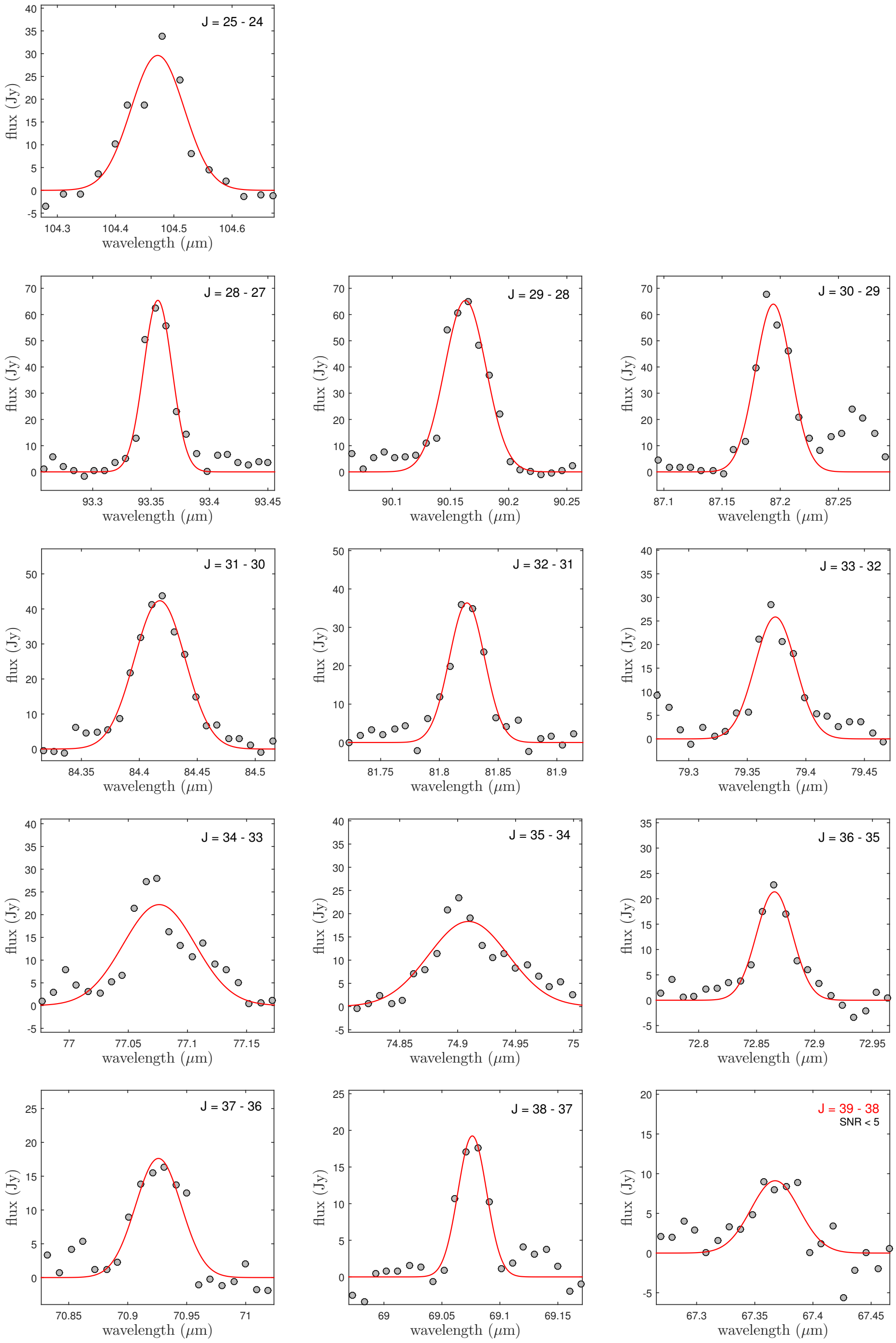
J = 25 - 24
J = 28 - 27
J = 29 - 28
J = 30 - 29
J = 31 - 30
J = 32 - 31
J = 33 - 32
J = 34 - 33
J = 35 - 34
J = 36 - 35
J = 37 - 36
J = 38 - 37
J = 39 - 38
SNR < 5
flux (Jy)
wavelength (μm)

B.5 Spectra of carbon-rich stars

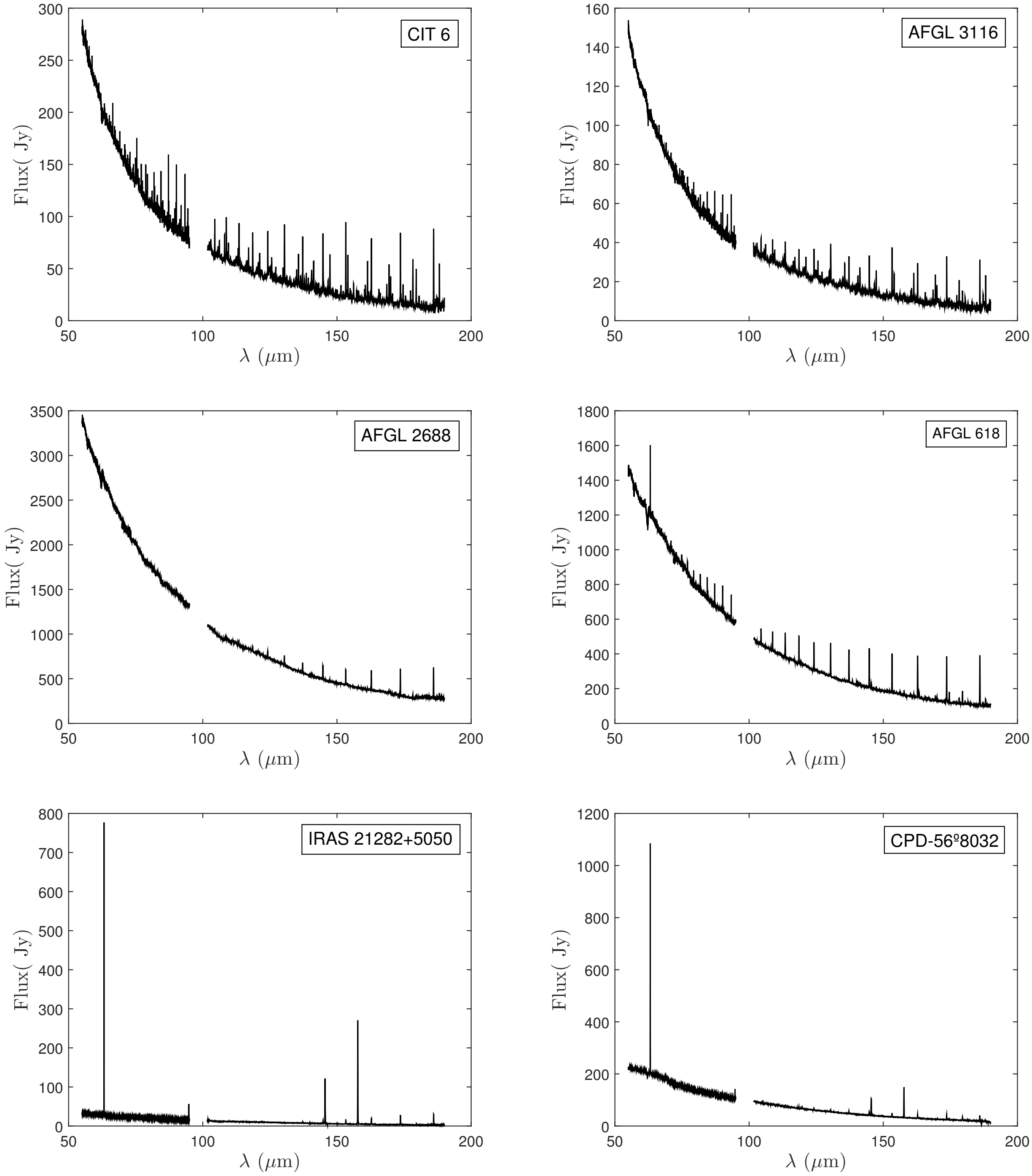

Fig. B.5.1: PACS range spectra of C-rich stars. (Continues on the next page)

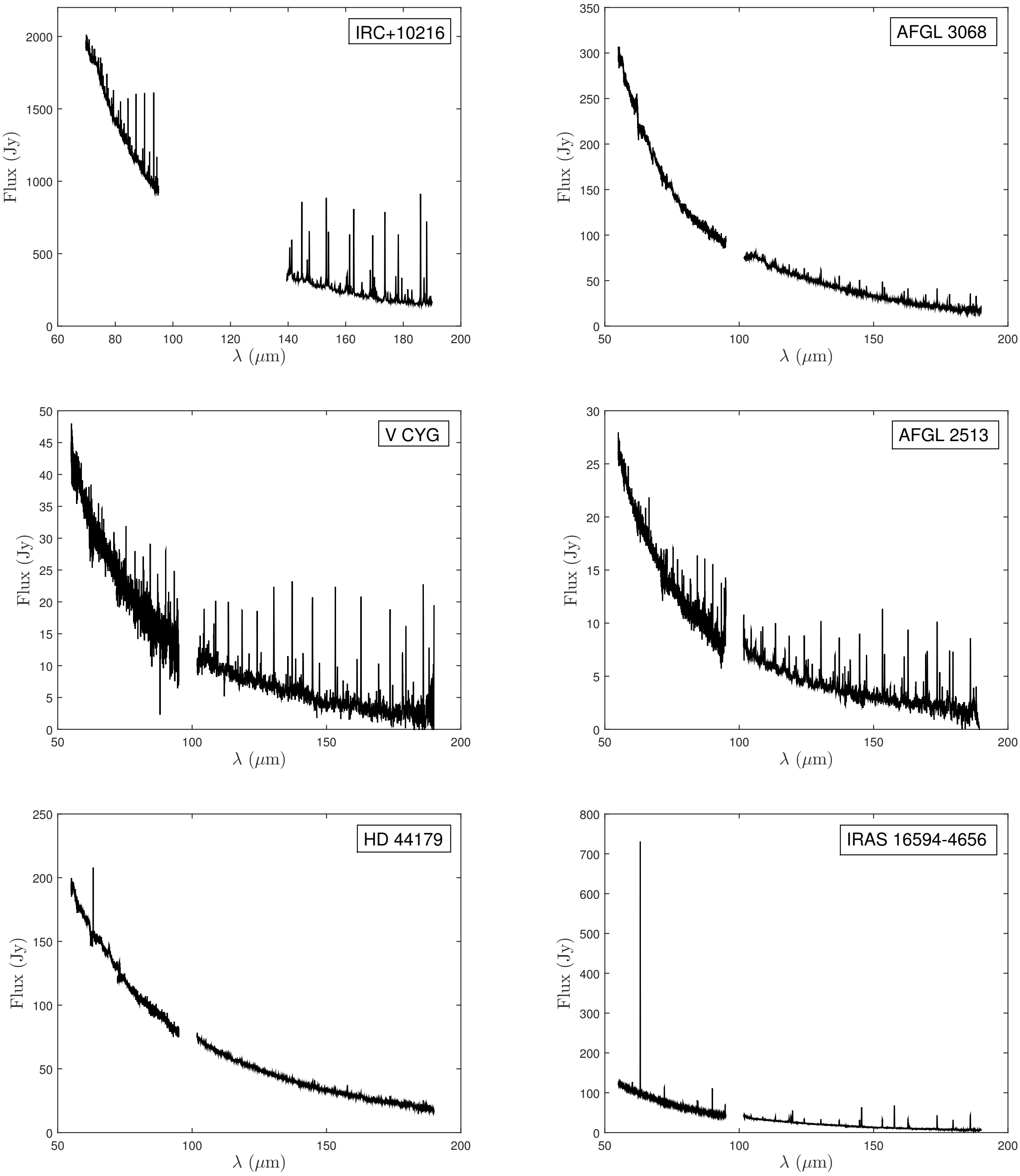
IRC+10216
AFGL 3068
V CYG
AFGL 2513
HD 44179
IRAS 16594-4656
Flux (Jy)
λ (μm)

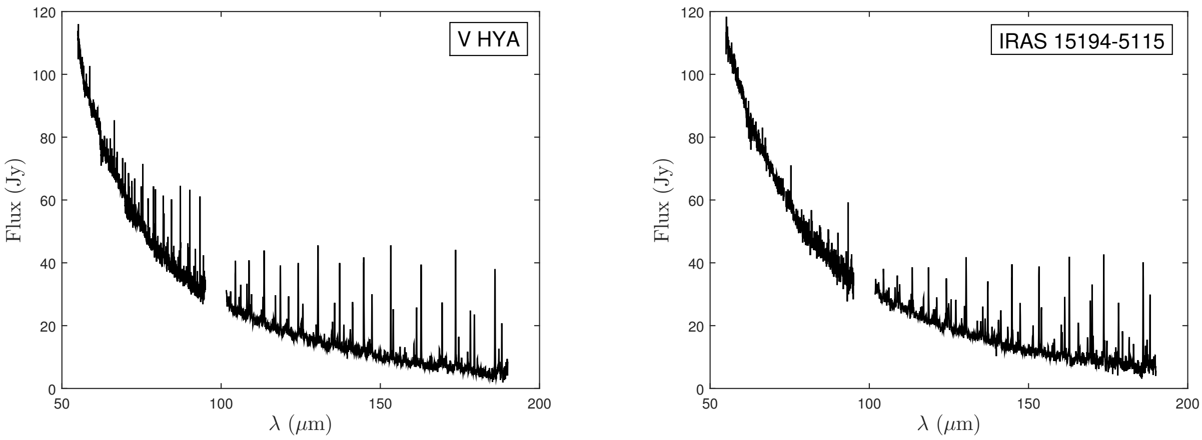
V HYA
Flux (Jy)
λ (μm)
IRAS 15194-5115
Flux (Jy)
λ (μm)